Measurement of the $H \to WW^* \to l\nu l\nu$ decay using same-flavour leptons in pp collisions at $\sqrt{s} = 13$ TeV with the ATLAS detector

Kla Karava

St Cross College

University of Oxford

A thesis submitted for the degree of

Doctor of Philosophy

Trinity 2023

Abstract

Higgs boson production via gluon-gluon fusion and vector-boson fusion in the $H \rightarrow WW^* \rightarrow l\nu l\nu$ decay mode is measured in the same-flavour channel, where the two leptons are either both electrons or both muons. The proton-proton collision data used in this analysis were produced at the Large Hadron Collider with a centre-of-mass energy of 13 TeV and recorded by the ATLAS detector between 2015 and 2018, corresponding to an integrated luminosity of 139 fb^{-1}. This thesis utilizes the traditional cut-based approach, which involves defining event selection criteria purely based on kinematic or geometric observables. The goal of this analysis is to measure the total cross-sections of the gluon-gluon fusion and vector-boson fusion Higgs production modes and compare them to the values predicted by the Standard Model.

Acknowledgements

First of all, I would like to thank Prof. Chris Hays for believing in me and giving me this opportunity to fulfil my teenage dream of pursuing a doctorate in physics. I am grateful for all your supervision and guidance throughout all these years. I will be forever indebted to your attention to detail and rigour as well as your kindness and patience. I also would like to thank my directors of studies back at Cambridge, Prof. Paul Wood and Prof. Mete Atatüre, for setting up this long and winding path for me in the first place. Looking back from now, I could not imagine how my life would have turned out on a different path at all. I also need to thank Prof. Chris Ford for your supervision during my master's degree and for making it possible for me to continue my study into DPhil.

Thanks to the members of the ATLAS HWW group, with Hayden, Carsten, David, Tae, and Gabija in particular, for the support throughout all these long years. The completion of this thesis would not be possible without all your help. And I would like to thank Jeanette, Max, Emma, and Doug of the ATLAS JetEtmiss group for helping me settle in during my first year. I learned a lot from all of you during my time at the group. Thanks to Sue and Kim at the Oxford Particle Physics group for being the nicest admins one can ever find. And thanks to Surapat and Piriya for keeping company during my year abroad at CERN. Thanks for introducing me to the love of my life called ski and following me to the rough slopes later when I overtook both of you on the skill curve.

For my friends at Oxford, thanks to Nurfikri and Mariyan for going to Five Guys with me every Friday and helping me debugging all the codes in my first year. Thanks to Fabio for being the best tennis hitting partner I could find and for your constant stream of dank memes sent to me every half an hour. I might have been bored to death during lockdown if my flatmate had not been gone by

the name Iwan. Thanks for all the colourful moments during our time together in Summertown, especially the daily kitchen-sink sports banter and the rooftop (inflatable) pool party and the 'chuck ball' session every afternoon in the park that made me feel a step closer to becoming Tom Brady.

This DPhil would not be possible without the financial support from the Institute for the Promotion of Teaching Science and Technology and the Royal Thai Government. Special thanks to Ajarn Wudhibhan and Ajarn Suwan for giving me this opportunity to study abroad and pursue my dream.

I would like to thank my mum and my late dad for raising me to be the person I am today. Thanks for unconditionally supporting me in whatever path I choose to walk on. And lastly, I would like to thank Tha. You show me that there is still meaning to be found in this otherwise meaningless world.

Contents

List of Figures

List of Tables

« Le monde extérieur avait ses propres lois, et ces lois n'étaient pas humaines. »

— Michel Houellebecq,
Les Particules élémentaires

1 Introduction

The first direct observation of the Higgs boson was made by the ATLAS [1] and CMS [2] experiments at CERN in 2012 using the Run-1 dataset consisting of proton-proton (pp) collisions at centre-of-mass energies of 7 and 8 TeV. The mass of this Higgs boson was measured to be approximately 125 GeV, consistent with the mass of the Standard Model (SM) Higgs boson predicted by the electroweak fit of the SM.

From 2015 through 2018, Run-2 of the Large Hadron Collider (LHC) produced pp collisions at a centre-of-mass energy of 13 TeV, and the ATLAS detector collected data corresponding to an integrated luminosity of 139 fb^{-1}. One of the primary goals of the ongoing LHC programme is to conduct precision measurements of the properties of the Higgs boson in order to constrain potential beyond-the-SM (BSM) processes. Any deviations observed in these precision measurements will indicate such BSM phenomena.

The analysis described in this thesis is part of the ATLAS Higgs programme consisting of measurements of several production mechanisms: single Higgs bosons, Higgs bosons in association with two quarks, and Higgs bosons in association with a W or Z boson. By combining these results with many other ATLAS measurements, a comprehensive and general set of constraints can be placed on the contribution of new physical processes to final states with SM particles.

For a Higgs boson with a mass of 125 GeV, the WW^* decay mode[1] has the second largest branching fraction (22%) [3], making it a prime candidate for the Higgs observation. This channel provided the most precise Higgs boson cross-section measurement in Run-1 [4]. The signal purity is highest when the W bosons decay leptonically ($W \to l\nu$ where l is an electron, muon, or a leptonically decaying τ-lepton). However, the $H \to WW^* \to l\nu l\nu$ decay suffers from poorer mass resolution than other decay channels because of the presence of neutrinos in the final-state.

This thesis presents a study of the $H \to WW^* \to l\nu l\nu$ decay channel using Run-2 data. The Higgs boson is produced via the two most dominant production modes: gluon-gluon fusion (ggF) and vector-boson fusion (VBF). The ggF process probes the Higgs boson couplings to heavy quarks, particularly the top quark, whereas the VBF process probes the couplings to the W and Z vector bosons. This thesis focuses on the final state where the two leptons are of the same flavour. Since a dedicated same-flavour analysis has not yet been conducted for Run-2 data, a preliminary study of the same-flavour channel is performed by following the well-established methodology of the different-flavour analysis in Run-2 [5, 6] as well as the methodology of the same-flavour analysis in Run-1 [7]. The primary goal of the analysis is to measure the signal strength parameters of the ggF and VBF production modes, defined as the ratio of the measured cross-section times the $H \to WW^*$ decay branching fraction to that predicted by the SM.

This thesis is structured as follows. Chapter 2 provides an overview of the theoretical aspects of the SM and the properties of the Higgs boson. Chapter 3 describes the different components of the ATLAS detector as well as the methods and techniques involved in the reconstruction of the different types of particles. Chapter 4 outlines the overall strategy of the $H \to WW^* \to l\nu l\nu$ same-flavour analysis, which includes descriptions of signal and background processes as well as how event selection criteria are defined in order to construct different analysis regions to be used in the analysis. Chapter 5 describes the sources of systematic uncertainties in the measurements. Chapter 6 builds on the analysis regions and

[1] One of the W bosons (denoted by an asterisk) must be off-shell because the mass of the Higgs boson is smaller than that of two W bosons.

systematic uncertainties defined in the previous two chapters to perform a statistical analysis based on the maximum likelihood formalism to produce final results. And lastly, the thesis is concluded in Chapter 7.

Author's contributions

I was one of the main analyzers of the $H \to WW^* \to l\nu l\nu$ same-flavour analysis, which was part of the ATLAS HWW legacy analysis. I was tasked with a purely cut-based approach, which is to serve as a cross-check to the new approach based on machine learning techniques employed by the other group members. Since the same-flavour channel had not been studied in Run-2 before, my supervisor and I had to design and develop an overall analysis strategy from scratch. This started with the construction of signal regions for different categories based on jet multiplicity and dominant Higgs production modes. Several sets of event selection requirements were studied and optimized before the set reported in this thesis was finalized. I was in charge of designing the $N_{\text{jet}} = 0$, $N_{\text{jet}} = 1$, and $N_{\text{jet}} \geq 2$ VBF-enriched categories, while my supervisor's other student, Hayden Smith, was tasked with the $N_{\text{jet}} \geq 2$ ggF-enriched category. Hayden and I worked in parallel in developing the two $N_{\text{jet}} \geq 2$ categories since they need to be mutually exclusive to one another. Once the analysis regions were finalized, I worked on deriving systematic uncertainties for all N_{jet} categories. Before a fit to observed data could be performed, I conducted validation studies by using the so-called hybrid fits for the different N_{jet} categories separately. And lastly, I developed and optimized the statistical analysis for the combined measurement of the signal strength parameters of the ggF and VBF production modes.

In my first year as a DPhil student, I had to work on a qualification task in order to gain an ATLAS author status. I was part of the JetEtmiss group working on improvements of the performance of missing transverse momentum reconstruction in ATLAS Run-2. I worked on the development and optimization of the working points that were designed to suppress pile-up jets by employing the jet-vertex tagging (JVT) and forward-JVT (fJVT) algorithms. In addition,

I also worked on the derivation of systematic uncertainties associated with the different JVT and fJVT working points for the group. And during the latter stage, the particle flow algorithm was introduced as a new recommendation for jet reconstruction in ATLAS, and I performed optimization and derived systematic uncertainties for the working points to be used with particle flow jets. The results of this study can be found in Section 3.3.6.

2
Theory overview

This chapter provides the theoretical foundation on which the $H \to WW^* \to l\nu l\nu$ analysis is based. A brief, qualitative overview of the Standard Model of particle physics as well as the reason why the Higgs boson is needed for its completeness are presented in Section 2.1. The various properties of the Higgs boson discovered at the LHC are discussed in Section 2.2.

2.1 The Standard Model

The Standard Model (SM) is a quantum field theory that provides a mathematical framework to explain and calculate the properties of all known elementary particles and their interactions. Elementary particles can be categorized according to their spin-statistics into fermions and bosons, which are half-spin and integer-spin particles respectively.

The elementary fermions can be further classified into two groups of six depending on how they interact: quarks and leptons. Quarks carry colour charge in addition to conventional electric charge and can interact via the strong interaction as well as the electroweak interaction. On the other hand, leptons do not possess colour charge. Among the six leptons, e, μ, and τ carry electric charge and can interact via both the electromagnetic and weak interactions. However, the remaining

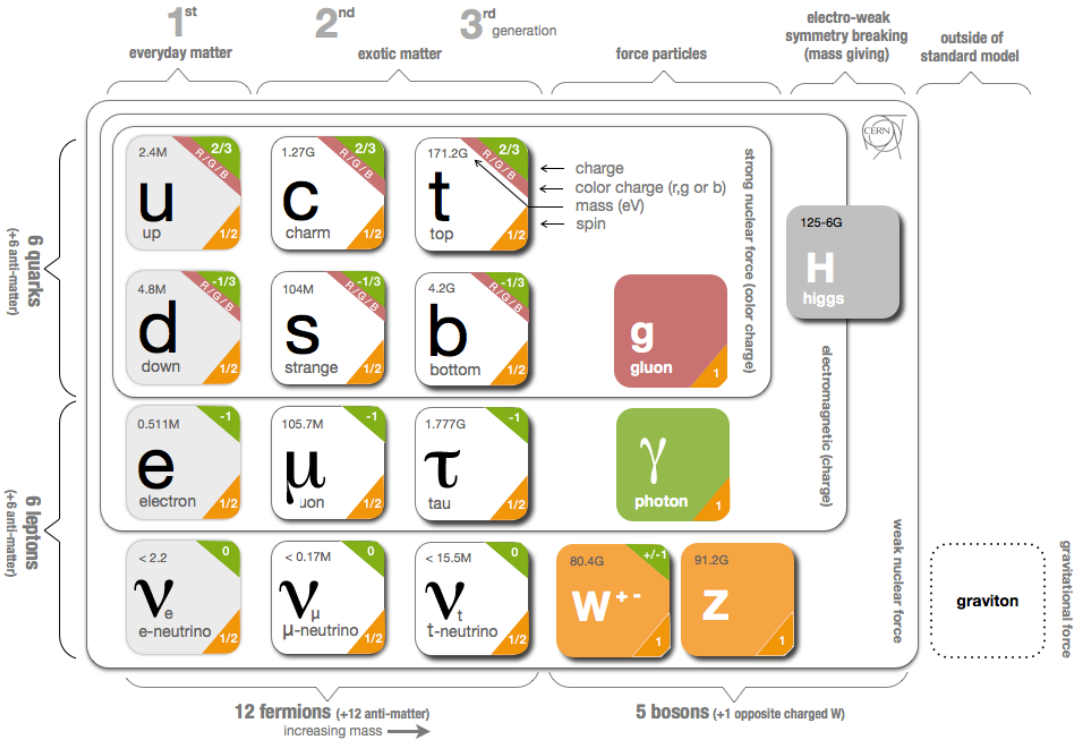

Figure 2.1: The elementary particles in the Standard Model [8].

three neutrinos ν are neutral and can only interact via the weak interaction. The twelve fermions can be split into three so-called *generations* according to the mass hierarchy as shown in Figure 2.1.

Gauge bosons are spin-1 particles that act as mediators of the interactions between particles in the SM. The strong interaction is mediated by gluons, the weak interaction by the W and Z bosons, and the electromagnetic interaction by photons. The strong interaction is described by an $\mathrm{SU(3)_C}$ group, where C denotes colour charge, in the theory known as *quantum chromodynamics* (QCD). The electromagnetic and weak interactions can be merged into a unified electroweak interaction. In terms of gauge group, the electroweak interaction is described by an $\mathrm{SU(2)_L} \times \mathrm{U(1)_Y}$ group, where L denotes that the gauge bosons interact with chiral left-handed particles only and Y refers to hypercharge. Therefore, the overall gauge group of the SM is $\mathrm{SU(3)_C} \times \mathrm{SU(2)_L} \times \mathrm{U(1)_Y}$.

The caveat to the SM is that these elementary particles are inherently massless. The fermion and gauge boson mass terms are forbidden in the SM Lagrangian

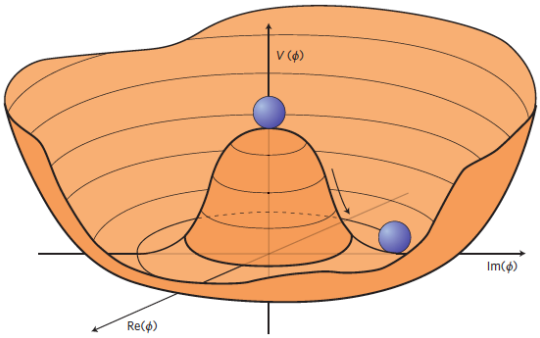

Figure 2.2: The 'Mexican hat' Higgs potential [10].

because they would violate gauge invariance. QCD and its $SU(3)_C$ gauge group are sufficient for describing the strong interaction since gluons are found to be massless. However, things are more complicated with the electroweak interaction. The physical photon is massless, but the W and Z bosons are massive and the Z boson can also interact with right-handed particles. This means that the gauge bosons prescribed in the $SU(2)_L \times U(1)_Y$ theory cannot readily be the physical gauge bosons that we observe. These conundrums signal a missing piece in the SM.

These problems are solved by introducing a scalar field called the *Higgs field* to the SM. The Higgs field is incorporated into the SM though the introduction of a new electroweak SU(2) doublet. By choosing a particular value of the Higgs potential from which perturbations can be made (i.e. vacuum expectation value v)[1], the symmetry of the potential is broken. This prompts a mixing of the neutral gauge bosons of the $SU(2)_L$ and $U(1)_Y$ groups, and the physical Z boson and photon are formed as a result. Another consequence of spontaneous symmetry breaking is it gives rise to mass terms for the W and Z bosons in the Lagrangian while the photon remains massless. The Yukawa interaction terms between the Higgs boson and fermions give rise to the masses of the fermions. A good introduction to the SM and the Higgs mechanism as well as their mathemathical formulation can be found in [9].

[1]The choice of the vacuum expectation value v can be made arbitrarily because the Higgs potential is azimuthally symmetric (having a shape of the 'Mexican hat'). See Figure 2.2.

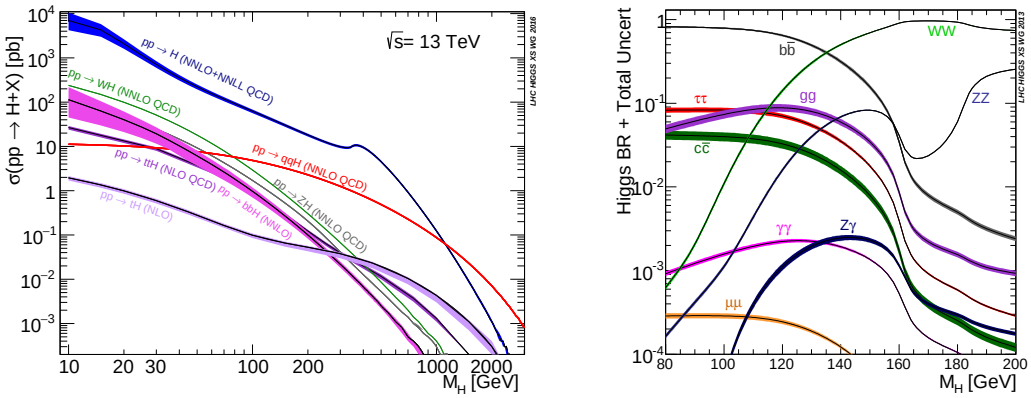

(a) Production cross-sections [12] **(b)** Decay branching ratios [3]

Figure 2.3: Standard Model predictions of Higgs boson (a) production cross-sections at $\sqrt{s} = 13$ TeV and (b) decay branching ratios as a function of Higgs boson mass.

2.2 Higgs boson

The Higgs boson must be a scalar boson (spin-0) because the mass of a particle that interacts with it has to be independent of the orientation of the frame of measurement, which is defined by the spin of the Higgs boson if it exists. Its mass is, however, a parameter in the SM and can only be determined experimentally. The Higgs mass was measured in LHC Run-1 to be 125.09±0.21(stat.)±0.11(syst.) GeV by the ATLAS and CMS experiments [11].

2.2.1 Higgs production modes

There are four main processes through which the Higgs boson can be produced: gluon-gluon fusion (ggF), vector-boson fusion (VBF), associated production with a vector boson (VH), and associated production with top quarks ($t\bar{t}H$). The SM-predicted production cross-sections of the different modes at the centre-of-mass energy of LHC Run-2 are shown in Figure 2.3a. The two most dominant production modes, ggF and VBF, are the main focus of this analysis.

In the ggF production mode, the Higgs boson is produced via a virtual heavy-quark (t or b) loop, which is in turn generated by a pair of gluons from the two colliding protons, as shown in Figure 2.4a. This is the production mode with the largest cross-section at the LHC due to the large top quark Yukawa coupling

and large QCD colour factors associated with vertices involving gluons. The ggF production process thus probes Higgs boson couplings to heavy quarks. Additional jets accompanying the Higgs boson are possible due to initial state radiation.

The next most dominant production mode at the LHC is VBF. The Higgs boson is produced as a result of a merging of two vector bosons, each radiated from a quark inside the proton via a weak interaction, as shown in Figure 2.4b. The VBF process is essentially a scattering of two quarks without QCD colour charge exchange between them, leading to a unique topology where two high-energy hadrons are produced almost parallel to the beam line. The VBF process probes Higgs boson couplings to the W and Z bosons.

In the VH production mode, the Higgs boson is radiated from a W or Z boson, which is produced from an annihilation of a quark and anti-quark, as shown in Figure 2.4c. This process is also referred to as *Higgs-strahlung* due to its resemblance to bremsstrahlung radiation ($e^{\pm} \rightarrow e^{\pm}\gamma$). The VH process also probes Higgs boson couplings to the W and Z bosons.

And lastly, the $t\bar{t}H$ production mode occurs when each of the two colliding gluons splits into a pair of a top quark and anti-top quark, and each (anti-)top quark from each pair fuses to form the Higgs boson, as shown in Figure 2.4d. This $t\bar{t}H$ process provides a direct opportunity to study the Higgs-top Yukawa coupling.

2.2.2 Higgs decay modes

Since the Higgs boson has a very short lifetime on the order of 10^{-22} s [12], it is not possible to directly observe it with current technology. Its existence as well as properties are inferred from the intermediary and final-state particles it produces. There are a number of terms in the SM Lagrangian that describe interactions between the Higgs boson and other elementary particles. The decay branching ratios of the Higgs boson to various particles depend on both the masses of the particles and of the Higgs boson itself, as shown in Figure 2.3b. The decay branching ratios predicted by the SM for a Higgs boson with a mass of 125 GeV are given in Table 2.1. The 2012 Higgs discovery was made by analysing the $H \rightarrow ZZ \rightarrow 4l$

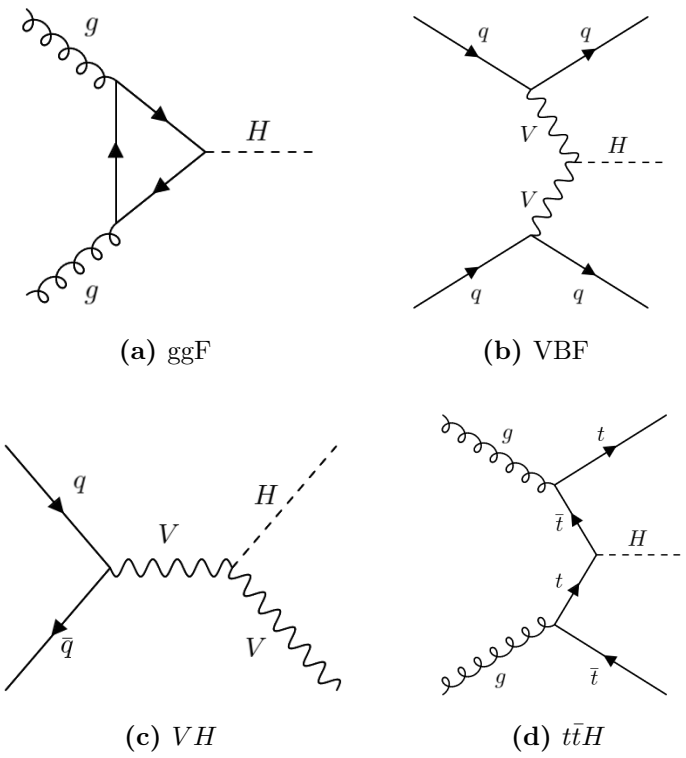

(a) ggF **(b)** VBF

(c) VH **(d)** $t\bar{t}H$

Figure 2.4: Leading-order Feynman diagrams for the four main Higgs production modes: (a) gluon-gluon fusion (ggF); (b) vector-boson fusion (VBF); (c) associated production with a vector boson (VH); and (d) associated production with top quarks ($t\bar{t}H$).

Table 2.1: Standard Model predicted decay branching ratios for the Higgs boson with a mass of 125 GeV [3].

Decay mode	Branching ratio	Rel. uncertainty
$H \to b\bar{b}$	5.77×10^{-1}	$^{+3.2\%}_{-3.3\%}$
$H \to WW$	2.15×10^{-1}	$^{+4.3\%}_{-4.2\%}$
$H \to \tau\tau$	6.32×10^{-2}	$^{+5.7\%}_{-5.7\%}$
$H \to ZZ$	2.64×10^{-2}	$^{+4.3\%}_{-4.1\%}$
$H \to \gamma\gamma$	2.28×10^{-3}	$^{+5.0\%}_{-4.9\%}$
$H \to Z\gamma$	1.54×10^{-3}	$^{+9.0\%}_{-8.9\%}$
$H \to \mu\mu$	2.19×10^{-4}	$^{+6.0\%}_{-5.9\%}$

and $H \to \gamma\gamma$ decay modes because these two modes produce final-state particles that can be measured very precisely in the detector, resulting in a mass resolution of approximately 1–2% [13]. The $H \to WW^* \to l\nu l\nu$ decay, however, has a much larger mass resolution of about 20% due to the neutrinos in the final state [13].

3

The LHC and ATLAS experiment

Motivated by the development of the Standard Model in the second half of the 20$^{\text{th}}$ century, numerous particle accelerators were built to validate it. Probably the most well-known and significant accelerator of all was the Large Electron-Positron collider (LEP) at CERN[1] completed in 1989. It was then the largest particle accelerator ever built and was able to reach a centre-of-mass energy of 209 GeV by the end of its lifetime. Its greatest achievement was in the precise measurements of the W and Z boson masses as well as their couplings, which were fully compatible with the Standard Model predictions [14]. However, one thing the LEP was unable to find was the elusive Higgs boson, which was the final missing piece of the Standard Model. In order to achieve this, the energy and the number of collisions had to be higher. This led CERN to commission the construction of the Large Hadron Collider (LHC) as well as the conception of various experiments that make use of it.

This chapter provides a brief description of the LHC (Section 3.1) and the ATLAS experiment (Section 3.2), of which this analysis is part. The methods involved in identifying and reconstructing different types of particles are described in Section 3.3.

[1]The acronym derives from the organization's original name in French, ***C**onseil **e**uropéen pour la **r**echerche **n**ucléaire*.

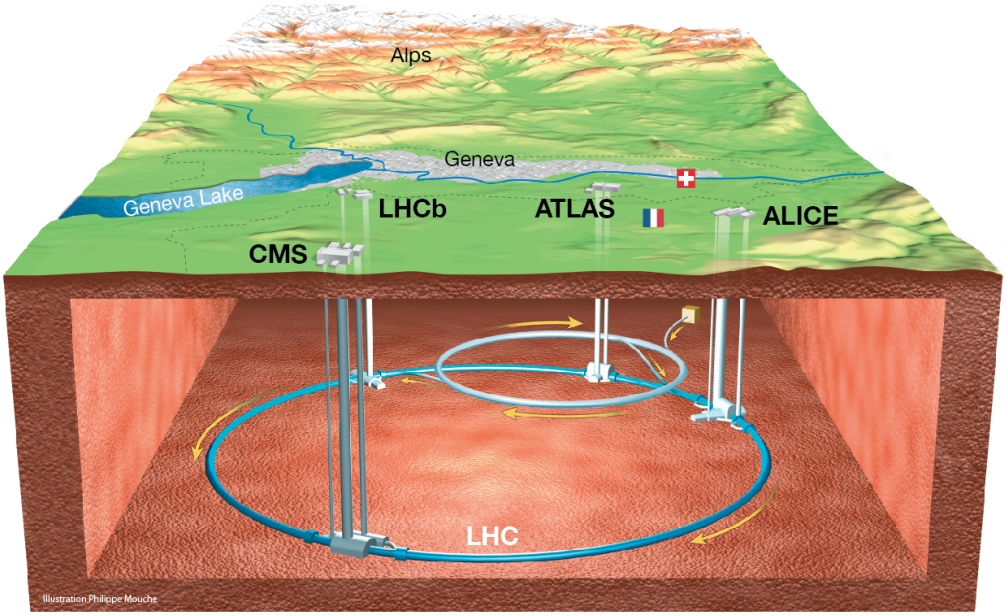

Figure 3.1: Schematic display of the LHC beneath the greater Geneva area on the France-Switzerland border [16]. The four main detectors of the LHC are labelled.

3.1 The Large Hadron Collider

The Large Hadron Collider [15], or more commonly known by its acronym LHC, is the largest and most powerful particle accelerator ever built to date, designed to be able to operate at a centre-of-mass energy $\sqrt{s}$ up to 14 TeV. The LHC is located at the site of the European Organization for Nuclear Research or CERN, straddling the France-Switzerland border near Geneva with its immense 27 km circumference as shown in Figure 3.1. It was built in the circular underground tunnel previously occupied by LEP. The depth from the earth surface to the tunnel ranges from 50 to 175 m, primarily to prevent cosmic rays from interfering with the experiments as well as to prevent harmful radiation originating from the experiments from reaching the inhabitants of the metropolitan area above.

The LHC was completed in 2008, and its first operational run (Run-1) took place between 2009 and 2013 with $\sqrt{s} = 7 - 8$ TeV, where it quickly fulfilled one of its primary goals by discovering the Higgs boson. Then, it was shut down in early 2013 for its two-year upgrade programme known as Long Shutdown 1 (LS1)

and restarted again for Run-2 which lasted from 2015 to 2018 with an increase in $\sqrt{s}$ to 13 TeV. Long Shutdown 2 (LS2) was initially planned for the start of 2019 until the end of 2020. However, due to the COVID-19 global pandemic, LS2 was prolonged, and the start of Run-3 was postponed to mid-2022. The $\sqrt{s}$ in Run-3 is only slightly increased to 13.6 TeV, but the integrated luminosity by the end of its run in 2025 is expected to be more than the first two runs combined. Long Shutdown 3 (LS3) is currently planned to commence in 2026 for major upgrades for the High-Luminosity LHC (HL-LHC) project [17], which is the succesor to the current LHC. The HL-LHC is designed to operate at $\sqrt{s} = 14$ TeV and generate a total integrated luminosity ten times larger than that of the LHC. The HL-LHC is scheduled to become operational in 2029.

The LHC ring contains two adjacent parallel beam pipes where two particle beams circulate in opposite directions. The two beams are brought into collision only at four interaction points (IPs) where the detectors of the four main experiments are located as shown in Figure 3.2. The four main experiments of the LHC are:

- ATLAS (*A Toroidal LHC ApparatuS*) [18]: a general-purpose detector for studying a wide range of Standard Model physics phenomena arising from pp collisions as well as searching for new particles and interactions beyond the Standard Model.

- CMS (*Compact Muon Solenoid*) [19]: also a general-purpose detector whose usage is similar to ATLAS but with a different magnet system design.

- LHCb (*Large Hadron Collider beauty*) [20]: a specialized detector dedicated to measurements of CP violation and rare decays of b-hadrons from pp collisions in the forward regions.

- ALICE (*A Large Ion Collider Experiment*) [21]: a heavy-ion detector designed for studying the physics of strongly interacting matter and quark-gluon plasma at extreme energy densities and temperature from collisions of lead ions.

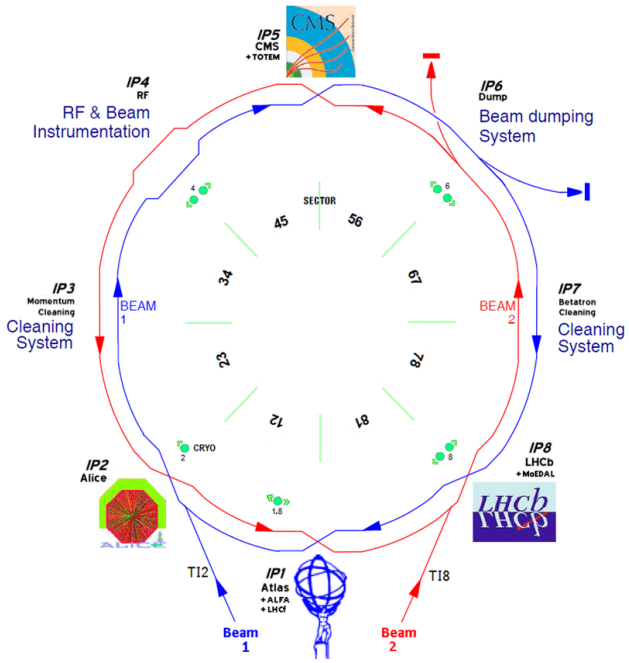

Figure 3.2: Schematic layout of the 8 interaction points (IPs) of the LHC [22]. The two proton beams shown in blue and red circulate in opposite directions. The four main LHC experiments ATLAS, ALICE, CMS, and LHCb are installed at IP1, IP2, IP5, and IP8 respectively. Other IPs are used for maintenance or research & development purposes.

3.1.1 Operation of the LHC

The high-energy protons used in these experiments do not begin their journey in the LHC itself but are prepared through a series of smaller accelerators as shown in Figure 3.3. Protons are first obtained by passing hydrogen gas through a strong electric field to remove electrons from hydrogen atoms. The protons are accelerated to an energy of 50 MeV by the linear accelerator LINAC 2[2]. Then, these protons are injected into a sequence of circular acccelerators which push their energy up further: the Proton Synchrotron Booster (PSB) to 1.4 GeV; the Proton Synchrotron (PS) to 25 GeV; and the Super Proton Synchrotron (SPS) to 450 GeV. After the SPS, the protons are transferred to the two beam pipes of the LHC, which accelerates them further to the final energy of 6.5 TeV for each beam. The accelerators are fitted with metallic chambers containing an electromagnetic field; these are known

[2]LINAC 2 was used in LHC Run-2 upon which this analysis was based. Since 2020, LINAC 4 has been used to accelerate hydrogen anions H^- instead, and a higher energy of 160 MeV is achieved. The two electrons are removed during injection into the Proton Synchrotron Booster.

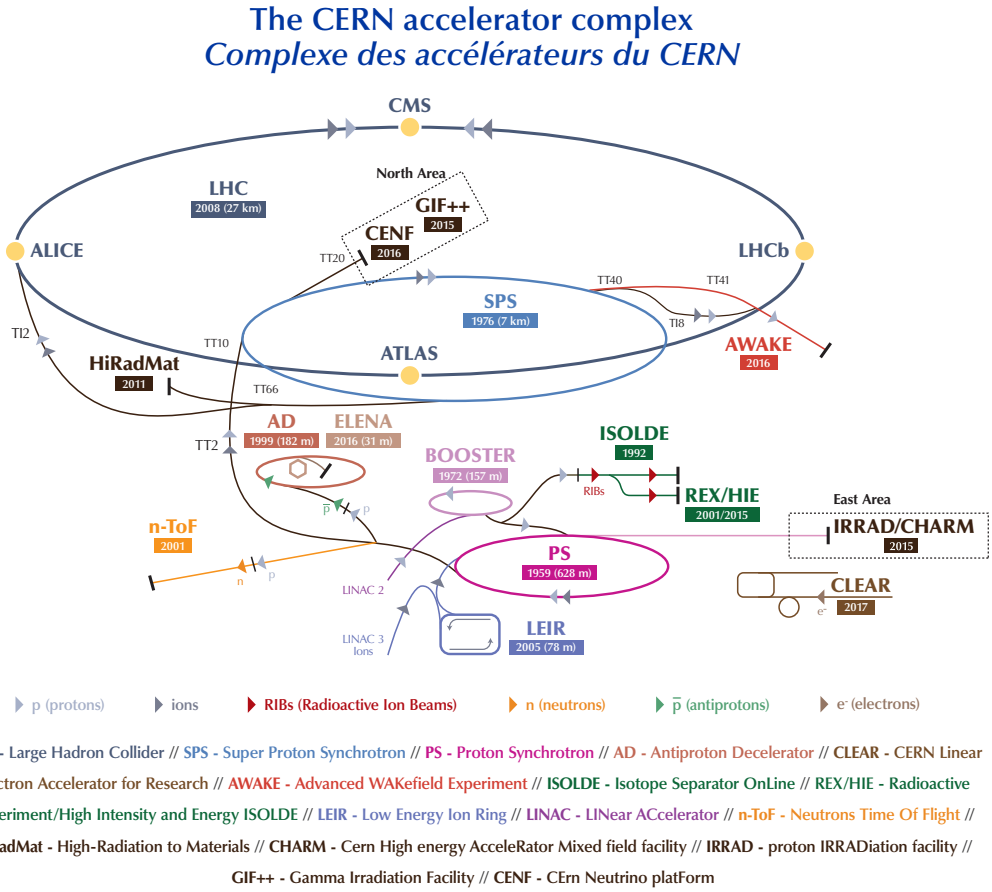

Figure 3.3: Schematic layout of the CERN accelerator complex in LHC Run-2 in 2018 [23], including the relative location of the experiments as well as the main elements of the LHC accelerator chain. The proton beams are denoted with grey arrows.

as radiofrequency (RF) cavities. Charged particles traversing this field receive an electrical impulse that accelerates them.

The LHC is not a perfect circle. Instead, it consists of eight 2.45-km-long arcs and eight 545-m-long straight sections. The straight sections are where the eight IPs are (see Figure 3.2). At IP4 there are four cryomodules, each containing four RF cavities (two for each beam pipe) used for accelerating the protons in the LHC ring. Cryomodules are cylindrical refrigerators that cool the RF cavities to 4.5 K so that they operate in a superconducting state. In order to avoid collisions with atmospheric gas molecules, the two beam pipes are operated in ultra-high vacuum conditions on the order of 10^{-10} to 10^{-11} mbar. At each of the eight arcs, 154 dipole magnets are used to steer the proton beams into a near circular path.

Each dipole magnet is 15 m long and their coils are made of niobium-titanium (NbTi) filaments. Superfluid helium is used to cool the dipole magnets to 1.9 K to ensure superconductivity. Under this condition, the dipoles can generate a magnetic field up to 8.3 T. In addition, various multipole magnets such as quadrupoles and sextupoles are used for focusing the beams and maintaining their orbits. These multipole magnets are especially important at the four main IPs where the two proton beams are brought to collide with one another.

Since the RF cavities are used to accelerate the proton beams, the beams are not continuous streams but are instead clumped together in bunches. At its full intensity, each beam has 2808 bunches, with about 10^{11} protons per bunch. The bunches are grouped into a discrete number of bunch trains. Each bunch in a train are separated by 25 ns, which would result in peak crossing rate of 40 MHz. However, since there are gaps between trains, the average crossing rate at a given IP for protons with a revolution frequency of 11.245 kHz[3] is 31.6 MHz [15].

3.1.2 Luminosity

The intensity of the colliding proton beams is referred to as the instantaneous luminosity $\mathcal{L}$, which is related to the rate of production of a given interaction i by:

$$\frac{\mathrm{d}N_i}{\mathrm{d}t} = \sigma_i \mathcal{L}(t) \tag{3.1}$$

where σ_i and N_i are the production cross-section and the number of events produced by interaction i respectively. Integrating this equation with respect to time yields:

$$N_i = \sigma_i \int \mathcal{L}(t)\mathrm{d}t = \sigma_i L \tag{3.2}$$

where $L = \int \mathcal{L}(t)\mathrm{d}t$ is referred to as the integrated luminosity. The instantaneous luminosity is a function of various parameters pertaining to properties of the LHC itself:

$$\mathcal{L} = \frac{N_b^2 n_b f_{\mathrm{rev}} \gamma_{\mathrm{rel}}}{4\pi \epsilon_{\mathrm{N}} \beta^*} F \tag{3.3}$$

[3]This value of frequency is that of a proton with an energy of 6.5 TeV completing a full lap of the 27-km-long LHC ring.

where N_b is the number of protons per bunch; n_b is the total number of bunches per beam; f_{rev} is the revolution frequency of the bunches around the LHC; γ_{rel} is the relativistic factor; ϵ_{N} is the normalized transverse beam emittance, which refers to the area spread by the protons in a bunch in position-and-momentum phase space; β^* is the beta function[4] at the collision point; and F is the geometric luminosity reduction factor to account for the fact that the beams collide at an angle. The values of ϵ_{N} and β^* at a given IP are 3.75 μm and 0.55 m respectively [15]. For the proton beams with properties described in Section 3.1.1, this results in an instantaneous luminosity of about 10^{-34} cm^{-2}s^{-1}.

If the interaction of interest i in Equation 3.2 is a Higgs signal process which has a very small production cross-section σ_i, the luminosity has to be very high for the detector to observe such events. The luminosity can be increased in a few ways such as increasing the number of bunches or protons per bunch, or reducing the transverse area at the IP by squeezing the beams into smaller sizes.

Over the course of Run-2 between 2015 and 2018, the LHC delivered an integrated luminosity of 156 fb^{-1}. The ATLAS detector was able to record 147 fb^{-1}, which is 94% of the total delivered luminosity. However, only a total of 139 fb^{-1} passed the quality criteria set by ATLAS and was declared *good for physics* [24] as shown in Figure 3.4a.

3.1.3 Pile-up

There are, however, some drawbacks to increasing the luminosity of the accelerator. With high luminosity, the chance that there are also additional pp interactions other than a single *hard-scatter interaction*[5] of interest per bunch crossing increases. These additional pp interactions are referred to as *pile-up*. Pile-up can interfere with the measurement of the hard-scatter interaction and therefore should be suppressed by the detector. There are two types of pile-up:

[4] The transverse size of the beam is given by $\sqrt{\epsilon_{\text{N}}\beta^*}$.

[5] The hard-scatter interaction is the pp interaction in a given bunch that has the largest $\sum p_{\text{T}}^2$ of detected particles associated with it.

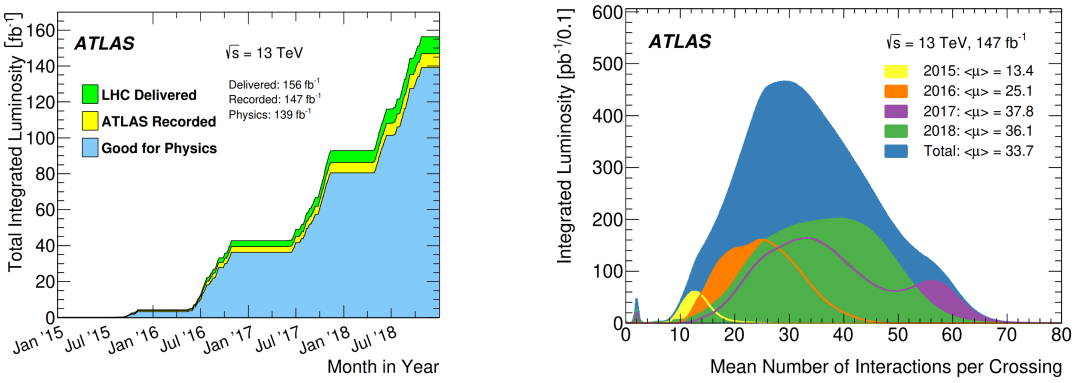

(a) **(b)**

Figure 3.4: Run-2 pp collision data-taking at $\sqrt{s} = 13$ TeV between 2015 and 2018 (Run-2) showing: (a) the cumulative integrated luminosity as a function of time delivered to the LHC (green), recorded by the ATLAS detector (yellow), and classified as good data for physics (blue); (b) the luminosity-weighted distribution of the mean number of interactions per bunch crossing $\langle\mu\rangle$ by year of data-taking [24].

- In-time pile-up: additional interactions originating from the same bunch crossing as the hard-scatter interaction.

- Out-of-time pile-up: additional interactions from the previous or following bunch crossing due to the latency of the particle detection system, i.e. the time it takes for the system to reconstruct and identify particles might be longer than the bunch spacing of 25 ns.

The amount of pile-up can be quantified with the mean number of interactions per bunch crossing $\langle\mu\rangle$, which is given by:

$$\langle\mu\rangle = \frac{\mathcal{L}\sigma_{pp}}{n_b f_{\text{rev}}} \tag{3.4}$$

where $\mathcal{L}$ is the total instantaneous luminosity; n_b is the number of bunches; f_{rev} is the revolution frequency of the proton bunches in the LHC; and σ_{pp} is the inelastic pp cross-section, which is 80 mb at $\sqrt{s} = 13$ TeV [25]. The average number of pile-up interactions per bunch crossing in Run-2 is 33.7 as shown in Figure 3.4b.

3.2 The ATLAS detector

The ATLAS detector [18] is one of the two general-purpose detectors of the LHC, located at the interaction point (IP) closest the CERN main site in Meyrin near Geneva, Switzerland. The ATLAS detector has an octagonal prism shape with a length of 44 m and a diameter of 25 m, with a total weight of around 7000 tonnes. It is designed to study a wide range of Standard Model physics phenomena as well as to search for new physics beyond the Standard Model. Its greatest achievement came in 2012 when it announced the discovery of the Higgs boson with a mass of 125 GeV [1]. Since then, one of its primary focuses has been in the precision measurement of the properties of the Higgs boson.

The ATLAS detector is designed to cover nearly the entire solid angle around the collision point at its centre. Its main components include an inner tracking detector surrounded by a thin superconducting solenoid, electromagnetic and hadronic calorimeters, and a muon spectrometer incorporating three large air-core toroidal superconducting magnets as shown in Figure 3.5.

The point where the two protons collide is called the *primary vertex*. Then, the intermediate particles that are the results of the pp collision at the primary vertex may travel further briefly before decay into final-state particles. The points at which the intermediate particles decay are called the *secondary vertices*. Different types of final-state particles can be measured and reconstructed by the different components of the ATLAS detector.

3.2.1 Coordinate systems in ATLAS

The ATLAS detector defines a right-handed Cartesian coordinate system with the origin at the nominal primary vertex and the z-axis along the beam axis. The x-axis points towards the centre of the LHC ring and the y-axis points upwards. In addition, a spherical polar coordinate system (r, ϕ, θ) is also used, where ϕ is the azimuthal angle around the z-axis and θ is the polar angle measured with respect to the $+z$-direction.

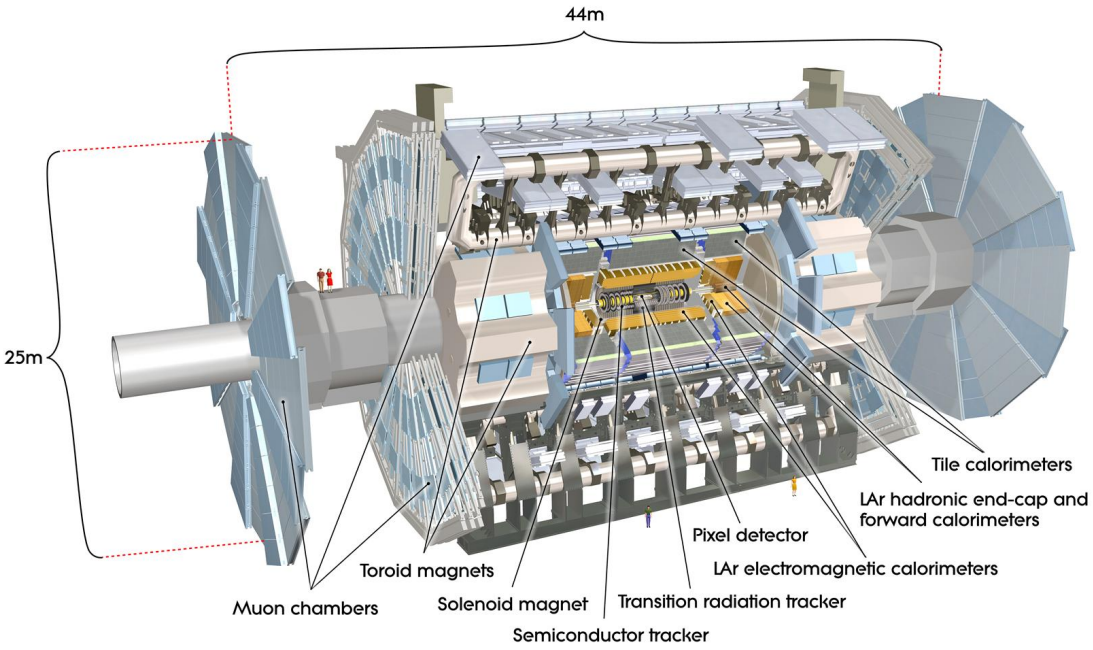

Figure 3.5: Computer generated image of the ATLAS detector and its key components inside [18].

Since actual collisions arise from partons (quarks) inside the protons and not between the protons themselves, the exact values of longitudinal momenta of the colliding partons are unknown. Therefore, the polar angle θ measured in the laboratory frame is not appropriate to represent of the kinematics of the zero-momentum frame of the colliding partons, i.e. because θ is not Lorentz-invariant.

In order to find a new variable that both measures the polar angle and is Lorentz-invariant, *rapidity* is considered. It is defined in terms of the particle's energy E and momentum in the direction of the beam pipe p_z as:

$$y = \frac{1}{2} \ln \left(\frac{E + p_z}{E - p_z} \right) . \tag{3.5}$$

It can be shown that the difference between the rapidity of two particles, Δy, is Lorentz-invariant [26].

The concept of pseudorapidity η is closely related to rapidity y. Instead of defining in terms of energy and momentum, η is written as a function of the polar

angle θ that the particle makes with the beam axis:

$$\eta = -\ln\left[\tan\left(\frac{\theta}{2}\right)\right] . \tag{3.6}$$

For an ultra-relativistic particle, it can be shown that the two quantities become equivalent, $y \to \eta$ [26]. Therefore, the difference between the pseudorapidity of two ultra-relativistic particles, $\Delta\eta$, is also Lorentz-invariant. $\Delta\eta$ is used extensively in the analysis because we are normally concerned with the angular difference between two particles and not their individual values.

The pseudorapidity is defined such that $\eta = 0$ corresponds to $\theta = \pi/2$ which is the plane perpendicular to the beam axis, whereas $|\eta| \to \infty$ corresponds to the directions parallel to the beam axis. The ATLAS detector is able to cover up to $|\eta| < 4.9$.

The geometric distance in (η, ϕ) coordinates:

$$\Delta R = \sqrt{\Delta\phi^2 + \Delta\eta^2} \tag{3.7}$$

is also used to define the size of the cone spanned by a given pair of particles.

The x-y plane perpendicular to the beam axis is referred to as the *transverse plane*. Kinematic variables in the transverse planes are unaffected by a Lorentz boost along the z-axis, and the sum of the transverse momenta of all final-state particles is zero because the incoming protons (and partons) only travel longitudinally along the beam axis. The transverse momentum vector in Cartersian coordinates is given by:

$$\mathbf{p}_{\mathrm{T}} = (p_x, p_y) \tag{3.8}$$

with a magnitude of $p_{\mathrm{T}} = \sqrt{p_x^2 + p_y^2}$.

3.2.2 Magnet system

The ATLAS detector is equipped with a superconducting magnet system [27] that bends the trajectories of charged particle so that their momenta and their charges can be measured precisely. It consists of three components: the central solenoid, the barrel toroid, and the endcap toroids, as shown schematically in Figure 3.6. The central solenoid is located between the inner detector and electromagnetic

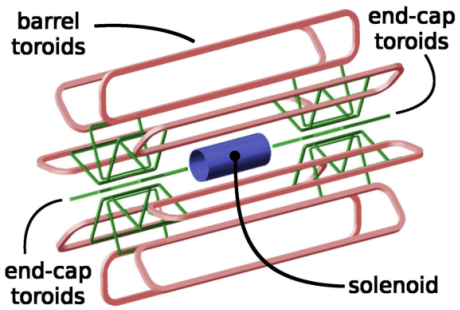

Figure 3.6: Schematic display of the ATLAS magnet system and its components [27].

calorimeter. It can provide a 2 T axial magnetic field to the inner detector, which bends the trajectories of charged particles in the transverse plane. The barrel and two end-cap toroids can provide the muon spectrometer with toroidal magnetic fields up to 3.5 T, which bend the trajectories of muons longitudinally.

3.2.3 Inner detector

The ATLAS inner detector (ID) [28] is the innermost component of the detector. It is designed to measure the trajectories or *tracks* of charged particles as well as to identify primary and secondary vertices from which these charged tracks originate. The ID is immersed in a 2 T axial magnetic field generated by the central solenoid. The ID consists of the silicon pixel detector, semiconductor tracker (SCT), and transition radiation tracker (TRT) as shown in Figures 3.7 and 3.8. The components of the ID are arranged differently in the two regions: barrel region, where the components are arranged concentrically; and end-cap region, where the components are horizontally stacked next to one another along the beam pipe.

3.2.3.1 Silicon pixel detector

The innermost sub-component of the ATLAS inner detector is the silicon pixel detector [32], covering the range of $|\eta| < 2.5$. Possessing the finest granularity of the sub-detectors, the pixel detector is designed to primarily identify and reconstruct secondary vertices from long-lived particles. It consists of three barrel layers ($|\eta| < 1.5$) and three end-cap discs ($1.5 < |\eta| < 2.5$) for either end, as shown in Figure

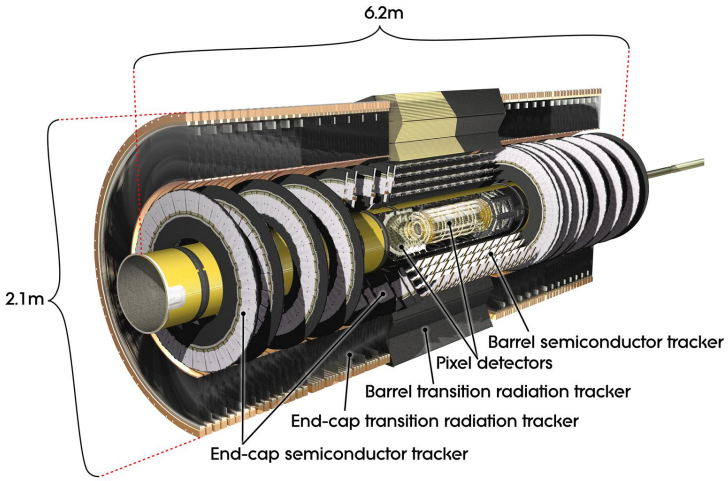

Figure 3.7: Computer generated image of the ATLAS inner detector with its sub-components inside [29].

3.9. When charged particles pass through doped silicon, they will create electron-hole pairs in the conduction band. Under an external electric field, the electron-hole pairs will drift towards the electrodes, and electric signals can be recorded.

In LHC Run-2, an additional layer called the insertable B-layer (IBL) [33] is introduced and is placed inside the innermost barrel layer of the original pixel detector to increase the resolution which helps improve the identification of b-jets (see Figure 3.10). The IBL covers the range of $|\eta| < 3.03$. The size of each silicon pixel is 50 μm × 250 μm with intrinsic spatial resolution of 10 μm and 75 μm in the r-ϕ and z directions respectively. There are about 12 million silicon pixels in the IBL.

The three outer barrel layers and three end-caps on either end are together made of about 80 million silicon pixels of the size 50 μm × 400 μm, corresponding to intrinsic spatial resolution of 10 μm and 115 μm in r-ϕ and z respectively.

3.2.3.2 Semiconductor tracker

The silicon micro-strip semiconductor tracker (SCT) surrounds the silicon pixel detector, covering the range of $|\eta| < 2.5$. It consists of four cylindrical barrel layers [36] and nine end-cap discs [37] on each side as shown in Figure 3.8. The SCT operates in a similar manner to the silicon pixel detector when measuring the trajectories of charged particles.

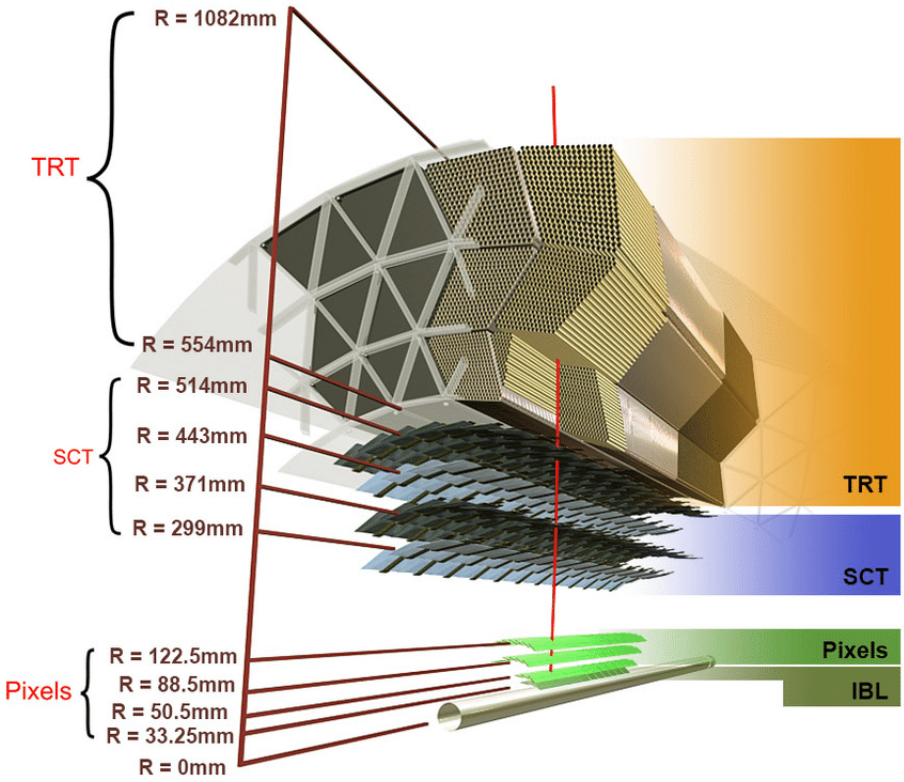

(a) Barrel region [30]

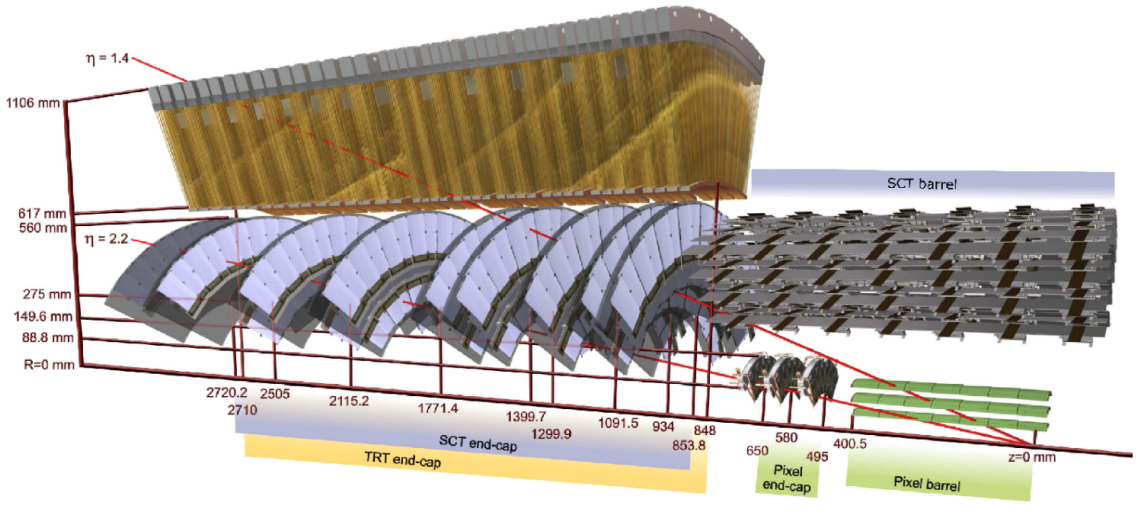

(b) End-cap region [31]

Figure 3.8: Schematic cut-away view of the ATLAS inner detector in the: (a) barrel region; (b) end-cap region. The distance between each of the components and the *pp* interaction point is stated.

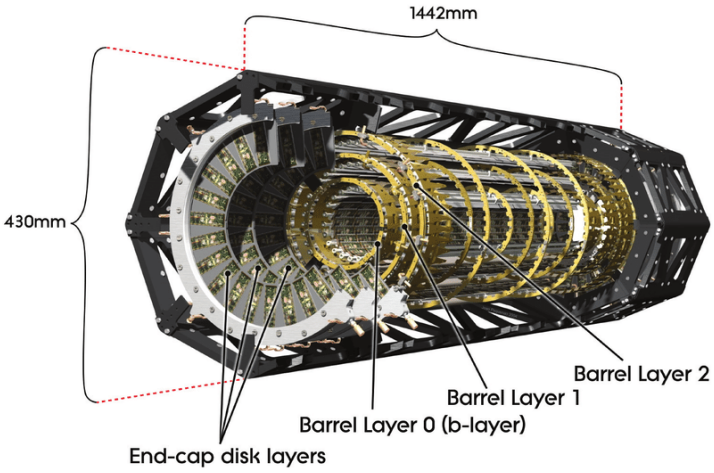

Figure 3.9: Computer generated image of the silicon pixel detector before the inclusion of the insertable B-layer (IBL) [34].

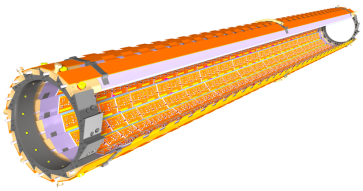

Figure 3.10: Computer generated image of the insertable B-layer (IBL) introduced to the silicon pixel detector for LHC Run-2 [35].

Each SCT module is made of two silicon strip sensors at a stereo rotation angle of 40 mrad to enable a point-in-space measurement as shown in Figure 3.11. The modules are mounted longitudinally on the barrel layers and radially on the end-cap discs. The intrinsic resolution of point-in-space measurements for each SCT module is 16 µm in the r-ϕ direction and 580 µm in the z direction. There are approximately a total of 6 million readout channels in the SCT.

3.2.3.3 Transition radiation tracker

The transition radiation tracker (TRT) [38] is the outer most component of the ID. It covers the range of $|\eta| < 2.0$. The TRT consists of about 300,000 straw drift tubes with a diameter of 4 mm, arranged parallel to the beam axis in the barrel region and radially in the end-cap region, as shown in Figure 3.8. Each tube is made from wound Kapton and reinforced with thin carbon fibres, and a

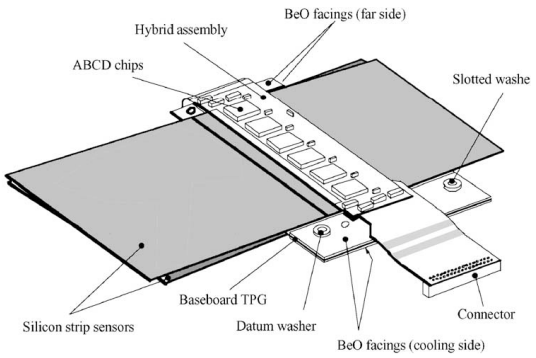

Figure 3.11: Sketch of a module of the semiconductor tracker (SCT) [36].

gold-plated tungsten wire is placed at its centre. The wall is kept at a voltage of -1.5 kV and the wire grounded. The tubes are filled with a mixture of gas: 70% Xe, 27% CO_2, and 3% O_2. In Run-1, several large leaks developed in some of the gas tubes used to supply Xe gas to the detector. In most cases, the leaks are located in inaccessible areas and repair is not possible. For these modules, Ar is used instead of Xe in the gas mixture to save cost [39].

When a charged particle passes through a straw tube, it ionizes the gas molecules inside. The electrons then drift towards the wire, and electric signals can be measured. Since the tubes in the barrel region are only segmented at $z = 0$, the TRT predominantly provides track information in the transverse direction. The intrinsic single-point resolution of the TRT in the r-ϕ direction is 120 μm.

In addition, the TRT can be used for particle identification. The spaces between the tubes are filled with polypropylene fibres (barrel) or foils (end-cap). When a relativistic charged particle traverses the material boundary, it emits X-ray transition radiation as a result of a change in dielectric constant. The X-ray can be absorbed well by Xe atoms, depositing additional energy in the gas atoms and leading to stronger readout signals. Charged particles with different masses can be distinguished due to the differences in the amount of X-ray transition radiation (and hence signals) they produce. For example, electrons can be differentiated from the much heavier charged pions. However, Ar has a much lower transition radiation absorption efficiency than Xe, making Ar-filled TRT modules unsuitable

for electron identification, but they still possess similar tracking capabilities as Xe-filled modules [40].

3.2.4 Calorimetry system

Surrounding the inner detector is the calorimetry system, which consists of two components (see Figure 3.12): the electromagnetic (EM) calorimeter, which measures the energy and position of electromagnetic showers created by electrons or photons; and the hadronic calorimeter, which measures hadronic showers created by jets. They are *sampling calorimeters*, meaning that energy deposition is sampled by using alternate active and passive layers. The passing particles interact mainly with the passive layer and create particle showers. The passive layer is also referred to as absorber. Subsequently, the particle showers ionize the active layer and generate an electric current that can be measured.

Highly energetic electrons and photons lose their energies via bremsstrahlung ($e^{\pm} \rightarrow e^{\pm}\gamma$) and pair production ($\gamma \rightarrow e^{+}e^{-}$) respectively by interacting with the passive layer. These processes repeat for the outgoing electrons and photons, whereby electromagnetic (EM) showers are produced. The showers cascade until their energies are lower than the critical values required to generate further bremsstrahlung or pair production. The radiation length X_0 is defined as the average distance an electron travels before losing $1/e$ of its initial energy via bremsstrahlung, or 7/9 of the mean free path for pair production by a photon.

Hadrons lose their energies in matter via inelastic nuclear interactions. When a hadron collides with an absorber nucleus, they interact strongly and generate secondary particles that could either form a further hadronic (e.g. $\pi^{\pm}, K^{\pm}, p, n$, meta-stable nuclei) or electromagnetic (e.g. $\pi^0 \rightarrow \gamma\gamma$, $\eta \rightarrow \gamma\gamma$) cascade, making hadronic showers much more complex than their EM counterparts. The nuclear interaction length λ is the mean free path travelled by a hadron before undergoing an inelastic nuclear interaction.

X_0 and λ are characteristics of different materials. Typically, $\lambda > X_0$, e.g. $X_0 = 0.56$ cm and $\lambda = 17.59$ cm for lead, and $X_0 = 1.44$ cm and $\lambda = 15.32$ cm for

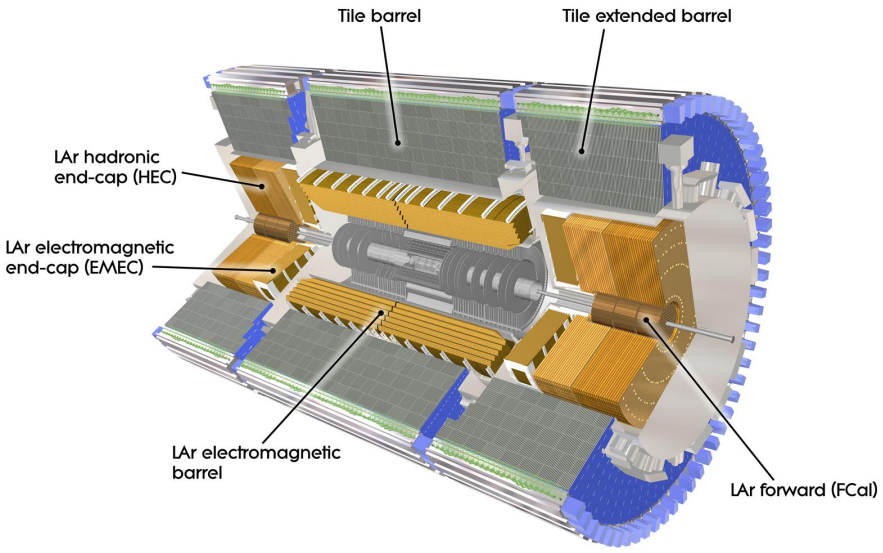

Figure 3.12: Computer generated image of the ATLAS calorimetry system [41].

copper [13]. Therefore, hadronic showers are typically much longer and broader than EM showers. Different absorber materials as well as their lengths are carefully chosen in the construction of the EM and hadronic calorimeters in order to contain the respective showers within certain ranges. The EM calorimeter is placed inside the hadronic calorimeter and is designed to contain all EM showers so that only hadronic showers can enter the hadronic calorimeter on the outside, which contains all hadronic jets and prohibits them from entering the muon spectrometer.

3.2.4.1 Electromagnetic calorimeter

The electromagnetic (EM) calorimeter uses liquid argon (LAr) as an active material and lead as a passive material [42]. Liquid argon is filled inside the cavities of an accordion-shaped structure of lead plates and copper-Kapton electrodes as shown in Figure 3.13a. The accordion geometry provides complete ϕ coverage without azimuthal cracks.

The EM calorimeter covers $|\eta| < 1.475$ in the barrel region and $1.375 < |\eta| < 3.2$ in the end-cap regions. The barrel region is made up of two half-barrels with a small gap at $z = 0$. The end-cap region on each side consists of two contiguous wheels: the outer wheel ($1.375 < |\eta| < 2.5$) and the inner wheel ($2.5 < |\eta| < 3.2$).

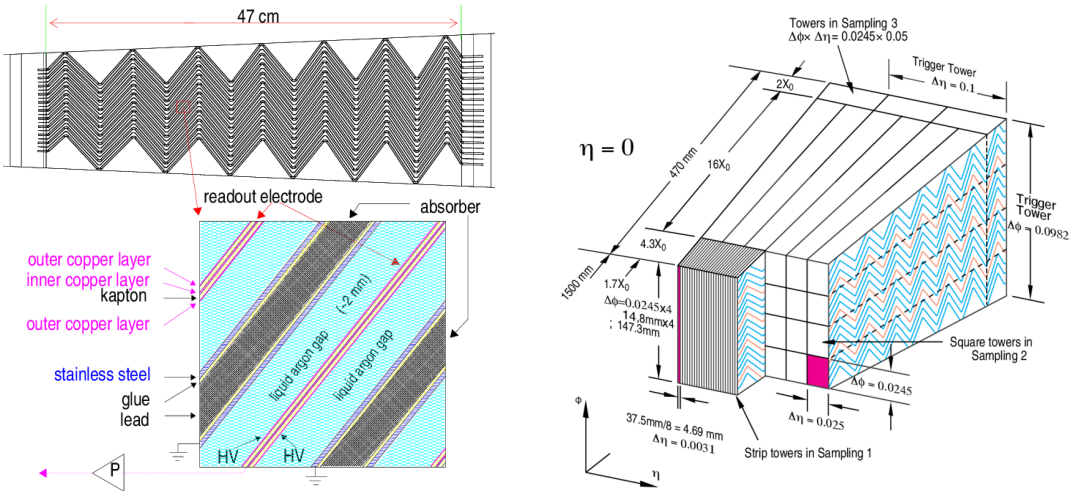

(a) Accordian structure [43] **(b)** Three sampling layers [18]

Figure 3.13: Sketches of the accordian geometry and the three sampling layers with different lengths and granularities of the LAr electromagnetic calorimeter.

The LAr EM barrel and outer end-cap calorimeters have three sampling layers with different granularities along the shower depth as shown in Figure 3.13b, while the inner end-cap has only two layers. The first layer has the finest granularity of 0.0031×0.098 in the η-ϕ plane, which helps to differentiate photons from neutral pions decaying to two photons as well as to measure the trajectories of neutral particles. This layer has a thickness of $6X_0$. The second layer has a coarser granularity of 0.025×0.025 in the η-ϕ plane with a radial length of $16X_0$ to stop most EM showers, so the largest proportion of energy is deposited here. Only a small amount of showers can penetrate into the third layer with a thickness of $2X_0$ and the coarsest granularity of 0.05×0.025 in the η-ϕ plane. The third layer is used to measure the energy deposits of the tails of the most energetic showers.

3.2.4.2 Hadronic calorimeter

Located outside the LAr EM calorimeter is the tile barrel calorimeter [44] (see Figure 3.14), which is used to identify hadronic jets and measure their energies. The hadronic calorimeter is larger than the EM calorimeter because hadronic showers are typically wider and longer than their EM counterparts. The central tile barrel covers $|\eta| < 1.0$ while the two tile extended barrels cover $0.8 < |\eta| < 1.7$. The tile

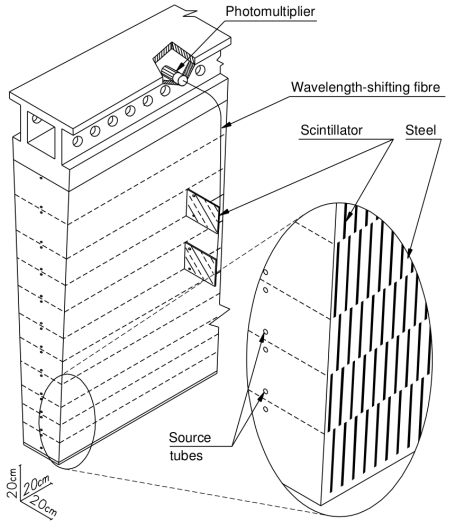

Figure 3.14: Sketch of a module of the tile barrel calorimeter [18].

calorimeter has three sampling layers with plastic scintillator as an active material and steel as a passive material. The photons emitted by the plastic scintillators are measured with photomultiplier tubes. The three layers of the tile calorimeter are 1.4λ, 4.0λ, and 1.8λ thick. The $\eta \times \phi$ granularities are 0.1×0.1 in the first two layers and 0.2×0.1 in the third layer.

The LAr hadronic end-cap calorimeter ($1.5 < |\eta| < 3.2$) uses liquid argon as an active material and copper as a passive material in its four sampling layers [42]. Each end-cap consists of two contiguous wheels. The LAr hadronic calorimeter is coarser than the LAr EM calorimeter with $\eta \times \phi$ granularities of 0.1×0.1 in the first three layers and 0.2×0.2 in the fourth layer. The total thickness of the LAr hadronic end-cap calorimeter is 12λ.

The coverage is extended in the forward region ($3.1 < |\eta| < 4.9$) with the LAr hadronic forward calorimeter, consisting of three adjacent wheels on either side. There are two sampling layers. The passive material is copper in the first layer, and tungsten in the second layer. Liquid argon is used as an active material for both layers. The $\eta \times \phi$ granularity is 0.2×0.2 in both layers. The total length of the LAr hadronic forward calorimeter is 9.5λ.

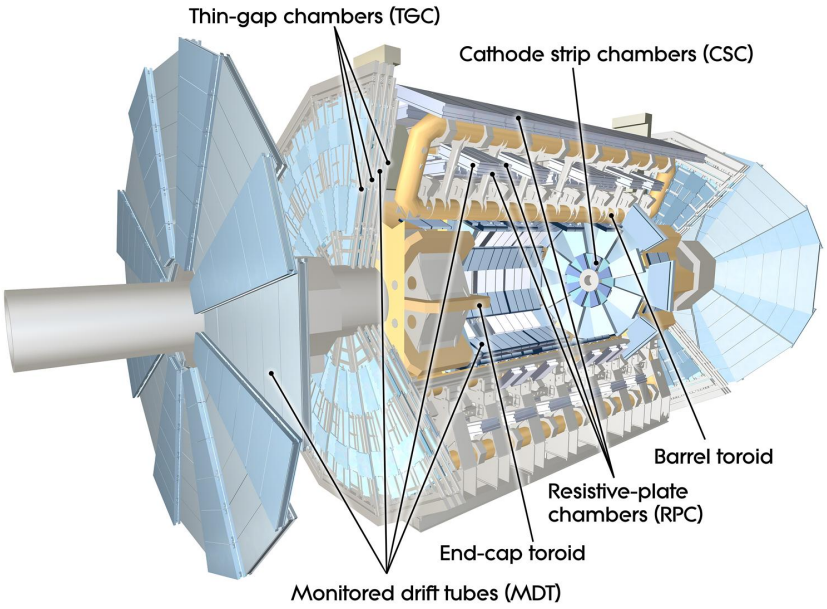

Figure 3.15: Computer generated image of Muon Spectrometer [46].

3.2.5 Muon spectrometer

Muons produced from pp collisions at the LHC energy scale are minimum-ionizing particles, i.e. they traverse the calorimeters without generating any showers. The muon spectrometer (MS) [45] encloses the calorimeters and is designed to solely detect muons and measure their momenta. The MS consists of one barrel ($|\eta| < 1.05$) and two end-caps ($1.05 < |\eta| < 2.7$) as shown in Figure 3.15. A system of three large air-core toroidal superconducting magnets, each with eight coils, generates a magnetic field of 0.5 T in the barrel and 1 T in the end-caps. Monitored drift tubes (MDT) are used as precision measurement chambers in the barrel and end-cap regions up to $|\eta| < 2.7$, except in the end-cap inner station ($2.0 < |\eta| < 2.7$) where cathode strip chambers (CSC) are used.

The MS can also provide fast trigger decisions on events containing high energy muons. Resistive plate chambers (RPCs) in the barrel and thin gap chambers (TGCs) in the end-cap region are used as fast trigger chambers, covering $|\eta| < 1.05$ and $1.05 < |\eta| < 2.4$ respectively.

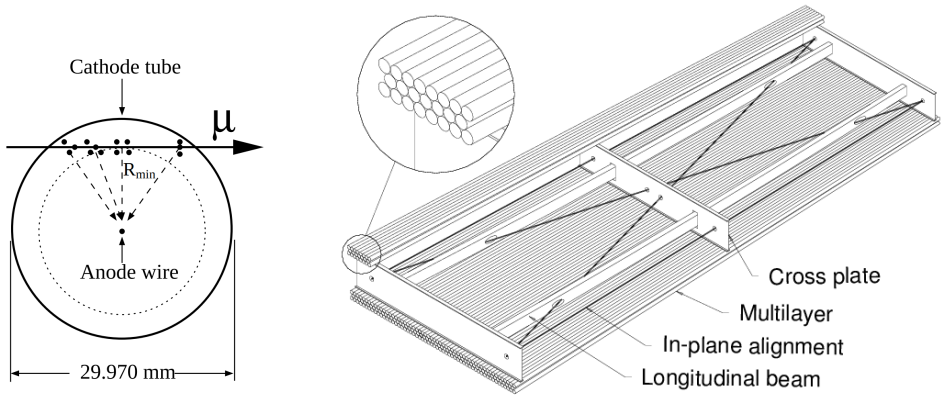

(a) Cross-section of a drift tube

(b) An MDT chamber

Figure 3.16: Sketches of the monitored drift tube (MDT) chamber [18].

3.2.5.1 Monitored drift tube chambers

The monitored drift tube (MDT) chambers [47] are used to provide precise measurements of muon momenta in the η-z plane where the longitudinal bending of the muons occurs due to the presence of a toroidal magnetic field. The MDT chambers of the barrel and end-cap regions together cover the range of $|\eta| < 2.7$ (except for a small window $2.0 < |\eta| < 2.7$). Each MDT chamber consists of aluminium tubes with a diameter of approximately 30 mm filled with a gas mixture of Ar (93%) and CO_2 (7%) at a pressure of 3 bar, and a central wire made of tungsten-rhenium alloy held at 3,080 V as shown in Figure 3.16. The spatial resolution in the z-direction is 80 μm per tube and 35 μm per chamber. The MDT chambers work in a similar manner to the TRT in the inner detector (see Section 3.2.3.3).

3.2.5.2 Cathode strip chambers

A system of cathode strip chambers (CSCs) [48] are used in the forward region ($2.0 < |\eta| < 2.7$) in the innermost layer of the end-cap due to their higher rate capability and time resolution. Each CSC contains four layers, and each layer consists of two sets of cathode copper strips (X- and Y-strips) at a right angle to one another, and anode wires parallel to the Y-strips as shown in Figure 3.17. The cavity within each layer is filled with Ar-CO_2 (80%-20%) gas mixture at 1 bar of

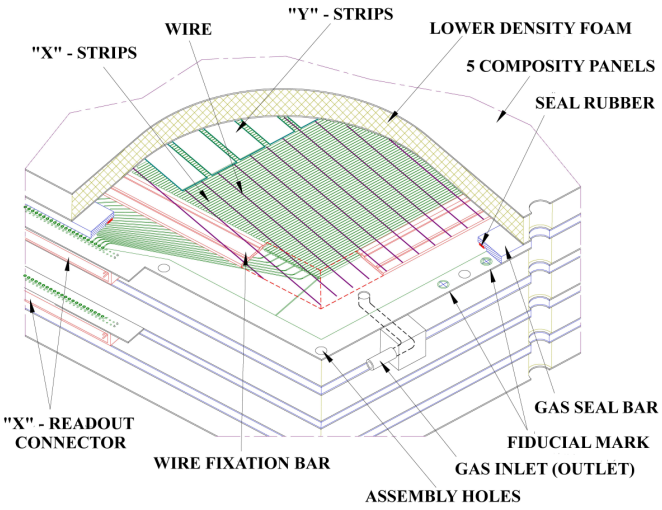

Figure 3.17: Sketch of a layer of the cathode strip chamber (CSC) [48].

pressure. When a muon passes through a layer of the CSC, it ionizes electrons from the gas atoms. The electrons then move towards the anode wires, creating an avalanche of electrons, which in turn induce electric signals in the cathode strips (Y-strips) parallel to the anode wires. On the other hand, the positive gas ions move towards the cathode X-strips, inducing electric signals that can also be measured. Therefore, the information on the (x, y) coordinates of the muon passing through the layers of a CSC can be obtained, and its trajectory and momentum can be measured. The spatial resolution of a CSC is 40 μm in the bending plane and 5 mm in the transverse plane.

3.2.5.3 Resistive plate chambers

The resistive plate chamber (RPC) [49] is a gaseous parallel electrode-plate (no wire) detector. RPCs are used in the barrel region ($|\eta| < 1.05$) of the MS. Its operation is based on the ionization of gas molecules when muons pass through it like the MDT and CSC. Each detector layer is made of two resistive plates are made of 2-mm-thick melaminic resins and are kept spaced at 2 mm by polycarbonate spacers as shown in Figure 3.18. The space between the resin plates is filled with a gas mixture (94.7% $C_2H_2F_4$, 5% iso-C_4H_10, 0.3% SF_6) at 1 bar of pressure. The outer surfaces of the plates are coated by thin layers of graphite to make them

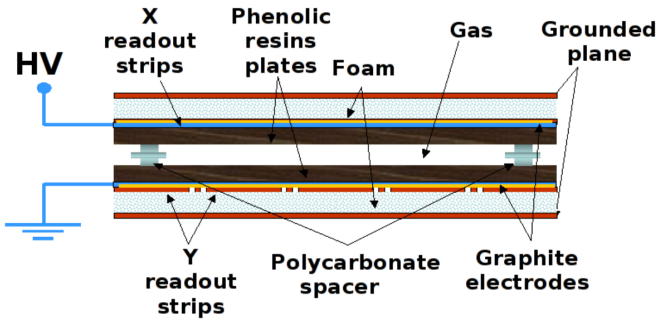

Figure 3.18: Sketch of a layer of the resistive plate chamber (RPC) [49].

electrodes, which are connected to a high voltage of 9.8 kV. The ionized electrons gain energy from the electric field and can ionize gas molecules further, creating an avalanche of electrons and thus very strong signal readouts. An RPC is built from two units with each consisting of two independent detector layers whose readout strips are perpendicular making the measurement of (η, ϕ) coordinates possible, which complements the measurement of the MDT in the bending (η) direction. The spatial resolution of an RPC is 10 mm in both the bending and transverse planes.

In the barrel middle station (BM), an MDT is sandwiched between two RPCs. In the barrel outer station (BO), only one RPC is placed on the outside (inside) of an MDT in the large (small) sector as shown in Figure 3.19. This construction allows for redundancy in the track measurement which can be used to define a first-level muon trigger based on logic coincidences: low-p_{T} trigger (6-9 GeV); high-p_{T} trigger (9-35 GeV).

3.2.5.4 Thin gap chambers

In the end-cap regions ($1.05 < |\eta| < 2.7$), thin gap chambers (TGCs) [51] are used instead of RPCs. The TGC is a multi-wire proportional chamber (similar to the CSC) with the characteristic that the wire-to-cathode distance of 1.4 mm is smaller than the wire-to-wire distance of 1.8 mm as shown in Figure 3.20a. The cathode planes consist of 1.6-mm-thick garolite (G-10) plates, graphite coated on the inside (facing the wires), and copper cladding on the outside. The operation principle of the TGC is similar to that of the CSC where signal readouts are generated by

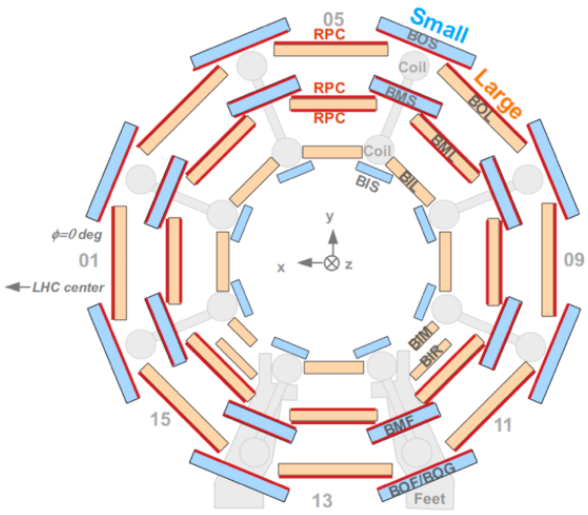

Figure 3.19: Cross-sectional view of the barrel muon spectrometer perpendicular to the beam axis [50]. The MDT chambers in the small sectors are shown in light blue, the MDT chambers in the large sectors are shown in orange, and the RPC chambers in red. The eight coils are also shown in grey.

ionized electrons being collected at the anode wires and by gas ions at the cathode plates. Here, the gas mixture used is 55% CO_2 and 45% C_5H_{12} at a pressure of 1 bar. The wires are connected to a high voltage of 2.9 kV to promote an avalanche of ionized electrons. The TGC can provide spatial resolution of 2–6 mm in the bending plane and 3–7 mm in the transverse plane.

A gas volume containing a wire plane and two cathodes is called a chamber. Three or two chambers in a triplet or doublet arrangement is called a unit, as shown in Figure 3.20b. The triplet arrangement is needed in order to minimize false coincidences from background hits, which are more likely in the end-cap than in the barrel. Different combinations of triplets and doublets of TGCs are stacked next to the MDTs in the end-cap regions (similar to RPCs and MDTs in the barrel) to provide complementary track measurements in the non-bending (ϕ) direction as well as a first-level muon trigger system based on logic coincidences.

3.2.6 Forward detectors

In addition to the components of the main ATLAS detector described in the previous sections, there are also three smaller detectors on either side of ATLAS: LUCID,

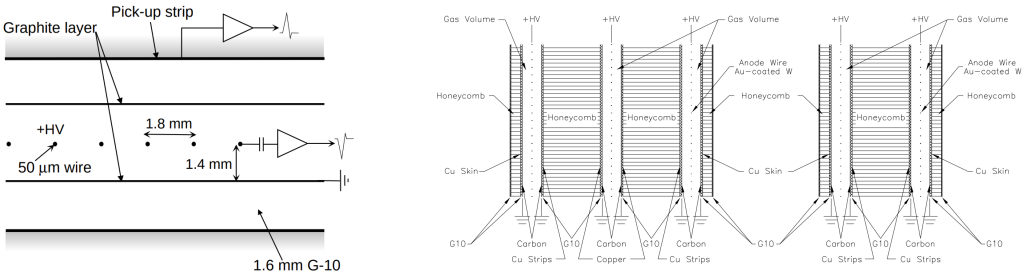

(a) Cross-sectional view of a chamber

(b) A triplet with three chambers and a doublet with two chambers

Figure 3.20: Sketches of the thin gap chamber (TGC) [18].

ALFA, and ZDC. These three detectors are collectively known as the forward detectors. They are located at in the extreme forward regions with respect to the *pp* interaction point as shown in Figure 3.21.

The LUCID (LUminosity measurement using Cerenkov Integrating Detector) [52] is located 17 m from the *pp* interaction point just inside the outer end-cap of the muon spectrometer on either side, covering $5.6 < |\eta| < 6$. It is used for online monitoring of beam stability and the instantaneous luminosity of inelastic *pp* collisions [25]. The LUCID uses the thin quartz windows of photomultipliers as Cherenkov medium for event counting.

The furthest sub-detector is the ALFA (Absolute Luminosity For ATLAS) [53], located at about ±240 m away from the main ATLAS detector. The ALFA is designed to measure the *pp* total cross-section and luminosity by measuring elastic *pp* scattering at very large pseudorapidity, $|\eta| > 8.5$ [54]. It is made of multi-layer scintillating fibre structures housed inside Roman Pots[6], which are designed to be as close as 1 mm to the beam.

And the last system is the ZDC (Zero Degree Calorimeter) [56], located at about ±140 m from the interaction point. It is used to provide a further hermeticity to the ATLAS detector in the extreme forward region almost parallel to the beam, $|\eta| > 8.3$. The ZDC consists of one electromagnetic and three hadronic calorimeters that can be

[6] A Roman Pot is a vessel for detectors that is connected to the beam pipe via bellows, allowing the detector to approach the beam very close without entering the machine vacuum [55].

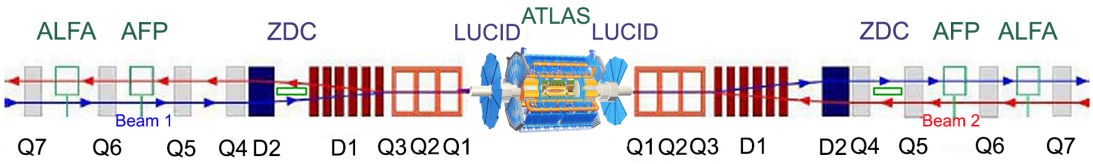

(a) The placement of the forward detectors on either side of the ATLAS detector [57]

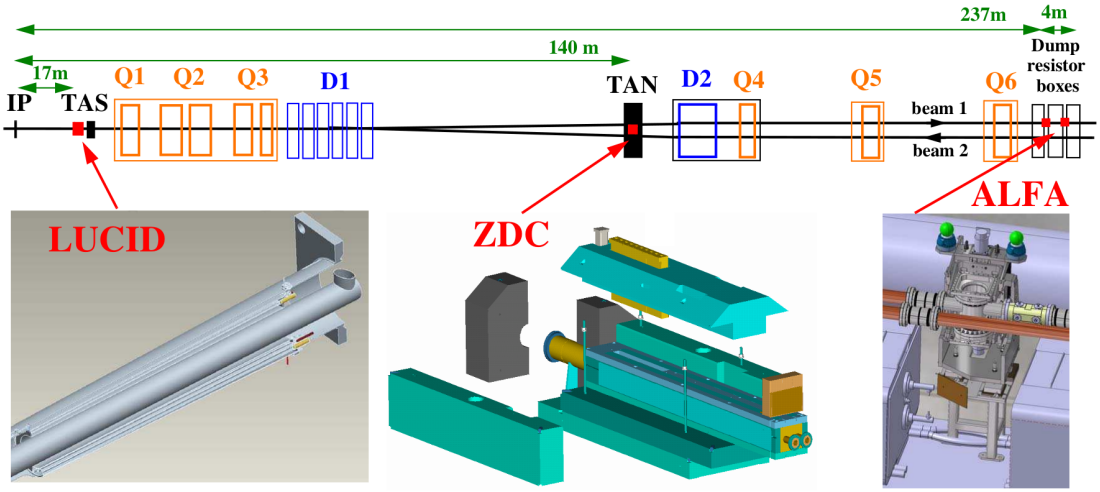

(b) Zoom in on the right hand side of ATLAS [18]

Figure 3.21: The placement of the forward detectors along the beam-line around the ATLAS interaction point. The distances between the forward detectors and ATLAS are stated.

used to study both *pp* and heavy-ion collisions. In addition, it can also function as a luminosity monitor to tune the parameters of the LHC during the first day of the run.

3.2.7 Trigger system and data acquisition

The full information of all *pp* collisions is not feasible to record due to an immensely high data rate, exceeding the current limits of data recording technology. Moreover, the majority of these collisions are not interesting to physics analyses. The ATLAS trigger and data acquisition (TDAQ) system [58] selects only a small fraction of these events where interesting interactions occur, greatly reducing the data rate so that events can be recorded by the front-end electronics of the detector. The ATLAS Run-2 trigger system consists of two independent levels: first-level (L1) and high-level trigger (HLT). A flowchart summarizing the ATLAS TDAQ system is provided in Figure 3.22.

The L1 trigger is hardware-based and uses reduced-granularity information from some components of the detector to form a rudimentary set of event selection criteria: L1Calo uses information from the calorimeters to identify e, γ, τ, jets, and missing transverse energy above a programmable threshold; L1Muon uses information from the RPC and TGC trigger chambers of the muon spectrometer and applies logic coincidence requirements. Introduced for Run-2, the L1Topo trigger applies various topological requirements to geometric (e.g. $\Delta\phi$, $\Delta\eta$, ΔR) or kinematic (e.g. E_{T}, p_{T}) combinations between trigger objects received from the L1Calo and L1Muon triggers. This results in an improved background rejection with minimal signal loss. The L1 trigger decision is then formed by the Central Trigger Processor (CTP), which receives inputs from the L1Calo, L1Muon, and L1Topo triggers. With a 2.5 µs fixed latency, the L1 trigger reduces the data rate from 40 MHz[7] to around 100 kHz.

For each L1-accepted event, all of the data in the event are read out by the Front-End (FE) electronics of the different components of the ATLAS detector. The Read-Out Drivers (RODs) perform initial processing and formatting of the data before buffering is done by the Read-Out System (ROS). In addition to its role as the first stage of event selection, the L1 trigger system also identifies Regions of Interest (RoIs), which are the (η, ϕ) coordinates of the regions where significant detector activities have been detected, to be investigated by the HLT in the second stage.

The HLT selection is performed by software running on a commodity PC farm, through fast trigger algorithms to provide early rejection and followed by more precise algorithms with some codes in common with the offline reconstruction to make the final selection. It conducts a detailed analysis by requesting either a full set or some fragments of event data from within an RoI. Then, a hypothesis test is performed based on the information on the reconstructed objects in the event to decide whether the trigger condition is satisfied or not. The HLT is able to reduce the data rate of the L1 output from 100 kHz to 1.2 kHz. Once accepted by the HLT, the data are sent to permanent storage for offline reconstruction and processing by the ATLAS Tier-0 facility.

[7] This is the peak bunch crossing rate of 40 MHz, corresponding to the spacing between bunches of 25 ns.

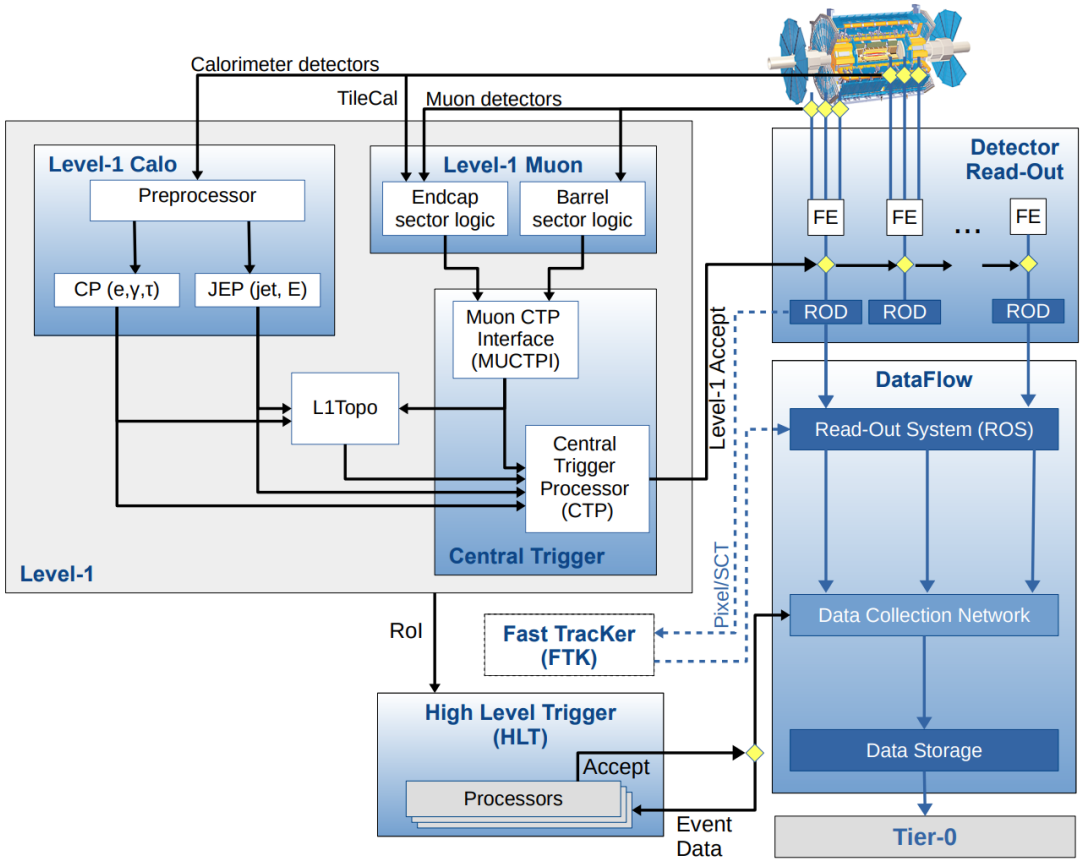

Figure 3.22: Flowchart of the ATLAS trigger and data acquisition (TDAQ) system in Run-2 [58].

3.3 Object reconstruction

Each type of particles can be identified through its distinctive signature that it leaves behind in the different components of the ATLAS detector, as demonstrated in Figure 3.23. Events with interesting physics activities are selected by the trigger and data acquisition system, and the complete set of event information is passed through a sequence of sophisticated algorithms in order to accurately identify and reconstruct the energies and momenta of the particles in each event. Reconstructed particles are referred to as *objects*. These objects are subsequently calibrated to account for any mismeasurements or inaccuracies of the detector components so that they resemble the actual particles that they represent as closely as possible. However, only certain particles produced from pp collisions or subsequent secondary decays are stable enough to be detected by the ATLAS detector. The existence and properties of these short-lived intermediate particles are inferred from the final-state particles they produce. This section aims to describe the offline reconstruction of the different types of objects pertaining to the $H \to WW^* \to l\nu l\nu$ analysis: electrons, muons, jets, and missing transverse momentum.

3.3.1 Tracks and vertices

A *track* is the trajectory of a charged particle in the inner detector (ID) reconstructed from spatial information provided by the silicon pixel detector and semiconductor tracker (SCT) as well as timing information provided by the transition radiation tracker (TRT). There are two approaches to how tracks are reconstructed: 'inside-out' and 'outside-in' [60].

The 'inside-out' approach begins in the pixel detector and SCT before extending outwards to the TRT. The first step starts with the formation of three-dimensional space-points, which are locations of where silicon pixel hits occur. Track seeds are created with three space-points in each, and a combinatorial Kalman filter [61] is applied in order to extrapolate the track trajectory outwards by following the most likely path using knowledge of the detector material and magnetic field configuration. These track candidates with $p_{\mathrm{T}} > 400$ MeV are then fitted using

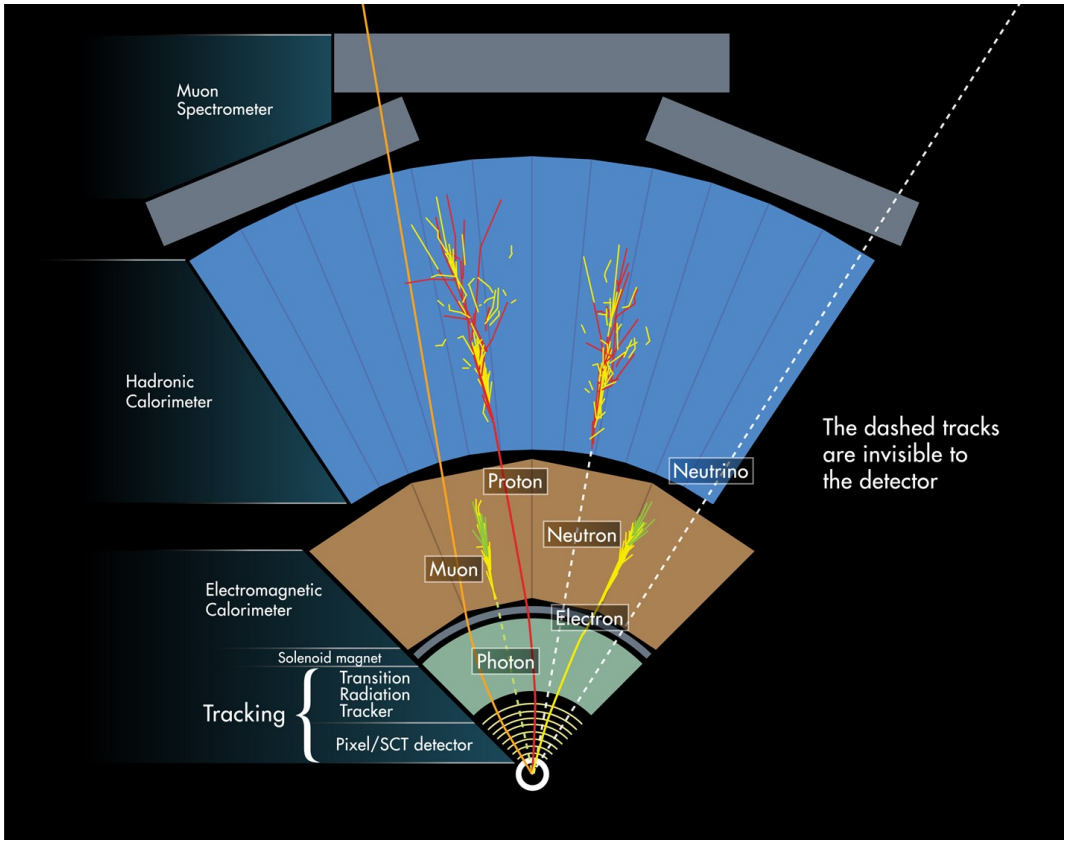

Figure 3.23: Schematic cross-sectional view depicting the paths of the different types of final-state particles as they traverse the layers of the ATLAS detector [59]. A solid line through a component means that the particle in question can be detected by the component, whereas a dashed line means that it cannot be detected by the component.

the ATLAS Global χ^2 Track Fitter [62], which also resolve ambiguities in hits associated with mulitiple track candidates. The surviving track candidates are extended into the TRT by matching with drift-circles[8] in the traversed straw tubes. The TRT extension improves the accuracy of momentum measurement due to an increased track length. The 'inside-out' approach is designed for reconstruction of particles produced from primary pp interactions. The different stages of the 'inside-out' approach are illustrated in Figure 3.24.

On the other hand, the 'outside-in' approach works in reverse by starting in the TRT before extending inwards to the pixel detector and SCT. Tube hits that are in close proximity are combined into segments, which are in turn made into

[8] A drift-circle is an imaginary circle inside a straw tube of the TRT whose radius is determined from the time the ionized electrons take to arrive at the centre straw wire, whereby a hit is recognized.

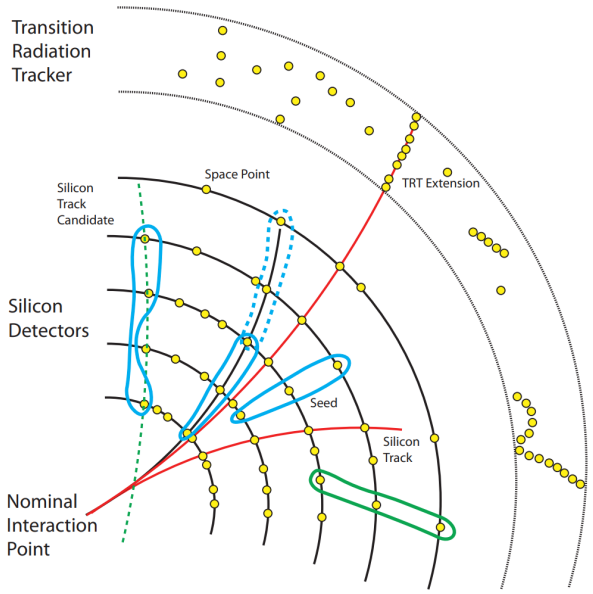

Figure 3.24: Illustration of the 'inside-out' track reconstruction approach in the inner detector [63]. Space-points are shown in yellow. Valid track seeds are shown in blue. The dashed blue seed illustrates the case where two seeds are of the trajectory of the same particle and ambiguities occur. The green seed and dashed line are rejected because they are inconsistent with the nominal interaction point. The long red line corresponds to a fully reconstructed track with TRT extension, while the short red line is without TRT extension.

track candidates by means of Kalman filter extrapolation. Shared track ambiguities among the candidates are resolved with the ATLAS Global χ^2 Track Fitter. The surviving track candidates are extrapolated into the pixel detector and SCT on the inside. Tracks with a TRT segment without an extension into the silicon detector are referred to as TRT-standalone tracks. The 'outside-in' approach is designed to reconstruct tracks that originate from secondary interactions occurring at a greater distance from the beamline.

Under an axial magnetic field provided by the central solenoid, a charged particle exhibits a helical motion which requires five so-called 'perigee' parameters to fully describe its trajectory, as depicted in Figure 3.25. The perigee parameters are $\left(d_0, z_0, \phi, \theta, \frac{q}{p}\right)$ where: d_0 is the transverse impact parameter, which is the shortest distance in the transverse plane from the track to the beam line; z_0 is the longitudinal impact parameter, which is the shortest distance along the beam line between the track and the reference point; ϕ is the azimuthal angle between

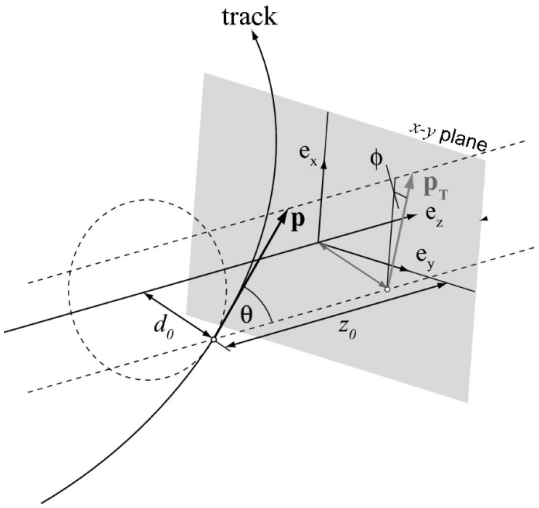

Figure 3.25: Illustration of a track and five perigee parameters $(d_0, z_0, \phi, \theta, \frac{q}{p})$ that describe it [64].

the transverse component of the particle's momentum and the vertical axis; θ is the polar angle between the momentum and the beam axis; and $\frac{q}{p}$ is the ratio of the measured charge of the track to its momentum. These parameters are measured for each reconstructed track.

A *primary vertex* (PV) is the location where two protons collide. Reconstruction of primary vertices proceeds in two simultaneous steps: vertex finding and vertex fitting [65]. First, reconstructed tracks are required to satisfy certain preselection criteria. The preselected tracks are extrapolated to the beam axis, and z_0 is computed for every track with respect to the nominal centre of the beam spot. A seed position for the first vertex is formed by considering the track points of closest approach to the nominal centre. Then, the adaptive vertex fitting algorithm [66] is applied to the seed to find the vertex position. The compatibility between each track and the seed is quantified by a weight assigned to the track. In each iteration, less compatible tracks are down-weighted, and the vertex position is re-computed. After the vertex position is determined, the incompatible tracks are removed and used to seed a new vertex. This procedure is repeated until there are no tracks left to seed.

In each bunch crossing, there can be more than one pp collision, resulting in a number of primary vertices being reconstructed. The *hard-scatter vertex* is defined as the primary vertex with the largest $\sum p_{\mathrm{T}}^2$ of all tracks associated with it. It is

the vertex where interesting physics phenomena are most likely to take place due to the high p_{T} nature of its final-state particles. Other primary vertices are referred to as *pile-up vertices* (see Section 3.1.3). The number of primary vertices N_{PV} can be used to quantify the amount of in-time pile-up, and the average number of pp interactions per bunch crossing $\langle\mu\rangle$ reflects the amount of out-of-time pile-up.

A *secondary vertex* (SV) is where the intermediate particle produced from the primary pp collision decays into final-state particles. The procedure for reconstruction of secondary vertices is similar to that for primary vertices, except that the fit is constrained by the primary vertices from which they originate instead of the nominal beam spot centre.

3.3.2 Calorimeter clusters

For all objects apart from muons, energy deposits and signals in the calorimeters are essential to their reconstruction. Contiguous calorimeter cells are collected to form three-dimensional topological clusters (or *topo-clusters* in short) via a calorimeter clustering algorithm [67]. The primary observable governing the formation of topo-clusters is the *cell signal significance*:

$$\varsigma_{\mathrm{cell}}^{\mathrm{EM}} = \frac{E_{\mathrm{cell}}^{\mathrm{EM}}}{\sigma_{\mathrm{noise,cell}}^{\mathrm{EM}}} \tag{3.9}$$

where $E_{\mathrm{cell}}^{\mathrm{EM}}$ is the cell signal, and $\sigma_{\mathrm{noise,cell}}^{\mathrm{EM}}$ is the average (expected) noise in this cell. Both $E_{\mathrm{cell}}^{\mathrm{EM}}$ and $\sigma_{\mathrm{noise,cell}}^{\mathrm{EM}}$ are measured on the electromagnetic (EM) energy scale to give the same response for EM showers from electrons or photons. However, the EM scale does not consider energy losses for hadrons in both active and inactive material due to the non-compensating character of the ATLAS calorimeters. As a result, hadronic interactions produce calorimeter responses that are lower than the nominal EM scale by amounts depending on where the showers develop. To account for this, a local hadronic cell weighting (LCW) scheme is used for jet calibration [67].

The formation of topo-clusters is a sequence of *seed and collect steps*, which are repeated until all topologically connected cells passing the following criteria are found:

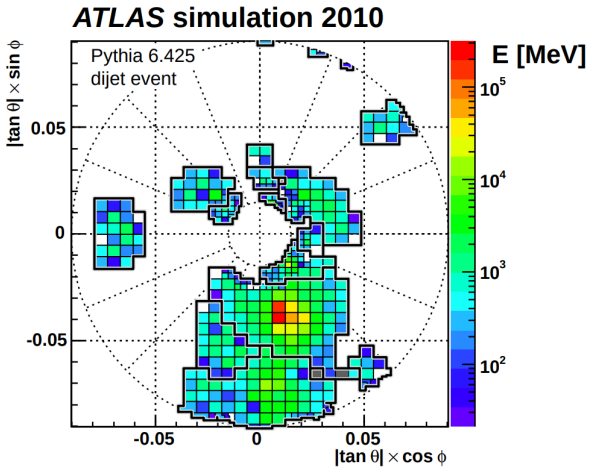

Figure 3.26: Simulation of the final stage in the formation of topo-clusters [67]. The colour of each square represents the energy in each calorimeter cell.

- Cells with $|\varsigma^{\mathrm{EM}}_{\mathrm{cell}}| > S$ (where S is the primary seed threshold) are labelled seed cells. Each seed cell forms a proto-cluster.

- The cells neighbouring[9] a seed and satisfying $|\varsigma^{\mathrm{EM}}_{\mathrm{cell}}| > N$ (where N is the threshold for growth control) are collected into the corresponding proto-cluster. If the neighbouring cells of the cells neighbouring the seed also have signal significances above N, they are added to the proto-cluster as well. If a particular neighbour is a seed cell, the two proto-clusters are merged. If a cell neighbours two different proto-clusters and its signal significance is above N, the two proto-clusters are merged.

- The previous step iteratively proceeds until the last set of neighbouring cells with $|\varsigma^{\mathrm{EM}}_{\mathrm{cell}}| > P$ (where P is the principal cell filter) but not $|\varsigma^{\mathrm{EM}}_{\mathrm{cell}}| > N$ is collected. The boundaries of the topo-clusters are set.

In Run-2, the configuration of $\{S = 4, N = 2, P = 0\}$ is optimized for hadronic final-state reconstruction. In this way, cells with insignificant signals which are not in close proximity to cells with significant signals (and hence interesting physics) are removed.

[9]Here, *neighbouring* is defined as two cells being directly next to each other in a given sampling layer. If two cells are in adjacent sampling layers, they must have at least partial overlap in the η-ϕ plane.

3.3.3 Electrons

Electrons are reconstructed using track information in the ID and energy deposits in the EM calorimeter. Track information is most accurate in the region $|\eta| < 2.47$ covered by the ID acceptance. However, the $1.37 < |\eta| < 1.52$ transition regions between the barrel and end-caps of the EM calorimeter are excluded since they contain a large amount of inactive material.

In Run-2, electrons are reconstructed using a *superclustering* algorithm [68]. Firstly, EM topo-clusters are matched to ID tracks, which are re-fitted using the Gaussian Sum Filter (GSF) algorithm [69] where the non-linear effects of energy losses from radiated photons (bremsstrahlung) are taken into account. After ID tracks and EM topo-clusters are matched, seed cluster candidates are formed. In order to become a seed, a topo-cluster must have $E_{\mathrm{T}} > 1$ GeV and must be matched to an ID track with at least four hits in the silicon pixel detector or SCT. Topo-clusters that neighbour the seed are referred to as *satellites* and are added to the seed if they fall within a window of $\Delta\eta \times \Delta\phi = 0.075 \times 0.125$ around the seed cluster barycentre, as they tend to originate from electrons and photons of secondary EM showers emitted by the initial electron. This window corresponds to 3×5 cells of the second layer of the LAr EM calorimeter whose sizes are 0.025×0.025. The window is chosen to be asymmetrical with a longer ϕ-side because the axial magnetic field in the ID bends electron trajectories in the transverse r-ϕ plane. Photons from EM showers, on the other hand, are electrically neutral and do not bend under the magnetic field, causing a wider spread in the ϕ-direction. A topo-cluster is also considered a satellite if it is within a window of $\Delta\eta \times \Delta\phi = 0.125 \times 0.300$ (corresponding to 5×12 cells) around the barycentre and its best-matched track is also the best-matched track for the seed. The seed clusters and their satellites form *superclusters*, as shown in Figure 3.27.

Further quality criteria known as *identification working points* are used to improve the purity of candidate prompt electrons. They are defined based on their performance in differentiating prompt isolated electrons from hadronic jets misidentified as electrons, from converted photons, and from electrons produced

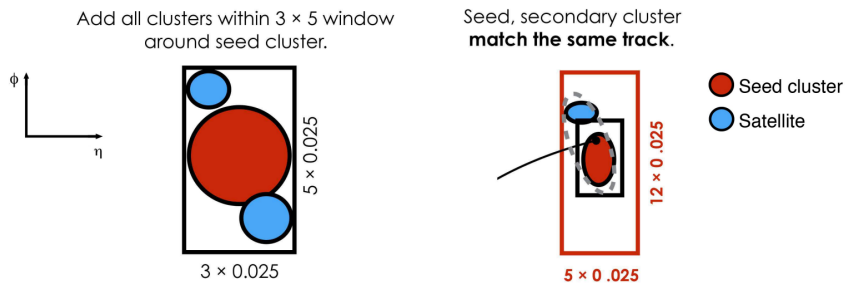

Figure 3.27: Demonstration of the superclustering algorithm for electron reconstruction [68]. Seed clusters are shown in red, and satellite clusters in blue.

in the decays of heavy-flavour hadrons. For this purpose, a likelihood-based method taking into account various discriminating variables including shower shapes, track and calorimeter properties, and track-cluster compatibility is used. Three identification working points are `Loose`, `Medium`, and `Tight` in an increasing order of prompt electron purity at a cost of decreasing efficiency. They are defined to suit a wide range of analyses and topologies which demand different levels of electron identification precision and background rejection. For typical electroweak processes, the average efficiencies are 93%, 87%, and 79% for `Loose`, `Medium`, and `Tight` respectively [70].

Electrons from electroweak processes typically produce clean, *isolated* signals, i.e. only a small amount of detector activity occurs in their vicinity, which is in contrast to electrons produced from heavy-flavour decays or light hadrons misidentified as electrons where there is a lot of activity, particularly in the calorimeters. The amount of activity near electrons can be quantified from the tracks of nearby charged particles or from energy deposits in the calorimeters, leading to two isolation variables that can be simultaneously used to define *isolation working points*. The definitions and efficiencies of electron isolation working points can be found in [70].

3.3.4 Muons

Muons are reconstructed by combining track information from the muon spectrometer (MS) with other detector components, such as tracks in the ID and energy deposits in the calorimeters [71]. Reconstruction of MS tracks begins with the identification of short straight-line track segments from hits in an individual MS

station (MDT or CSC). Information from precision track segments in the η-z bending plane is then combined with measurements of the ϕ coordinate from the trigger chambers (RPCs or TGCs) to create three-dimensional track candidates by using the ATLAS Global χ^2 Track Fitter [62], which takes into account the possible interactions between muons and detector material as well as possible misalignments between the different MS components. A loose constraint is made on the extrapolation of a track candidate in the MS to the nominal pp interaction point. Outlier hits are removed, and hits that were not originally assigned to the track candidate are added to improve fit quality.

Muons are classified based the set of detector components used to reconstruct them:

- Standalone: muons with only MS track information and without extrapolation to other detector components.

- Combined (CB): muons with matching MS tracks and ID tracks in the $|\eta| < 2.5$ region. A global fit is performed based on hits in the ID and the MS, taking into account energy losses in the calorimeters. For $|\eta| > 2.5$, MS tracks may be combined with short ID track segments from hits in the SCT, leading to a subset of CB muons known as silicon-associated forward (SiF) muons.

- Inside-out combined (IO): muons reconstructed with a complementary 'inside-out' algorithm (see Section 3.3.1), where ID tracks are extrapolated to the MS. The ID track, energy losses in the calorimeters, and hits in the MS are used in a combined track fit. This approach can be used for reconstructing low-p_{T} muons which might not reach the MS middle station, or for regions with limited MS coverage.

- Muon-spectrometer extrapolated (ME): muons that are not matched to any ID tracks but their MS tracks are extrapolated to the beam line. This extends the coverage of muon reconstruction beyond the acceptance of the ID.

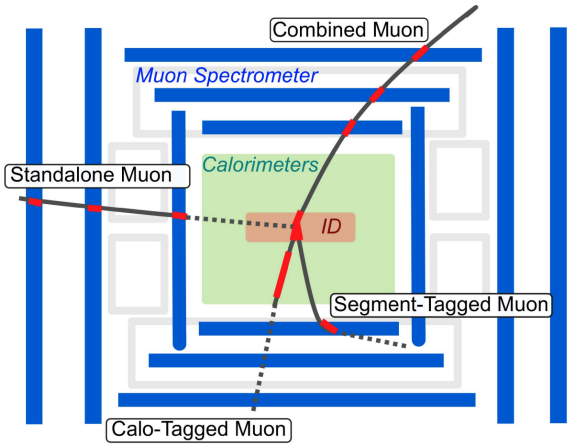

Figure 3.28: Schematic diagram depicting some examples of the different types of reconstructed muons in the ATLAS detector [72].

- Segment-tagged (ST): ID tracks are extrapolated to at least one reconstructed segment in the MS. The muon candidates inherit measurements and parameters from their corresponding ID tracks.

- Calorimeter-tagged (CT): ID tracks are extrapolated through the calorimeters to search for energy deposits consistent with the behaviour of the minimum-ionizing particle. Tagged candidates inherit measurements and parameters from their corresponding ID tracks.

Standalone, CB, ST, and CT muons as well as their reconstruction methodology are schematically illustrated in Figure 3.28. CB muons constitute the majority of muon candidates reconstructed in the ATLAS detector.

After reconstruction, muon candidates are required to pass quality requirements in order to be identified as muons. Similar to electrons, these requirements are referred to as *identification working points*, which are designed to offer different levels of prompt muon identification performance and reconstruction efficiency. Among non-prompt muons, an explicit distinction is made between muon candidates produced in the semi-leptonic decays of light hadrons and those produced from the decays of heavy-flavour hadrons. Light hadrons generally produce muon tracks with lower quality because their trajectories are constantly diverted by the in-flight decays as they traverse the detector layers. In order of increasing prompt-muon purity and

decreasing efficiency, the standard identification working points are `Loose`, `Medium`, and `Tight`, where the muons passing the `Medium` (`Tight`) working point are a subset of those passing the `Loose` (`Medium`) working point. The `Tight` and `Medium` working points only accept CB and IO muons within the ID acceptance range of $|\eta| < 2.5$, while the `Loose` working point also accepts CT and ST muons. Further details on the performance and efficiency of the working points can be found in [71].

Like in the case of electrons, muons from prompt decays of weak bosons typically produce clean signals, leading to low detector activity in their vicinity. Several *isolation working points* are defined based on their performance in rejecting non-prompt muons. Further details on these working points can also be found in [71].

3.3.5 Jets

Due to the *colour confinement* phenomenon, isolated quarks and gluons cannot be observed in normal conditions. Instead, as two colour charges separate, it becomes energetically favourable for a new quark-antiquark pair to appear, forming a collimated spray of colour-neutral hadrons as well as other particles that decay from them. These clustered, indistinguishable particles are collectively known as a *jet*, which is a physics object that can be measured by the detector. The energy and momentum of the original quark or gluon emitted from an interaction vertex can be inferred from the reconstructed and calibrated jet objects.

Jet reconstruction

There are several approaches to how jets are reconstructed. The jet reconstruction algorithm currently used in ATLAS is the *anti-k_t* algorithm [73], which belongs to the *sequential recombination* algorithm family (which also includes the *Cambridge/Aachen* [74, 75] and k_t [76, 77] algorithms), where input objects are added to form a jet one at a time. The differences between the various sequential recombination algorithms lie in the choice of parameter p in the definitions of distance measures d_{ij} (distance between objects i and j) and d_{iB} (distance between

object i and the beam):

$$d_{ij} = \min(k_{ti}^{2p}, k_{tj}^{2p}) \frac{\Delta R_{ij}^2}{R^2} \tag{3.10}$$

$$d_{iB} = k_{ti}^{2p} \tag{3.11}$$

where k_{ti}, y_i, and ϕ_i are the transverse momentum, rapidity, and azimuthal angle of object i respectively; $\Delta R_{ij}^2 = (y_i - y_j)^2 + (\phi_i - \phi_j)^2$ is the angular distance in the y-ϕ space between objects i and j; R is the jet radius parameter, which determines the closest proximity that two reconstructed jets can be located with respect to each another; and p is the parameter governing the relative power of the energy versus geometrical scales. For a set of input objects, distance measures d_{ij} and d_{iB} are computed between all pairs and for all individual objects respectively. Then, the minimum distance is found. If the minimum distance is a d_{ij}, objects i and j are combined, and d_{ij} and d_{iB} are re-computed the updated set of objects. If the new minimum is a d_{iB}, object i is declared a jet and is removed from the set. This process repeats until no objects remain in the set.

The anti-k_t, Cambridge/Aachen, and k_t algorithms correspond to $p = -1$, 0, and 1 respectively. In the anti-k_t algorithm, the negative power index means that objects with highest p_{T} are merged to form jets first, and low-p_{T} objects, which are typically caused by soft radiation emitted from the hard jets or by pile-up jets, are added later. As a result, the anti-k_t algorithm is particularly resilient against soft radiation from the underlying event and pile-up. In addition, it also generates circular cone-shaped jets as opposed to irregular-shaped jets produced by the k_t or Cambridge/Aachen algorithm, where soft and collinear branchings are combined first, as shown in Figure 3.29. From the experimental perspective, the benefit of circular cone-shaped jets is that they are easy for identification, measurement, and calibration. For these reasons, the anti-k_t algorithm is preferred over the Cambridge/Aachen and k_t algorithms in all of the modern-day LHC collarborations.

Jet reconstruction starts with the formation of calorimeter topo-clusters using a clustering algorithm described in 3.3.2. Originally, jet reconstruction in ATLAS only uses topo-clusters calibrated at the EM scale as inputs to the anti-k_t algorithm with

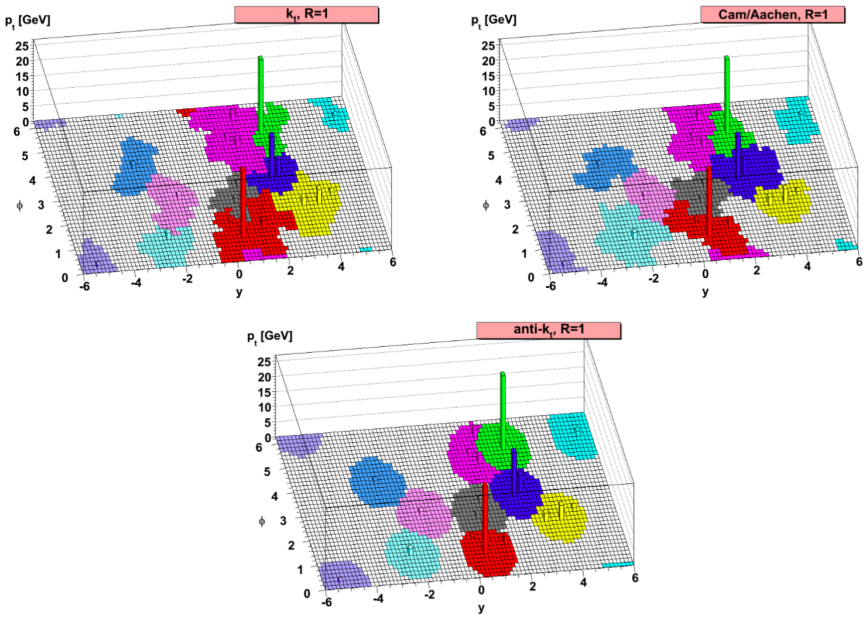

Figure 3.29: Simulation of jet reconstruction in the y-ϕ space for the k_t, Cambridge/Aachen, and anti-k_t algorithms [73]. Each coloured area represents a jet.

$R = 0.4$ or $R = 1.0$; these jets are referred to as *EMTopo* jets. ID track information may be added to EMTopo jets only after they are fully reconstructed for purposes such as jet calibration, particle identification, pile-up removal, improving momentum resolution for low-p_{T} charged tracks, providing higher angular granularity, etc.

Due to the high luminosity nature of LHC Run-2, pile-up has become a significant problem to the reconstruction of hard-scatter jets, which led to the development of an alternative *particle flow* (PFlow) algorithm [78]. The ATLAS PFlow algorithm combines the measurements of tracks in the ID and topo-clusters in the calorimeters. A flowchart summarizing how the PFlow algorithm operates is provided in Figure 3.30. First, charged-particle tracks passing quality criteria are matched to topo-clusters in the calorimeters (any tracks matched to candidate electrons or muons are not selected) [79]. The expected energy deposited in the calorimeters, $\langle E_{\mathrm{dep}} \rangle$, is computed by multiplying the track momentum by the mean response, which is determined by summing the energies of topo-clusters around the extrapolated track position[10] based on single-pion samples. However, it is not uncommon for a single charged hadron to deposit energy in multiple topo-clusters via shower

[10]Selected tracks are extrapolated to the second layer of the EM calorimeter.

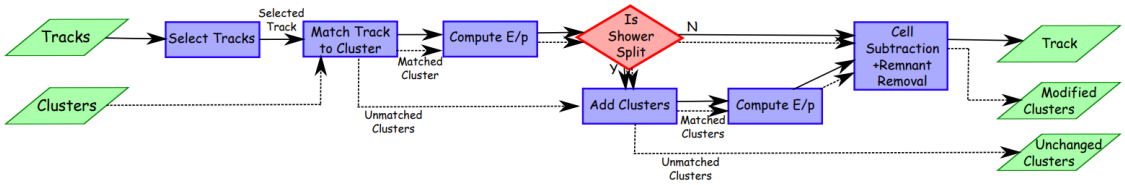

Figure 3.30: Flowchart summarizing the particle flow (PFlow) algorithm [78].

splitting. For each matched track/topo-cluster system, the algorithm evaluates the probability that the particle's energy was deposited in more than one topo-cluster and decides whether it is necessary to add more topo-clusters to the system in question in order to recover the full shower energy of the original particle. If $\langle E_{\text{dep}} \rangle$ of the charged particle that created the track exceeds the total energy of the set of matched topo-clusters, the topo-clusters are completely removed; otherwise, energy subtraction is performed on a cell-by-cell basis. Finally, if the remaining energy in the track/topo-cluster system is consistent with the expected shower fluctuations, the topo-cluster remnants are removed. These final energy subtraction steps are done in order to avoid double-counting of particle's energy in the ID and calorimeters. At the end, the PFlow algorithm outputs so-called *particle flow objects*, which comprise tracks of charged hadrons, unmodified topo-clusters which have not been matched to any tracks, and remnants of topo-clusters which have had part of their energy removed. These particle flow objects are then used as inputs to the anti-k_t algorithm to fully reconstruct jets. In ATLAS Run-2, the PFlow algorithm is only available for $R = 0.4$ and topo-clusters calibrated at the EM scale; jets reconstructed this way are referred to as *EMPFlow* jets.

The main benefit of the PFlow algorithm is that low-energy jets are reconstructed using track information while high-energy jets are still exclusively reconstructed using calorimeter information. This exploits the complementary nature of the ATLAS sub-detector systems where the ID trackers provide better resolution at low energies (their ability to measure track curvature degrades with increasing p_{T}) while the calorimeters are superior at high energies (fluctuations become less relevant at high p_{T}).

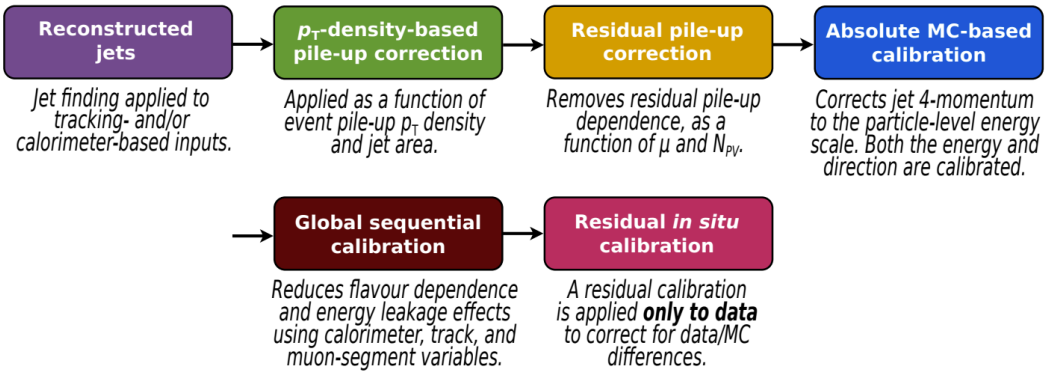

Figure 3.31: Flowchart summarizing the stages of the jet energy scale (JES) calibration [79].

Jet calibration

After jet objects are reconstructed, a sequence of corrections collectively known as the *jet energy scale* (JES) calibration are applied to restore the energy of each jet to that of the particle level [79, 80]. Corrections are applied to the 4-momenta of the jets which affect their mass, energy, and p_{T}. A summary of the stages of the JES calibration is provided in Figure 3.31.

In addition to the JES calibration, the *jet energy resolution* (JER) is also crucial for precise measurements of reconstructed jets as well as missing transverse momentum. The dependence of the JER on jet p_{T} can be parameterized as:

$$\frac{\sigma(p_{\mathrm{T}})}{p_{\mathrm{T}}} = \frac{N}{p_{\mathrm{T}}} \oplus \frac{S}{\sqrt{p_{\mathrm{T}}}} \oplus C \tag{3.12}$$

where the noise term N is due to electronic noise of the detector front-end electronics as well as due to pile-up, the stochastic term S is the due to statistical fluctuations in the amount of energy deposited in the calorimeters, and the constant term C corresponds to fluctuations that are a constant fraction of the jet p_{T}. The JER is measured using dijet events, where the two jets in each event are perfectly balanced against one another in the transverse plane, such that their p_{T} can be measured precisely [79].

Pile-up jet suppression

Pile-up interactions (also see Section 3.1.3) can lead to additional jets being reconstructed by the detector. An application of a p_{T} threshold on reconstructed jets in an event could reduce the amount of pile-up jets. However, this method does not take into account the case where there is a potential overlap between hard-scatter and pile-up jets. In order to mitigate this, a *jet-vertex tagging* (JVT) algorithm [81] has been developed for differentiating hard-scatter and pile-up jets in the central region ($|\eta| < 2.4$) where ID track information is available.

In Run-1, it was shown that pile-up jets could be effectively removed by imposing a minimum threshold based on the *jet-vertex fraction* (JVF) variable on the jets in an event, but this led to hard-scatter jet efficiencies that were dependent on the number of reconstructed primary vertices (N_{PV}) in the event. In Run-2, a correction has been made to the definition of JVF to make it insensitive to pile-up:

$$\mathrm{corrJVF} = \frac{\sum_i p_{\mathrm{T}}^{\mathrm{track}_i}(\mathrm{PV}_0)}{\sum_i p_{\mathrm{T}}^{\mathrm{track}_i}(\mathrm{PV}_0) + \frac{\sum_{k\geq 1}\sum_j p_{\mathrm{T}}^{\mathrm{track}_j}(\mathrm{PV}_k)}{k \cdot n_{\mathrm{track}}^{\mathrm{PU}}}} \tag{3.13}$$

where $\sum_i p_{\mathrm{T}}^{\mathrm{track}_i}(\mathrm{PV}_0)$ is the scalar p_{T} sum of all tracks that are associated with the jet and originate from the hard-scatter vertex, and $\sum_{k\geq 1}\sum_j p_{\mathrm{T}}^{\mathrm{track}_j}(\mathrm{PV}_k) = p_{\mathrm{T}}^{\mathrm{PU}}$ is the scalar p_{T} sum of the tracks that originate from any of the pile-up vertices. Since $\langle p_{\mathrm{T}}^{\mathrm{PU}} \rangle$ increases linearly with the total number of pile-up tracks per event $n_{\mathrm{track}}^{\mathrm{PU}}$, the $p_{\mathrm{T}}^{\mathrm{PU}}$ term is divided by $k \cdot n_{\mathrm{track}}^{\mathrm{PU}}$ to correct for this effect. The scaling factor k is set to be 0.01, which is roughly the gradient of the $\langle p_{\mathrm{T}}^{\mathrm{PU}} \rangle$-$n_{\mathrm{track}}^{\mathrm{PU}}$ curve[11]. The value of corrJVF roughly corresponds to the probability that the jet originates from a hard-scatter vertex. The distribution of corrJVF for hard-scatter and pile-up jets is shown in Figure 3.32a. A value of corrJVF $= -1$ is assigned to jets with no associated tracks.

The variable $R_{p_{\mathrm{T}}}$ is defined as the ratio of the scalar p_{T} sum of all tracks that are associated with the jet and originate from the hard-scatter vertex to

[11] Furthermore, the distribution of corrJVF with $k = 0.01$ is found to be similar to that of the original JVF.

the fully calibrated jet p_{T}:

$$R_{p_{\mathrm{T}}} = \frac{\sum_i p_{\mathrm{T}}^{\mathrm{track}_i}(\mathrm{PV}_0)}{p_{\mathrm{T}}^{\mathrm{jet}}} \ . \tag{3.14}$$

For pile-up jets, $R_{p_{\mathrm{T}}}$ is peaked at 0 and falls off rapidly since no tracks from the hard-scatter vertex are expected from them. For hard-scatter jets, $R_{p_{\mathrm{T}}}$ represents a charged p_{T} fraction of jets originating from the hard-scatter interaction. The spread of the $R_{p_{\mathrm{T}}}$ distribution for hard-scatter jets is larger than for that for pile-up jets, as shown in Figure 3.32b.

The so-called *jet-vertex tagger* (JVT) discriminant is constructed from a two-dimensional likelihood of corrJVF and $R_{p_{\mathrm{T}}}$ based on a k-nearest-neighbour (kNN) algorithm [82]. Hard-scatter jets tend to have large corrJVF and large $R_{p_{\mathrm{T}}}$, which correspond to a high value of JVT approaching 1. On the other hand, pile-up jets are concentrated at low corrJVF and low $R_{p_{\mathrm{T}}}$ values, resulting in a small JVT value close to 0. The distribution of the JVT discriminant for hard-scatter and pile-up jets is given in Figure 3.32c. A value of JVT $= -0.1$ is assigned to jets with no associated tracks.

In the forward region ($2.5 < |\eta| < 4.5$), however, the JVT algorithm cannot be used since it is outside the ID coverage and thus no tracking information is available. The inclusion of forward jets improves the precision of $E_{\mathrm{T}}^{\mathrm{miss}}$ calculation, but at a cost of increased pile-up dependency. In Run-2, a novel *forward*-JVT (fJVT) algorithm [84] has been introduced in order to suppress pile-up jets in the forward region. The fact that pile-up jets are mostly produced in pairs can be exploited. Due to the conservation of total transverse momentum, the two jets will be back-to-back in the transverse plane. If one of the jets is reconstructed and identified as a pile-up jet by the JVT algorithm in the central region, the other jet can be readily identified as a forward pile-up jet beyond the coverage of the ID. However, the main limitation of this approach is that it assumes that both jets are fully reconstructed. In order to mitigate this, the fJVT algorithm works by considering the total transverse momenta of tracks and jets associated with each primary vertex independently; and it makes a more generalized assumption that

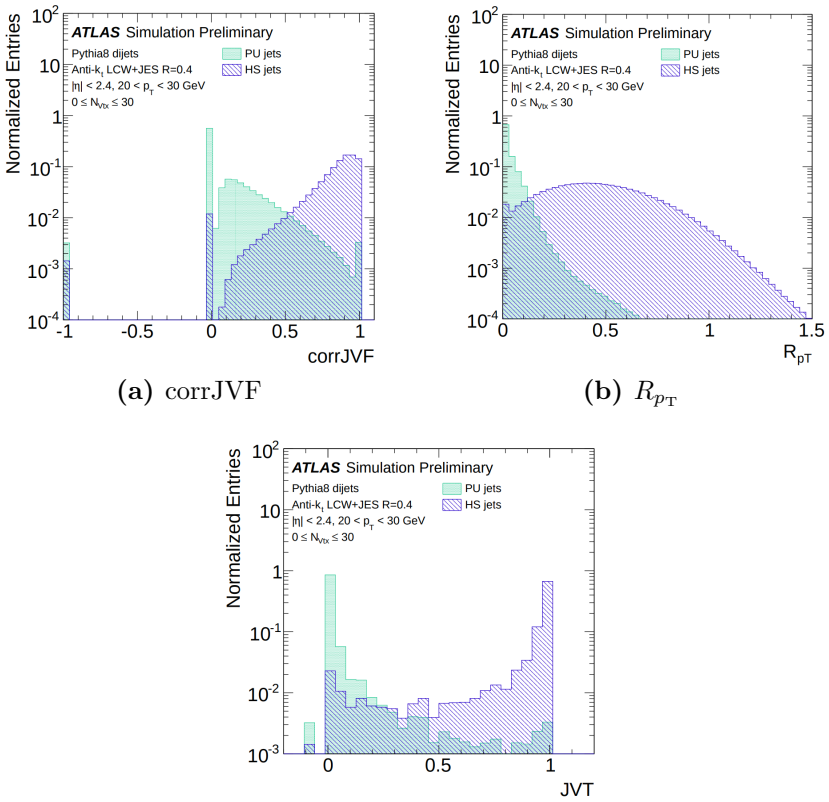

(a) corrJVF **(b)** $R_{p_{\mathrm{T}}}$

(c) JVT

Figure 3.32: Distributions of corrJVF, $R_{p_{\mathrm{T}}}$, and JVT for hard-scatter (blue) and pile-up (green) jets with $20 < p_{\mathrm{T}} < 30$ GeV and $|\eta| < 2.4$ based on MC simulated dijet events [83].

the transverse momentum of each pile-up interaction in the central region should be balanced, and any imbalance would be attributed to a forward jet originating from one of the pile-up interactions. For each primary vertex i, the expected missing transverse momentum $\langle \mathbf{p}_{\mathrm{T},i}^{\mathrm{miss}} \rangle$ is computed as the weighted vector $\mathbf{p}_{\mathrm{T}}$ sum of all tracks and reconstructed jets associated with the vertex:

$$\langle \mathbf{p}_{\mathrm{T},i}^{\mathrm{miss}} \rangle = -\frac{1}{2}\left(\sum_{\mathrm{tracks}\in \mathrm{PV}_i} k \cdot \mathbf{p}_{\mathrm{T}}^{\mathrm{track}} + \sum_{\mathrm{jets}\in \mathrm{PV}_i} \mathbf{p}_{\mathrm{T}}^{\mathrm{jet}} \right) . \tag{3.15}$$

where the weight factor k accounts for intrinsic differences between the track and jet terms: neutral particles do not contribute to the track term, whereas soft QCD emissions with $p_{\mathrm{T}} < 20$ GeV are not included in the jet term. The value of $k = 2.5$ is selected since it is found to optimize the overall rejection of forward pile-up jets [84]. Then, the fJVT discriminant for a given forward jet with respect to the primary vertex i is defined as the normalized projection of $\langle \mathbf{p}_{\mathrm{T},i}^{\mathrm{miss}} \rangle$ onto the

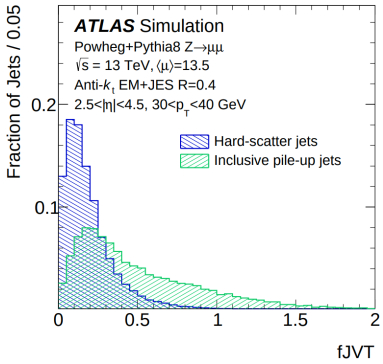

Figure 3.33: Distribution of fJVT for hard-scatter (blue) and pile-up (green) forward jets with $30 < p_{\mathrm{T}} < 40$ GeV and $2.5 < |\eta| < 4.5$ based on MC simulated Z+jets events [84].

transverse momentum of the forward jet:

$$\mathrm{fJVT}_i = \frac{\langle \mathbf{p}_{\mathrm{T},i}^{\mathrm{miss}} \rangle \cdot \mathbf{p}_{\mathrm{T}}^{\mathrm{fwd.jet}}}{|\mathbf{p}_{\mathrm{T}}^{\mathrm{fwd.jet}}|^2} \ . \tag{3.16}$$

If the forward jet does originate from the primary vertex i, the value of fJVT_i should be large as $\mathbf{p}_{\mathrm{T}}^{\mathrm{fwd.jet}}$ closely resembles $\langle \mathbf{p}_{\mathrm{T},i}^{\mathrm{miss}} \rangle$. The fJVT_i discriminant is then computed for all primary vertices in the event, and the overall fJVT discriminant for the forward jet in question is taken as the maximum value in the cohort:

$$\mathrm{fJVT} = \max_i(\mathrm{fJVT}_i) \ . \tag{3.17}$$

The fJVT discriminant tends to have larger values for pile-up jets, whereas hard-scatter jets are concentrated at low values and the distribution falls off steeply, as shown in Figure 3.33.

The JVT and fJVT discriminants can be used in conjunction to suppress both central and forward pile-up jets in an event. Several working points are defined with different hard-scatter jet selection efficiencies and pile-up suppression performance to suit a wide range of analyses. The JVT+fJVT working points are discussed in more detail in context of $E_{\mathrm{T}}^{\mathrm{miss}}$ performance in Section 3.3.6.

Flavour tagging

The identification of jets containing b-hadrons (b-jets), c-hadrons but no b-hadrons (c-jets), or neither b- nor c-hadrons (light-flavour jets) are collectively referred to as *flavour tagging* [85]. The relatively long lifetime of the b-hadron (~ 1.5 ps) means

that it can travel some distance on the order of millimetres from the primary vertex before decaying into final-state particles, leading to a distinct secondary vertex that can be reconstructed and identified. In addition, its high mass ($\sim$ 5 GeV) can lead to creation of a relatively large number of final-state particles, which in turn lead to a high amount of activity in the detector's sub-components. These properties can be exploited by the various algorithms used for flavour tagging. In Run-2, flavour tagging is based on a two-stage approach: low-level algorithms, which reconstruct the characteristic features of the heavy-flavour jets; and high-level algorithms, which consist of multivariate classifiers.

The low-level algorithms can be classified into two groups based on what subset of the characteristic features of b-jets are exploited. The first group exploits the large impact parameters of tracks originating from b-hadron decays. The IP3D algorithm utilizes both the transverse (d_0) and longitudinal (z_0) impact parameters as well as their correlation, while the IP2D algorithm considers only the transverse impact parameter [86]. The new RNNIP algorithm [87] has been introduced for Run-2. It is a recurrent neural network which takes into account the correlations between the impact parameters of the final-state-particle tracks in order to output the probability that the decaying jet in question is a b-jet, c-jet, or light-flavour jet. The second group explicitly reconstructs displaced vertices. The SV1 algorithm [88] works by identifying a single displaced secondary vertex inside a jet, whereas the JetFitter algorithm [89] reconstructs the full decay chain of a b-hadron to a c-hadron by combining information from multiple vertices.

To maximize the performance of flavour tagging, a series of high-level algorithms called DL1r [85, 90] combines the outputs from the five low-level algorithms and provides a probability that a jet is likely to be a b-jet, c-jet, or light-flavour jet. Large (small) correlations between the outputs of the IP2D, IP3D, SV1, and JetFitter are observed for heavy-flavour (light-flavour) jets. On the other hand, the output of the RNNIP algorithm is not strongly correlated with the others. The DL1r algorithm neural network training exploits these correlation differences to achieve the best flavour tagging performance. Working points for b-tagging are defined

based on b-jet identification efficiencies achieved by applying different thresholds on the output scores of DL1r. The four available working points correspond to 60%, 70%, 77%, and 85% b-tagging efficiency as measured in simulated $t\bar{t}$ events, where each W boson decay to a lepton and neutrino [85].

3.3.6 Missing transverse momentum

The missing transverse momentum ($\mathbf{E}_{\mathrm{T}}^{\mathrm{miss}}$) is the total amount of momentum in the transverse plane of an event that is not detected by the detector but is expected due to the conservation of energy and momentum. The sources of missing transverse momentum can be attributed to undetected particles such as neutrinos or BSM particles, or to limited resolution in object reconstruction. The conservation of momentum in the transverse plane can be expressed as:

$$\mathbf{E}_{\mathrm{T}}^{\mathrm{miss}} = -\Bigg\{ \underbrace{\sum_{\text{electrons}} \mathbf{p}_{\mathrm{T}} + \sum_{\text{photons}} \mathbf{p}_{\mathrm{T}} + \sum_{\substack{\text{hadronic} \\ \tau\text{-leptons}}} \mathbf{p}_{\mathrm{T}} + \sum_{\text{muons}} \mathbf{p}_{\mathrm{T}} + \sum_{\text{jets}} \mathbf{p}_{\mathrm{T}}}_{\text{hard term}} + \underbrace{\sum_{\substack{\text{unused} \\ \text{tracks}}} \mathbf{p}_{\mathrm{T}}}_{\text{soft term}} \Bigg\} \tag{3.18}$$

where $\mathbf{E}_{\mathrm{T}}^{\mathrm{miss}} = (E_x^{\mathrm{miss}}, E_y^{\mathrm{miss}})$ with magnitude $E_{\mathrm{T}}^{\mathrm{miss}} = \sqrt{(E_x^{\mathrm{miss}})^2 + (E_y^{\mathrm{miss}})^2}$. There are two groups of contributions to the total reconstructed $E_{\mathrm{T}}^{\mathrm{miss}}$: hard and soft terms. The hard term consists of fully reconstructed and calibrated particles: electrons, photons, hadronically decaying τ-leptons, muons, and jets. These objects are labelled 'hard' because they typically possess high p_{T}. The hard term is particularly insensitive to pile-up because it only includes fully calibrated objects, where appropriate pile-up corrections are applied and objects tagged as originating from pile-up vertices are removed. The soft term includes all detector signals in the event that are not associated with any of the reconstructed objects included in the hard term. The soft term used in this analysis is exclusively the *track-based soft term* (TST) [91], which consists of high-quality ID tracks from the hard-scatter vertex that are not matched with any of the hard objects. Soft neutral particle

signals in the calorimeters suffer from significant contributions from pile-up and thus are not included in the soft term. The particular choice of using only tracks from the hard-scatter vertex for the soft term suppresses a significant amount of in-time pile-up from entering the $E_{\mathrm{T}}^{\mathrm{miss}}$ calculation and almost completely eliminates its dependency on out-of-time pile-up.

$E_{\mathbf{T}}^{\mathbf{miss}}$ performance

For a given final state, the composition of the $E_{\mathrm{T}}^{\mathrm{miss}}$ calculation can fluctuate significantly since p_{T} of the objects can vary from event to event. The resolution of each type of objects is also a function of p_{T}, which means that the resolution of $E_{\mathrm{T}}^{\mathrm{miss}}$ is characterized by a high level of complexity. Due to its inherent dependency on other reconstructed objects, both the $E_{\mathrm{T}}^{\mathrm{miss}}$ response and resolution change as a function of the total event activity and are affected by pile-up. This study focuses on the effects that the different jet definitions and selection criteria have on $E_{\mathrm{T}}^{\mathrm{miss}}$ resolution.

The $Z \to ee$ (Drell-Yan) event is especially useful for the study of $E_{\mathrm{T}}^{\mathrm{miss}}$ performance because it contains no genuine missing transverse momentum[12] so that any reconstructed $E_{\mathrm{T}}^{\mathrm{miss}}$ can be solely attributed to limited resolution or mismeasurements in object reconstruction. The $Z \to ee$ samples are generated with either Sherpa 2.2.1 [92] or Powheg-box v2 [93]. For the Powheg-box v2 samples, the parton-level output is passed to Pythia 8.186 [94] to model soft QCD processes involved in underlying events and parton showering (UEPS). The full Run-2 dataset (2015–2018) is also used for this study. Samples are categorized into two types of jet selection: *veto-jet selection* does not contain any jets that pass the working point's selection criteria and is useful for studying the soft term performance; and *inclusive-jets selection* contains jets that pass the selection criteria and is useful for studying the contribution of jets to $E_{\mathrm{T}}^{\mathrm{miss}}$.

Electrons are reconstructed using the method described in Section 3.3.3 and are required to be within $|\eta| < 1.37$ or $1.52 < |\eta| < 2.47$, and pass the `Medium`

[12] Neutrinos are produced only through very rare heavy-flavour decays in the hadronic recoil due to the jets in the $Z \to ee$ event

identification working point. Each event is required to have exactly two reconstructed electrons of opposite charges. The (sub-)leading lepton in the pair must have $p_{\mathrm{T}} > 30$ (20) GeV, and the invariant mass of the pair must be consistent with the Z boson mass within a 25 GeV window, i.e. $|m_{ee} - m_Z| < 25$ GeV.

Reconstructed jets used in the $E_{\mathrm{T}}^{\mathrm{miss}}$ calculation can be either EMTopo or EMPFlow jets (see Section 3.3.5). All jets are required to have at least $p_{\mathrm{T}} > 20$ GeV. JVT working points are applied to preselected events in order to distinguish hard-scatter jets from pile-up jets based on the value of JVT discriminant. A summary of the different JVT working points is provided in Table 3.1. The `Tight` working point comprehensively removes soft forward jets in the forward region, which are more likely to be pile-up jets than hard-scatter jets. For mid-range-p_{T} central jets, however, it becomes more difficult to readily identify hard-scatter and pile-up jets based on p_{T} alone. Therefore, a JVT > 0.59 (0.50) requirement is made on EMTopo (EMPFlow) jets in order to improve pile-up suppression. For high-p_{T} jets, no JVT requirement is applied since they are already likely to be hard-scatter jets. The `Tighter` working point is identical to `Tight` except that the threshold for forward jets is increased from 30 to 35 GeV. And lastly, the `Tenacious` working point imposes a stringent JVT threshold for low-p_{T} central jets to ensure that as many pile-up jets as possible are excluded, and at higher-p_{T} the JVT threshold are increasingly loosened to include jets that are more likely to be hard-scatter jets. The JVT minimum thresholds of 0.11, 0.50, 0.59, and 0.91 correspond to 97%, 96%, 92%, and 85% of hard-scatter jet selection efficiency respectively. For EMTopo jets, fJVT working points are introduced to further suppress forward pile-up jets. The event selection criteria of the different fJVT working points are summarized in Table 3.2. The `TightFJVT` working point has a smaller maximum threshold because the value of fJVT discriminant is lower for hard-scatter forward jets than for pile-up. The fJVT threshold values of 0.4 and 0.5 correspond to 85% and 92% of forward hard-scatter jet selection efficiency respectively.

The $E_{\mathrm{T}}^{\mathrm{miss}}$ resolution is determined by the width of the combined distribution of the differences between the measured E_i^{miss} and the true missing transverse

Table 3.1: Summary of the selection requirements for the different JVT working points used in the study of $E_{\mathrm{T}}^{\mathrm{miss}}$ performance. Jets are reconstructed as either EMTopo or EMPFlow jets and are required to have at least $p_{\mathrm{T}} > 20$ GeV.

Jet type	JVT working point	Selection requirement		
		η	p_{T}	JVT
EMTopo	`Tight`	$\lvert\eta\rvert < 2.4$	$20 < p_{\mathrm{T}} < 60$ GeV	JVT > 0.59
			$p_{\mathrm{T}} > 60$ GeV	-
		$2.4 < \lvert\eta\rvert < 4.5$	$p_{\mathrm{T}} > 30$ GeV	-
	`Tighter`	$\lvert\eta\rvert < 2.4$	$20 < p_{\mathrm{T}} < 60$ GeV	JVT > 0.59
			$p_{\mathrm{T}} > 60$ GeV	-
		$2.4 < \lvert\eta\rvert < 4.5$	$p_{\mathrm{T}} > 35$ GeV	-
	`Tenacious`	$\lvert\eta\rvert < 2.4$	$20 < p_{\mathrm{T}} < 40$ GeV	JVT > 0.91
			$40 < p_{\mathrm{T}} < 60$ GeV	JVT > 0.59
			$60 < p_{\mathrm{T}} < 120$ GeV	JVT > 0.11
			$p_{\mathrm{T}} > 120$ GeV	-
		$2.4 < \lvert\eta\rvert < 4.5$	$p_{\mathrm{T}} > 35$ GeV	-
EMPFlow	`Tight`	$\lvert\eta\rvert < 2.4$	$20 < p_{\mathrm{T}} < 60$ GeV	JVT > 0.50
			$p_{\mathrm{T}} > 60$ GeV	-
		$2.4 < \lvert\eta\rvert < 4.5$	$p_{\mathrm{T}} > 30$ GeV	-
	`Tenacious`	$\lvert\eta\rvert < 2.4$	$20 < p_{\mathrm{T}} < 40$ GeV	JVT > 0.91
			$40 < p_{\mathrm{T}} < 60$ GeV	JVT > 0.59
			$60 < p_{\mathrm{T}} < 120$ GeV	JVT > 0.11
			$p_{\mathrm{T}} > 120$ GeV	-
		$2.4 < \lvert\eta\rvert < 4.5$	$p_{\mathrm{T}} > 35$ GeV	-

Table 3.2: Summary of the selection requirements for the different fJVT working points used in the study of $E_{\mathrm{T}}^{\mathrm{miss}}$ performance. The fJVT working points are only available for EMTopo jets. Jets are required to have at least $p_{\mathrm{T}} > 20$ GeV.

Jet type	fJVT working point	Selection requirement		
		η	p_{T}	fJVT
EMTopo	`TightFJVT`	$2.5 < \lvert\eta\rvert < 4.5$	$20 < p_{\mathrm{T}} < 60$ GeV	fJVT < 0.4
			$p_{\mathrm{T}} > 60$ GeV	-
	`LooseFJVT`	$2.5 < \lvert\eta\rvert < 4.5$	$20 < p_{\mathrm{T}} < 60$ GeV	fJVT < 0.5
			$p_{\mathrm{T}} > 60$ GeV	-

momentum $E_i^{\text{miss,true}}$, where $i = x, y$. The width is measured in terms of the root mean square (RMS). In the $Z \to ee$ event, $E_i^{\text{miss,true}} = 0$, and the $E_{\text{T}}^{\text{miss}}$ resolution is given by:

$$\text{RMS}_{x,y}^{\text{miss}} = \text{RMS}(E_{x,y}^{\text{miss}}) \ . \tag{3.19}$$

The $E_{\text{T}}^{\text{miss}}$ resolution is measured as a function of the total event activity, which can be quantified by the scalar p_{T} sum of all objects included in the $E_{\text{T}}^{\text{miss}}$ calculation:

$$\Sigma E_{\text{T}} = \underbrace{\sum_{\text{electrons}} p_{\text{T}} + \sum_{\text{photons}} p_{\text{T}} + \sum_{\substack{\text{hadronic} \\ \tau\text{-leptons}}} p_{\text{T}} + \sum_{\text{muons}} p_{\text{T}} + \sum_{\text{jets}} p_{\text{T}}}_{\text{hard term}} + \underbrace{\sum_{\substack{\text{unused} \\ \text{tracks}}} p_{\text{T}}}_{\text{soft term}} \ . \tag{3.20}$$

In Figure 3.34a, it can be seen that the scaling is roughly $\text{RMS}_{\text{x,y}}^{\text{miss}} \propto \sqrt{\Sigma E_{\text{T}}}$, which is dominated by the jet p_{T}-resolution as the contribution from jets increases with increasing ΣE_{T} [95]. In the lower ΣE_{T} range, all working points have identical resolution. For $\Sigma E_{\text{T}} \gtrsim 160$ GeV, however, `Tenacious+LooseFJVT` has the best overall resolution. For the veto-jet selection in Figure 3.34b, since there is no contribution from jets, the resolution does not increase with ΣE_{T} as steeply as in the inclusive-jets selection. The fluctuations arise from the electron p_{T}-resolution and the incomplete reconstruction of the hadronic recoil. All of the working points yield almost identical resolution.

The dependence of $E_{\text{T}}^{\text{miss}}$ resolution on the in-time and out-of-time pile-up is measured by the number of primary vertices N_{PV} and the average number of interactions per bunch crossing $\langle\mu\rangle$ respectively. In Figure 3.34c, an abrupt increase in the RMS from the first bin to the second bin is observed because events start to have additional primary vertices from in-time pile-up interactions. The non-linearity of the relationship between the resolution and N_{PV} is a result of vertex merging as pile-up increases (not all pile-up jets are identified and removed), and the resolution deteriorates as the pile-up activity increases as a result. However, this non-linear effect is less pronounced for out-of-time pile-up due to the inclusion of only tracks in the soft term of $E_{\text{T}}^{\text{miss}}$, as shown in Figure

3.34e. As in the case of the ΣE_{T}-dependence, `Tenacious+LooseFJVT` has better resolution than `Tenacious+NoneFJVT`, `Tighter+TightFJVT`, `Tight+TightFJVT`, and `Tight+NoneFJVT` respectively. Both the JVT and fJVT algorithms have proven to be very effective in suppressing pile-up jets. Figures 3.34d and 3.34f indicate that for the veto-jet selection the resolution increases linearly with increasing N_{PV} and $\langle\mu\rangle$ and is therefore independent of pile-up. `Tenacious+LooseFJVT` yields the worst resolution in the veto-jet selection because it wrongly considers a large number of events that actually contain jets but the jets are excluded due to its stringent jet selection criteria.

The performance of pile-up mitigation of EMTopo and EMPFlow jets is compared the context of $E_{\mathrm{T}}^{\mathrm{miss}}$ resolution, as shown in Figure 3.35. It can be seen that for the same JVT working point used EMPFlow jets produce better $E_{\mathrm{T}}^{\mathrm{miss}}$ resolution for both the inclusive-jet and veto-jet selections. What this means is EMPFlow jets can suppress pile-up more effectively than EMTopo jets while at the same time do not suffer from reduced performance when the level of pile-up is low or non-existent. Since pile-up jets tend to have low energies, they are reconstructed from track information by means of the PFlow algorithm. By matching calorimeter clusters to tracks, each jet can be traced back to its originating vertex, and pile-up jets can be readily identified and removed as such. This makes EMPFlow jets a natural choice for ATLAS Run-2 jet reconstruction, and the `Tight` JVT working point is recommended as the default working point. However, the implementation of the fJVT algorithm on EMPFlow jets is not available at the time of writing this thesis.

$E_{\mathrm{T}}^{\mathrm{miss}}$ systematic uncertainties

In an event topology where there is no genuine missing transverse momentum, such as the $Z \to ee$ event, the transverse momenta of all visible objects in the event can be written as:

$$\mathbf{E}_{\mathrm{T}}^{\mathrm{miss,hard,true}} + \mathbf{E}_{\mathrm{T}}^{\mathrm{miss,soft,true}} = 0 = -\mathbf{p}_{\mathrm{T}}^{\mathrm{hard,true}} - \mathbf{p}_{\mathrm{T}}^{\mathrm{soft,true}} , \tag{3.21}$$

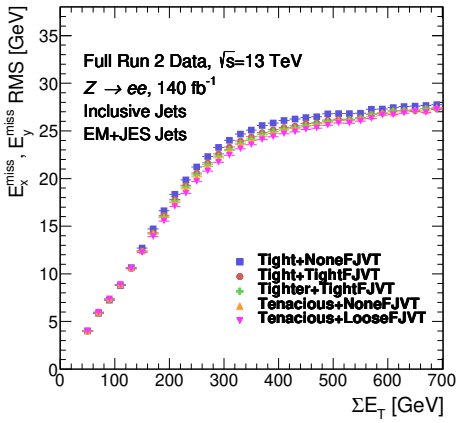

(a) ΣE_{T}, inclusive jets

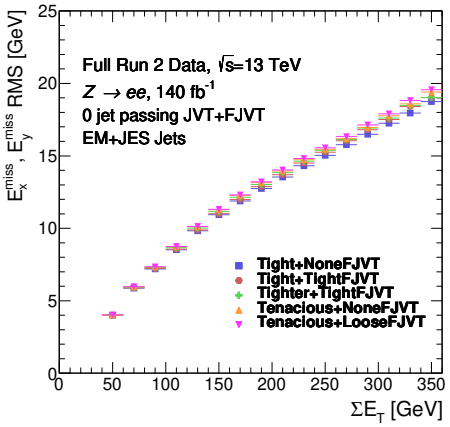

(b) ΣE_{T}, veto jet

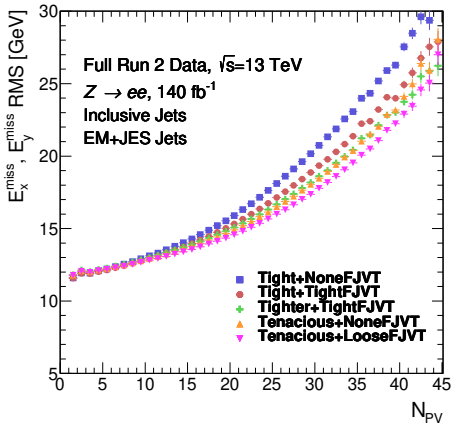

(c) N_{PV}, inclusive jet

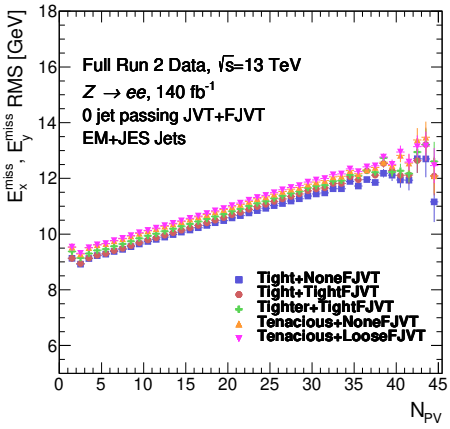

(d) N_{PV}, veto jet

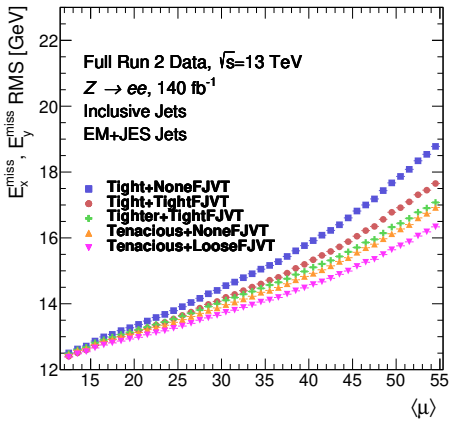

(e) $\langle\mu\rangle$, inclusive jets

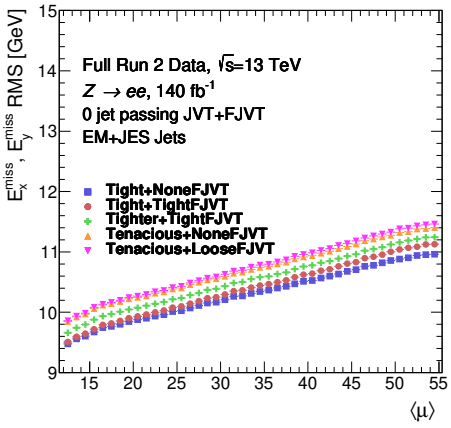

(f) $\langle\mu\rangle$, veto jet

Figure 3.34: The $E_{\mathrm{T}}^{\mathrm{miss}}$ resolution for the full Run-2 data sample favouring the $Z \to ee$ topology with or without associated jets plotted as functions of the total event activity ΣE_{T}, the number of primary vertices N_{PV}, and the average number of interactions per bunch crossing $\langle\mu\rangle$. Jets are reconstructed as EMTopo jets and are applied with different JVT+fJVT working points.

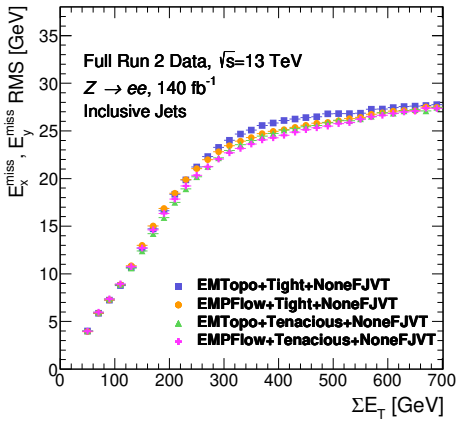

(a) ΣE_{T}, inclusive jets

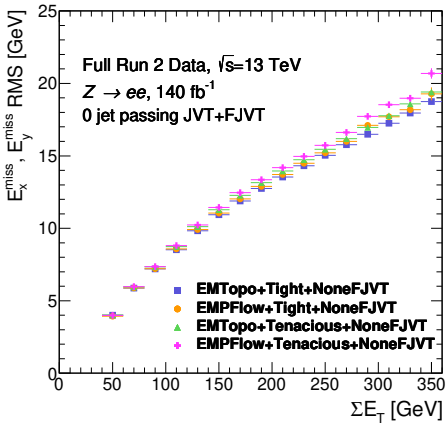

(b) ΣE_{T}, veto jet

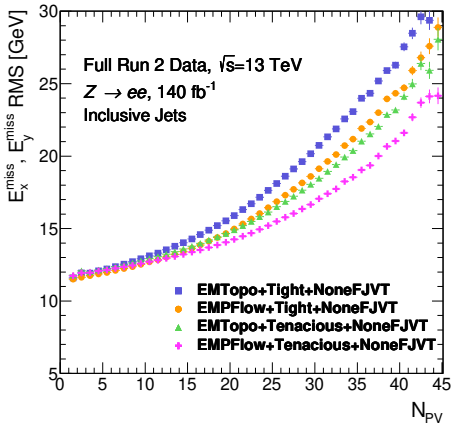

(c) N_{PV}, inclusive jet

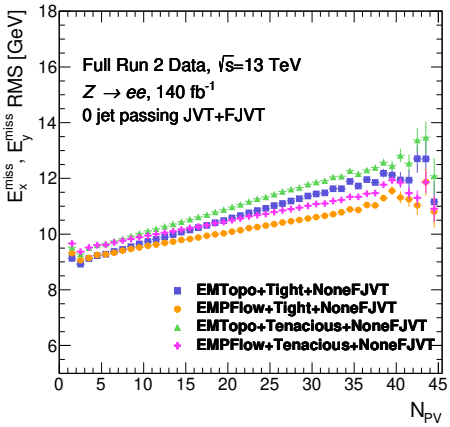

(d) N_{PV}, veto jet

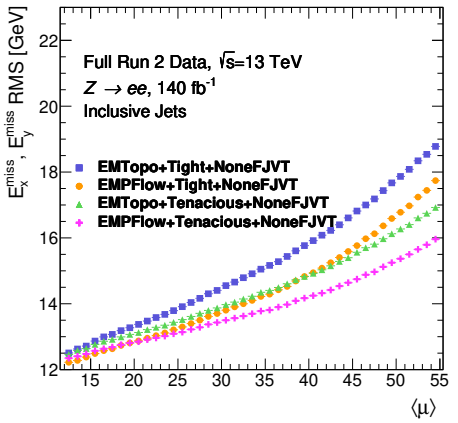

(e) $\langle\mu\rangle$, inclusive jets

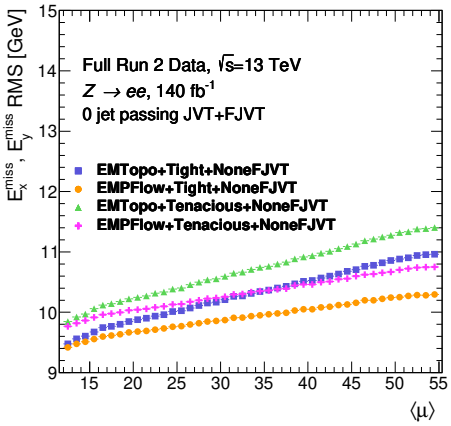

(f) $\langle\mu\rangle$, veto jet

Figure 3.35: The $E_{\mathrm{T}}^{\mathrm{miss}}$ resolution for the full Run-2 data sample favouring the $Z \to ee$ topology with or without associated jets plotted as functions of the total event activity ΣE_{T}, the number of primary vertices N_{PV}, and the average number of interactions per bunch crossing $\langle\mu\rangle$. Jets are reconstructed as either EMTopo or EMPFlow jets and are applied with different JVT working points. The fJVT working points are not used since they are not available for EMPFlow jets.

or equivalently:

$$\mathbf{p}_{\mathrm{T}}^{\mathrm{hard,true}} = (\mathbf{E}_{\mathrm{T}}^{\mathrm{miss,soft,true}} = -\mathbf{p}_{\mathrm{T}}^{\mathrm{soft,true}}) \ . \tag{3.22}$$

In other words, the soft-term momentum is expected to be perfectly balanced against the hard term. In practice, however, this relation does not hold due to limited detector resolution and object reconstruction inefficiencies. Despite the imperfections, the measured $\mathbf{p}_{\mathrm{T}}^{\mathrm{soft}}$ is nevertheless expected to point along the direction of the hadronic recoil opposite to $\mathbf{p}_{\mathrm{T}}^{\mathrm{hard}}$, which is equivalent to $\mathbf{p}_{\mathrm{T}}^{Z}$ in the case of the veto-jet selection. The deviation from this expectation is measured in terms of the parallel and perpendicular projections of $\mathbf{p}_{\mathrm{T}}^{\mathrm{soft}}$ onto $\mathbf{p}_{\mathrm{T}}^{\mathrm{hard}}$, as shown schematically in Figure 3.36. The parallel scale of the soft term is given by:

$$E_{\parallel}^{\mathrm{miss,soft}} = \mathbf{E}_{\mathrm{T}}^{\mathrm{miss,soft}} \cdot \frac{\mathbf{p}_{\mathrm{T}}^{\mathrm{hard}}}{p_{\mathrm{T}}^{\mathrm{hard}}} \ , \tag{3.23}$$

and the average parallel scale $\langle E_{\parallel}^{\mathrm{miss,soft}} \rangle$ calculated for each bin of the $p_{\mathrm{T}}^{\mathrm{hard}}$ distribution measures the $E_{\mathrm{T}}^{\mathrm{miss}}$ response, with $\langle E_{\parallel}^{\mathrm{miss,soft}} \rangle = \langle p_{\mathrm{T}}^{\mathrm{hard}} \rangle$ being the perfect response for that bin. The $E_{\mathrm{T}}^{\mathrm{miss}}$ resolution contributed by the soft term is measured by the parallel resolution:

$$\sigma^2(E_{\parallel}^{\mathrm{miss,soft}}) = \langle (E_{\parallel}^{\mathrm{miss,soft}})^2 \rangle - \langle E_{\parallel}^{\mathrm{miss,soft}} \rangle^2 \ , \tag{3.24}$$

and the perpendicular resolution[13]:

$$\sigma^2(E_{\perp}^{\mathrm{miss,soft}}) = \langle (E_{\perp}^{\mathrm{miss,soft}})^2 \rangle \ . \tag{3.25}$$

The $E_{\mathrm{T}}^{\mathrm{miss}}$ scale and resolution systematic uncertainties due to the TST are determined from the maximum discrepancy between the data and either of the two MC samples in each $p_{\mathrm{T}}^{\mathrm{hard}}$ bin. This first step is done separately for the inclusive-jets and veto-jet selections. Then, the final values of systematic uncertainties are chosen as the maximal variation of either of these two jet-selection cases on a bin-by-bin basis. The TST systematic uncertainties for EMPFlow jets with the `Tight+NoneFJVT` working point applied, which is the default configuration for jets used in this analysis, are presented in Figure 3.37.

[13]The average perpendicular projection $\langle E_{\perp}^{\mathrm{miss,soft}} \rangle$ is statistically zero.

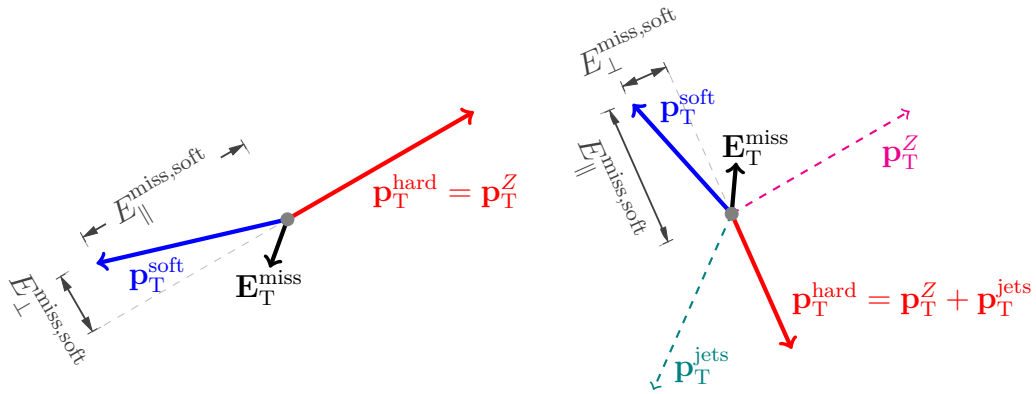

(a) Veto jet **(b)** Inclusive jets

Figure 3.36: Schematics of the projections of $\mathbf{p}_{\text{T}}^{\text{soft}}$ onto $\mathbf{p}_{\text{T}}^{\text{hard}}$ for the $Z \to ee$ event for (a) veto-jet and (b) inclusive-jets selections.

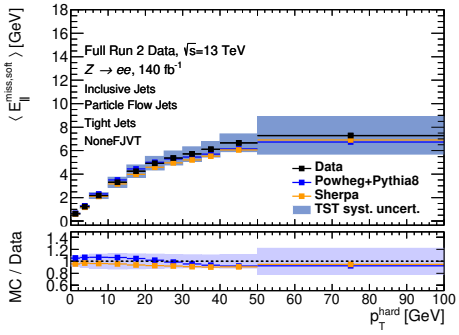

(a) Parallel scale, inclusive jets

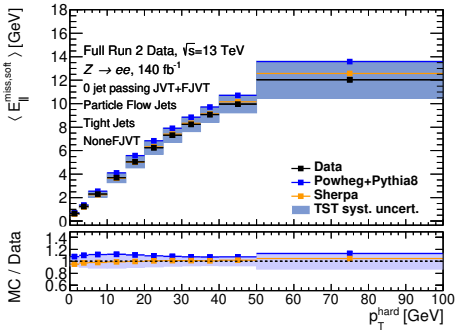

(b) Parallel scale, veto jet

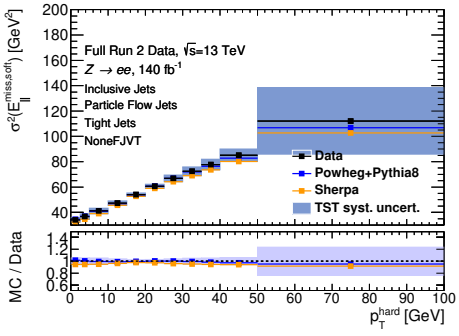

(c) Parallel resolution, inclusive jets

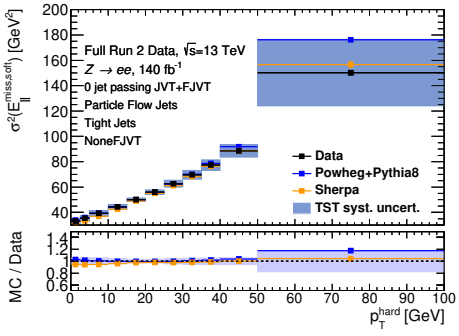

(d) Parallel resolution, veto jet

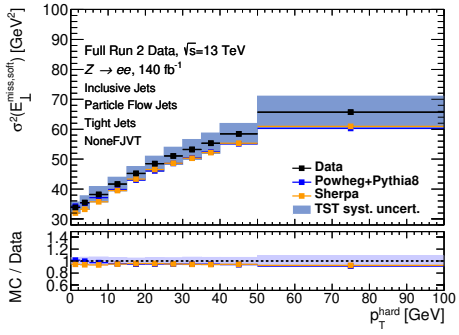

(e) Perpendicular resolution, inclusive jets

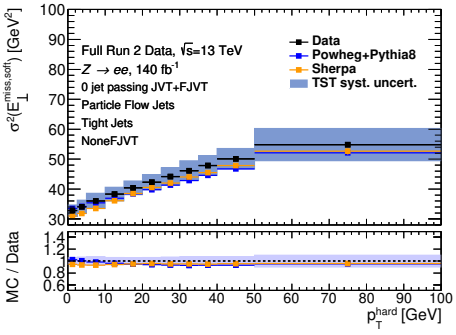

(f) Perpendicular resolution, veto jet

Figure 3.37: Performance plots for the TST $E_{\mathrm{T}}^{\mathrm{miss}}$ as a function of $p_{\mathrm{T}}^{\mathrm{hard}}$ for EMPFlow jets with the `Tight+NoneFJVT` working point applied. The blue bands represent the TST systematic uncertainties, which are derived from differences between full Run-2 data and MC samples using the $Z \to ee$ process. The uncertainty value in each bin is taken from the larger data-MC discrepancy of either the inclusive-jets or veto-jet selection and is then directly applied to the jet selection case where the discrepancy is smaller.

4

The $H \to WW^* \to l\nu l\nu$ same-flavour analysis

This chapter presents the strategy and pre-statistical-fit results of the $H \to WW^* \to l\nu l\nu$ same-flavour analysis by employing the cut-based approach. The aim of the analysis is to measure the inclusive (total) signal strength μ of the ggF and VBF production modes in the same-flavour channel. This is to complement the inclusive μ measured in the different-flavour channel [6]. This analysis utilizes a traditional cut-based approach, which involves event selection criteria (also known as *cuts*) purely based on kinematic observables. Cuts are devised by exploiting the differences in the topologies and characteristics of different processes and are applied successively to construct regions enriched with signal or background processes.

This cut-based analysis serves as a baseline or reference point for the novel Deep Neural Network (DNN) approach involving machine learning techniques [96–98]. The DNN technique is new to the Run-2 analysis and was first used on the VBF topology in the different-flavour analysis [6]. However, as progress has been made towards understanding the new technique, the DNN technique has been introduced to both the ggF and VBF topologies in the same-flavour analysis and the outcome will be cross-checked against the cut-based approach.

The results presented in this chapter are obtained from the full Run-2 dataset recorded at the LHC between 2015 and 2018 corresponding to an integrated luminosity of 139 fb^{-1} at a centre-of-mass energy of 13 TeV.

This chapter is structured as follows. The characteristics of signal and background processes involved in the $H \to WW^* \to l\nu l\nu$ analysis are described in Section 4.1. The details of data and MC samples used in this analysis are presented in Section 4.2. The definitions of the reconstructed objects and observables pertaining to the analysis are given in Sections 4.3 and 4.4 respectively. And lastly, the methodology for event selection and pre-fit results are presented in Section 4.5.

4.1 Characteristics of processes

The $H \to WW^* \to l\nu l\nu$ signal process produces a pair of oppositely charged leptons that can be recorded by the detector. However, the same final state particles can also be produced by other processes. These processes are referred to as background processes. Some processes possess unique characteristics that can be utilized for extracting such processes from others during the event selection stage. This section discusses the characteristics of the different processes relevant to the $H \to WW^* \to l\nu l\nu$ analysis.

4.1.1 Signal processes

The topological signature of the $H \to WW^* \to l\nu l\nu$ decay arises from the spin-0 nature of the Higgs boson. The two emergent spin-1 W bosons must have anti-parallel spins due to the conservation of angular momentum. The chiralities of the outgoing neutrino and anti-neutrino are always left-handed and right-handed respectively according to the electroweak theory. Since neutrinos are massless in the Standard Model, they always travel at the speed of light and the concept of chirality becomes equivalent to helicity[1]. As a result, this means that the spin of the outgoing neutrino (anti-neutrino) must anti-align (align) with its direction of travel. Given that the charged leptons are emitted at very high energy, their chirality is

[1]Helicity is defined as the projection of a particle's spin onto its direction of travel.

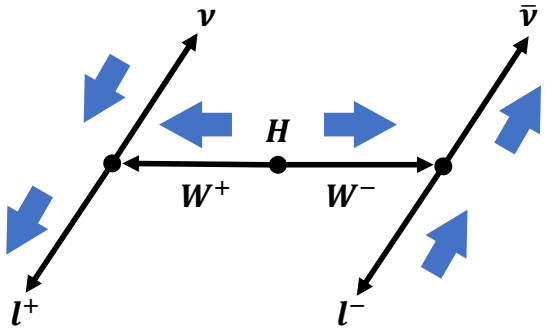

Figure 4.1: Schematic diagram of the kinematic topology of the $H \to WW^* \to l\nu l\nu$ decay. The small arrows indicate the particles' directions of motion and the large blue arrows indicate their spin projections.

approximately equivalent to helicity, and therefore the spin of the outgoing lepton (anti-lepton) must also anti-align (align) with its direction. As shown in Figure 4.1, the spins of the $l^+\nu$ and $l^-\bar{\nu}$ pairs also tend to align with the spins of the parent W bosons from which they emerge due to angular momentum conservation. This results in a small angular separation between the two final-state leptons, leading to a small combined invariant mass m_{ll} and a small difference in azimuthal angle $\Delta\phi_{ll}$ between them in the plane transverse to the proton beam.

The VBF production mode is characterized by a unique topology where two high-energy quarks from the proton-proton pair scatter and leave the interaction point towards the forward regions almost parallel to the beam axis. This opens a large angular separation along the beam axis between them and therefore a high combined invariant mass m_{jj}. Since the two quarks do not strongly interact with each other but via a weak vector boson, there is no colour exchange and this leads to a low level of QCD hadronic activity, making the signal from the VBF production process 'cleaner' than that of the process of ggF production with high jet multiplicity. The Higgs boson is produced between these quarks so the charged leptons are generally within the (pseudo)rapidity gap spanned by the jet pair, as depicted in Figure 4.2. This is another feature intrinsic to the VBF production mode which will be exploited during the event selection stage.

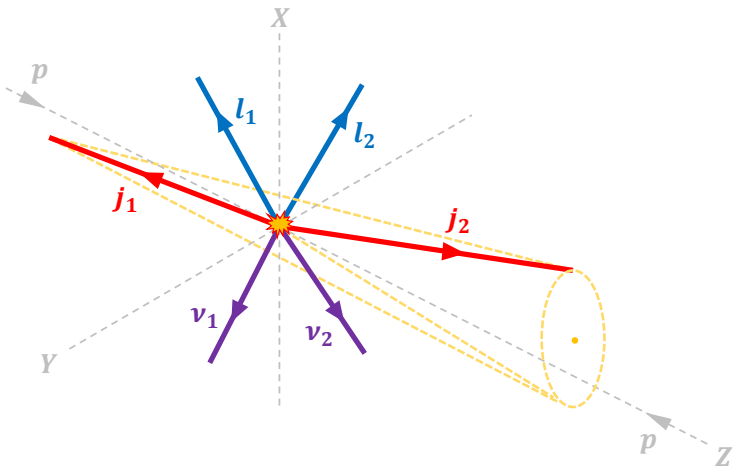

Figure 4.2: Schematic diagram of the kinematic topology of the VBF process as observed in the laboratory frame with a Cartesian coordinate system. The two proton beams travel along the z-axis in opposite directions and collide at the origin. The two scattered leading jets (red arrows) leave the interaction point towards the forward region almost parallel to the beam axis. The two leptons (blue arrows) and two neutrinos (purple arrows) are emitted within the rapidity gap spanned by the jet pair, i.e. through the lateral side of the imaginary cone spanned by the directions of the two leading jets.

4.1.2 Background processes

Background processes produce the same reconstructed final state as the signal process. The event selection criteria for extracting the signal process are constructed based on how well they reject different background processes by exploiting the properties of these processes. The background processes relevant to the $H \to WW^* \to l\nu l\nu$ analysis are presented in this section.

WW production

A pair of W bosons can be produced via three main processes: quark-antiquark scattering ($q\bar{q} \to WW$), gluon-gluon fusion ($gg \to WW$), and electroweak (EW) WW pair production. The leading-order Feynman diagrams for these processes are shown in Figure 4.3. The $q\bar{q} \to WW$ process can be either a t-channel $q\bar{q}$ scattering or an s-channel $q\bar{q}$ annihilation into an off-shell Z or γ boson, which subsequently splits into a WW boson pair; both are tree-level diagrams. The $gg \to WW$ process is through a quark-loop box diagram, resulting in a smaller contribution to the overall WW background than the $q\bar{q} \to WW$ process. And lastly, the smallest

contribution comes from the EW WW pair production as even the lowest order diagrams involve $O(\alpha^6)$ weak coupling or a quadruple weak boson vertex. Since the two W bosons are not a result of the spin-0 Higgs boson decay, the final-state leptons tend to be more separated than those of the signal process, i.e. larger $\Delta\phi_{ll}$.

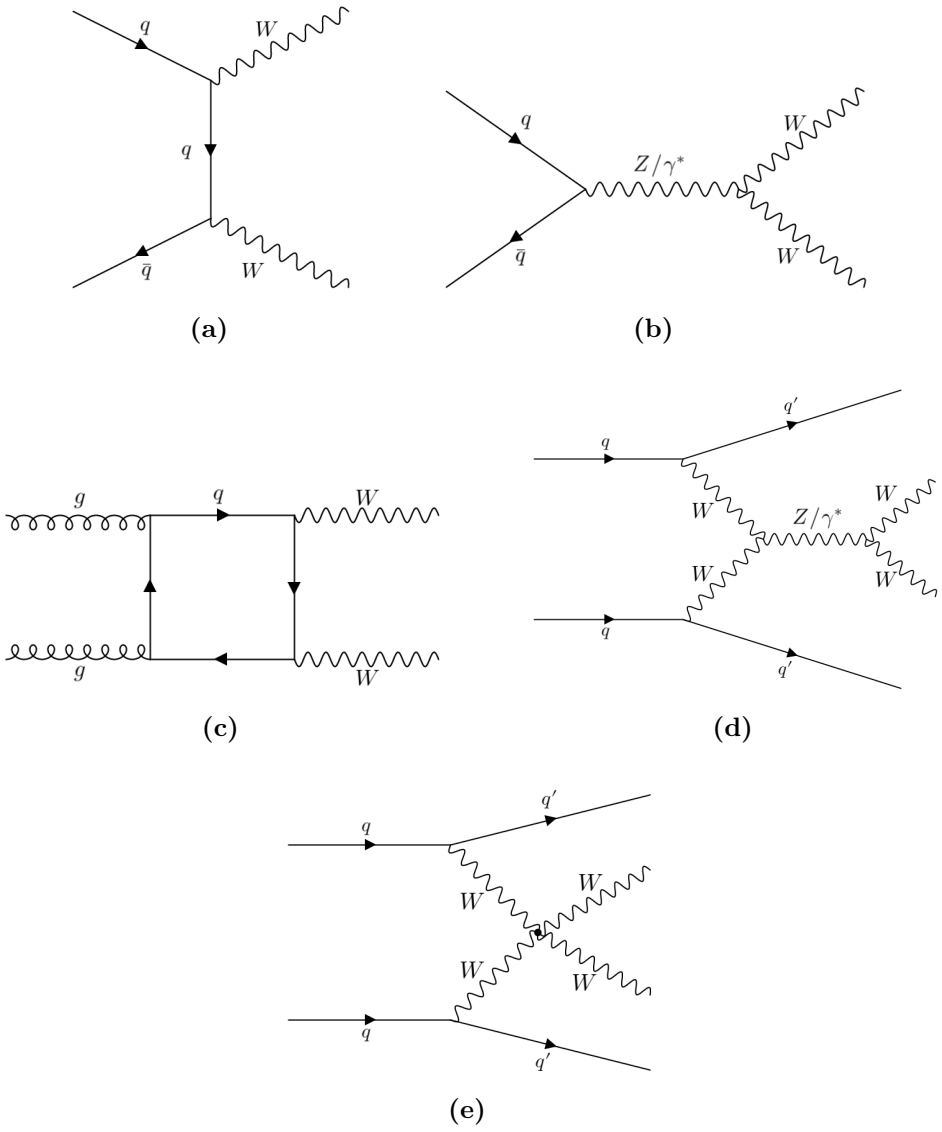

Figure 4.3: Leading-order Feynman diagrams for WW production via: (a) $q\bar{q} \to WW$ t-channel; (b) $q\bar{q} \to WW$ s-channel; (c) $gg \to WW$ through a quark loop; (d) EW WW through vector-boson scattering; (e) EW WW through a quadruple boson vertex.

Z/γ^* (Drell-Yan) process

In the Drell-Yan process, a quark and an antiquark from the two colliding hadrons annihilate in the s-channel and create a Z or γ^* vector boson, which subsequently

decays into a pair of oppositely charged leptons as shown in Figure 4.4. The Drell-Yan process is denoted by $Z/\gamma^* \to ll$, where l is an electron, muon, or leptonically decaying τ-lepton. This process is the most dominant background in the $H \to WW^* \to l\nu l\nu$ same-flavour analysis. The Drell-Yan process may produce final-state leptons with different flavours when a pair of τ-leptons is produced by the vector boson: $Z/\gamma^* \to \tau\tau$. However, in the same-flavour channel, the $Z/\gamma^* \to \tau\tau$ decay where the τ-leptons decay into final-state leptons of the same flavour is negligible compared to the $Z/\gamma^* \to ee/\mu\mu$ decays. Like the WW background, $\Delta\phi_{ll}$ tends to be larger than that of the signal. The important characteristic of the Drell-Yan process (except $Z/\gamma^* \to \tau\tau$) is there is no genuine missing transverse momentum since the lepton pair are produced directly from a Z boson decay and not from W decays like other background processes.

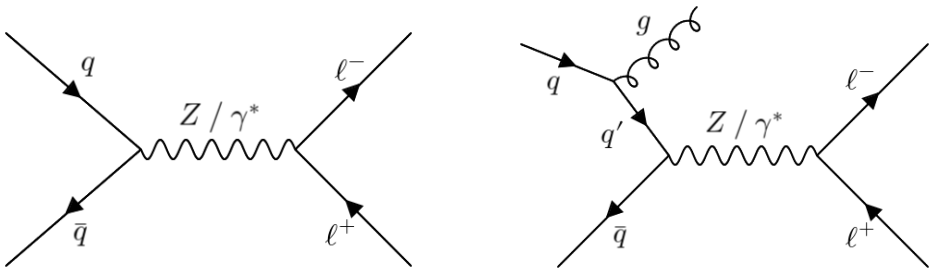

(a) **(b)**

Figure 4.4: Leading-order Feynman diagrams for the Drell-Yan (Z/γ^*) process with: (a) 0 jet; (b) 1 jet.

Top quark production

Top quarks can be produced via two main processes: pair production ($t\bar{t}$) and production in association with a W boson (Wt), as shown in Figure 4.5. The top quark undergoes a weak decay almost exclusively into a W boson and a bottom quark. The W boson then decays leptonically into a lepton and a neutrino. The distinguishing feature of this process is the presence of high energy b-jets. The b-jets can be tagged in order to suppress this background. However, the background still remains large because top quark production involves only tree-level diagrams.

At next-to-leading-order (NLO), there can be overlap between the Wt and $t\bar{t}$ processes. Removal of this overlap is necessary as to avoid double-counting. Details of the overlap removal procedure are provided in Section 5.3.3.

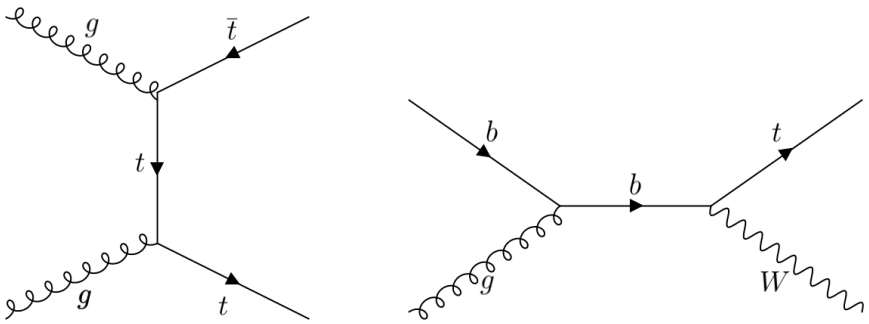

(a) (b)

Figure 4.5: Leading-order Feynman diagrams for top quark production via: (a) $t\bar{t}$; (b) Wt.

Other VV processes

Diboson processes other than WW are collectively known as Other VV processes. These include $W\gamma^{(*)}, WZ, ZZ$, and $Z\gamma^{(*)}$ productions which can be generated via one or more of the three tree-level diagrams shown in Figure 4.6. The $W\gamma$ process mimics the signal when the W boson decays leptonically and the photon is misidentified as a lepton. In the $W\gamma^*$ and WZ processes, the $l\nu ll$ final state mimics the signal when one of the leptons is not identified or is outside of the detector acceptence. In the $Z\gamma^*$ process, a $\nu\nu ll$ final state results from the Z boson decaying into a pair of neutrinos and the virtual photon splitting into a pair of leptons. The $Z\gamma$ process mimics the signal when one of the leptons from the Z boson decay is not identified and the photon is misidentified as a lepton, or when the photon is outside acceptance. And lastly, for the ZZ process, there are two final states that could mimic the signal: $llll$ when only two of the leptons are identified; and $ll\nu\nu$, which is the same final state as the signal.

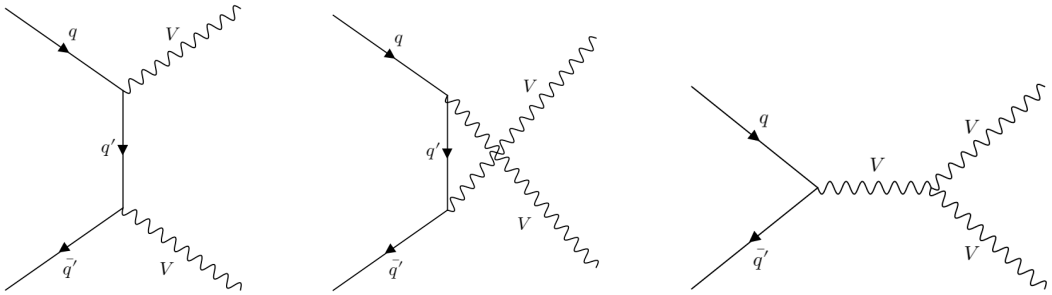

(a) **(b)** **(c)**

Figure 4.6: Leading-order Feynman diagrams for other diboson VV production where V can be a $\gamma^{(*)}$, W, or Z boson.

VVV processes

Triboson processes involve production of three massive weak bosons. The possible combinations are WWW, WWZ, WZZ, and ZZZ. Similar to other diboson VV processes, triboson processes may imitate the signal when either or both of these scenarios happen: one of the bosons decays hadronically to jets; or only two leptons out of three or four produced are identified. These processes constitute a very small number of events in the analysis because the energy required to produce three weak bosons is high and they involve multiple weak vertices or a higher-order vertex even in the tree-level diagrams, as shown in Figure 4.7.

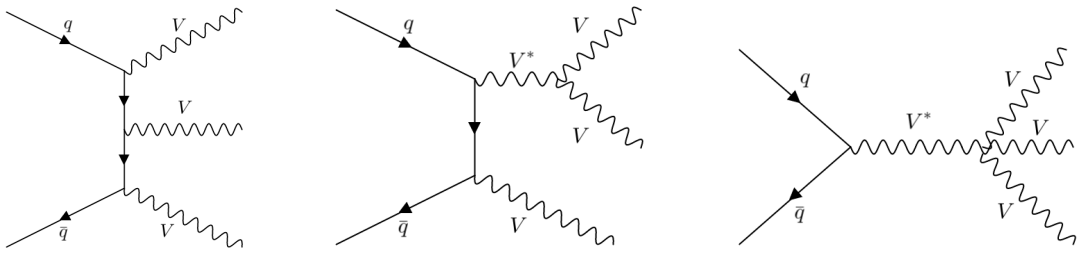

(a) **(b)** **(c)**

Figure 4.7: Leading-order Feynman diagrams for triboson VVV production where V can be a W or Z boson.

Misidentification of leptons

Another important source of background is a process where a W boson is created in association with one or more jets and one of the jets is misidentified as a lepton

(W+jets). This can also happen, albeit less significantly, in a multijet process where two jets are misidentified as leptons and missing transverse momentum $E_{\mathrm{T}}^{\mathrm{miss}}$ is large due to mismeasurements. The estimation of the W+jets process is described in Section 4.5.2. Some examples of the W+jets process are shown in Figure 4.8.

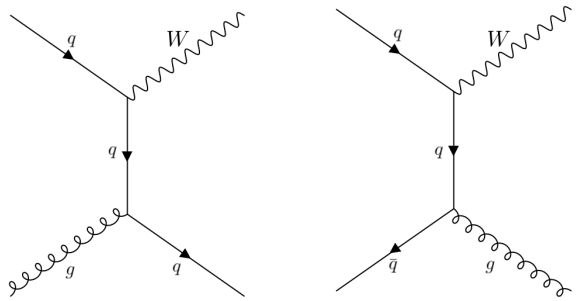

Figure 4.8: Examples of leading-order Feynman diagrams for the W+jets process.

$H \to \tau\tau$ decay

The $H \to \tau\tau$ background is a process in which the Higgs boson decays directly into a pair of τ-leptons. The τ-leptons subsequently decay into neutrinos and W bosons, which in turn decay leptonically into final-state leptons and neutrinos, as shown in Figure 4.9. Due to the high momentum of the τ-lepton, the neutrinos tend to be collinear with the final-state charged leptons, allowing a mass reconstruction that can be used to discriminate this background from the signal process. As can be seen from Figure 2.3b, the branching ratio of the $H \to \tau\tau$ decay is small but not negligible when compared to the $H \to WW$ signal for a Higgs mass of 125 GeV.

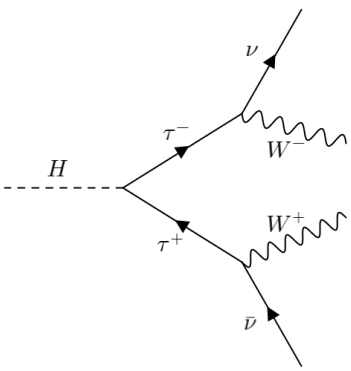

Figure 4.9: A leading-order Feynman diagram for the $H \to \tau\tau$ decay.

Table 4.1: List of the e and μ single-lepton triggers used by the $H \to WW^* \to l\nu l\nu$ same-flavour analysis. The triggers are sorted by year of data collection. First-level (L1) triggers and high-level triggers (HLTs) require leptons to be above certain E_{T} and p_{T} thresholds (in GeV) respectively. The HLTs also apply likelihood identification criteria (`lhtight`, `lhmedium`, and `lhloose`) [99] or/and isolation criteria (`iloose`, `ivarloose`, and `ivarmedium`) [100] for improving the efficiency of lepton selection. Tigher criteria are placed on triggers with lower p_{T} thresholds.

Year	Lepton	L1 trigger	High-level trigger		
		E_{T}	low-p_{T}	intermediate-p_{T}	high-p_{T}
2015	e	20	24-`lhmedium`		
		22		60-`lhmedium`	
		22			120-`lhloose`
	μ	15	20-`iloose`		
		20		50	
2016-2018	e	22	26-`lhtight-ivarloose`		
		22		60-`lhmedium`	
		22			140-`lhloose`
	μ	20	26-`ivarmedium`		
		20		50	

4.2 Data and Monte Carlo samples

4.2.1 Data samples

The dataset used in the analysis is composed of pp collision data collected from 2015 through 2018 during Run-2 of the LHC. The centre-of-mass energy is $\sqrt{s} = 13$ TeV and the integrated luminosity is approximately 139 fb^{-1} with an uncertainty of 1.7%. The spacing between proton bunches is 25 ns.

The lepton event triggers available for Run-2 data collection at the ATLAS detector are either single-lepton or dilepton triggers [99, 100]. This $H \to WW^* \to l\nu l\nu$ same-flavour analysis only uses data samples collected with single-electron or single-muon triggers. An event is accepted if it has at least one lepton that passes the appropriate object selection criteria as listed in Table 4.1.

4.2.2 Monte Carlo samples

The Monte Carlo (MC) technique is used to generate samples that model the signal and background processes, except the W+jets process where a data-driven technique is used to estimate event yields (Section 4.5.2).

Table 4.2: Summary of the Monte Carlo (MC) simulation tools used to generate the nominal signal and background processes in the $H \to WW^* \to l\nu l\nu$ same-flavour analysis sorted by their matrix-element calculations, parton distribution function (PDF) sets, underlying event/parton showering (UEPS) models, and prediction orders for inclusive cross-sections ($\sigma_{incl.}$).

Process	Matrix element	PDF set	UEPS model	Precision of $\sigma_{incl.}$
ggF H	Powheg-box v2 [93, 105–108] NNLOPS [107, 109, 110]	PDF4LHC15nnlo [111]	Pythia 8 [112]	N^{3}LO QCD + NLO EW [12, 113–122]
VBF H	Powheg-box v2 [93, 105–107, 110]	PDF4LHC15nlo	Pythia 8	NNLO QCD + NLO EW [123–125]
VH	Powheg-box v2	PDF4LHC15nlo	Pythia 8	NNLO QCD + NLO EW [126–130]
$t\bar{t}H$	Powheg-box v2	NNPDF3.0nlo [104]	Pythia 8	NLO [12]
$q\bar{q} \to WW$	Sherpa 2.2.2 [92]	NNPDF3.0nnlo	Sherpa 2.2.2 [131–136]	NLO [137–139]
$gg \to WW/ZZ$	Sherpa 2.2.2	NNPDF3.0nnlo	Sherpa 2.2.2	NLO [140]
EW WW	MadGraph 5 [141]	NNPDF3.0nlo	Pythia 8	LO [6]
$WZ, V\gamma^*, ZZ$	Sherpa 2.2.2	NNPDF3.0nnlo	Sherpa 2.2.2	NLO [142]
$V\gamma$	Sherpa 2.2.8 [92]	NNPDF3.0nnlo	Sherpa 2.2.8	NLO [142]
VVV	Sherpa 2.2.2	NNPDF3.0nnlo	Sherpa 2.2.2	NLO [142]
Z/γ^*	Sherpa 2.2.11 [143]	NNPDF3.0nnlo	Sherpa 2.2.11	NNLO [144]
Wt	Powheg-box v2	NNPDF3.0nlo	Pythia 8	NNLO [145, 146]
$t\bar{t}$	Powheg-box v2	NNPDF3.0nlo	Pythia 8	NNLO+NNLL [147–152]

The Geant4 package [101] is used to simulate the propagation of long-lived particles through the sub-components of the ATLAS detector including their interactions with detector material [102]. Additional pp interactions in an event (pile-up) are included for all generated events such that the average number of pp interactions per bunch crossing reproduces that observed in the data. This is done by overlaying hard-scattering events with inelastic pp events simulated with Pythia 8.186 [94] with the A3 tune [103] and NNPDF2.3lo PDF set [104].

The MC simulation tools used in the sample generation of the different processes are summarized in Table 4.2.

Signal samples

The ggF Higgs production mode is simulated at next-to-next-leading-order (NNLO) level of accuracy in QCD using the Powheg-box v2 NNLOPS package [93, 105–108] with the PDF4LHC15nnlo [111] PDF set. The rapidity spectrum of the Higgs boson in Hj-MiNLO [109, 153, 154] is reweighted to that of HNNLO [155] to achieve NNLO accuracy for inclusive $gg \to H$ observables. It is then interfaced with Pythia 8.212 [112] with the AZNLO tune [156] for effects from underlying event, hadronization, and parton showering (UEPS). The MC prediction is normalized to

the next-to-next-to-next-to-leading-order (N^3LO) inclusive cross-section accuracy in QCD and next-to-leading-order (NLO) in EW [12, 113–122].

The VBF Higgs production mode is generated with POWHEG-BOX v2 [93, 105–107, 110] interfaced with PYTHIA 8.230 with the AZNLO tune and the dipole recoil option enabled to model parton showering and non-perturbative effects. The set of PDFs used is PDF4LHC15NLO. The MC prediction is normalized to the NNLO QCD cross-section calculation with NLO EW corrections [123–125].

The $H \to \tau\tau$ decay with leptonically decaying τ-leptons is also included in the ggF and VBF modes during sample generation.

The VH production process is modelled with POWHEG-BOX v2 interfaced with PYTHIA 8.212 with the AZNLO tune. PDF4LHC15NLO is used as the PDF set. The samples are normalized to the cross-section obtained from the NNLO QCD prediction with NLO EW corrections [126–130].

The $t\bar{t}H$ production process is generated with the POWHEG-BOX v2 generator and the NNPDF3.0NLO [104] PDF set. The UEPS is modelled by PYTHIA 8.230 with the A14 tune [157]. The MC prediction is normalized to the cross-section with NLO accuracy in both QCD and EW [12].

The Higgs boson mass is set to 125 GeV in all signal samples, with the uncertainty in the Higgs boson mass being negligible for kinematic distributions. The SM-predicted branching ratio of the $H \to WW^*$ decay is calculated with HDECAY [158–160] and PROPHECY4F [161–163]. An uncertainty of 2.16% [12] is assigned to the branching ratio.

Background samples

The quark-initiated $q\bar{q} \to WW$, WZ, ZZ, and $V\gamma^*$ processes are generated by SHERPA 2.2.2 [92] which also includes parton showering, hadronization, and underlying event simulation [131–136]. The NNPDF3.0NNLO [104] PDF set is used. Fully leptonic final states are generated using matrix elements calculated at NLO accuracy in QCD for emissions of zero and one jet and at leading-order (LO) for up to three jets. The loop-induced $gg \to WW/ZZ$ processes are generated

using matrix elements calculated at LO precision for up to one additional jet. All of these samples are normalized to the inclusive cross-section calculated at NLO in QCD [137–140, 142].

The EW WW production process is generated by MadGraph 5 [141] with LO matrix elements using the NNPDF3.0nlo PDF set. The parton showering is modelled by Pythia 8.244 with the A14 tune. The sample is normalized to the cross-section at LO precision in QCD [6].

The $V\gamma$ processes are simulated with Sherpa 2.2.8 [92] with matrix elements at NLO accuracy in QCD for zero and one jet and at LO for up to three jets. NNPDF3.0nnlo is used as the PDF set. The samples are normalized to the NLO QCD cross-section [142].

The triboson (VVV) processes are generated with Sherpa 2.2.2 using factorized gauge-boson decays. The level of accuracy of the matrix elements is NLO for the inclusive process and LO for emissions of up to two jets. The NNPDF3.0nnlo PDF set is used. The samples are normalized to the NLO QCD cross-section [142].

The production of the Drell-Yan (Z/γ^*) process is simulated with Sherpa 2.2.11 [143] using NLO matrix elements for up to two jets and LO matrix elements for up to four jets. The NNPDF3.0nnlo PDF set is used and the generated samples are normalized to the NNLO QCD cross-section [144]. The Z/γ^* samples are produced separately for the low-mass and high-mass regimes with a cut-off at $m_{ll} = 40$ GeV.

The single top-quark (Wt) production is generated at NLO in QCD using Powheg-box v2 with the five-quark-flavour scheme and the NNPDF3.0nlo PDF set. The simulated events are interfaced with Pythia 8.230 with the A14 tune and the NNPDF2.3lo PDF set to model parton showering, hadronization, and the underlying event. The decays of charm and bottom hadrons are simulated by EvtGen 1.6.0 [164]. The interference and overlap with the $t\bar{t}$ production are removed using the diagram removal scheme [165, 166]. The samples are normalized to the cross-section calculated at NNLO precision [145, 146].

The $t\bar{t}$ production is simulated with Powheg-box v2 at NLO in QCD with the NNPDF3.0nlo set of PDFs. The h_{damp} parameter in the generator is set to

$1.5 \times m_{\text{top}}$ [167]. The parton showering, hadronization, and underlying events are modelled with Pythia 8.230 with the A14 tune and the NNPDF2.3lo PDF set. An NNLO reweighting is applied to correct for any mismodelling of the leading-lepton p_{T} due to an absence of higher-order corrections [168]. The samples are normalized to the cross-section derived at NNLO+NNLL (next-to-next-to-leading-logarithm) accuracy [147–152].

The W+jets and multijet processes are estimated using a data-driven technique (Section 4.5.2) where simulated samples for W+jets and Z+jets processes are used to derive extrapolation and correction factors to estimate the number of such events in the analysis region. These MC samples are generated with Powheg-box v2 interfaced with Pythia 8.186, with Sherpa 2.2.1, and with MadGraph 5 interfaced with Pythia 8.186.

4.3 Object definitions

The reconstruction of all physics objects (particles) involves the determination of the primary interaction vertices in the crossing of protons. In Run-2, only tracks with $p_{\text{T}} > 500$ MeV and passing quality cuts are considered [169]. The hard-scatter vertex is defined as the primary vertex with the largest Σp_{T}^2 of the tracks associated with it. Other primary vertices that may exist in an event are referred to as pile-up vertices (see Section 3.1.3).

There are two stages in which objects are defined: the production-level preselection, where the objects that are used for overlap removal[2] and for reconstructing $\mathbf{E}_{\text{T}}^{\text{miss}}$ are defined; and the final selection, which is applied to the objects after overlap removal. Details of how individual objects are reconstructed can be found in Section 3.3.

[2]Ambiguities in object reconstruction can arise since a signal from one particle may be reconstructed as multiple objects. An overlap removal procedure is necessary for differentiation of such objects from one another.

4.3.1 Electrons

Electrons are reconstructed from clusters in the EM calorimeter associated with a matched ID track, as described in Section 3.3.3. To distinguish them from photons and jets, identification and isolation working points are applied.

At the production-level preselection, electrons are required to have $p_{\mathrm{T}} > 10$ GeV and $|\eta| < 2.47$. They are identified with the `VeryLoose` likelihood working point and need to satisfy the impact parameter requirements $|d_0|/\sigma_{d_0} < 5$ and $|z_0 \sin\theta| < 0.5$ mm.

At the final selection stage, electrons are required to be within $|\eta| < 1.37$ or $1.52 < |\eta| < 2.47$ (i.e. excluding the transition region between the barrel and end-caps in the LAr EM calorimeter), and pass the `Tight` identification working point for electrons with $p_{\mathrm{T}} < 25$ GeV or `Medium` for $p_{\mathrm{T}} > 25$ GeV. Lastly, the `FCTight` isolation working point is applied.

4.3.2 Muons

Muons are reconstructed by matching an ID track with an MS track or segment, with corrections based on the energy loss in the calorimeter, as described in 3.3.4. The isolation of a muon candidate is required to differentiate prompt muons from those produced as a result of intermediary processes like semi-leptonic decays. Isolation describes the amount of track or calorimeter activity in the vicinity of the muon candidate.

At the production-level preselection, muons are required to have $p_{\mathrm{T}} > 10$ GeV and $|\eta| < 2.7$ as well as passing the `Loose` identification working point. They must satisfy the impact parameter requirements $|d_0|/\sigma_{d_0} < 15$ and $|z_0 \sin\theta| < 1.5$ mm.

In the final selection, muons are required to be in the narrower pseudorapidity range of $|\eta| < 2.5$. The `Tight` identification working point is applied, which matches an ID track with an MS track or segment and imposes stringent quality cuts on muon selection. For isolation, the `FCTight` working point is chosen to maximize sensitivity.

4.3.3 Jets

In Run-2, reconstructed PFlow-algorithm objects are passed on to the FastJet package [170] which is used to build jets using the anti-k_t algorithm with a jet radius parameter $R = 0.4$. The reconstructed jets are fully calibrated using the EM+JES scheme including a correction for pile-up. Details of jet reconstruction and calibration can be found in Section 3.3.5.

At the production-level preselection, jets are required to have $p_{\mathrm{T}} > 20$ GeV and $|\eta| < 4.5$. The jet-vertex tagging (JVT) algorithm is applied in order to distinguish hard-scatter jets from pile-up jets based on the value of the likelihood JVT discriminant. The `Tight` working point corresponding to JVT > 0.5 is used for central EMPFlow jets with $20 < p_{\mathrm{T}} < 60$ GeV (see Table 3.1). The forward-JVT (fJVT) working point was not used since the efficiency scale factors were not available for PFlow jets at the time of this analysis.

In the final selection, jets are required to have $p_{\mathrm{T}} > 30$ GeV to be considered for jet counting. Jets that pass only the production-level preselection ($20 < p_{\mathrm{T}} < 30$ GeV) are still retained by the analysis and are referred to as *sub-threshold jets*.

Jets containing b-hadrons are identified using a set of low-level b-tagging algorithms followed by a high-level DL1r algorithm. The b-tagged jets with $p_{\mathrm{T}} > 20$ GeV and $|\eta| < 2.5$ are referred to as b-jets in the analysis. To be selected for the analysis, these b-jets need to satisfy the DL1r working point with 85% b-tagging efficiency.

4.3.4 Missing transverse momentum

The calculation of missing transverse energy ($E_{\mathrm{T}}^{\mathrm{miss}}$) in this analysis uses the track-based soft term (TST), which determines the net momentum of unreconstructed objects by summing the momentum of tracks with $p_{\mathrm{T}} > 500$ MeV and $|z_0 \sin\theta| < 2.0$ mm that fail to be considered as hard objects. The TST calculation significantly suppresses contributions from out-of-time pile-up (see Section 3.3.6).

Additionally, the object-based $E_{\mathrm{T}}^{\mathrm{miss}}$ significance is used in the analysis in order to suppress the dominant Z/γ^* background. More details on $E_{\mathrm{T}}^{\mathrm{miss}}$ significance can be found in Section 4.4.1.

4.3.5 Overlap removal

Since particles are reconstructed independently by the different components of the detector, the same particle may be reconstructed as multiple objects. Such duplication is referred to as *overlap*. An algorithm to resolve the source object is referred to as *overlap removal* (OR). Only production-level preselected objects (electrons, muons, τ-leptons, and jets) are considered. The procedure for OR is to take the following steps:

- Electron-electron: If two electron candidates share an ID track, the electron with lower E_{T} is removed.

- Electron-muon: The duplication of a muon as an electron can occur when the muon radiates a photon, and the subsequent energy deposit in the calorimeter is matched with the muon track. This leads to an identification of an electron that shares an ID track with the muon (typically $\Delta R < 0.01$ between then). If this happens, the electron candidate is removed.

- Electron-jet: Electrons can also be identified as a jet because they both deposit energy in the calorimeter. The jet candidate is removed if $\Delta R_{\mathrm{jet},e} < 0.2$ and it is not identified as a b-jet. For any surviving jets, the electron candidate is removed if $\Delta R_{\mathrm{jet},e} < 0.4$ since it is likely that the electron candidate is in fact the product of a hadronic decay of the jet. Another reason is that if the electron candidate is in fact an electron, its energy reconstruction becomes biased by the jet in close proximity.

- Muon-jet: The duplication of a muon as an electron often comes with its duplication as a jet as well. The jet candidate is removed if $\Delta R_{\mathrm{jet},\mu} < 0.2$ and there are less than three tracks with $p_{\mathrm{T}} > 500$ MeV associated with it. For the remaining jets, the muon candidate is removed if $\Delta R_{\mathrm{jet},\mu} < 0.4$.

4.4 Observable definitions

This section gives a summary of all of the observables used in the analysis. Different observables can be used to construct event selection criteria in order to distinguish a particular process (particularly signal) from others by exploiting the differences in the distributions of the processes.

4.4.1 Common observables

These are observables common to all categories of the analysis. 'T' in the subscript means that the observable is measured in the plane transverse to the proton beam.

- $p_{\mathrm{T}}^{\mathrm{lead}}$ and $p_{\mathrm{T}}^{\mathrm{sublead}}$: Transverse momentum of the leading lepton and subleading lepton respectively. The leading lepton is the lepton in the pair that has higher p_{T}. These two observables are also interchangeably written as $p_{\mathrm{T}}^{l_1}$ and $p_{\mathrm{T}}^{l_2}$ respectively.

- m_{ll}: Invariant mass of the lepton pair originating from the same hard scattering vertex.

- $\Delta\phi_{ll}$: Azimuthal angle between the two leptons in the transverse plane.

- p_{T}^{ll}: Transverse momentum of the lepton pair.

- $E_{\mathrm{T}}^{\mathrm{miss}}$: Track-based soft term (TST) missing transverse momentum (see Section 4.3.4).

- $\Delta\phi_{ll,E_{\mathrm{T}}^{\mathrm{miss}}}$: Azimuthal angle between the lepton pair and the direction of $\mathbf{E}_{\mathrm{T}}^{\mathrm{miss}}$.

- $E_{\mathrm{T}}^{\mathrm{miss}}$ significance: Object-based missing transverse momentum significance [171] employs the likelihood formalism to evaluate the statistical significance of how likely the $E_{\mathrm{T}}^{\mathrm{miss}}$ value measured in an event arises from limited resolution, mis-measurements, and inefficiencies of object reconstruction. If $\mathcal{L}(\mathbf{p}_{\mathrm{T}}^{\mathrm{inv}}|\mathbf{E}_{\mathrm{T}}^{\mathrm{miss}})$ is the likelihood function[3] of the total transverse momentum carried by invisible

[3] This is written in the standard notation, where $\mathcal{L}(\theta|x)$ is the likelihood function of parameter θ given known or observed value x.

particles parameter $\mathbf{p}_{\mathrm{T}}^{\mathrm{inv}}$ given measured $\mathbf{E}_{\mathrm{T}}^{\mathrm{miss}}$, the square of the significance is defined as:

$$\mathcal{S}^2 = 2\ln\Big(\frac{\max_{\mathbf{p}_{\mathrm{T}}^{\mathrm{inv}}\neq 0}\mathcal{L}(\mathbf{p}_{\mathrm{T}}^{\mathrm{inv}}|\mathbf{E}_{\mathrm{T}}^{\mathrm{miss}})}{\max_{\mathbf{p}_{\mathrm{T}}^{\mathrm{inv}}=0}\mathcal{L}(\mathbf{p}_{\mathrm{T}}^{\mathrm{inv}}|\mathbf{E}_{\mathrm{T}}^{\mathrm{miss}})}\Big) \tag{4.1}$$

where the numerator and denominator are calculated from maximizing the likelihood function given the hypotheses that there is genuine missing transverse momentum carried by invisible particles ($\mathbf{p}_{\mathrm{T}}^{\mathrm{inv}} \neq 0$) and there is no such momentum carried by invisible particles ($\mathbf{p}_{\mathrm{T}}^{\mathrm{inv}} = 0$) respectively.

For each reconstructed object i that enters the calculation of $\mathbf{E}_{\mathrm{T}}^{\mathrm{miss}}$, the probability that the true value is $\boldsymbol{\pi}_{\mathrm{T}}^{i}$ given that $\mathbf{p}_{\mathrm{T}}^{i}$ is measured is assumed to take the form of a Gaussian $\mathcal{G}(\boldsymbol{\pi}_{\mathrm{T}}^{i}|\mathbf{p}_{\mathrm{T}}^{i})$ with associated covariance matrix $\mathbf{V}^{i}$, which encapsulates resolution and inefficiencies involved in such object reconstruction. According to the conservation of momentum, the total transverse momenta of all the reconstructed objects and of the invisible particles are related by $\sum_i \mathbf{p}_{\mathrm{T}}^{i} = -\mathbf{E}_{\mathrm{T}}^{\mathrm{miss}}$ and $\sum_i \boldsymbol{\pi}_{\mathrm{T}}^{i} = -\mathbf{p}_{\mathrm{T}}^{\mathrm{inv}}$ respectively. In addition, the measurement of each reconstructed object i is assumed to be independent. Under these assumptions, the likelihood function can be expressed as:

$$\mathcal{L}(\mathbf{p}_{\mathrm{T}}^{\mathrm{inv}}|\mathbf{E}_{\mathrm{T}}^{\mathrm{miss}}) \propto \exp\Big[-\frac{1}{2}(\mathbf{E}_{\mathrm{T}}^{\mathrm{miss}} - \mathbf{p}_{\mathrm{T}}^{\mathrm{inv}})^{\mathrm{T}} \cdot \Big(\sum_i \mathbf{V}^{i}\Big)^{-1} \cdot (\mathbf{E}_{\mathrm{T}}^{\mathrm{miss}} - \mathbf{p}_{\mathrm{T}}^{\mathrm{inv}})\Big] \ . \tag{4.2}$$

The square of the significance $\mathcal{S}^2$ then becomes a χ^2 variable with two degrees of freedom:

$$\mathcal{S}^2 = 2\ln\Big(\frac{\mathcal{L}(\mathbf{p}_{\mathrm{T}}^{\mathrm{inv}} = \mathbf{E}_{\mathrm{T}}^{\mathrm{miss}}|\mathbf{E}_{\mathrm{T}}^{\mathrm{miss}})}{\mathcal{L}(0|\mathbf{E}_{\mathrm{T}}^{\mathrm{miss}})}\Big) = (\mathbf{E}_{\mathrm{T}}^{\mathrm{miss}})^{\mathrm{T}} \cdot \Big(\sum_i \mathbf{V}^{i}\Big)^{-1} \cdot (\mathbf{E}_{\mathrm{T}}^{\mathrm{miss}}) \ . \tag{4.3}$$

The implication of this equation is that a large value of $\mathcal{S}$ indicates that the event is more likely to feature genuine $E_{\mathrm{T}}^{\mathrm{miss}}$ from undetected particles such as neutrinos or exotic BSM particles, whereas a small value of $\mathcal{S}$ implies that $E_{\mathrm{T}}^{\mathrm{miss}}$ is likely fake and arises from limited resolution and inefficiencies of object reconstruction instead.

- m_{T}: Transverse mass of the final-state lepton pair and $E_{\mathrm{T}}^{\mathrm{miss}}$, defined as:

$$m_{\mathrm{T}} = \sqrt{(E_{\mathrm{T}}^{ll} + E_{\mathrm{T}}^{\mathrm{miss}})^2 - |\mathbf{p}_{\mathrm{T}}^{ll} + \mathbf{E}_{\mathrm{T}}^{\mathrm{miss}}|^2} \tag{4.4}$$

  where $E_{\mathrm{T}}^{ll} = \sqrt{(p_{\mathrm{T}}^{ll})^2 + m_{ll}^2}$. Since the longitudinal momenta of the proton beams are not known precisely (i.e. the two colliding protons may have different longitudinal momenta), the resonant particle may be boosted along the axis of the beam and therefore its mass cannot be fully reconstructed. The true transverse mass of a resonant-particle decay has an upper limit at the true invariant mass: $m_{\mathrm{T}} \leq m$ (neglecting the particle width).

- $m_{\mathrm{T}}^{(l,E_{\mathrm{T}}^{\mathrm{miss}})}$: Transverse mass of a charged lepton and $E_{\mathrm{T}}^{\mathrm{miss}}$, defined as::

$$m_{\mathrm{T}}^{(l,E_{\mathrm{T}}^{\mathrm{miss}})} = \sqrt{(E_{\mathrm{T}}^{l} + E_{\mathrm{T}}^{\mathrm{miss}})^2 - |\mathbf{p}_{\mathrm{T}}^{l} + \mathbf{E}_{\mathrm{T}}^{\mathrm{miss}}|^2}\ . \tag{4.5}$$

  For a W boson decaying to a lepton and neutrino the true transverse mass has an upper limit at the W boson mass (neglecting the W boson width). Since the lepton travels at a relativistic speed and the neutrino is massless in the Standard Model, this reduces to:

$$m_{\mathrm{T}}^{(l,E_{\mathrm{T}}^{\mathrm{miss}})} = \sqrt{2p_{\mathrm{T}}^{l}E_{\mathrm{T}}^{\mathrm{miss}}(1 - \cos\Delta\phi_{l,E_{\mathrm{T}}^{\mathrm{miss}}})}\ . \tag{4.6}$$

- m_{T2}: Stransverse mass of the (dilepton, $E_{\mathrm{T}}^{\mathrm{miss}}$) final state assuming an intermediate pair of W bosons [172–174]. It is defined as:

$$m_{\mathrm{T2}} = \min_{\mathbf{p}_{\mathrm{T}}^{\nu_1}+\mathbf{p}_{\mathrm{T}}^{\nu_2}=\mathbf{E}_{\mathrm{T}}^{\mathrm{miss}}} \left\{ \max\left[m_{\mathrm{T}}(\mathbf{p}_{\mathrm{T}}^{l_1}, \mathbf{p}_{\mathrm{T}}^{\nu_1})\,,\, m_{\mathrm{T}}(\mathbf{p}_{\mathrm{T}}^{l_2}, \mathbf{p}_{\mathrm{T}}^{\nu_2}) \right] \right\} \tag{4.7}$$

  where $m_{\mathrm{T}}(\mathbf{p}_{\mathrm{T}}^{l_i}, \mathbf{p}_{\mathrm{T}}^{\nu_i})$ is the transverse mass of the (l_i,ν_i) final state defined in Equation 4.5, represented here as a function of the constituent momenta. Since the transverse momenta of the individual neutrinos cannot be be measured, an initial guess value for $\mathbf{p}_{\mathrm{T}}^{\nu_1}$ needs to be set manually, and $\mathbf{p}_{\mathrm{T}}^{\nu_2}$ is subsequently inferred from the constraint $\mathbf{p}_{\mathrm{T}}^{\nu_1} + \mathbf{p}_{\mathrm{T}}^{\nu_2} = \mathbf{E}_{\mathrm{T}}^{\mathrm{miss}}$. Transverse masses $m_{\mathrm{T}}(\mathbf{p}_{\mathrm{T}}^{l_1}, \mathbf{p}_{\mathrm{T}}^{\nu_1})$ and $m_{\mathrm{T}}(\mathbf{p}_{\mathrm{T}}^{l_2}, \mathbf{p}_{\mathrm{T}}^{\nu_2})$ are computed, and the larger of the two values is selected.

Then, the simplex method[4] is performed iteratively to obtain new input values for $\mathbf{p}_{\mathrm{T}}^{\nu_1}$ and $\mathbf{p}_{\mathrm{T}}^{\nu_2}$, and the calculation for m_{T} is repeated. The smallest value among these iterations is chosen as the final m_{T2} value for this event.

- N_{jet}: Number of jets with $p_{\mathrm{T}} > 30$ GeV and passing the `Tight` JVT selection criterion.

- $N_{b\text{-jet}}$: Number of jets with $p_{\mathrm{T}} > 20$ GeV (i.e. all jets including sub-threshold jets) identified as b-hadrons using the DL1r b-tagging algorithm at 85% efficiency.

- $m_{\tau\tau}$: Invariant mass of the τ-lepton pair. The final-state charged leptons are the products of a leptonically decaying τ-lepton pair which in turn originate from a resonant particle (such as a Higgs or Z boson). Since the Higgs mass is larger than twice the mass of the τ-lepton, the emitted charged leptons and their associated neutrinos will be Lorentz-boosted. According to the Collinear Approximation Method [176], the charged lepton and neutrino are assumed to be collinear with the τ-lepton from which they are emitted. As a result, the transverse momentum of the lepton can be written as $\mathbf{p}_{\mathrm{T}}^{l_i} = x_i \mathbf{p}_{\mathrm{T}}^{\tau_i}$, where x_i is the momentum fraction. The values of x_1 and x_2 can be solved analytically from the conservation of transverse momentum, $\mathbf{p}_{\mathrm{T}}^{\tau_1} + \mathbf{p}_{\mathrm{T}}^{\tau_2} = \mathbf{p}_{\mathrm{T}}^{l_1} + \mathbf{p}_{\mathrm{T}}^{l_2} + \mathbf{E}_{\mathrm{T}}^{\mathrm{miss}}$. The invariant mass of the τ-lepton pair becomes:

$$m_{\tau\tau} = \frac{m_{ll}}{\sqrt{x_1 x_2}} \ . \tag{4.8}$$

The Collinear Approximation is only valid when the resonant particle has large p_{T}, such as in the case where a Higgs or Z boson is produced with an accompanying jet that recoils against it. This reduces the fraction of back-to-back τ-leptons, which lead to back-to-back neutrinos and the loss of

[4]The Nelder-Mead simplex method [175] is a heuristic direct search method for minimizing an unconstrained scalar function of N variables. A *simplex* is a generalized geometric object in N dimensions that is a convex hull of $N+1$ vertices. In each iteration, a new vertex for the simplex is generated. If the value of the function at the new vertex is lower than that at one of the other existing vertices, the worst vertex is replaced by the new vertex. The volume of the simplex becomes smaller for every iteration as a result, and the algorithm stops when the simplex has been reduced to a certain size.

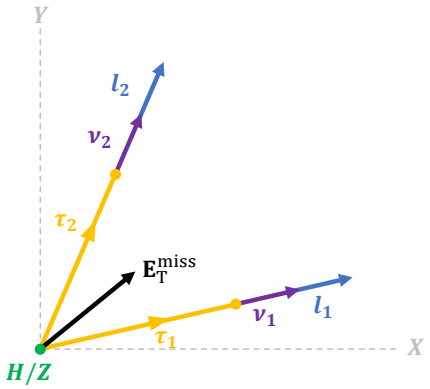

Figure 4.10: The Collinear Approximation Method applied to the Lorentz boosted $H \to \tau\tau$ or $Z \to \tau\tau$ decay. The $\mathbf{E}_{\mathrm{T}}^{\mathrm{miss}}$ vector lies between the directions of the leptons.

$\mathbf{E}_{\mathrm{T}}^{\mathrm{miss}}$ information. As a result, $\mathbf{E}_{\mathrm{T}}^{\mathrm{miss}}$ lies between the directions of the two τ-leptons, as shown in Figure 4.10. On the other hand, in processes such as the top or WW process, the neutrinos from W-boson decays can produce a different topology, and unphysical values of $m_{\tau\tau}$ are frequently obtained as a result.

4.4.2 VBF observables

As described in Section 4.1.1, $H \to WW^* \to l\nu l\nu$ events produced via the VBF process have some salient features that can be useful for extracting such events. Observables that can take advantage of these features are listed in this section.

- $p_{\mathrm{T}}^{\mathrm{total}}$: Total transverse momentum in an event. $\mathbf{p}_{\mathrm{T}}^{\mathrm{total}}$ is defined as a vector sum:

$$\mathbf{p}_{\mathrm{T}}^{\mathrm{total}} = \mathbf{p}_{\mathrm{T}}^{\mathrm{lead}} + \mathbf{p}_{\mathrm{T}}^{\mathrm{sublead}} + \mathbf{E}_{\mathrm{T}}^{\mathrm{miss}} + \Sigma\mathbf{p}_{\mathrm{T}}^{\mathrm{jets}} \ . \tag{4.9}$$

- m_{jj}: Invariant mass of the two leading jets (jets with highest p_{T}) in an event.

- Δy_{jj}: Difference between the rapidities of the two leading jets. Two high-energy jets travelling in opposite directions almost parallel to the beam axis will have a large Δy_{jj} between them.

- CJV: Central Jet Veto. The central jet is defined as the jet with the largest p_{T} among all jets that have their rapidity values between those of the two

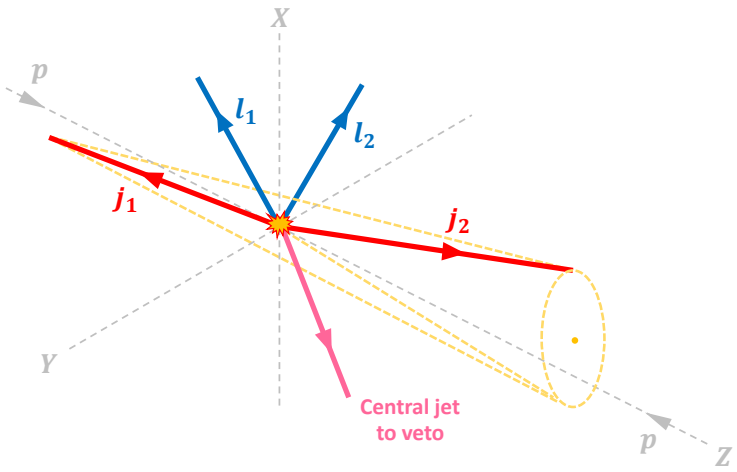

Figure 4.11: Schematic diagram demonstrating the Central Jet Veto (CJV). An additional central jet (pink arrow) exists within the rapidity gap spanned by the two leading jets (red arrows), i.e. the central jet emerges through the lateral side of the imaginary cone spanned by the directions of the two leading jets. If CJV is set to true, this event is not selected.

leading jets (i.e. lying within the rapidity gap of by the two leading jets). Hadronic objects are fully classfied as jets only if their $p_{\mathrm{T}} > 30$ GeV and the `Tight` JVT selection criterion is satisfied. CJV is a variable defined as:

$$\mathrm{CJV} = \begin{cases} \text{true : no central jet exists in the rapidity gap of the two leading jets.} \\ \text{false : a central jet is present.} \end{cases} \tag{4.10}$$

An illustration of how the CJV works is given in Figure 4.11.

- OLV: Outside Lepton Veto. The relative direction of the lepton with respect to the two leading jets in pseudorapidity space can be described by its *centrality*:

$$C_{l_i} = 2 \left| \frac{\eta_{l_i} - \bar{\eta}}{\eta_{j_1} - \eta_{j_2}} \right| \tag{4.11}$$

where $\bar{\eta} = (\eta_{j_1} + \eta_{j_2})/2$ is the average η of the two leading jets. Centrality quantifies how far the lepton is from the centre of the (pseudo)rapidity gap spanned by the two leading jets compared to the width of the gap itself. The possible scenarios are:

$$C_{l_i} \begin{cases} < 1 : \text{the lepton lies within the gap between the two leading jets.} \\ > 1 : \text{the lepton is outside the gap.} \end{cases} \tag{4.12}$$

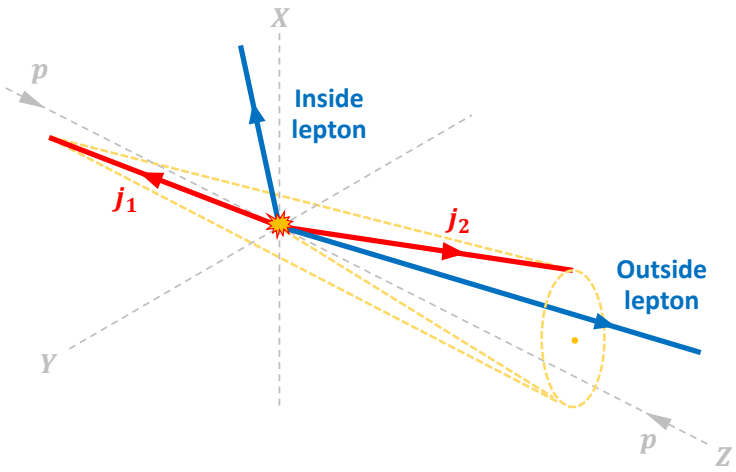

Figure 4.12: Schematic diagram demonstrating the Outside Lepton Veto (OLV). The lepton (blue arrow) is considered to be 'outside' if $C_{l_i} > 1$, which is equivalent to it emerging through the base of the imaginary cone whose axis is defined by j_1 and circumference is spanned by j_2. On the other hand, the 'inside' lepton has $C_{l_i} < 1$ which means that it emerges through the lateral side of the cone spanned by the two jets, i.e. within the rapidity gap. If OLV is required to be true, this event is not selected since at least of the leptons lies outside the rapidity gap.

OLV is a boolean defined as:

$$\text{OLV} = \begin{cases} \text{true} : C_{l_1} \text{ and } C_{l_2} < 1. \\ \text{false} : C_{l_1} \text{ or } C_{l_2} > 1. \end{cases} \tag{4.13}$$

In other words, OLV = true requires both of the leptons in an event to be inside the (pseudo)rapidity gap between the two leading jets while OLV=false has one or both of the leptons outside the gap. This definition of OLV is motivated by the characteristic property of the VBF process discussed in Section 4.1.1. The manner in which the OLV works is perhaps better understood by looking at a graphic demonstration in Figure 4.12.

4.5 Event selection and categorization

4.5.1 Overview of analysis strategy

The objective of event selection is to reduce the background processes without sacrificing a significant amount of the signal. The event selection procedures employed in this cut-based $H \to WW^* \to l\nu l\nu$ same-flavour analysis generally follow those of the different-flavour analysis for the full Run-2 dataset [6], which in

turn builds upon the Run-1 analysis [7]. However, some modifications need to be made in order to optimize the measurement precision in the same-flavour lepton final state and to account for the differences in the composition of the background processes. The procedures of the analysis are as follows.

Firstly, events are required to pass a set of preliminary event selection criteria known as *preselection* (Section 4.5.3). These involve application of software-based HLTs, selection of events that contain two oppositely charged leptons of the same flavour as final-state particles, requirements on p_{T} of the leptons, and preliminary suppression of certain background processes.

The preselected events are then split into different categories based on the number of jets that are present alongside the final-state leptons: $N_{\mathrm{jet}} = 0$, $N_{\mathrm{jet}} = 1$, and $N_{\mathrm{jet}} \geq 2$. This division is motivated by the variation of the background composition with N_{jet}, as shown in Figure 4.15. The $N_{\mathrm{jet}} = 0$ and $N_{\mathrm{jet}} = 1$ categories are ggF-enriched. This is because jets in the ggF production mode originate from initial-state radiation (ISR) emitted by the incoming partons. The contribution from the ggF process decreases sharply with increasing jet multiplicity because the more ISR jets emitted, the higher the order of the QCD coupling is involved. The $N_{\mathrm{jet}} \geq 2$ category is further divided into two categories: ggF-enriched and VBF-enriched. This is because the VBF production mode has a unique topology where two jets are naturally produced in the forward regions and have a large (pseudo)rapidity gap between them. The observables described in Section 4.4.2 can be effectively used to extract the VBF signal by exploiting this signature. The $N_{\mathrm{jet}} \geq 2$ ggF-enriched category can subsequently be made by requiring the selection criteria to be orthogonal (mutually exclusive) to those of the VBF-enriched category. A summary of the categorization of the $H \to WW^* \to l\nu l\nu$ analysis is shown in Figure 4.13. This analysis only considers the two most dominant Higgs production modes, ggF and VBF, as signal processes. The VH and $t\bar{t}H$ modes are treated as backgrounds.

In each of the 4 categories, a set of event selection criteria (cuts) are applied to the samples with the primary goal of maximizing the $H \to WW^* \to l\nu l\nu$ signal while keeping the background to a minimum. This step defines the *signal regions*

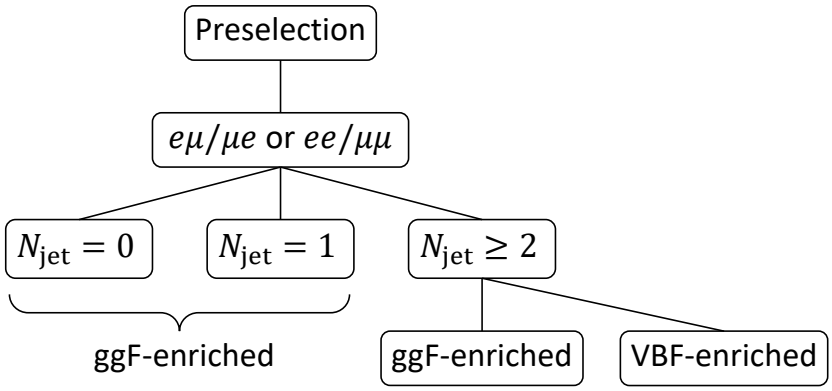

Figure 4.13: Summary of the event categorization in the $H \to WW^* \to l\nu l\nu$ analysis.

(SRs) of the analysis (Sections 4.5.4–4.5.7). The specific values of the different cuts that define each SR are chosen based on the maximization of the expected signal significance, which is given by[5]:

$$Z = \sqrt{2\left\{n \ln\left[\frac{n(b+\Delta b^2)}{b^2+n\Delta b^2}\right] - \frac{b^2}{\Delta b^2}\ln\left[1+\frac{\Delta b^2(n-b)}{b(b+\Delta b^2)}\right]\right\}} \tag{4.14}$$

where b is the number of background events with uncertainty Δb, and n is the total number of expected events, which is the sum of signal and background events.

The contributions of the three major background processes, namely Z/γ^*, WW, and top quark, to the SRs are estimated with dedicated *control regions* (CRs) enriched in the corresponding backgrounds. The backgrounds with misidentified leptons are estimated using a data-driven technique. These background estimation methods are described in Section 4.5.2. The event selection criteria that define the SRs and CRs of all four categories in the cut-based $H \to WW^* \to l\nu l\nu$ same-flavour analysis are given in Tables 4.3–4.6.

Each of the SRs in each of the categories is further spilt into sub-SRs based on m_{ll} and $p_{\text{T}}^{\text{sublead}}$ during the likelihood fit stage. This is to enhance the sensitivity of the measurement of the *signal strength*, which is defined as the ratio of the observed Higgs boson yield in data to its SM prediction:

$$\mu_{i\to H\to f} = \frac{(\sigma_i \times \text{BR}_f)_{\text{observed}}}{(\sigma_i \times \text{BR}_f)_{\text{SM}}} \tag{4.15}$$

[5]This is the full formula for the Poisson-Poisson distribution, which also includes the background uncertainty term Δb [177].

for Higgs production mode i and decay channel f, which is specifically $WW^* \to l\nu l\nu$ of the same flavour in this analysis.

The sub-SRs and CRs in each category enter a likelihood fit using m_{T} as a discriminating fit variable. The $N_{\mathrm{jet}} = 0$ and $N_{\mathrm{jet}} = 1$ categories are fitted simultaneously due to their similarity whereas the $N_{\mathrm{jet}} \geq 2$ ggF- and VBF-enriched categories are fitted separately. The results from the three fits are combined to obtain an overall μ of the same-flavour channel. The statistical treatment and likelihood fit are fully explored in Chapter 6.

The analysis was performed blind, i.e. the data in the SRs were removed until an unblinding was approved by the analysis group conveners. This procedure avoids analysis biases. In this analysis, an exclusion window $80 < m_{\mathrm{T}} < 130$ GeV was used as the definition for data blinding for all categories. The CRs are not blinded because they have low signal yields by design and are constructed in order to verify or correct data-MC discrepancies of background processes. All plots and event yield tables presented in this chapter were produced after unblinding.

4.5.2 Background estimation methods

The $H \to WW^* \to l\nu l\nu$ signal regions (SRs) can be contaminated by various background processes including non-resonant WW, single top-quark Wt and top-quark pair $t\bar{t}$, other diboson VV and triboson VVV, and Drell-Yan Z/γ^* (see Section 4.1.2). Among these, the WW, top quark, and Z/γ^* processes constitute the majority of the overall background in the analysis. Dedicated *control regions* (CRs), designed to be enriched in a particular background process and low in expected signal, are used for estimating the contributions of these backgrounds in the SRs. The background arising from misidentification of jets as leptons through the W+jets and multijet processes are estimated with a data-driven technique. Estimation of other minor backgrounds, namely the diboson and triboson processes, are obtained from simulated samples normalized to the theoretical cross-sections for these processes.

Control regions

A *control region* (CR) for a given background process is constructed to be kinematically similar to the SR that it is designed to normalize, but enriched in that background instead of signal. This can be achieved by modifying some event selection criteria of the original SR to suit the nature of the background process. For example, the defining characteristic of the $H \to WW^* \to l\nu l\nu$ signal process is that the lepton pair are produced at a small angle so that their m_{ll} and $\Delta\phi_{ll}$ are rather small. However, the lepton pair produced by the Z/γ^* process are well-separated, meaning that their m_{ll} and $\Delta\phi_{ll}$ are typically larger than those of the signal. By selecting appropriate values of these two observables, a Z/γ^* CR can be defined.

The CR is required to be orthogonal to the SR to which it extrapolates as well as the CRs of other backgrounds. However, not all observables that define the SR should be modified when constructing a CR. Only observables involving leptons such as m_{ll} and $\Delta\phi_{ll}$ should be adjusted because leptons are modelled with a high level of precision by MC generators, while other objects such as jets and missing transverse momentum are not. By tweaking, for instance, a jet observable, the kinematic nature of the CR might be changed significantly and it no longer resembles the kinematics of the original SR, making any extrapolation or estimation of the background in the SR less accurate. Since $E_{\mathrm{T}}^{\mathrm{miss}}$ observables also take jets into consideration, any changes in $E_{\mathrm{T}}^{\mathrm{miss}}$ between the SR and CR should also be avoided.

Once the CR is defined for a particular background, a *normalization factor* (β_{bkg}) can be computed from:

$$\beta_{\mathrm{bkg}} = \frac{N_{\mathrm{data}}^{\mathrm{CR}} - N_{\mathrm{other,MC}}^{\mathrm{CR}}}{N_{\mathrm{bkg,MC}}^{\mathrm{CR}}} \tag{4.16}$$

where the numerator is the observed yield of the background process in the CR, which is calculated by subtracting the expected MC yields of all other processes from the total observed data yield in the CR; and the denominator is the expected MC yield of that background process in the CR.

The estimated event yield of the background process in the SR is obtained by multiplying the expected MC yield of that process in the SR by β_{bkg}:

$$N^{\text{SR}}_{\text{bkg,est}} = \beta_{\text{bkg}} \times N^{\text{SR}}_{\text{bkg,MC}}. \tag{4.17}$$

Substituting Equation 4.16 into Equation 4.17 gives:

$$N^{\text{SR}}_{\text{bkg,est}} = \left(\frac{N^{\text{CR}}_{\text{data}} - N^{\text{CR}}_{\text{other,MC}}}{N^{\text{CR}}_{\text{bkg,MC}}} \right) \times N^{\text{SR}}_{\text{bkg,MC}} = (N^{\text{CR}}_{\text{data}} - N^{\text{CR}}_{\text{other,MC}}) \times \alpha_{\text{bkg}} \tag{4.18}$$

where:

$$\alpha_{\text{bkg}} = \frac{N^{\text{SR}}_{\text{bkg,MC}}}{N^{\text{CR}}_{\text{bkg,MC}}} \tag{4.19}$$

is called an *extrapolation factor* from the CR to the SR for this particular background.

The benefits of using the normalization factor method to estimate the background yield in the SR can be deduced from Equation 4.18. Because the extrapolation factor α is a ratio between expected MC yields in the SR and CR, the systematic uncertainties associated with the MC sample of this background process largely cancel out provided that the SR and CR are kinetically similar. By contrast, the absolute expected background yield in the SR term $N^{\text{SR}}_{\text{bkg,MC}}$ has a full set of systematic uncertainties associated with it. Therefore, by using the normalization factor method, the systematic uncertainties on the estimated background yields in the SR are substantially reduced. Further details on the treatment of experimental and theoretical systematic uncertainties can be found in Chapter 5.

The normalization factor method of estimating background yields in the SRs is used for the three main background processes in the $H \to WW^* \to l\nu l\nu$ analysis: WW, top quark, and Z/γ^*. The normalization factors for the Z/γ^* background are derived from Z/γ^* CRs exclusively constructed for the same-flavour channel. The normalization factors for the WW and top quark backgrounds used in this cut-based same-flavour analysis are derived from the different-flavour channel. The rationale behind this approach is that the Z/γ^* background is overwhelmingly the most dominant background in the same-flavour channel. As a result, WW and top quark CRs built for the same-flavour channel would suffer from a high level of Z/γ^* contamination. On the contrary, the WW and top quark CRs in the different-flavour

channel have significantly higher purities because the only possible way in which the Drell-Yan process can result in an $e\mu$ final state is through the $Z/\gamma^* \to \tau\tau \to e\mu\nu\nu\nu\nu$ decay which has a much smaller cross-section than the same-flavour $Z/\gamma^* \to ee/\mu\mu$ decay. This method can be done because *lepton universality* implies that the kinematics of top quark or WW decay are independent of lepton flavour.

Data-driven estimation

The main contributions of events with misidentified leptons (also referred to as 'fake leptons') to the total background are the W+jets and multijet processes where one or two jets are misidentified as leptons. However, the rate of such misidentification is low and is therefore difficult to accurately model using full MC samples. Instead, this background is estimated with the *data-driven fake factor method*. This section gives a brief overview of the method. Further details can be found in [178].

The W+jets control sample is designed to be enriched in misidentified leptons. It is defined by the same kinematic event selection criteria as the analysis region but requires one of the two leptons to satisfy the lepton selection criteria and the other instead to meet a looser set of criteria while failing the lepton selection criteria. The former lepton is said to be identified (ID) and the latter anti-identified (Anti-ID or $\not{\text{ID}}$). The multijet control sample can be constructed in a similar fashion by requiring two Anti-ID leptons.

The number of background events with at least one fake lepton in an analysis region (SR or other CR) can be estimated by scaling the control sample with an associated extrapolation factor known as the *fake factor* F:

$$N^{>0 \text{ fakes}}_{\text{analysis}} = F_1 N^{\not{\text{ID}},\text{ID}}_{W+\text{jets}} + F_2 N^{\text{ID},\not{\text{ID}}}_{W+\text{jets}} - F_1 F_2 N^{\not{\text{ID}},\not{\text{ID}}}_{\text{multijet}} \tag{4.20}$$

where F_1 and F_2 are the fake factors for the first and second lepton respectively; $N^{\not{\text{ID}},\text{ID}}_{W+\text{jets}}$ is the number of events in the control sample where the first lepton is Anti-ID and the second lepton is ID; and similarly for $N^{\text{ID},\not{\text{ID}}}_{W+\text{jets}}$ and $N^{\not{\text{ID}},\not{\text{ID}}}_{\text{multijet}}$. The first two terms in Equation 4.20 represent the contribution of the W+jets process where one of the two leptons in an event is fake (single-fake). The last term is a

correction that avoids double counting of the contribution of the multijet process where both leptons are fake (double-fakes).

The number of events in the W+jets control sample with a fake lepton can be calculated by subtracting the number of an MC simulated sample with prompt ID and Anti-ID leptons from data:

$$N_{W+\text{jets}}^{\not{\text{ID}},\text{ID}} = N_{\text{data}}^{\not{\text{ID}},\text{ID}} - N_{\text{MC}}^{\not{\text{ID}},\text{ID}(\text{both prompt})}. \tag{4.21}$$

The expressions for $N_{W+\text{jets}}^{\text{ID},\not{\text{ID}}}$ and $N_{\text{multijet}}^{\not{\text{ID}},\not{\text{ID}}}$ can be written similarly. In the MC sample, both leptons are known with certainty to be prompt while the same cannot be said for data. Therefore, this subtraction gives an estimate of the number of events with jets being misidentified as leptons in the W+jets control sample. The MC term in Equation 4.21 is sometimes referred to as the 'electroweak subtraction term'.

The fake factor F is determined as a function of p_{T} and, in the case of fake muons, η. This is under an assumption that the fake factor only depends on the kinematic properties of the lepton alone and not on the remainder of the event. This assumption is reasonable because lepton reconstruction only takes information from a few small regions of the detector. Therefore, the fake factor can be evaluated from another process with a different number of leptons. The most similar process to W+jets is Z+jets, where two prompt leptons and a fake lepton can be produced. The fake factor based on the Z+jets control sample is defined as:

$$F_{Z+\text{jets}}(p_{\text{T}}, \eta) = \frac{N_{Z+\text{jets}}^{\text{ID},\text{ID},\text{ID}}}{N_{Z+\text{jets}}^{\text{ID},\text{ID},\not{\text{ID}}}}. \tag{4.22}$$

According to the previous assumption, the fake factor derived in a three-lepton Z+jets sample $F_{Z+\text{jets}}$ can be used as a subtitute for the two-lepton W+jets fake factor $F_{W+\text{jets}}$. However, this does not take any potential sample dependence into account. This issue can be mitigated by introducing a *correction factor* (CF) made by comparing fake factors measured in Z+jets and W+jets MC samples:

$$CF = \frac{F_{W+\text{jets}}^{\text{MC}}}{F_{Z+\text{jets}}^{\text{MC}}}. \tag{4.23}$$

The correction factor is then multiplied by the fake factor derived in the Z+jets selection in data to obtain a fake factor that can be applied to W+jets data:

$$F^{\text{data}}_{W+\text{jets}} = CF \times F^{\text{data}}_{Z+\text{jets}}. \tag{4.24}$$

This expression is valid as long as the ratio of the fake factors is the same in data as in MC samples: $\frac{F^{\text{data}}_{W+\text{jets}}}{F^{\text{data}}_{Z+\text{jets}}} = \frac{F^{\text{MC}}_{W+\text{jets}}}{F^{\text{MC}}_{Z+\text{jets}}}$. Since fake leptons are very difficult to model, MC samples will not accurately estimate the number of fake leptons and the fake factors on its own. By introducing the ratio of two MC fake factors, any mis-estimation of the number of ID or Anti-ID leptons will be cancelled out as long as the amount of such mis-estimation is the same in the W+jets and Z+jets selections.

Since the fake factor is assumed to be dependent only on basic kinematic properties of leptons, the data-driven fake factor method can be independently applied to the distributions of any observable at a given cut on a bin-by-bin basis.

4.5.3 Preselection

Preselection requirements are applied to all events entering the analysis. Events selected using the single-lepton triggers are required to pass the following selection:

- Two isolated, oppositely charged leptons of the same flavour (ee or $\mu\mu$).
- The leading and subleading leptons must have $p_{\text{T}}^{\text{lead}} > 27$ GeV and $p_{\text{T}}^{\text{sublead}} > 15$ GeV respectively to favour the $H \to WW^*$ signal as the off-shell W^* boson produces a lepton with a slightly lower energy.
- $m_{ll} > 12$ GeV to remove low-mass meson resonances.
- $|m_{ll} - m_Z| > 15$ GeV to reduce the Z/γ^* background near the Z-boson resonance in the same-flavour channel. This cut is omitted for the different-flavour channel.
- $E_{\text{T}}^{\text{miss}}$ significance > 4 to suppress the Z/γ^* and misidentification backgrounds.

These preselection cuts generally follow the Run-2 different-flavour analysis [6], but with a few modifications. Firstly, the requirement on the minimum transverse momentum of the leading lepton $p_{\mathrm{T}}^{\mathrm{lead}}$ is increased from 22 GeV to 27 GeV to accommodate the higher p_{T} thresholds of the single-lepton triggers. And secondly, a new $E_{\mathrm{T}}^{\mathrm{miss}}$ significance observable is introduced as a means to suppress the Z/γ^* background, which is the most dominant background in the same-flavour channel, instead of using $E_{\mathrm{T}}^{\mathrm{miss,track}}$ like the different-flavour analysis[6]. Several $E_{\mathrm{T}}^{\mathrm{miss}}$-related observables were considered during the course of the analysis, and $E_{\mathrm{T}}^{\mathrm{miss}}$ significance was found to be the most effective method for suppressing the Z/γ^* background while retaining a high level of signal acceptance and significance.

The main benefit of $E_{\mathrm{T}}^{\mathrm{miss}}$ significance over other $E_{\mathrm{T}}^{\mathrm{miss}}$ observables is that it also takes the resolution of other objects present in the event into account and evaluates how likely it is to originate from undetected particles such as neutrinos. The Z/γ^* process has no genuine $E_{\mathrm{T}}^{\mathrm{miss}}$, and $E_{\mathrm{T}}^{\mathrm{miss}}$ significance is generally low in these events, as shown in Figure 4.14.

The preselected events are then classified into one of four categories based on jet multiplicity: $N_{\mathrm{jet}} = 0$, $N_{\mathrm{jet}} = 1$, $N_{\mathrm{jet}} \geq 2$ ggF-enriched, and $N_{\mathrm{jet}} \geq 2$ VBF-enriched. The different background compositions of the different jet multiplicities as observed in Figure 4.15 motivate this categorization. The Z/γ^* process is the most dominant background in low jet multiplicities $N_{\mathrm{jet}} \leq 1$ whereas the top quark background dominates high jet multiplicities $N_{\mathrm{jet}} \geq 2$.

From Figure 4.15, it can be seen that there are notable discrepancies between data and MC in the low jet multiplicity bins. This kind of mismodelling should not occur at the preselection stage. To investigate this, the m_{ll} distributions before the cut on $E_{\mathrm{T}}^{\mathrm{miss}}$ significance are made for the three jet categories (no ggF/VBF separation in preselection) and are shown in Figure 4.16. The Z/γ^* samples are generated separately as low-mass and high-mass slices with a cut-off at $m_{ll} = 40$ GeV since the energy scale is different in the two mass regimes. In the low-mass regime

[6] In addition, $E_{\mathrm{T}}^{\mathrm{miss,track}}$ was deprecated by the ATLAS JetEtmiss working group at the time of this analysis.

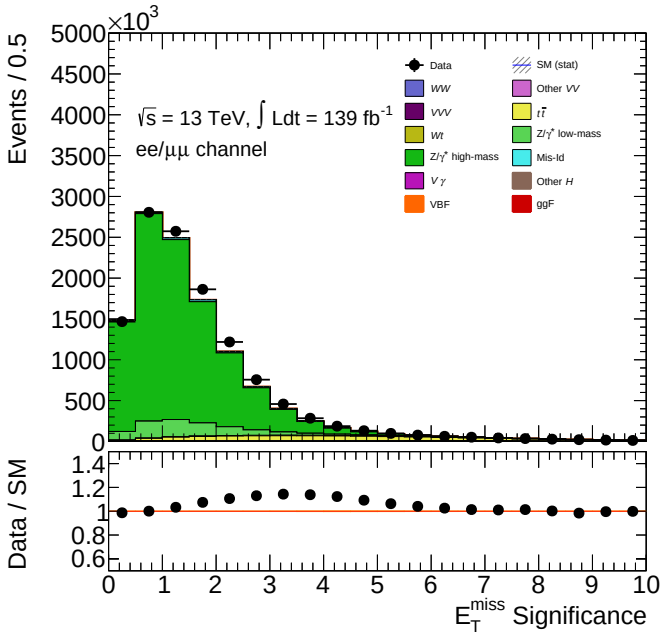

Figure 4.14: $E_{\mathrm{T}}^{\mathrm{miss}}$ significance distribution after applying all other preselection cuts except the cut on $E_{\mathrm{T}}^{\mathrm{miss}}$ significance itself. The Z/γ^* process is overwhelmingly the most dominant background in the same-flavour channel. No normalization factors are applied at the preselection stage.

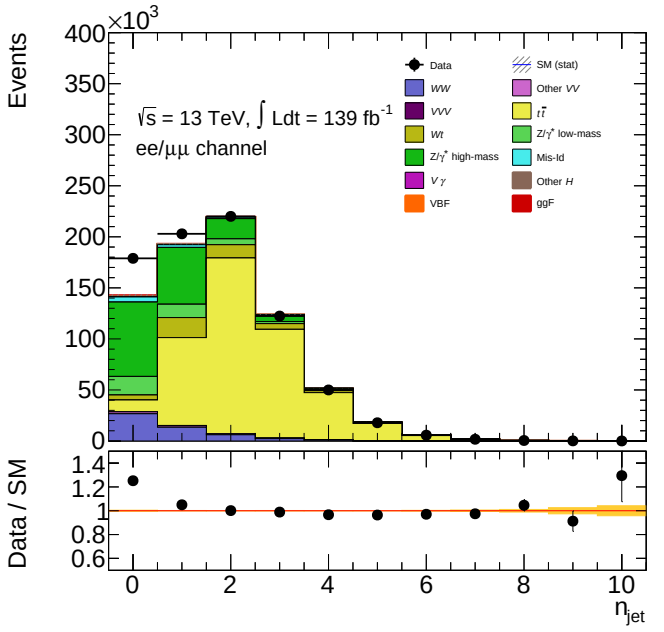

Figure 4.15: Jet multiplicity distribution after applying all preselection cuts (including the cut on $E_{\mathrm{T}}^{\mathrm{miss}}$ significance). No normalization factors are applied at the preselection stage.

Table 4.3: Summary of event selection criteria (cuts) used to define the signal regions (SRs) of the different N_{jet} categories in the cut-based $H \to WW^* \to l\nu l\nu$ same-flavour analysis. Successive cuts as the order progresses down the table are linked by the logical operator 'and' unless stated otherwise as 'or'.

Category	$N_{\text{jet}} = 0$ SR	$N_{\text{jet}} = 1$ SR	$N_{\text{jet}} \geq 2$ ggF-enriched SR	$N_{\text{jet}} \geq 2$ VBF-enriched SR
Preselection	Two isolated, oppositely charged leptons of the same flavour (ee or $\mu\mu$) $p_{\text{T}}^{\text{lead}} > 27$ GeV and $p_{\text{T}}^{\text{sublead}} > 15$ GeV $m_{ll} > 12$ GeV $\lvert m_{ll} - m_Z \rvert > 15$ GeV $E_{\text{T}}^{\text{miss}}$ significance > 4			
Background rejection	$N_{b\text{-jet},(p_{\text{T}}>20\text{GeV})} = 0$			
	$\Delta\phi_{ll,E_{\text{T}}^{\text{miss}}} > \pi/2$ $p_{\text{T}}^{ll} > 30$ GeV		$m_{\tau\tau} < m_Z - 25$ GeV	
	$E_{\text{T}}^{\text{miss}}$ significance > 4.5		$\Delta\phi_{ll,E_{\text{T}}^{\text{miss}}} < 2$	
VBF topology			$m_{jj} < 350$ GeV or $\Delta y_{jj} < 3$ or $p_{\text{T}}^{\text{total}} > 15$ GeV or fail Central Jet Veto	$m_{jj} > 350$ GeV $\Delta y_{jj} > 3$ $p_{\text{T}}^{\text{total}} < 15$ GeV Central Jet Veto Outside Lepton Veto
$H \to WW^* \to l\nu l\nu$ topology	$m_{ll} < 55$ GeV $\Delta\phi_{ll} < 1.8$			
Z/γ^* low-mass CR orthogonality	$m_{ll} > 20$ GeV or $\Delta\phi_{ll} > 0.3$		$m_{ll} > 20$ GeV	

the jets make a significant contribution to the energy scale of the interaction, whereas in the high-mass range the scale is dominated by the dilepton mass. In Figure 4.16, it can be seen that data is modelled poorly by the Z/γ^* low-mass samples in the low jet multiplicity categories $N_{\text{jet}} \leq 1$ while the high jet multiplicity category $N_{\text{jet}} \geq 2$ is affected to a much lesser extent. The discrepancies can be reduced by changing the factorization scale in the calculation by a factor of two. No such discrepancies are observed for the high-mass regime in any of the categories. To account for this difference, separate CRs are constructed for the Z/γ^* low-mass and high-mass samples in each of the analysis categories, and the systematic uncertainties on the Z/γ^* process are also evaluated separately for the two mass regimes.

The discrepancies observed at low mass also affect the modelling of lepton p_{T} at low p_{T}, shown in Figure 4.17 at the preselection stage. These discrepancies are expected to be reduced following the application of normalization factors derived from control regions.

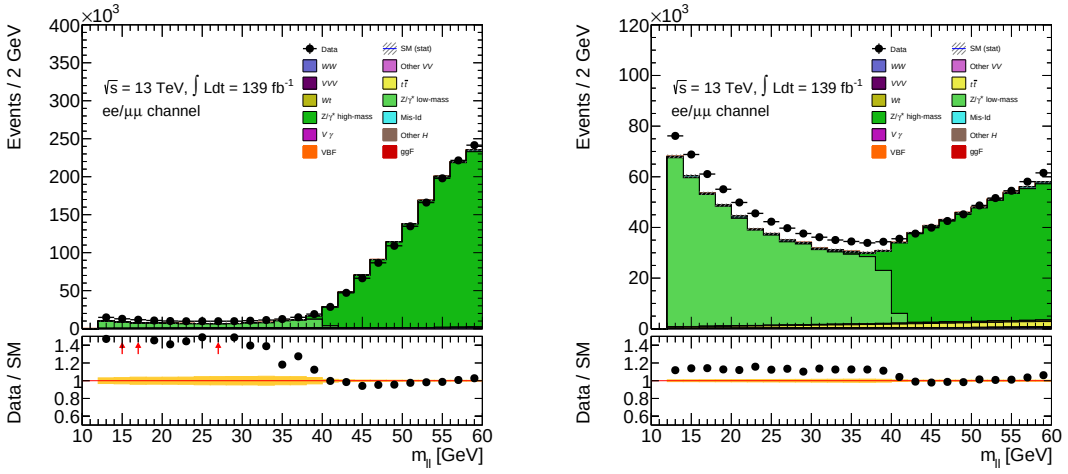

(a) $N_{\text{jet}} = 0$ **(b)** $N_{\text{jet}} = 1$

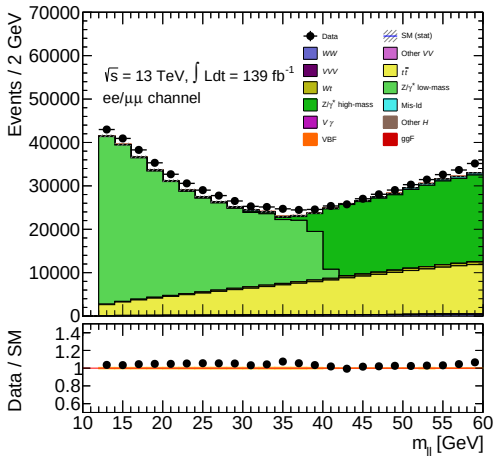

(c) $N_{\text{jet}} \geq 2$

Figure 4.16: Distributions of m_{ll} in the $N_{\text{jet}} = 0, 1$, and 2 jet categories after applying all preselection cuts except the cut on $E_{\text{T}}^{\text{miss}}$ significance. The Z/γ^* low-mass (high-mass) samples are shown with a lighter (darker) shade of green. The hatched bands in the upper plot and the shaded bands in the ratio plot give the statistical uncertainties on the MC samples. No normalization factors are applied at the preselection stage.

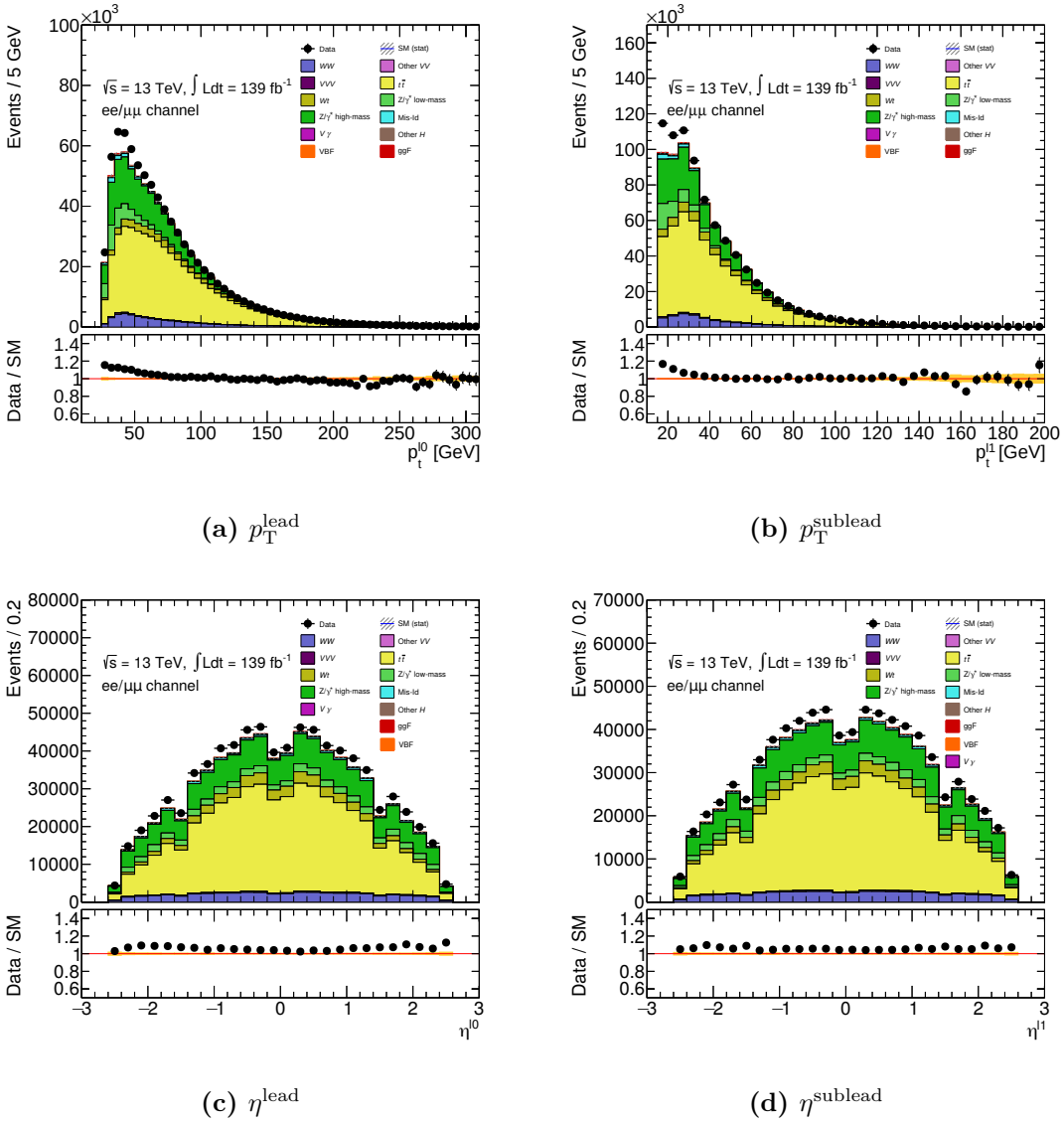

(a) $p_{\mathrm{T}}^{\mathrm{lead}}$ **(b)** $p_{\mathrm{T}}^{\mathrm{sublead}}$

(c) η^{lead} **(d)** η^{sublead}

Figure 4.17: Distributions of the transverse momentum $p_{\mathrm{T}}^{l_i}$ and pseudorapidity η^{l_i} of the leading and subleading leptons after applying all preselection cuts including the cut on $E_{\mathrm{T}}^{\mathrm{miss}}$ significance. The hatched bands in the upper plot and the shaded bands in the ratio plot give the statistical uncertainties on the MC samples. However, the statistical uncertainties are extremely small due to large number of events in each bin, resulting in the hatched bands not visible in the upper plots. No normalization factors are applied at the preselection stage.

Table 4.4: Summary of event selection criteria (cuts) used to define the Z/γ^* control regions (CRs) associated with the $N_{\text{jet}} = 0$ and $N_{\text{jet}} = 1$ categories in the cut-based $H \to WW^* \to l\nu l\nu$ same-flavour analysis. Each of the ggF categories has two separate Z/γ^* CRs for high-mass and low-mass regions. Successive cuts as the order progresses down the table are linked by the logical operator 'and'.

Category	$N_{\text{jet}} = 0$		$N_{\text{jet}} = 1$	
	Z/γ^* low-mass CR	Z/γ^* high-mass CR	Z/γ^* low-mass CR	Z/γ^* high-mass CR
Preselection	Two isolated, oppositely charged leptons of the same flavour (ee or $\mu\mu$) $p_{\text{T}}^{\text{lead}} > 27$ GeV and $p_{\text{T}}^{\text{sublead}} > 15$ GeV $m_{ll} > 12$ GeV $\lvert m_{ll} - m_Z \rvert > 15$ GeV $E_{\text{T}}^{\text{miss}}$ significance > 4			
Z/γ^* CR cuts	$N_{b\text{-jet},(p_{\text{T}}>20\text{GeV})} = 0$ $E_{\text{T}}^{\text{miss}}$ significance > 4.5			
	$p_{\text{T}}^{ll} > 30$ GeV $\Delta\phi_{ll,E_{\text{T}}^{\text{miss}}} > \pi/2$		$m_{\tau\tau} < m_Z - 25$ GeV	
	$m_{ll} < 20$ GeV $\Delta\phi_{ll} < 0.3$	$55 < m_{ll} < 75$ GeV	$m_{ll} < 20$ GeV $\Delta\phi_{ll} < 0.3$	$55 < m_{ll} < 75$ GeV

Table 4.5: Summary of event selection criteria (cuts) used to define the Z/γ^* control regions (CRs) associated with the $N_{\text{jet}} \geq 2$ ggF- and VBF-enriched categories in the cut-based $H \to WW^* \to l\nu l\nu$ same-flavour analysis. The $N_{\text{jet}} \geq 2$ ggF-enriched category has two separate Z/γ^* CRs for high-mass and low-mass regions while the VBF-enriched category has a single Z/γ^* CR. Successive cuts as the order progresses down the table are linked by the logical operator 'and' unless stated otherwise as 'or'.

Category	$N_{\text{jet}} \geq 2$ ggF-enriched		$N_{\text{jet}} \geq 2$ VBF-enriched
	Z/γ^* low-mass CR	Z/γ^* high-mass CR	Z/γ^* CR
Preselection	Two isolated, oppositely charged leptons of the same flavour (ee or $\mu\mu$) $p_{\text{T}}^{\text{lead}} > 27$ GeV and $p_{\text{T}}^{\text{sublead}} > 15$ GeV $m_{ll} > 12$ GeV $\lvert m_{ll} - m_Z \rvert > 15$ GeV $E_{\text{T}}^{\text{miss}}$ significance > 4		
Z/γ^* CR cuts	$N_{b\text{-jet},(p_{\text{T}}>20\text{GeV})} = 0$ $m_{\tau\tau} < m_Z - 25$ GeV $\Delta\phi_{ll,E_{\text{T}}^{\text{miss}}} < 2$		
	$m_{jj} < 350$ GeV or $\Delta y_{jj} < 3$ or $p_{\text{T}}^{\text{total}} > 15$ GeV or fail Central Jet Veto		$m_{jj} > 350$ GeV $\Delta y_{jj} > 3$ $p_{\text{T}}^{\text{total}} < 15$ GeV Central Jet Veto
	$m_{ll} < 20$ GeV	$55 < m_{ll} < 75$ GeV	fail Outside Lepton Veto

Table 4.6: Summary of event selection criteria (cuts) used to define the top control regions (CRs) of the different jet categories in the cut-based $H \to WW^* \to l\nu l\nu$ same-flavour analysis. The top quark CRs are constructed using the different-flavour $e\mu/\mu e$ samples for higher purity. Successive cuts as the order progresses down the table are linked by the logical operator 'and' unless stated otherwise as 'or'.

Category	$N_{\text{jet}} = 0$ Top quark CR	$N_{\text{jet}} = 1$ Top quark CR	$N_{\text{jet}} \geq 2$ ggF-enriched Top quark CR	$N_{\text{jet}} \geq 2$ VBF-enriched Top quark CR
Preselection	Two isolated, oppositely charged leptons of the different flavour ($e\mu$ or μe) $p_{\text{T}}^{\text{lead}} > 27$ GeV and $p_{\text{T}}^{\text{sublead}} > 15$ GeV $m_{ll} > 12$ GeV $E_{\text{T}}^{\text{miss}}$ significance > 4			
Top quark CR cuts	$N_{b\text{-jet},(20<p_{\text{T}}<30\text{GeV})} > 0$ $p_{\text{T}}^{ll} > 30$ GeV $\Delta\phi_{ll,E_{\text{T}}^{\text{miss}}} > \pi/2$ $\Delta\phi_{ll} < 2.8$	$N_{b\text{-jet},(20<p_{\text{T}}<30\text{GeV})} = 0$ $N_{b\text{-jet},(p_{\text{T}}>30\text{GeV})} = 1$	$N_{b\text{-jet},(p_{\text{T}}>20\text{GeV})} = 0$	$N_{b\text{-jet},(p_{\text{T}}>20\text{GeV})} = 1$
		$m_{\tau\tau} < m_Z - 25$ GeV		
		$\max_{i=1,2}\{m_{\text{T}}^{(l_i,E_{\text{T}}^{\text{miss}})}\} > 50$ GeV	$m_{\text{T2}} < 165$ GeV $\Delta\phi_{ll} < 1.8$ $m_{ll} > 80$ GeV	
			$\lvert m_{jj} - 85\rvert > 15$ GeV or $\Delta y_{jj} > 1.2$	
			fail Central Jet Veto or fail Outside Lepton Veto	Central Jet Veto Outside Lepton Veto

Table 4.7: Summary of event selection criteria (cuts) used to define the WW control regions (CRs) of the different N_{jet} categories in the cut-based $H \to WW^* \to l\nu l\nu$ same-flavour analysis. The WW CRs are constructed using the different-flavour $e\mu/\mu e$ samples for higher purity. There is no WW CR for the $N_{\text{jet}} \geq 2$ VBF-enriched category. Successive cuts as the order progresses down the table are linked by the logical operator 'and' unless stated otherwise as 'or'.

Category	$N_{\text{jet}} = 0$ WW CR	$N_{\text{jet}} = 1$ WW CR	$N_{\text{jet}} \geq 2$ ggF-enriched WW CR
Preselection	Two isolated, oppositely charged leptons of the different flavour ($e\mu$ or μe) $p_{\text{T}}^{\text{lead}} > 27$ GeV and $p_{\text{T}}^{\text{sublead}} > 15$ GeV $m_{ll} > 12$ GeV $E_{\text{T}}^{\text{miss}}$ significance > 4		
WW CR cuts	$N_{b\text{-jet},(p_{\text{T}}>20\text{GeV})} = 0$		
	$55 < m_{ll} < 110$ GeV	$m_{ll} > 80$ GeV	
	$p_{\text{T}}^{ll} > 30$ GeV $\Delta\phi_{ll,E_{\text{T}}^{\text{miss}}} > \pi/2$ $\Delta\phi_{ll} < 2.6$	$\lvert m_{\tau\tau} - m_Z\rvert > 25$ GeV $\max_{i=1,2}\{m_{\text{T}}^{(l_i,E_{\text{T}}^{\text{miss}})}\} > 50$ GeV	$m_{\tau\tau} < m_Z - 25$ GeV $m_{\text{T2}} > 165$ GeV
			$\lvert m_{jj} - 85\rvert > 15$ GeV or $\Delta y_{jj} > 1.2$
			fail Central Jet Veto or fail Outside Lepton Veto

4.5.4 $N_{\text{jet}} = 0$ category

The SR is constructed with the goal of maximizing the ggF Higgs signal acceptance while at the same time trying to primarily reduce the contamination from Z/γ^* events, which is the dominant background in the $N_{\text{jet}} = 0$ category. Two separate CRs are defined for the Z/γ^* background to account for differences in the data-MC modelling behaviour between the low and high m_{ll} regimes where different MC samples are used. The WW and top quark CRs are constructed using the different-flavour $e\mu/\mu e$ channel to ensure high purity of the respective events. To obtain an initial estimate of the expected precision of the measurement, a likelihood fit is performed using data from the CRs and MC from the SRs. The resulting background normalization factors are used to estimate the pre-fit yields of signal and background processes for the $N_{\text{jet}} = 0$ category (see Table 4.8).

Signal region

After the preselection cuts, the following cuts are applied in order to define the $N_{\text{jet}} = 0$ SR:

- 0 jets with $p_{\text{T}} > 30$ GeV and satisfying the `Tight` JVT working point.
- $\Delta\phi_{ll,E_{\text{T}}^{\text{miss}}} > \pi/2$ to remove pathological events where $E_{\text{T}}^{\text{miss}}$ points in the same direction of the lepton pair.
- $p_{\text{T}}^{ll} > 30$ GeV to reject mainly the Z/γ^* background, where the lepton pair are generally produced back-to-back and the dilepton momentum is small.
- b-jet veto on sub-threshold jets ($20 < p_{\text{T}} < 30$ GeV) to suppress the top quark background.
- $E_{\text{T}}^{\text{miss}}$ significance > 4.5 to further suppress the Z/γ^* background.
- $m_{ll} < 55$ GeV and $\Delta\phi_{ll} < 1.8$ to exploit the kinematic topology of the $H \to WW^* \to l\nu l\nu$ signal.

- $m_{ll} > 20$ GeV or $\Delta\phi_{ll} > 0.3$ to make the SR orthogonal to the Z/γ^* low-mass CR.

The distributions of these observables and event yields after each successive cut is applied are given in Figure 4.18 and Table 4.8 respectively. The expected ggF signal significance of the $N_{\text{jet}} = 0$ SR is 1.44. The m_{T} distribution of the $N_{\text{jet}} = 0$ SR before performing a fit to data is shown in Figure 4.19e.

Z/γ^* control regions

Most of the SR cuts are retained except for the cuts on m_{ll} and $\Delta\phi_{ll}$ which are modified to:

- Z/γ^* low-mass CR: $m_{ll} < 20$ GeV and $\Delta\phi_{ll} < 0.3$ to isolate the Z/γ^* low-mass process with high purity.
- Z/γ^* high-mass CR: $55 < m_{ll} < 75$ GeV to ensure orthogonality to the SR and to completely exclude the Z/γ^* low-mass sample.

The purities of the $N_{\text{jet}} = 0$ Z/γ^* low-mass and high-mass CRs are 82% and 67%, and the pre-fit normalization factors are found to be 1.82 ± 0.04(stat.) and 1.41 ± 0.02(stat.) respectively. The pre-fit m_{T} distributions of the two Z/γ^* CRs are shown in Figures 4.19a–4.19b.

Top quark control region

The following SR cuts are modified in order to define the top quark CR:

- No requirements on $E_{\text{T}}^{\text{miss}}$ significance and m_{ll} to ensure a large top quark sample size.
- At least one sub-threshold b-jet ($20 < p_{\text{T}} < 30$ GeV) is present in an event.
- $\Delta\phi_{ll} < 2.8$ is loosened from the SR value to also ensure large event yields.

The purity of the $N_{\text{jet}} = 0$ top quark CR is 92%, and the pre-fit normalization factor is 1.01 ± 0.01(stat.). The pre-fit m_{T} distribution of the $N_{\text{jet}} = 0$ top quark CR can be found in Figure 4.19d.

WW control region

The preselected $e\mu/\mu e$ events are required to pass the same cuts as the $N_{\text{jet}} = 0$ SR except for:

- No requirement on $E_{\text{T}}^{\text{miss}}$ significance > 4.5 to ensure a large WW sample size.
- $55 < m_{ll} < 110$ GeV to reduce contamination from top quark events.
- $\Delta\phi_{ll} < 2.6$ to reduce contamination from $Z/\gamma^* \to \tau\tau$ events.

The purity of the $N_{\text{jet}} = 0$ WW CR is 70%, and the normalization factor is found to be 1.05 ± 0.01(stat.). The pre-fit m_{T} distribution of the $N_{\text{jet}} = 0$ WW CR can be found in Figure 4.19c.

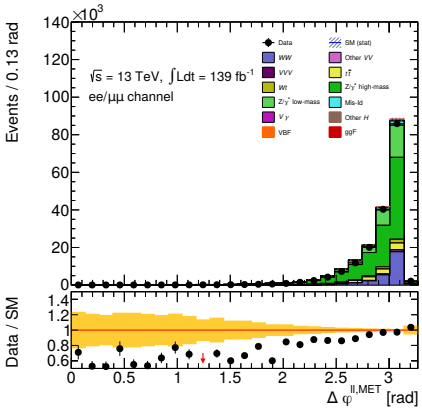

(a) $\Delta\phi_{ll,E_{\mathrm{T}}^{\mathrm{miss}}}$ after cut on $N_{\mathrm{jet}} = 0$

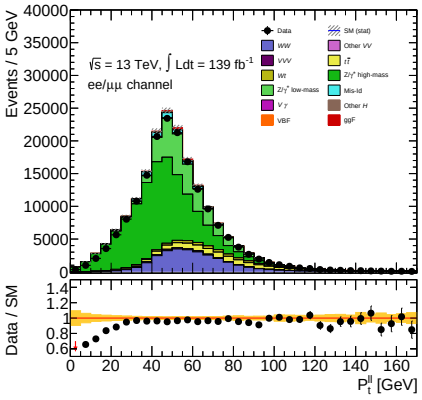

(b) p_{T}^{ll} after cut on $\Delta\phi_{ll,E_{\mathrm{T}}^{\mathrm{miss}}} > \pi/2$

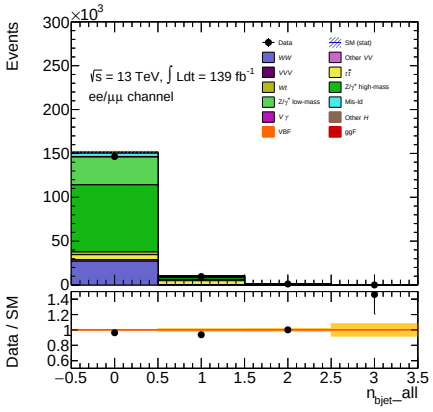

(c) $N_{b\text{-jet}}$ after cut on $p_{\mathrm{T}}^{ll} > 30$ GeV

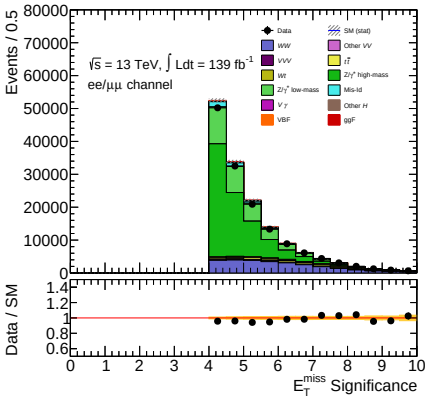

(d) $E_{\mathrm{T}}^{\mathrm{miss}}$ significance after cut on $N_{b\text{-jet}} = 0$

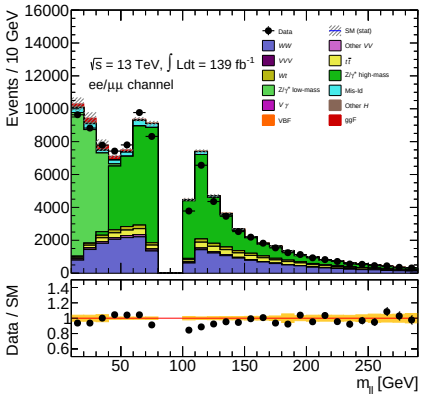

(e) m_{ll} after cut on $E_{\mathrm{T}}^{\mathrm{miss}}$ significance > 4.5

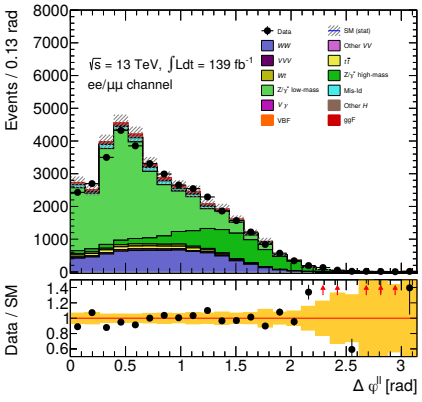

(f) $\Delta\phi_{ll}$ after cut on $m_{ll} < 55$ GeV

Figure 4.18: Distributions of the different cut observables after successive cuts are applied in the $N_{\mathrm{jet}} = 0$ SR. The hatched bands in the upper plot and the shaded bands in the ratio plot give the statistical uncertainty on the MC samples. Normalization factors are applied to the WW, top, and Z/γ^* backgrounds.

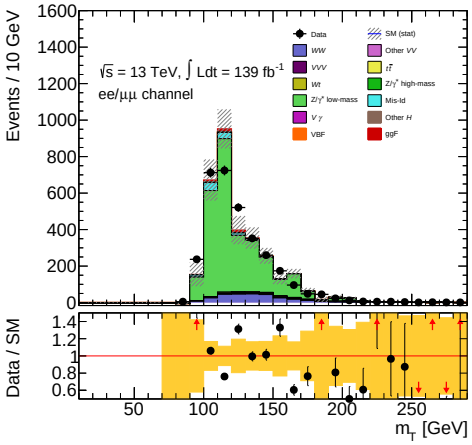

(a) Z/γ^* low-mass CR

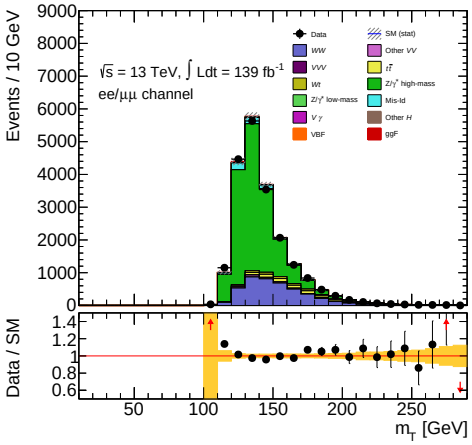

(b) Z/γ^* high-mass CR

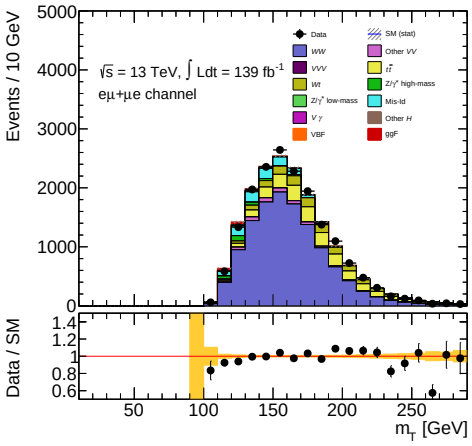

(c) WW CR

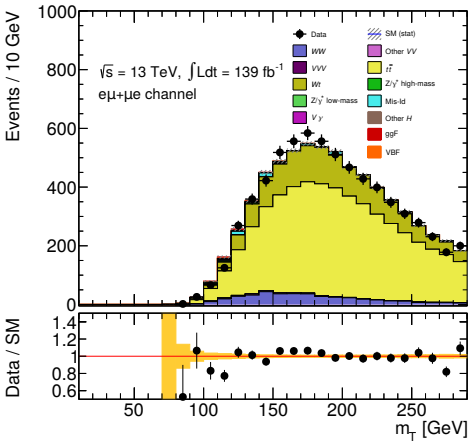

(d) Top quark CR

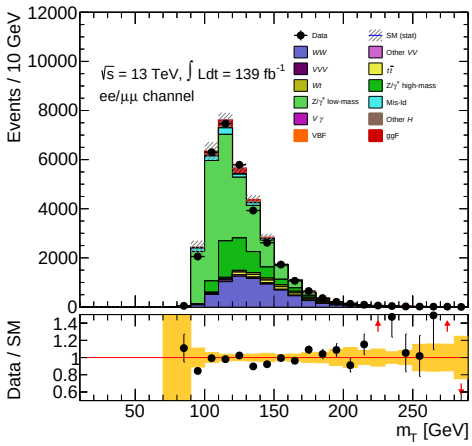

(e) $N_{\text{jet}} = 0$ SR

Figure 4.19: Pre-fit m_{T} distributions in the different analysis regions of the $N_{\text{jet}} = 0$ category. The hatched bands in the upper plot and the shaded bands in the ratio plot give the statistical uncertainty on the MC samples. Normalization factors are applied to the WW, top, and Z/γ^* backgrounds.

Table 4.8: Pre-fit event yields for signal and background processes after each successive cut is applied in the $N_{\text{jet}} = 0$ SR. Normalization factors derived from the WW, top, and Z/γ^* CRs are applied to the corresponding event yields. The uncertainties are statistical only.

$ee/\mu\mu$, $\sqrt{s} = 13$ TeV, $\mathcal{L} = 139$ fb^{-1}	H_{ggF}	H_{VBF}	Other H	WW	Other VV	VVV	$V\gamma$	Top	Z/γ^* high-mass	Z/γ^* low-mass	Mis-Id	Total Bkg.	All Processes	data
Preselection	2448 ± 5	203 ± 0	752 ± 1	49749 ± 72	5077 ± 18	255 ± 3	432 ± 25	493159 ± 155	156215 ± 615	39720 ± 570	10114 ± 219	755473 ± 884	758124 ± 884	800168
$N_{\text{jet}} = 0$	1483 ± 4	20 ± 0	85 ± 1	28077 ± 62	1853 ± 12	36 ± 1	215 ± 18	16622 ± 34	102961 ± 615	33024 ± 859	5003 ± 151	187876 ± 1069	189378 ± 1069	178917
$\Delta\phi_{\ell\ell,E_{\text{T}}^{\text{miss}}} > \pi/2$	1482 ± 4	20 ± 0	84 ± 1	28051 ± 61	1820 ± 12	35 ± 1	213 ± 18	16493 ± 34	101252 ± 607	33019 ± 859	4976 ± 150	185943 ± 1065	187445 ± 1065	177736
$p_{\text{T}}^{\ell\ell} > 30$ GeV	1456 ± 4	19 ± 0	78 ± 1	27446 ± 61	1714 ± 12	34 ± 1	203 ± 18	15868 ± 34	78948 ± 493	33042 ± 847	4562 ± 136	161895 ± 992	163370 ± 992	157162
$N_{b\text{-jet}} = 0$	1434 ± 4	19 ± 0	73 ± 1	27085 ± 60	1639 ± 12	32 ± 1	197 ± 17	8984 ± 26	76479 ± 488	31774 ± 834	4372 ± 134	150635 ± 978	152087 ± 978	146422
$E_{\text{T}}^{\text{miss}}$ significance > 4.5	1132 ± 4	16 ± 0	62 ± 0	23236 ± 56	1344 ± 10	30 ± 1	154 ± 15	8243 ± 25	42102 ± 345	20577 ± 643	2748 ± 107	98496 ± 740	99643 ± 740	96206
$m_{\ell\ell} < 55$ GeV	1041 ± 4	14 ± 0	31 ± 0	7182 ± 30	421 ± 5	6 ± 0	79 ± 11	1576 ± 11	6170 ± 119	20577 ± 643	1155 ± 95	37197 ± 661	38252 ± 661	37440
$\Delta\phi_{\ell\ell} < 1.8$	1012 ± 3	14 ± 0	30 ± 0	7054 ± 30	410 ± 5	6 ± 0	74 ± 10	1549 ± 11	5124 ± 101	20569 ± 643	1074 ± 94	35890 ± 658	36916 ± 658	35905
0-jet SR: $m_{\ell\ell} > 20$ GeV or $\Delta\phi_{\ell\ell} > 0.3$	948 ± 3	13 ± 0	28 ± 0	6758 ± 29	380 ± 5	6 ± 0	69 ± 10	1481 ± 11	5125 ± 101	17912 ± 609	960 ± 91	32718 ± 625	33680 ± 625	32667
0-jet Z/γ^* low-mass CR	64 ± 1	1 ± 0	2 ± 0	296 ± 6	30 ± 1	0 ± 0	5 ± 2	68 ± 2	0 ± 0	2657 ± 204	113 ± 24	3172 ± 205	3237 ± 205	3238
0-jet Z/γ^* high-mass CR	90 ± 1	2 ± 0	15 ± 0	4379 ± 24	275 ± 5	4 ± 0	26 ± 6	1181 ± 10	13605 ± 196	0 ± 0	679 ± 33	20163 ± 201	20255 ± 201	20260
0-jet WW CR ($e\mu/\mu e$)	140 ± 1	2 ± 0	26 ± 0	12363 ± 40	446 ± 7	11 ± 1	89 ± 11	3409 ± 17	271 ± 25	0	969 ± 26	17582 ± 58	17725 ± 58	17712
0-jet top quark CR ($e\mu/\mu e$)	23 ± 1	1 ± 0	5 ± 0	437 ± 8	43 ± 2	2 ± 0	11 ± 4	7393 ± 22	15 ± 6	0	74 ± 14	7980 ± 28	8003 ± 28	8002

4.5.5 $N_{\text{jet}} = 1$ category

The strategy for background suppression in the $N_{\text{jet}} = 1$ category generally follows that of $N_{\text{jet}} = 0$ since they share similar background composition and kinematic topology except for the boost of the final-state leptons due to the recoil from the jet. The Z/γ^* process remains the most dominant background. However, there is an increase in the contamination from the top quark background, particularly in the different-flavour WW CR. Normalization factors are computed using the same method as the $N_{\text{jet}} = 0$ category, and the pre-fit event yields of the signal and background processes in the SR and CRs of the $N_{\text{jet}} = 1$ category can be found in Table 4.9.

Signal region

The event selection criteria for the $N_{\text{jet}} = 1$ SR are as follows:

- 1 jet with $p_{\text{T}} > 30$ GeV and satisfying the `Tight` JVT working point.
- b-jet veto on all jets including sub-threshold jets ($p_{\text{T}} > 20$ GeV) to suppress the top quark background.
- $m_{\tau\tau} < m_Z - 25$ GeV to reject $Z/\gamma^* \to \tau\tau$ events.
- $E_{\text{T}}^{\text{miss}}$ significance > 4.5.
- $m_{ll} < 55$ GeV and $\Delta\phi_{ll} < 1.8$.
- $m_{ll} > 20$ GeV or $\Delta\phi_{ll} > 0.3$.

There are two notable deviations from the $N_{\text{jet}} = 0$ SR. Firstly, the cut $p_{\text{T}}^{ll} > 30$ GeV is dismissed because the dilepton momentum tends to be large for both the ggF signal and Z/γ^* background due to the recoil from the jet. Secondly, the jet recoil also causes the neutrinos to be closer to the leptons so that the cut on $\Delta\phi_{ll,E_{\text{T}}^{\text{miss}}} > \pi/2$ would not be as efficient.

The distributions of these observables and the event yields of the diferrent processes after each successive cut is applied can be found in Figure 4.20 and Table

4.9 respectively. The pre-fit m_{T} distribution of the $N_{\mathrm{jet}} = 1$ SR is shown in Figure 4.21e. The expected ggF signal significance of the $N_{\mathrm{jet}} = 1$ SR is 1.17.

Z/γ^* control regions

The Z/γ^* low-mass and high-mass CRs of the $N_{\mathrm{jet}} = 1$ category are constructed in the same way as those of the $N_{\mathrm{jet}} = 0$ category, but with an addition of the new cut on $m_{\tau\tau}$ from the SR:

- $m_{\tau\tau} < m_Z - 25$ GeV.
- Z/γ^* low-mass CR: $m_{ll} < 20$ GeV and $\Delta\phi_{ll} < 0.3$.
- Z/γ^* high-mass CR: $55 < m_{ll} < 75$ GeV.

The purities of the $N_{\mathrm{jet}} = 1$ Z/γ^* low-mass and high-mass CRs are 84% and 63% respectively. The pre-fit normalization factors are 1.34 ± 0.03(stat.) and 1.21 ± 0.02(stat.) for the Z/γ^* low-mass and high-mass backgrounds respectively. The pre-fit m_{T} distributions of the two Z/γ^* CRs are given in Figures 4.21a–4.21b.

Top quark control region

The top quark CR only shares the same $m_{\tau\tau}$ cut with the SR, and the following new cuts are defined:

- No requirements on $E_{\mathrm{T}}^{\mathrm{miss}}$, m_{ll}, and $\Delta\phi_{ll}$ to ensure large event yields.
- The only jet ($p_{\mathrm{T}} > 30$ GeV) in an event is required to be identified as a b-jet, and no sub-threshold jets ($20 < p_{\mathrm{T}} < 30$ GeV) are identified as b-jets.
- $\max\limits_{i=1,2}\{m_{\mathrm{T}}^{(l_i, E_{\mathrm{T}}^{\mathrm{miss}})}\} > 50$ GeV to reject $Z/\gamma^* \to \tau\tau$ and multi-jet events.

The purity of the $N_{\mathrm{jet}} = 1$ top quark CR is 98%, and the pre-fit normalization factor is 1.00 ± 0.01(stat.). The pre-fit m_{T} distribution of the $N_{\mathrm{jet}} = 1$ top quark CR can be found in Figure 4.21d.

WW control region

The WW CR of the $N_{\text{jet}} = 1$ category uses only the b-veto cut from the SR. The following new cuts are defined:

- No requirement on $E_{\text{T}}^{\text{miss}}$ significance and $\Delta\phi_{ll}$ to ensure large event yields.
- $|m_{\tau\tau} - m_Z| > 25$ GeV to reject $Z/\gamma^* \to \tau\tau$ events. The inclusion of the absolute value is to account for the possibility that $m_{\tau\tau}$ can be unphysically large in WW events, where the Collinear Approximation generally does not hold.
- $m_{ll} > 80$ GeV to reject $Z/\gamma^* \to \tau\tau$ events.
- $\max_{i=1,2}\{m_{\text{T}}^{(l_i, E_{\text{T}}^{\text{miss}})}\} > 50$ GeV to reject $Z/\gamma^* \to \tau\tau$ and multi-jet events.

The $N_{\text{jet}} = 1$ WW CR only results in a purity of 34% due to the contamination from the dominant top quark background. However, since the ratio of the WW to top quark events in the CR (0.59) is not significantly different from that of the SR (0.68), the composition of the WW CR is still representative of the SR, and the CR-to-SR extrapolation uncertainty remains small. The pre-fit normalization factor of the WW background is 0.88 ± 0.02(stat.). The pre-fit m_{T} distribution of the $N_{\text{jet}} = 1$ WW CR can be found in Figure 4.21c.

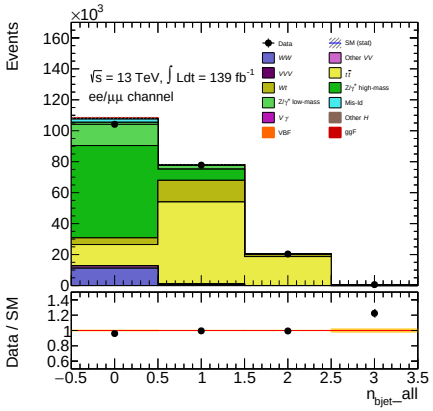

(a) $N_{b\text{-jet}}$ after cut on $N_{\text{jet}} = 1$

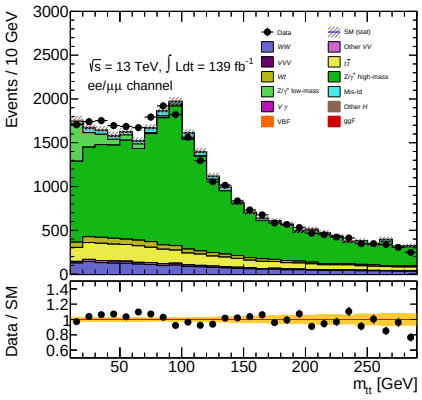

(b) $m_{\tau\tau}$ after cut on $N_{b\text{-jet}} = 0$

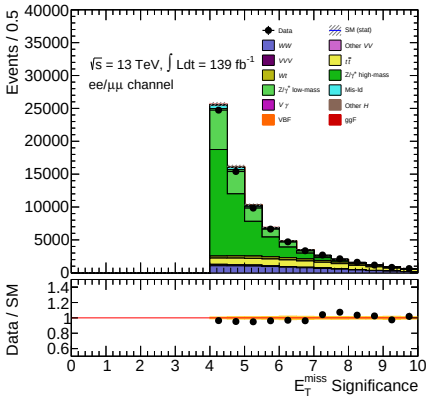

(c) $E_{\text{T}}^{\text{miss}}$ significance after cut on $m_{\tau\tau} < m_Z - 25$ GeV

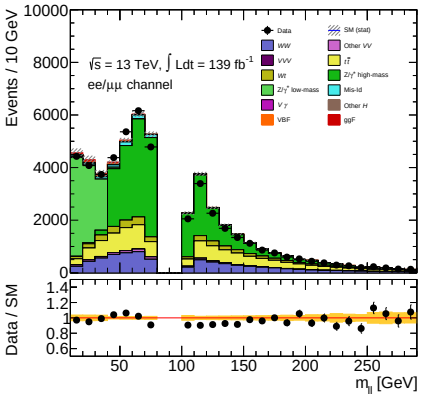

(d) m_{ll} after cut on $E_{\text{T}}^{\text{miss}}$ significance > 4.5

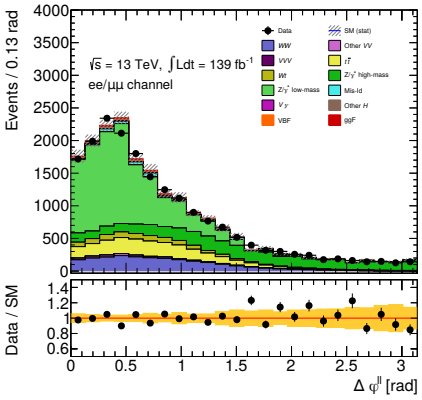

(e) $\Delta\phi_{ll}$ after cut on $m_{ll} < 55$ GeV

Figure 4.20: Distributions of the different cut observables after successive cuts are applied in the $N_{\text{jet}} = 1$ SR. The hatched bands in the upper plot and the shaded bands in the ratio plot give the statistical uncertainty on the MC samples. Normalization factors are applied to the WW, top quark, and Z/γ^* backgrounds.

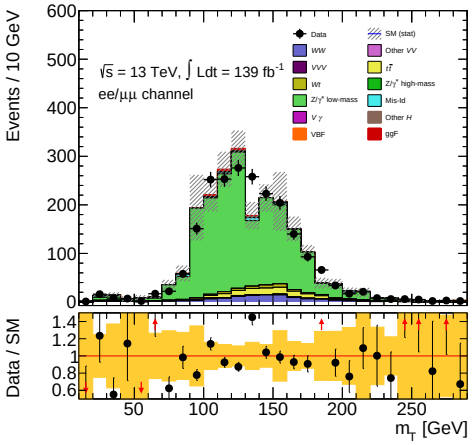

(a) Z/γ^* low-mass CR

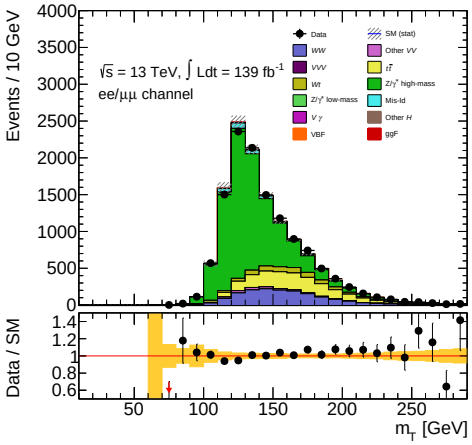

(b) Z/γ^* high-mass CR

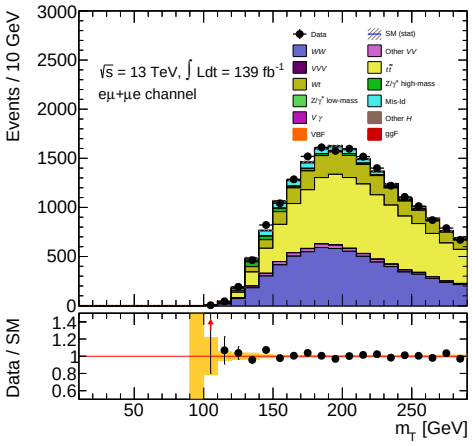

(c) WW CR

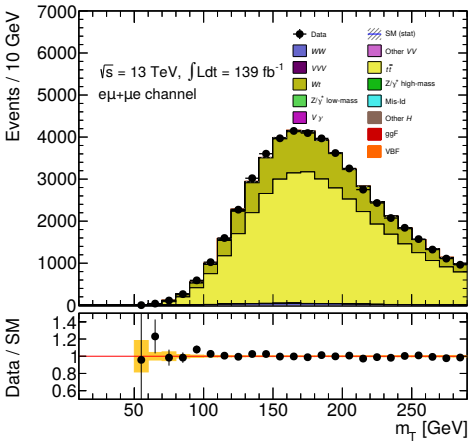

(d) Top quark CR

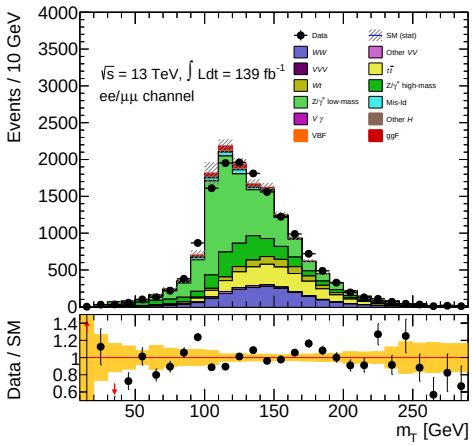

(e) $N_{\text{jet}} = 1$ SR

Figure 4.21: Pre-fit m_{T} distributions in the different analysis regions of the $N_{\text{jet}} = 1$ category. The hatched bands in the upper plot and the shaded bands in the ratio plot give the statistical uncertainty on the MC samples. Normalization factors are applied to the WW, top, and Z/γ^* backgrounds.

Table 4.9: Pre-fit event yields for signal and background processes after each successive cut is applied in the $N_{\text{jet}} = 1$ SR. Normalization factors derived from the WW, top quark, and Z/γ^* CRs are applied to the corresponding event yields. The uncertainties are statistical only.

$ee/\mu\mu$, $\sqrt{s} = 13$ TeV, $\mathcal{L} = 139$ fb^{-1}	H_{ggF}	H_{VBF}	Other H	WW	Other VV	VVV	$V\gamma$	Top	Z/γ^* high-mass	Z/γ^* low-mass	Mis-Id	Total Bkg.	All Processes	data
Preselection	2448 ± 5	203 ± 0	752 ± 1	49749 ± 72	5077 ± 18	255 ± 3	432 ± 25	493159 ± 155	156215 ± 615	39720 ± 570	10114 ± 219	755473 ± 884	758124 ± 884	800168
$N_{\text{jet}} = 1$	629 ± 2	79 ± 0	147 ± 1	11954 ± 35	1647 ± 10	72 ± 2	132 ± 12	105540 ± 78	67261 ± 399	17520 ± 356	2635 ± 113	206908 ± 554	207616 ± 554	202947
$N_{b\text{-jet}} = 0$	579 ± 2	72 ± 0	121 ± 1	11197 ± 34	1405 ± 9	63 ± 2	124 ± 11	18397 ± 34	59527 ± 385	15012 ± 334	2105 ± 99	107950 ± 522	108601 ± 522	104172
$m_{\tau\tau} < m_Z - 25$ GeV	537 ± 2	64 ± 0	66 ± 0	8568 ± 30	1028 ± 8	44 ± 1	96 ± 10	13699 ± 30	37364 ± 312	14918 ± 333	1490 ± 85	77272 ± 466	77873 ± 466	75479
$E_{\text{T}}^{\text{miss}}$ significance > 4.5	413 ± 2	52 ± 0	55 ± 0	7511 ± 28	819 ± 7	40 ± 1	72 ± 8	12430 ± 28	21156 ± 226	8704 ± 262	972 ± 66	51760 ± 355	52225 ± 355	50743
$m_{\ell\ell} < 55$ GeV	370 ± 2	47 ± 0	30 ± 0	2306 ± 15	272 ± 4	10 ± 1	35 ± 5	3302 ± 15	3796 ± 81	8703 ± 262	425 ± 52	18879 ± 280	19296 ± 280	19224
$\Delta\phi_{\ell\ell} < 1.8$	346 ± 2	45 ± 0	27 ± 0	2167 ± 15	249 ± 4	10 ± 1	34 ± 5	3149 ± 15	2324 ± 42	8672 ± 261	346 ± 50	16978 ± 270	17369 ± 270	17270
1-jet SR: $m_{\ell\ell} > 20$ GeV or $\Delta\phi_{\ell\ell} > 0.3$	317 ± 2	41 ± 0	25 ± 0	2054 ± 14	225 ± 3	9 ± 1	31 ± 5	2999 ± 14	2319 ± 42	6870 ± 230	321 ± 48	14854 ± 240	15212 ± 240	15112
1-jet Z/γ^* low-mass CR	28 ± 1	4 ± 0	2 ± 0	113 ± 3	24 ± 2	0 ± 0	3 ± 2	150 ± 3	5 ± 1	1802 ± 124	25 ± 13	2125 ± 124	2157 ± 124	2158
1-jet Z/γ^* high-mass CR	42 ± 1	5 ± 0	12 ± 0	1612 ± 13	211 ± 4	7 ± 1	15 ± 4	2422 ± 13	8037 ± 145	0 ± 0	294 ± 32	12611 ± 150	12658 ± 150	12663
1-jet WW CR ($e\mu/\mu e$)	2 ± 0	0 ± 0	33 ± 0	8396 ± 29	514 ± 6	47 ± 1	92 ± 10	14257 ± 30	390 ± 27	2 ± 2	704 ± 28	24436 ± 58	24438 ± 58	24431
1-jet top quark CR ($e\mu/\mu e$)	32 ± 1	4 ± 0	12 ± 0	489 ± 7	92 ± 2	5 ± 0	9 ± 4	54721 ± 59	93 ± 10	2 ± 1	251 ± 37	55672 ± 71	55708 ± 71	55747

4.5.6 $N_{\text{jet}} \geq 2$ VBF-enriched category

The VBF Higgs production process has a very specific topology as described in Section 4.1.1, which can be exploited to effectively extract the VBF signal from the background as well as separating it from the ggF signal with high jet multiplicity. For $N_{\text{jet}} \geq 2$, the most dominant backgrounds are Z/γ^* and top quark processes. No WW CR is constructed for this category because it is not possible to define one that is orthogonal to the $N_{\text{jet}} \geq 2$ ggF-enriched WW CR and also has an acceptable purity. In addition, only a single Z/γ^* CR is defined in the $N_{\text{jet}} \geq 2$ VBF-enriched category due to the limited number of MC events.

Signal region

Firstly, the cuts in common with the other categories are applied:

- At least 2 jets with $p_{\text{T}} > 30$ GeV and satisfying the `Tight` JVT working point.
- b-jet veto on all jets including sub-threshold jets ($p_{\text{T}} > 20$ GeV) to suppress the top quark background.
- $m_{\tau\tau} < m_Z - 25$ GeV to reject $Z/\gamma^* \to \tau\tau$ events.

Then, the unique kinematic features of the VBF process can be exploited by utilizing the various observables defined in Section 4.4.2:

- $m_{jj} > 350$ GeV: the leading-jet pair has a high invariant mass.
- $\Delta y_{jj} > 3$: there is a large rapidity gap between the two leading jets.
- $p_{\text{T}}^{\text{total}} < 15$ GeV: low activity in the transverse plane.
- CJV = true: ensuring that there are no other jets with $p_{\text{T}} > 30$ GeV within the central region, defined by the rapidity gap of the two leading jets.
- OLV = true: ensuring that the two leptons are produced within the rapidity gap of the two leading jets.

And lastly, the cuts favouring the $H \to WW^* \to l\nu l\nu$ kinematic topology are applied:

- $\Delta\phi_{ll,E_{\mathrm{T}}^{\mathrm{miss}}} < 2$ to account for the high-N_{jet} kinematic topology where the lepton pair and neutrino pair tend not to be emitted back-to-back due to the recoil from the jets.
- $m_{ll} < 55$ GeV and $\Delta\phi_{ll} < 1.8$.

The distributions of these observables and the event yields of the diferrent processes after each successive cut is applied are given in Figure 4.22 and Table 4.10 respectively. The expected VBF signal significance of the $N_{\mathrm{jet}} \geq 2$ VBF-enriched SR is 1.16. The pre-fit m_{T} distribution of the $N_{\mathrm{jet}} \geq 2$ VBF-enriched SR is shown in Figure 4.23c. Since the VBF process has a small cross-section, more cuts with more stringent requirements are needed to extract the VBF signal from the background, which result in small event yields and large statistical uncertainties in the SR. This is the main drawback of the purely cut-based approach to the construction of the VBF SR.

Z/γ^* control region

The Z/γ^* CR in the $N_{\mathrm{jet}} \geq 2$ VBF-enriched category is constructed by requiring the exact same cuts as the SR except:

- No requirements on m_{ll} and $\Delta\phi_{ll}$ to increase sample size.
- OLV = false: inversion of the OLV requirement, i.e. an event is required to have at least one lepton outside the rapidity gap of the two jets.

This method is only able to achieve a Z/γ^* purity of 38% as a result of large contamination from the top quark background. The pre-fit normalization factor of the Z/γ^* process is 0.65 ± 0.13(stat.), and the pre-fit m_{T} distribution of the CR is shown in Figure 4.23a. The sample size of the Z/γ^* process in the CR of this category is too small to split into low-mass and high-mass regions as in the other categories.

Top quark control region

The preselected $e\mu/\mu e$ events are required to pass only these cuts:

- Exactly one jet or sub-threshold jet ($p_{\mathrm{T}} > 20$ GeV) is required to be identified as a b-jet. By requiring only one instead of two b-jets, the flavour composition of the two leading jets in the CR remains similar to that in the SR, which reduces the effects of uncertainties from the b-jet selection.
- CJV = true.
- OLV = true.

The top quark CR is able to achieve a very high purity of 99%. The pre-fit normalization factor obtained from a hybrid fit is 0.99 ± 0.01(stat.). The pre-fit m_{T} distribution of the CR is shown in Figure 4.23b.

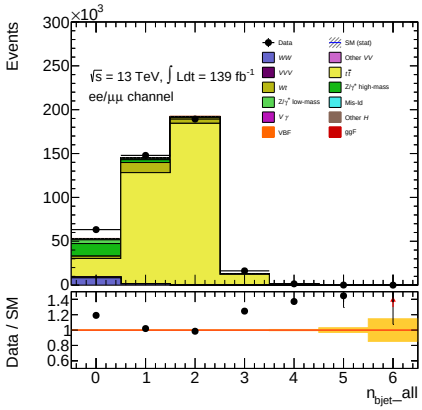

(a) $N_{b\text{-jet}}$ after cut on $N_{\text{jet}} \geq 2$

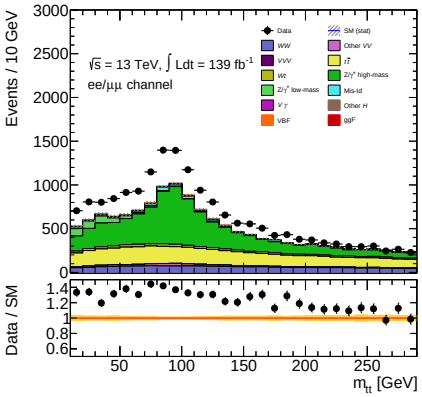

(b) $m_{\tau\tau}$ after cut on $N_{b\text{-jet}} = 0$

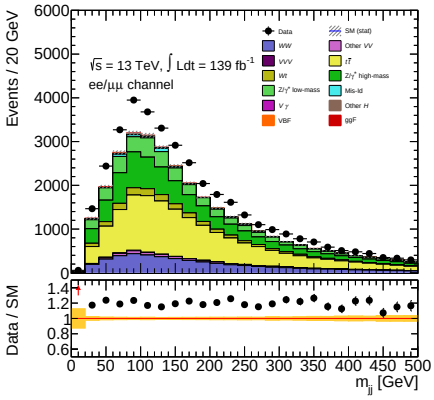

(c) m_{jj} after cut on $m_{\tau\tau} < m_Z - 25$ GeV

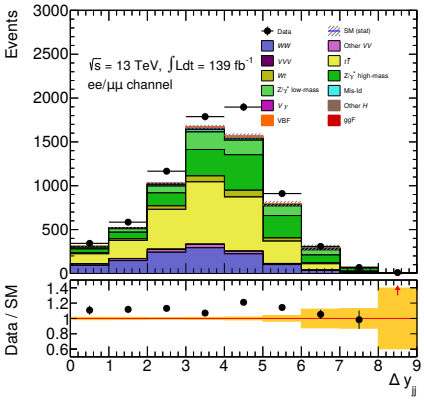

(d) Δy_{jj} after cut on $m_{jj} > 350$ GeV

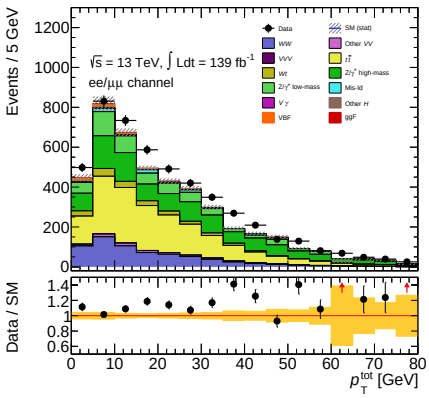

(e) $p_{\text{T}}^{\text{total}}$ after cut on $\Delta y_{jj} > 3$

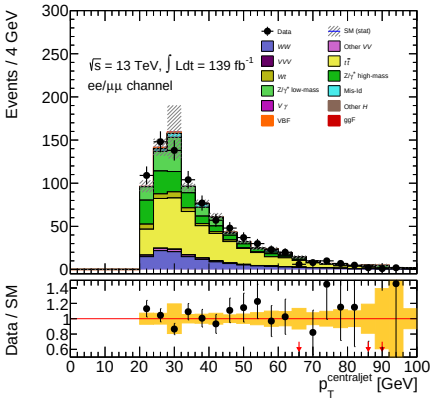

(f) $p_{\text{T}}^{\text{centraljet}}$ after cut on $p_{\text{T}}^{\text{total}} < 15$ GeV

Figure 4.22: Distributions of the different cut observables after successive cuts are applied in the $N_{\text{jet}} \geq 2$ VBF-enriched SR. The hatched bands in the upper plot and the shaded bands in the ratio plot give the statistical uncertainty on the MC samples. Normalization factors are applied to the top quark and Z/γ^* backgrounds.

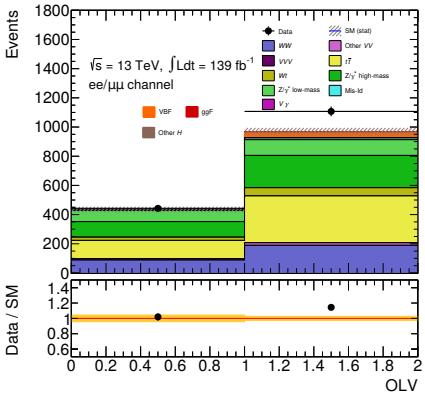

(g) OLV boolean after CJV = true

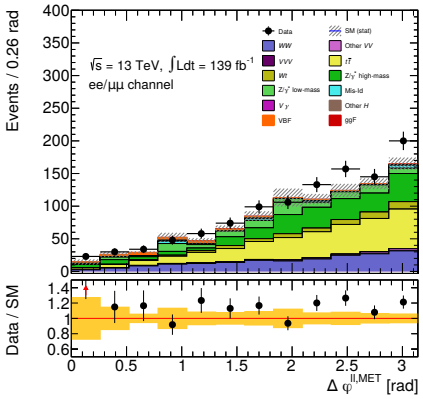

(h) $\Delta\phi_{ll,E_{\mathrm{T}}^{\mathrm{miss}}}$ after OLV = true

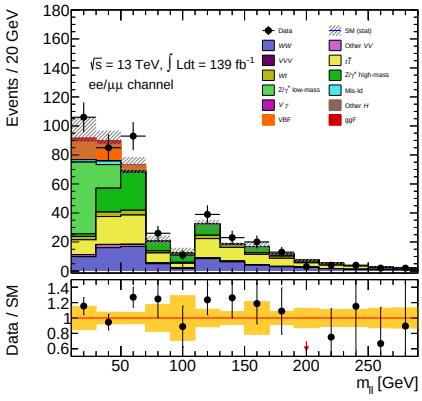

(i) m_{ll} after cut on $\Delta\phi_{ll,E_{\mathrm{T}}^{\mathrm{miss}}} < 2$

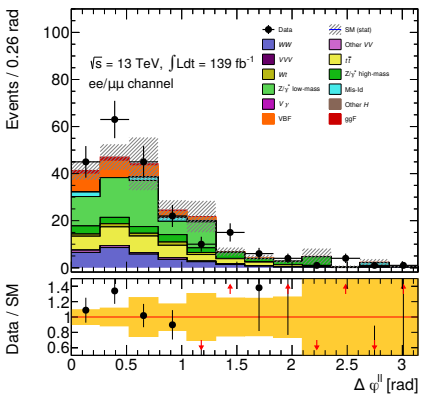

(j) $\Delta\phi_{ll}$ after cut on $m_{ll} < 55$ GeV

Figure 4.22: (continued) Distributions of the different cut observables after successive cuts are applied in the $N_{\mathrm{jet}} \geq 2$ VBF-enriched SR. The hatched bands in the upper plot and the shaded bands in the ratio plot give the statistical uncertainty on the MC samples. Normalization factors are applied to the top quark and Z/γ^* backgrounds.

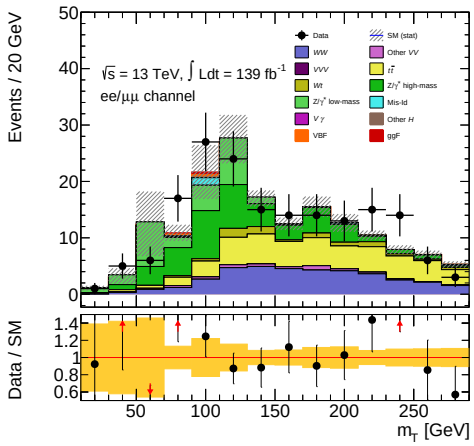

(a) Z/γ^* CR

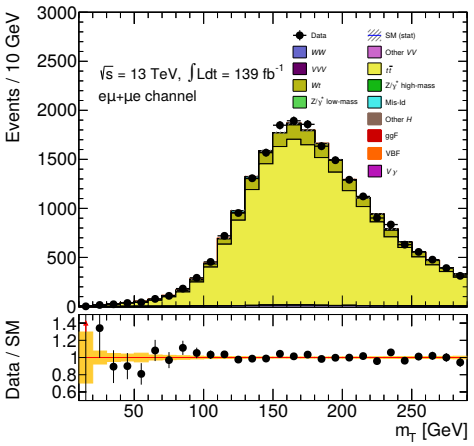

(b) Top quark CR

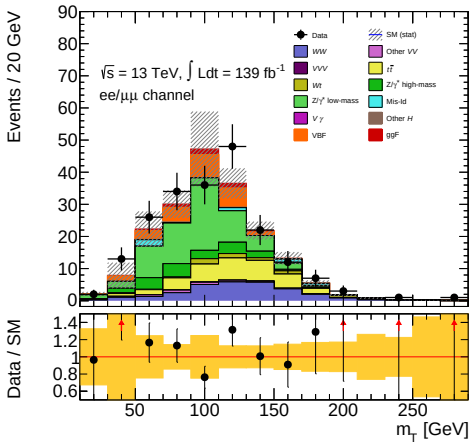

(c) $N_{\text{jet}} \geq 2$ VBF-enriched SR

Figure 4.23: Pre-fit m_{T} distributions in the different analysis regions of the $N_{\text{jet}} \geq 2$ VBF-enriched category. The hatched bands in the upper plot and the shaded bands in the ratio plot give the statistical uncertainty on the MC samples. Normalization factors are applied to the top quark and Z/γ^* backgrounds.

Table 4.10: Pre-fit event yields for signal and background processes after each successive cut is applied in the $N_{\text{jet}} \geq 2$ VBF-enriched SR. Normalization factors derived from the top quark and Z/γ^* CRs are applied to the corresponding event yields. The uncertainties are statistical only.

$ee/\mu\mu$, $\sqrt{s} = 13$ TeV, $\mathcal{L} = 139$ fb^{-1}	H_{ggF}	H_{VBF}	Other H	WW	Other VV	VVV	$V\gamma$	Top	Z/γ^* high-mass	Z/γ^* low-mass	Mis-Id	Total Bkg.	All Processes	data
Preselection	2448 ± 5	203 ± 0	752 ± 1	49749 ± 72	5077 ± 18	255 ± 3	432 ± 25	493159 ± 155	156215 ± 615	39720 ± 570	10114 ± 219	755473 ± 884	758124 ± 884	800168
$N_{\text{jet}} \geq 2$	337 ± 2	104 ± 0	520 ± 1	9685 ± 17	1579 ± 8	147 ± 3	85 ± 13	366056 ± 127	18073 ± 184	5504 ± 114	2472 ± 113	404122 ± 277	404563 ± 277	418304
$N_{\text{b-jet}} = 0$	283 ± 2	90 ± 0	151 ± 1	8260 ± 16	1177 ± 7	113 ± 2	74 ± 11	23833 ± 35	14298 ± 97	4248 ± 103	865 ± 61	53018 ± 160	53391 ± 160	63280
$m_{\tau\tau} < m_Z - 25$ GeV	238 ± 1	74 ± 0	72 ± 0	5210 ± 13	722 ± 5	69 ± 2	57 ± 9	16120 ± 29	7780 ± 74	4198 ± 102	474 ± 52	34703 ± 141	35015 ± 141	41583
$m_{jj} > 350$ GeV	44 ± 1	51 ± 0	9 ± 0	1142 ± 6	150 ± 2	15 ± 1	14 ± 3	2710 ± 12	1354 ± 32	675 ± 48	101 ± 19	6169 ± 62	6264 ± 62	7076
$\Delta y_{jj} > 3$	31 ± 1	47 ± 0	5 ± 0	661 ± 5	83 ± 2	5 ± 0	9 ± 3	1865 ± 10	1087 ± 31	538 ± 47	68 ± 16	4323 ± 60	4401 ± 60	4982
$p_{\text{T}}^{\text{total}} < 15$ GeV	16 ± 0	35 ± 0	2 ± 0	360 ± 4	35 ± 1	2 ± 0	5 ± 2	805 ± 6	397 ± 20	259 ± 39	24 ± 9	1889 ± 46	1939 ± 46	2063
CJV = true	13 ± 0	33 ± 0	2 ± 0	278 ± 4	26 ± 1	1 ± 0	2 ± 1	524 ± 5	328 ± 19	184 ± 24	13 ± 7	1357 ± 32	1403 ± 32	1550
OLV = true	10 ± 0	31 ± 0	1 ± 0	189 ± 3	18 ± 1	1 ± 0	0 ± 0	376 ± 5	221 ± 17	108 ± 18	12 ± 6	927 ± 26	968 ± 26	1107
$\Delta\phi_{ll,E_{\text{T}}^{\text{miss}}} < 2$	7 ± 0	27 ± 0	1 ± 0	80 ± 2	8 ± 0	0 ± 0	0 ± 0	129 ± 3	73 ± 9	66 ± 15	4 ± 4	361 ± 18	394 ± 18	437
$m_{ll} < 55$ GeV	6 ± 0	25 ± 0	0 ± 0	30 ± 1	4 ± 0	0 ± 0	0 ± 0	40 ± 1	24 ± 4	66 ± 15	6 ± 3	170 ± 16	201 ± 16	217
2-jet VBF SR: $\Delta\phi_{ll} < 1.8$	6 ± 0	24 ± 0	0 ± 0	29 ± 1	4 ± 0	0 ± 0	0 ± 0	39 ± 1	18 ± 3	66 ± 15	4 ± 3	160 ± 15	190 ± 15	205
2-jet VBF Z/γ^* CR	2 ± 0	1 ± 0	0 ± 0	45 ± 1	4 ± 1	0 ± 0	0 ± 0	63 ± 2	44 ± 5	27 ± 7	0 ± 2	183 ± 10	186 ± 10	187
2-jet VBF top quark CR ($e\mu/\mu e$)	9 ± 0	7 ± 0	8 ± 0	161 ± 2	22 ± 1	2 ± 0	3 ± 2	22531 ± 33	20 ± 1	1 ± 1	102 ± 24	22849 ± 41	22865 ± 41	22869

4.5.7 $N_{\text{jet}} \geq 2$ ggF-enriched category

In the Run-1 $H \to WW^* \to l\nu l\nu$ analysis [7], the $N_{\text{jet}} \geq 2$ ggF-enriched category was not defined for the same-flavour channel since it proved to be challenging to extract ggF signal events from both the Z/γ^* and top quark backgrounds, which are equally dominant in the high-N_{jet} topology. In contrast to the VBF process, there is no kinematic signature of the ggF process with high jet multiplicity that can be exploited to extract such signal events. However, a purely cut-based approach is attempted here for the first time to study the same-flavour channel using the full Run-2 dataset. This is to serve as a cross-check for the DNN approach employed by the main Run-2 same-flavour analysis.

Signal region

The SR of the $N_{\text{jet}} \geq 2$ ggF-enriched category is constructed by first applying the cuts in common with the VBF-enriched SR:

- At least 2 jets with $p_{\text{T}} > 30$ GeV and satisfying the `Tight` JVT working point.
- b-jet veto on all jets including sub-threshold jets ($p_{\text{T}} > 20$ GeV) to suppress the top quark background.
- $m_{\tau\tau} < m_Z - 25$ GeV to reject $Z/\gamma^* \to \tau\tau$ events.

The *VBF veto* is applied in order to ensure orthogonality with the VBF-enriched SR. The following cuts are linked by the logical operator 'or' instead of the implicit 'and':

- $m_{jj} < 350$ GeV,
- or $\Delta y_{jj} < 3$,
- or $p_{\text{T}}^{\text{total}} > 15$ GeV,
- or CJV = false.

And lastly, the cuts favouring the $H \to WW^* \to l\nu l\nu$ kinematic topology are applied:

- $\Delta\phi_{ll,E_{\mathrm{T}}^{\mathrm{miss}}} < 2$ to account for the high-N_{jet} kinematic topology where the lepton pair and neutrino pair tend not to be emitted back-to-back due to the recoil from the jets.

- $m_{ll} < 55$ GeV and $\Delta\phi_{ll} < 1.8$.

- $m_{ll} > 20$ GeV to make the SR orthogonal to the Z/γ^* low-mass CR.

The distributions of the different cut observables and the event yields of the diferrent processes after each successive cut is applied are given in Figure 4.24 and Table 4.11 respectively. The expected ggF signal significance of the $N_{\mathrm{jet}} \geq 2$ ggF-enriched SR is 1.26, and the pre-fit m_{T} distribution is shown in Figure 4.25e.

Z/γ^* control regions

In contrast to the $N_{\mathrm{jet}} \geq 2$ VBF-enriched, the Z/γ^* process can be split into separate low-mass and high-mass CRs due to the availibility of large sample statistics. All cuts from the SR are retained except:

- No requirement on $\Delta\phi_{ll}$.

- Z/γ^* low-mass CR: $m_{ll} < 20$ GeV.

- Z/γ^* high-mass CR: $55 < m_{ll} < 75$ GeV.

The Z/γ^* low-mass CR is able to achieve a high purity of 72%. However, the Z/γ^* high-mass CR suffers from large contamination from the top quark background and has a relatively lower purity of 46%. The pre-fit normalization factors are 0.81 ± 0.03(stat.) and 1.10 ± 0.07(stat.) for the Z/γ^* low-mass and high-mass backgrounds respectively. The pre-fit m_{T} distributions of the two Z/γ^* CRs are provided in Figures 4.25a–4.25b.

Top quark control region

Due to the inefficiencies of the b-tagging algorithm, a substantial amount of top quark events still remain in the SR even after requiring that $N_{b\text{-jet}} = 0$. This allows a top quark CR to be constructed without requiring true b-tagged jets to exist in events, which will reduce the experimental systematic uncertainties associated with b-tagging. This construction also ensures orthogonality with the top CR in the VBF-enriched category where a b-tagging requirement is made.

In addition to the b-quark and $Z/\gamma^* \to \tau\tau$ veto as well as the cut on $\Delta\phi_{ll} < 1.8$ in common with the SR, the following cuts are applied to the preselected $e\mu/\mu e$ events:

- $m_{ll} > 80$ GeV to reject mainly Z/γ^* events.
- $m_{\mathrm{T2}} < 165$ GeV to maintain orthogonality with the WW CR.
- $|m_{jj} - 85| > 15$ GeV or $\Delta y_{jj} > 1.2$ to ensure orthogonality with the VH analysis.
- CJV = false or OLV = false to ensure orthogonality with the VBF-enriched SR.

The top quark CR is able to achieve a high purity of 82%. The pre-fit normalization factor for this process in this category is 1.09 ± 0.04(stat.). The pre-fit m_{T} distribution of this CR is shown in Figure 4.25d.

WW control region

In addition to the b-quark and $Z/\gamma^* \to \tau\tau$ veto which are identical to the SR, the preselected $e\mu/\mu e$ events are required to satisfy the following selection criteria:

- $m_{ll} > 80$ GeV to reduce contamination from Z/γ^* events.
- $m_{\mathrm{T2}} > 165$ GeV to further suppress the top quark background. This favours WW events where the stransverse mass of the final-state leptons tends to be larger than the invariant mass of the W-boson pair due to the boost from the jets. On the other hand, the b-veto requirement means that events

usually do not contain true b-jets, but they are more likely to be misidentified light-flavour jets. As a result, m_{T2} in these events tend to be small.

- $|m_{jj} - 85| > 15$ GeV or $\Delta y_{jj} > 1.2$ to ensure orthogonality with the VH analysis.
- CJV = false or OLV = false to ensure orthogonality with the VBF-enriched SR.

The purity of the WW CR in this category is only 37% due to contamination from the top quark background, and the pre-fit normalization factor is found to be 0.62 ± 0.11(stat.). The pre-fit m_{T} distribution of this CR can be found in Figure 4.25c.

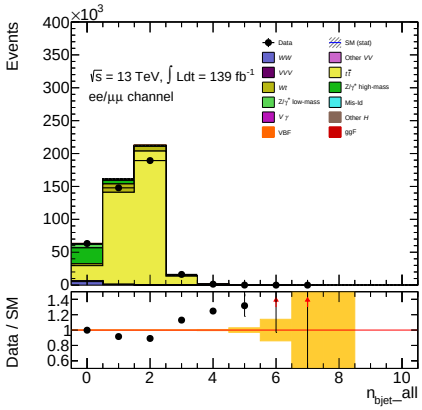

(a) $N_{b\text{-jet}}$ after cut on $N_{\text{jet}} \geq 2$

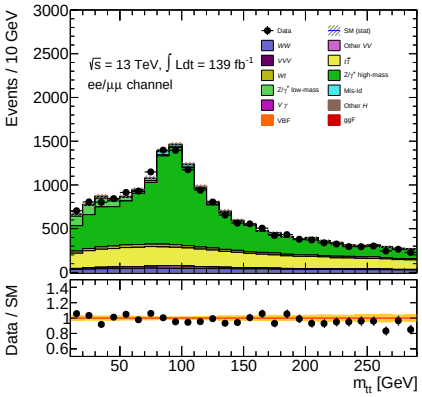

(b) $m_{\tau\tau}$ after cut on $N_{b\text{-jet}} = 0$

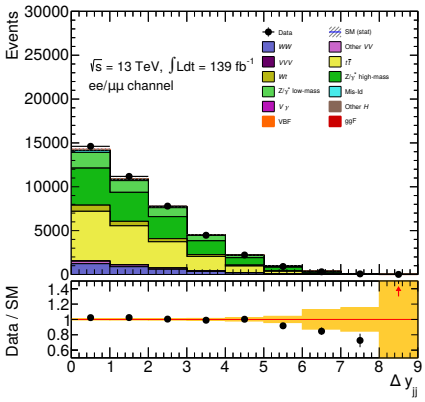

(c) Δy_{jj} after cut on $m_{\tau\tau} < m_Z - 25$ GeV

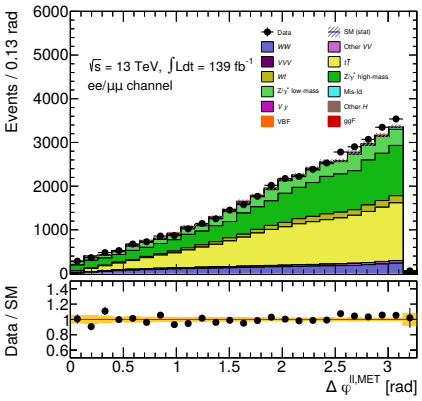

(d) $\Delta\phi_{ll,E_{\text{T}}^{\text{miss}}}$ after VBF veto

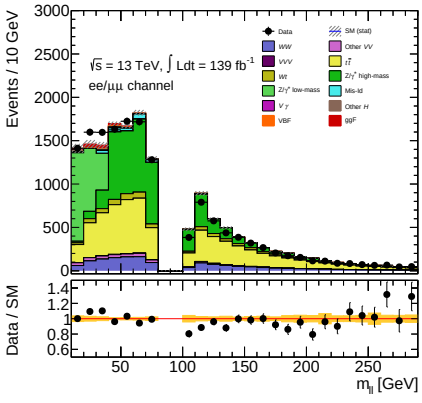

(e) m_{ll} after cut on $\Delta\phi_{ll,E_{\text{T}}^{\text{miss}}} < 2$

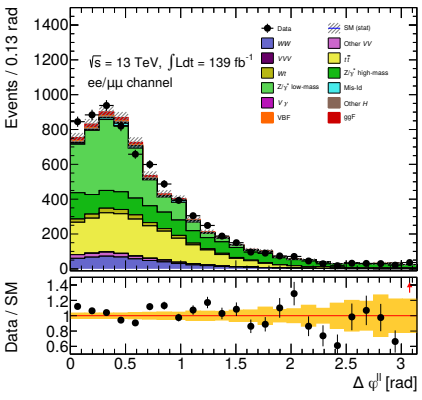

(f) $\Delta\phi_{ll}$ after cut on $m_{ll} < 55$ GeV

Figure 4.24: Distributions of the different cut observables after successive cuts are applied in the $N_{\text{jet}} \geq 2$ ggF-enriched SR. Only the distribution of Δy_{jj} which is a subset of the VBF veto is shown. The hatched bands in the upper plot and the shaded bands in the ratio plot give the statistical uncertainty on the MC samples. Normalization factors are applied to the WW, top quark, and Z/γ^* backgrounds.

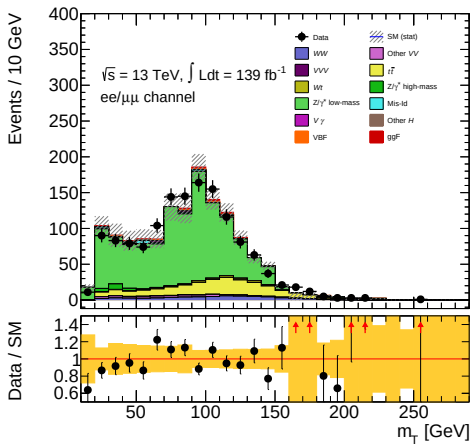

(a) Z/γ^* low-mass CR

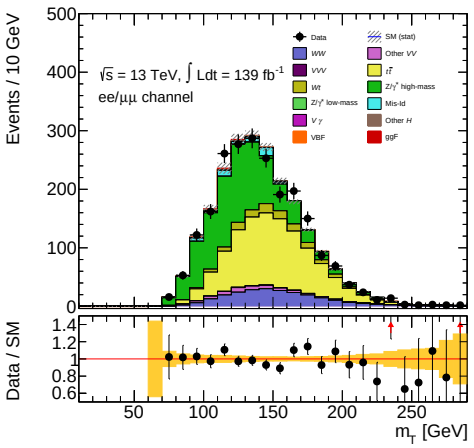

(b) Z/γ^* high-mass CR

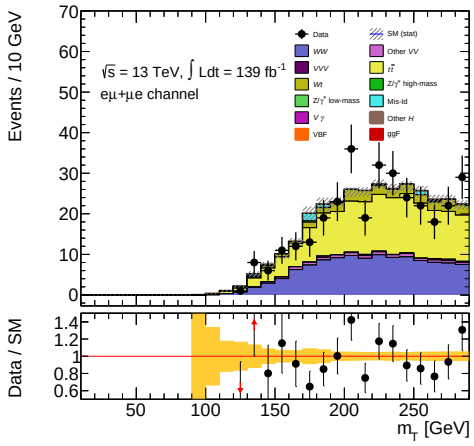

(c) WW CR

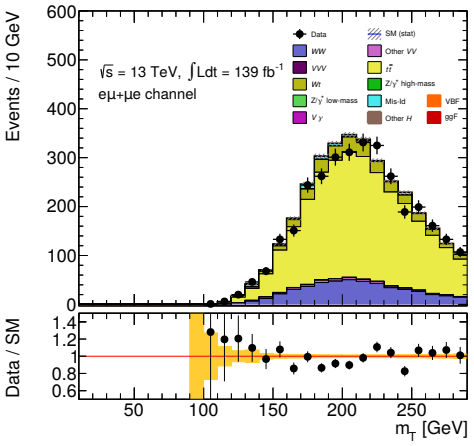

(d) Top quark CR

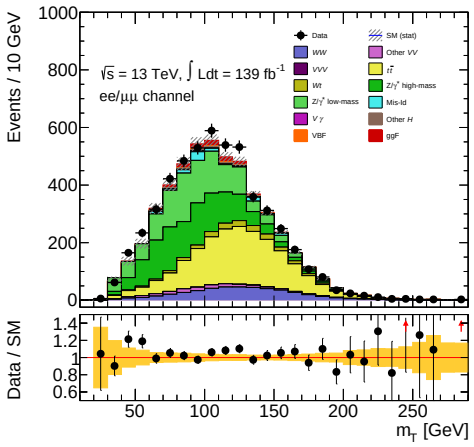

(e) $N_{\text{jet}} \geq 2$ ggF-enriched SR

Figure 4.25: Pre-fit m_{T} distributions in the different analysis regions of the $N_{\text{jet}} \geq 2$ ggF-enriched category. The hatched bands in the upper plot and the shaded bands in the ratio plot give the statistical uncertainty on the MC samples. Normalization factors are applied to the WW, top, and Z/γ^* backgrounds.

Table 4.11: Pre-fit event yields for signal and background processes after each successive cut is applied in the $N_{\text{jet}} \geq 2$ ggF-enriched SR. Normalization factors derived from the WW, top quark, and Z/γ^* CRs are applied to the corresponding event yields. The uncertainties are statistical only.

$ee/\mu\mu$, $\sqrt{s} = 13$ TeV, $\mathcal{L} = 139$ fb^{-1}	H_{ggF}	H_{VBF}	Other H	WW	Other VV	VVV	$V\gamma$	Top	Z/γ^* high-mass	Z/γ^* low-mass	Mis-Id	Total Bkg.	All Processes	data
Preselection	2448 ± 5	203 ± 0	752 ± 1	49749 ± 72	5077 ± 18	255 ± 3	432 ± 25	493159 ± 155	156215 ± 615	39720 ± 570	10114 ± 219	755473 ± 884	758124 ± 884	800168
$N_{\text{jet}} \geq 2$	337 ± 2	104 ± 0	520 ± 1	6153 ± 11	1579 ± 8	147 ± 3	85 ± 13	404405 ± 141	30432 ± 310	6837 ± 142	2472 ± 113	452630 ± 387	453071 ± 387	418304
$N_{b\text{-jet}} = 0$	283 ± 2	90 ± 0	151 ± 1	5247 ± 10	1177 ± 7	113 ± 2	74 ± 11	26330 ± 38	24075 ± 164	5277 ± 128	865 ± 61	63308 ± 221	63681 ± 221	63280
$m_{\tau\tau} < m_Z - 25$ GeV	238 ± 1	74 ± 0	72 ± 0	3315 ± 8	722 ± 5	69 ± 2	57 ± 9	17809 ± 32	13100 ± 125	5214 ± 127	474 ± 52	40833 ± 189	41144 ± 189	41583
VBF veto	225 ± 1	41 ± 0	70 ± 0	3137 ± 8	697 ± 5	68 ± 2	55 ± 9	17230 ± 31	12547 ± 121	4986 ± 123	461 ± 52	39252 ± 183	39518 ± 183	40033
$\Delta\phi_{ll,E_{\text{T}}^{\text{miss}}} < 2$	164 ± 1	33 ± 0	46 ± 0	1490 ± 5	326 ± 3	34 ± 1	31 ± 5	6601 ± 19	4665 ± 68	2179 ± 74	241 ± 33	15612 ± 108	15809 ± 108	15619
$m_{ll} < 55$ GeV	149 ± 1	30 ± 0	34 ± 0	536 ± 3	156 ± 2	12 ± 1	18 ± 4	2190 ± 11	1477 ± 26	2179 ± 74	89 ± 27	6691 ± 83	6870 ± 83	7088
$\Delta\phi_{ll} < 1.8$	146 ± 1	29 ± 0	33 ± 0	517 ± 3	149 ± 2	11 ± 1	17 ± 4	2101 ± 11	1197 ± 19	2182 ± 74	79 ± 26	6287 ± 81	6462 ± 81	6682
2-jet ggF SR: $M_{ll} > 20$ GeV	119 ± 1	24 ± 0	27 ± 0	457 ± 3	117 ± 2	10 ± 1	13 ± 3	1873 ± 10	1178 ± 18	1162 ± 54	70 ± 23	4908 ± 62	5050 ± 62	5269
2-jet ggF Z/γ^* low-mass CR	27 ± 0	5 ± 0	5 ± 0	60 ± 1	32 ± 1	2 ± 0	4 ± 3	228 ± 3	18 ± 1	1020 ± 50	10 ± 14	1379 ± 52	1411 ± 52	1413
2-jet ggF Z/γ^* high-mass CR	10 ± 0	2 ± 0	5 ± 0	241 ± 2	55 ± 1	5 ± 0	3 ± 2	1027 ± 8	824 ± 18	0	52 ± 8	2213 ± 22	2225 ± 22	2227
2-jet ggF WW CR ($e\mu/\mu e$)	0 ± 0	0 ± 0	1 ± 0	224 ± 2	18 ± 1	6 ± 1	1 ± 3	347 ± 5	2 ± 1	0 ± 0	6 ± 4	604 ± 7	604 ± 7	604
2-jet ggF top quark CR ($e\mu/\mu e$)	0 ± 0	0 ± 0	3 ± 0	563 ± 3	58 ± 1	10 ± 1	5 ± 2	3117 ± 13	3 ± 1	0 ± 0	60 ± 10	3819 ± 17	3819 ± 17	3814

5 Systematic uncertainties

Systematic uncertainties are classified into two groups according to their origins. Firstly, *experimental* systematic uncertainties are associated with object reconstruction and identification efficiency in the detector itself as well as energy resolution and scale, and trigger efficiency. And secondly, *theoretical* systematic uncertainties are those that arise from MC simulations of signal and background processes.

This chapter explores the systematic uncertainties considered in the cut-based $H \to WW^* \to l\nu l\nu$ same-flavour analysis before statistical treatment with a likelihood fit (see Chapter 6). The sources and effects of the various systematic uncertainties are the main focus of this chapter.

5.1 Impacts on event yields and distributions

Each systematic uncertainty (also referred to as *variation*) is made up of two components: the *normalization* component which affects the overall event yield of a given process; and the *shape* component which describes the effect that it has on the distribution (histogram) of the discriminating fit variable (m_{T} in this analysis). However, some systematic uncertainties may consist of only the normalization component.

The effect of a given normalization uncertainty is quantified through its *pre-fit impact*—the relative difference between the nominal and varied event yields:

$$\text{pre-fit impact} = \frac{N_{\text{variation}} - N_{\text{nominal}}}{N_{\text{nominal}}} . \tag{5.1}$$

The adjective *pre-fit* is explicitly stated because the value of this impact could be slightly different from that of the *post-fit* impact which is evaluated from the change in the uncertainty on the parameter of interest (POI) when performing unconditional and conditional fits (see Section 6.4.2).

The shape uncertainty of a systematic variation is evaluated by comparing the normalized[1] m_{T} histogram of the variation with that of the nominal sample on a bin-by-bin basis.

Generally, two variations, *up*/*down*, exist for each systematic, resulting in *high*/*low* uncertainties. If only one variation (*up*) is available, the *low* uncertainty is assigned to be the negative of the *high* uncertainty—*symmetrization* with respect to the nominal sample. In the case where more than two systematic variations are considered, an *envelope* of the variations is formed around the nominal sample and defines the magnitude of the uncertainty, which is symmetrized to give equal *high* and *low* uncertainties. However, an exception is made for theoretical systematic uncertainties on the parton distribution function (PDF) where the magnitude of the uncertainty is obtained from the standard deviation of the variations with respect to the nominal sample.

The manner in which systematic uncertainties are considered depends on whether the process in question is normalized to data or not. For the processes that are normalized directly from theory predictions (and not from data), systematic uncertainties on the absolute event yields in the signal regions (SRs) and control regions (CRs) are taken into account. In the case of the signal processes, these uncertainties also encompass potential migrations of event yields between the SRs. And for the background processes that are normalized to data using dedicated CRs, systematic uncertainties are correlated between each SR and the CR associated to it

[1]The number of entries in each bin of the histogram is divided by the total number of entries.

(see Section 4.5.2). An extrapolation factor can be defined from the CR to the SR to indicate the normalization systematic uncertainty in the SR, which is given by:

$$\Delta\alpha = \frac{N^{\mathrm{SR}}_{\mathrm{variation}}/N^{\mathrm{CR}}_{\mathrm{variation}}}{N^{\mathrm{SR}}_{\mathrm{nominal}}/N^{\mathrm{CR}}_{\mathrm{nominal}}} \ . \tag{5.2}$$

The extrapolation uncertainty $\Delta\alpha$ estimates how the event yield normalization in the CR is affected by a systematic uncertainty compared to the SR. Since $\Delta\alpha$ is a (double) ratio between predicted MC yields in the SR and CR, the systematic uncertainties affecting the two yields largely cancel out, especially if the SR and CR are kinetically similar. As a result, $\Delta\alpha$ is expected to be smaller than its absolute MC *impact* counterpart. This is the main advantage of the control region method for background estimation.

5.2 Experimental systematic uncertainties

Experimental systematic uncertainties are systematic uncertainties related to the energy (or momentum) scale and resolution of the detector, trigger efficiency, object reconstruction and identification efficiency, and isolation efficiency. Typically, these uncertainties are evaluated with MC simulations and then applied to data. They can be classified into two types based on how they are derived:

- Efficiency scale factor (SF) systematics: from comparing the nominal sample with the variation where the event weight is modified by $\pm1\sigma$.
- 4-momentum (P4) scale/resolution systematics: from comparing the nominal sample with the variation where the energy (momentum) of electrons or jets (muons) is shifted by a scale factor of $\pm1\sigma$.

The $\pm1\sigma$ variations correspond to the *up* and *down* variations. This procedure for the resolution P4 systematics is often referred to as *smearing*.

Experimental systematic uncertainties associated with leptons originate from the reconstruction and identification efficiency, isolation efficiency, the scale and resolution of measuring the energy (momentum) of electrons (muons) by the detector as well as an additional uncertainty on the efficiency of track-to-vertex association

(TTVA) for muons. These lepton systematic uncertainties are evaluated from various studies on $Z \to l^+l^-$, $J/\psi \to l^+l^-$, and $W \to l\nu$ processes [68, 71]. The uncertainties due to lepton trigger selection are also included [99, 100].

Uncertainties on the jet energy scale (JES) are derived from a combination of *in situ* measurements and simulations of Z+jets, γ+jets, and dijet events as well as test beam data [79, 80]. These also contain additional terms that account for contributions from η-intercalibration, punch-through jets[2], high-p_{T} single-particle response, jet flavour composition, hadronic calorimeter response to different jet flavours, and pile-up. The jet energy resolution (JER) uncertainties are similarly derived from resolution measurements using dijet events in combination with *in situ* measurements [79, 95]. The uncertainties on the efficiency of the b-jet identification (b-tagging) are evaluated from eigenvector decomposition, separately for jets containing b-hadrons, c-hadrons but no b-hadrons, and neither b- nor c-hadrons (light-flavour jets) [85, 90]. And lastly, the efficiency of the jet-vertex tagging (JVT) algorithm [81] is also considered.

Systematic uncertainties associated with the reconstruction of the track-based soft term (TST) $E_{\mathrm{T}}^{\mathrm{miss}}$ are derived using the comparison between data and Z+jets MC samples [91] where there is no genuine $E_{\mathrm{T}}^{\mathrm{miss}}$. There are three $E_{\mathrm{T}}^{\mathrm{miss}}$ uncertainties considered: scale, parallel resolution and perpendicular resolution. The scale uncertainty is measured by varying the soft-term energy up and down by $\pm 1\sigma$. The parallel (perpendicular) resolution uncertainty is obtained from the parallel (perpendicular) component of the soft-term momentum with respect to the direction of the hard-term momentum.

The uncertainty in the combined Run-2 integrated luminosity is 1.7%, obtained from the calibration of the luminosity scale using x-y beam-separation scans [179] and using the LUCID-2 detector [52] for the baseline luminosity measurements. The integrated luminosity uncertainty is only applied to the background processes that are not normalized to data. The uncertainty in the modelling of pile-up in

[2]Jets that exit the hadronic calorimeter and are not fully contained, biasing the energy measurement.

MC simulated samples is estimated by varying the reweighting of the pile-up in the simulation within its uncertainties.

Three sources of uncertainties related to the fake factors used in the data-driven estimation of the misidentification of leptons background are considered: statistical uncertainty on the fake factor; uncertainty associated with the electroweak subtraction of processes with two prompt leptons from the Z+jets-enriched sample used to derive the fake factor; and uncertainty in the sample composition correction factor. These uncertainties are evaluated separately for fake electrons and muons.

The experimental systematic uncertainties considered in this analysis and their sources are summarized in Table 5.1. The complete lists of the pre-fit impacts in the different categories can be found in Appendix A. The largest source of experimental systematic uncertainties is the JER in all four categories, followed by $E_{\mathrm{T}}^{\mathrm{miss}}$ and JES for the $N_{\mathrm{jet}} = 0$, $N_{\mathrm{jet}} = 1$ and $N_{\mathrm{jet}} \geq 2$ VBF-enriched, and $N_{\mathrm{jet}} \geq 2$ ggF-enriched categories respectively (see Section 6.5).

5.3 Theoretical systematic uncertainties

Theoretical systematic uncertainties are uncertainties that arise from the modelling and simulation of signal and background processes with the MC techniques. In general, the sources of theoretical systematic uncertainties in each process are:

- **QCD renormalization and factorization scale variations**: accounting for missing higher-order terms in the perturbative expansion of the hadronic cross-section.

  In a process where a pair of protons (p_1 and p_2) collide to form a final state X, the hadronic cross-section describing this process can be written as a *collinear factorization* [13] between parton distribution functions (PDFs)[3] and

[3]For parton i inside proton p, the PDF $f_{i/p}(x, Q^2)$ describes the probability that the parton carries a fraction x of the total proton momentum at the energy scale Q. PDFs are empirically determined from deep inelastic scattering at a certain energy scale and are extrapolated to other energy scales via the DGLAP equations [180–183].

Table 5.1: Summary of the experimental systematic uncertainties in the analysis.

Experimental systematic uncertainty	Description	Type
	Electrons	
EL_EFF_TRIG_TOTAL_1NPCOR_PLUS_UNCOR	trigger efficiency uncertainty	SF
EL_EFF_Reco_TOTAL_1NPCOR_PLUS_UNCOR	reconstruction efficiency uncertainty	SF
EL_EFF_Iso_TOTAL_1NPCOR_PLUS_UNCOR	isolation efficiency uncertainty	SF
EL_EFF_ID_CorrUncertainty_NP0 – 15	correlated identification efficiency uncertainty; split into 16 components	SF
EL_EFF_ID_UncorrUncertainty_NP0 – 17	uncorrelated identification efficiency uncertainty; split into 18 components	SF
EG_RESOLUTION_ALL	energy resolution uncertainty	P4
EG_SCALE_ALL	energy scale uncertainty	P4
EG_SCALE_AF2	energy scale uncertainty	P4
	Muons	
MUON_EFF_TrigStatUncertainty	trigger efficiency uncertainty	SF
MUON_EFF_TrigSystUncertainty	trigger efficiency uncertainty	SF
MUON_EFF_RECO_STAT	reconstruction and identification efficiency uncertainty for $p_{\mathrm{T}} > 15$ GeV	SF
MUON_EFF_RECO_SYS	reconstruction and identification efficiency uncertainty for $p_{\mathrm{T}} > 15$ GeV	SF
MUON_EFF_ISO_STAT	isolation efficiency uncertainty	SF
MUON_EFF_ISO_SYS	isolation efficiency uncertainty	SF
MUON_EFF_TTVA_STAT	track-to-vertex association efficiency uncertainty	SF
MUON_EFF_TTVA_SYS	track-to-vertex association efficiency uncertainty	SF
MUONS_ID	momentum resolution uncertainty from Inner Detector	P4
MUONS_MS	momentum resolution uncertainty from Muon Spectrometer	P4
MUONS_SCALE	momentum scale uncertainty	P4
MUONS_SAGITTA_RHO	charge-dependent momentum scale uncertainty	P4
MUONS_SAGITTA_RESBIAS	charge-dependent momentum scale uncertainty	P4
	Jets	
FT_EFF_Eigen_B_0 – 2	b-jet tagging efficiency uncertainties on jets containing b-hadrons (3), c-hadrons but no b-hadrons (3), and neither b- nor c-hadrons (4) respectively	SF
FT_EFF_Eigen_C_0 – 2	b-jet tagging efficiency uncertainties on jets containing b-hadrons (3), c-hadrons but no b-hadrons (3), and neither b- nor c-hadrons (4) respectively	SF
FT_EFF_Eigen_Light_0 – 3	b-jet tagging efficiency uncertainties on jets containing b-hadrons (3), c-hadrons but no b-hadrons (3), and neither b- nor c-hadrons (4) respectively	SF
FT_EFF_extrapolation	b-jet tagging efficiency uncertainty on the extrapolation to high-p_{T} jets	SF
FT_EFF_extrapolation_from_charm	b-jet tagging efficiency uncertainty on τ-jets	SF
JVT	jet-vertex-tagging efficiency uncertainty	SF
JER_DataVsMC	energy resolution uncertainty when the value from data is smaller than MC	P4
JER_EffectiveNP_1 – 12	energy resolution uncertainty; split into 12 components	P4
JES_EffectiveNP_Detector1 – 2	energy scale uncertainty from detector modelling; split into 2 components	P4
JES_EffectiveNP_Mixed1 – 3	energy scale uncertainty from heavy-flavour scale; split into 3 components	P4
JES_EffectiveNP_Modelling1 – 4	energy scale uncertainty from jet modelling; split into 4 components	P4
JES_EffectiveNP_Statistical1 – 6	energy scale uncertainty from statistical fluctuations; split into 6 components	P4
JES_EtaInter_Model	energy scale uncertainty on η-intercalibration from jet modelling	P4
JES_EtaInter_Stat	energy scale uncertainty on η-intercalibration from statistical fluctuations	P4
JES_EtaInter_NonClosure_highE	energy scale uncertainties on η-intercalibration from non-closure of jet modelling (high energy, negative η, and positive η components respectively)	P4
JES_EtaInter_NonClosure_negEta	energy scale uncertainties on η-intercalibration from non-closure of jet modelling (high energy, negative η, and positive η components respectively)	P4
JES_EtaInter_NonClosure_posEta	energy scale uncertainties on η-intercalibration from non-closure of jet modelling (high energy, negative η, and positive η components respectively)	P4
JES_Flavor_Comp	energy scale uncertainty on jet flavour composition	P4
JES_Flavor_Resp	energy scale uncertainty on jet flavour response of the hadronic calorimeter	P4
JES_BJES	energy scale uncertainty on b-jets response of the hadronic calorimeter	P4
JES_PunchThrough	energy scale uncertainty on punch-through jets (jets exiting the hadronic calorimeter)	P4
JES_HighPt	energy scale uncertainty on response of a single particle at high-p_{T}	P4
JES_PU_OffsetMu	energy scale uncertainty on pile-up (terms for number of interactions per bunch crossing, number of primary vertices, p_{T}, and ρ-topology of jets respectively)	P4
JES_PU_OffsetNPV	energy scale uncertainty on pile-up (terms for number of interactions per bunch crossing, number of primary vertices, p_{T}, and ρ-topology of jets respectively)	P4
JES_PU_PtTerm	energy scale uncertainty on pile-up (terms for number of interactions per bunch crossing, number of primary vertices, p_{T}, and ρ-topology of jets respectively)	P4
JES_PU_Rho	energy scale uncertainty on pile-up (terms for number of interactions per bunch crossing, number of primary vertices, p_{T}, and ρ-topology of jets respectively)	P4
	$E_{\mathrm{T}}^{\mathrm{miss}}$	
MET_SoftTrk_ResoPara	TST-related parallel resolution uncertainty	P4
MET_SoftTrk_ResoPerp	TST-related perpendicular resolution uncertainty	P4
MET_SoftTrk_Scale	TST-related longitudinal scale uncertainty	P4
	Event	
LUMI	uncertainty on total integrated luminosity	-
PRW_DATASF	uncertainty on data scale factor used for computing pile-up reweighting	SF
	Fake factors	
FakeFactor_el_STAT_combined_1 – 4_1 – 2	statistical uncertainties on the fake factor for fake electrons in data collecting campaigns: combined Run-2 (8), 2015 (4), 2016 (4), 2017 (4), and 2018 (4) respectively	SF
FakeFactor_el_STAT_2015_1 – 4_1	statistical uncertainties on the fake factor for fake electrons in data collecting campaigns: combined Run-2 (8), 2015 (4), 2016 (4), 2017 (4), and 2018 (4) respectively	SF
FakeFactor_el_STAT_2016_1 – 4_1	statistical uncertainties on the fake factor for fake electrons in data collecting campaigns: combined Run-2 (8), 2015 (4), 2016 (4), 2017 (4), and 2018 (4) respectively	SF
FakeFactor_el_STAT_2017_1 – 4_1	statistical uncertainties on the fake factor for fake electrons in data collecting campaigns: combined Run-2 (8), 2015 (4), 2016 (4), 2017 (4), and 2018 (4) respectively	SF
FakeFactor_el_STAT_2018_1 – 4_1	statistical uncertainties on the fake factor for fake electrons in data collecting campaigns: combined Run-2 (8), 2015 (4), 2016 (4), 2017 (4), and 2018 (4) respectively	SF
FakeFactor_mu_STAT_combined_1 – 3_1 – 2	statistical uncertainties on the fake factor for fake muons in data collecting campaigns: combined Run-2 (6), 2015 (6), 2016 (6), 2017 (6), and 2018 (6) respectively	SF
FakeFactor_mu_STAT_2015_1 – 3_1 – 2	statistical uncertainties on the fake factor for fake muons in data collecting campaigns: combined Run-2 (6), 2015 (6), 2016 (6), 2017 (6), and 2018 (6) respectively	SF
FakeFactor_mu_STAT_2016_1 – 3_1 – 2	statistical uncertainties on the fake factor for fake muons in data collecting campaigns: combined Run-2 (6), 2015 (6), 2016 (6), 2017 (6), and 2018 (6) respectively	SF
FakeFactor_mu_STAT_2017_1 – 3_1 – 2	statistical uncertainties on the fake factor for fake muons in data collecting campaigns: combined Run-2 (6), 2015 (6), 2016 (6), 2017 (6), and 2018 (6) respectively	SF
FakeFactor_mu_STAT_2018_1 – 3_1 – 2	statistical uncertainties on the fake factor for fake muons in data collecting campaigns: combined Run-2 (6), 2015 (6), 2016 (6), 2017 (6), and 2018 (6) respectively	SF
FakeFactor_el_EWSUBTR	uncertainty on electroweak subtraction for fake electrons and muons respectively	SF
FakeFactor_mu_EWSUBTR	uncertainty on electroweak subtraction for fake electrons and muons respectively	SF
FakeFactor_el_SAMPLECOMPOSITION	uncertainty on sample composition correction factor for fake electrons and muons respectively	SF
FakeFactor_mu_SAMPLECOMPOSITION	uncertainty on sample composition correction factor for fake electrons and muons respectively	SF

Table 5.2: Summary of the theoretical systematic uncertainties considered in the analysis and the methods used in their derivation. Full reco-level MC samples are used unless stated otherwise as truth-level or AFII (ATLAS fast simulation).

Process	Source	Derivation
ggF	QCD scale	Nominal vs. 19 weight variations
	PDF	Standard deviation of 30 weight variations
	α_S	2 weight variations
	Parton shower (UEPS)	Powheg+Pythia8 vs. Powheg+Herwig7
	ME generator matching/merging	Powheg+Pythia8 vs. MadGraph5_aMC@NLO+Pythia8
VBF	QCD scale	Nominal vs. 11 weight variations
	PDF	Standard deviation of 30 weight variations
	α_S	2 weight variations
	Parton shower (UEPS)	Powheg+Pythia8 vs. Powheg+Herwig7
	ME generator matching/merging	Powheg+Herwig7 vs. MadGraph5_aMC@NLO+Herwig7
Other H	Theoretical prediction	±50% normalization uncertainty
$q\bar{q} \to WW$	QCD scale	Envelope of nominal + 6 weight variations
	PDF	Standard deviation of 100 weight variations
	α_S	2 weight variations
	Parton shower recoil scheme	Nominal vs. 1 CSSKIN variation (truth-level)
	ME generator matching/merging	Nominal vs. 2 CKKW variations (truth-level)
	Resummation scale	Nominal vs. 2 QSF variations (truth-level)
EW WW	QCD scale	Envelope of nominal + 6 weight variations
	PDF	Standard deviation of 100 weight variations
	α_S	2 weight variations
	Parton shower (UEPS)	MadGraph5_aMC@NLO+Pythia8 vs. MadGraph5_aMC@NLO+Herwig7
	Electroweak correction	±15% normalization uncertainty
$gg \to WW$	Theoretical prediction	For $N_{\text{jet}} = 0$ and 1, NLO calculation. For $N_{\text{jet}} \geq 2$: $^{+100\%}_{-50\%}$ normalization uncertainty.
Z/γ^*	QCD scale	Envelope of nominal + 6 weight variations
	PDF	Standard deviation of 100 weight variations
	α_S	2 weight variations
	ME generator matching/merging+UEPS	Sherpa vs. MadGraph5_aMC@NLO+Pythia8
	Electroweak virtual correction	Envelope of nominal + 3 weight variations
$t\bar{t}$	QCD scale	Envelope of nominal + 6 weight variations
	PDF	Standard deviation of 100 weight variations
	Parton shower (UEPS)	MadGraph5_aMC@NLO+Pythia8 vs. MadGraph5_aMC@NLO+Herwig7 (AFII)
	ME generator matching/merging	Powheg+Pythia8 vs. MadGraph5_aMC@NLO+Pythia8 (AFII)
	initial-state radiation (ISR)	Nominal vs 2 Var3c A14 tune variations
	final-state radiation (FSR)	Nominal vs 2 weight variations
Wt	QCD scale	Envelope of nominal + 6 weight variations
	PDF	Standard deviation of 100 weight variations
	Parton shower (UEPS)	Powheg+Pythia8 vs. Powheg+Herwig7 (AFII)
	ME generator matching/merging	Powheg+Pythia8 vs. MadGraph5_aMC@NLO+Pythia8 (AFII)
	initial-state radiation (ISR)	Nominal vs 2 Var3c A14 tune variations
	final-state radiation (FSR)	Nominal vs 2 weight variations
	$Wt/t\bar{t}$ interference	Powheg+Pythia8 with DR scheme vs DS scheme
$V\gamma$	Theoretical prediction	$^{+100\%}_{-50\%}$ normalization uncertainty
Other VV	Theoretical prediction	±12% normalization uncertainty
VVV	Theoretical prediction	±12% normalization uncertainty

hard-scattering partonic cross-section[4] as:

$$\sigma_{p_1p_2\to X} = \sum_{i,j} \int dx_1 dx_2 \; f_{i/p_1}(x_1, \mu_F^2) f_{j/p_2}(x_2, \mu_F^2) \times \hat{\sigma}_{ij\to X}(x_1 x_2 s, \mu_R^2, \mu_F^2) \tag{5.3}$$

where s is the centre-of-mass energy of the p_1p_2 collision and the sum runs over all contributing parton types (six flavours of quarks and the gluon) in each of the colliding protons. The non-perturbative (soft) physics describing the structure of the individual protons[5] is separated from the perturbative physics of the hard-scattering interaction between the partons[6] at an energy scale called the *factorization scale* μ_F[7]. The choice of μ_F is arbitrary.

In the perturbative expansion of the partonic cross-section, the higher-order terms usually involve loop Feynman diagrams that could potentially lead to unphysical, infinite coupling constants, charges, or masses in the high energy regime. Such divergences can be removed by introducing an arbitrary *renormalization scale* μ_R, which defines the cut-off energy scale at which the divergent diagrams are absorbed into measurable, renormalized quantities [13].

Nominally, both μ_R and μ_F are set to the scale of the momentum transfer Q. The estimation for the QCD effects is done by varying the renormalization and factorization scales in the pair $\{\mu_R, \mu_F\}$ by a factor of 0.5 or 2. It is also required that the ratio between the scales is $0.5 \leq \mu_R/\mu_F \leq 2$. Thus, there are 7 $\{\mu_R, \mu_F\}$ pairs in total including the nominal pair. The QCD scale uncertainty is obtained by taking a 7-point envelope, i.e. the variation among the 6 $\{\mu_R, \mu_F\}$ pairs that produces the maximum difference from the nominal

[4]The hard-scattering partonic cross-section $\hat{\sigma}_{ij\to X}$ describes the actual interaction that occurs at the parton level between individual partons i and j to produce a final state X.

[5]At short distances (high energy scales), the strong coupling constant α_S is small. Therefore, the partons inside the proton behave as if they are free particles.

[6]At long distances (low energy scales), α_S is large and must be taken into account. Therefore, perturbative QCD must be considered in order to properly describe the partonic cross-section.

[7]When including all orders in perturbative QCD, the hadronic cross-section is inherently independent of μ_F. However, at a fixed, finite order in perturbation theory, the calculated cross-section depends on μ_F, and the dependency is usually more significant in the lower-order terms [184].

sample is taken as an uncertainty:

$$\sigma^{\text{QCD scale}} = \max_{\text{var}}\left\{\frac{|N_{\text{var}} - N_{\text{nom}}|}{N_{\text{nom}}}\right\} \tag{5.4}$$

where N_{var} and N_{nom} are the event yields produced from each of the individual $\{\mu_R, \mu_F\}$ variations and the nominal sample respectively in a given analysis region.

- **Choice of parton distribution functions (PDFs)**: accounting for experimental uncertainties entering the datasets used to determine the PDF sets, uncertainties from the choice of the functional form used in the PDF fits, and other theoretical uncertainties such as flavour scheme and nuclear effects.

  For the processes that use NNPDF3.0 [104] in the generation of MC samples, a total of 100 PDF sets are used. The PDF uncertainty is given by the standard deviation around the nominal sample:

$$\sigma^{\text{PDF}} = \sqrt{\frac{1}{99}\sum_{i=1}^{100}(N_i - N_0)^2} \tag{5.5}$$

  where N_i and N_0 correspond to the event yields produced from PDF set i and the nominal sample respectively in a given analysis region.

  However, the ggF and VBF Higgs signal processes use PDF4LHC15 [111], where 30 Hessian PDF eigenvectors are treated as independent uncertainties in the measurement [185]. The PDF uncertainty is instead given by:

$$\sigma^{\text{PDF}} = \sqrt{\sum_{j=1}^{30}(N_j - N_0)^2} \tag{5.6}$$

  where N_j and N_0 correspond to the event yields produced from PDF variation eigenvector j and the nominal sample respectively in a given analysis region.

- **Strong coupling constant (α_S)**: from experimental uncertainties in the determination of α_S and the truncation at a fixed order in perturbation theory of the renormalization group equation (RGE) [186] involved in the derivation of the PDF set used in MC sample generation.

Both NNPDF3.0 and PDF4LHC15 are produced using the same nominal value of α_S measured at the scale of the Z boson mass. However, the associated errors on α_S differ due to different theoretical calculations within them. For NNPDF3.0, this is given by $\alpha_S = 0.1180 \pm 0.0010$ [104]. And for PDF4LHC15, the value is $\alpha_S = 0.1180 \pm 0.0015$ [111]. The event yields corresponding to the *up* ($\alpha_S^{up} = \alpha_S + \delta\alpha_S$) and *down* ($\alpha_S^{down} = \alpha_S - \delta\alpha_S$) variations are symmetrized from their mid-point, and the α_S uncertainty associated with the PDF set is given by:

$$\sigma^{\alpha_S} = \frac{|N_{\alpha_S^{up}} - N_{\alpha_S^{down}}|}{2}. \tag{5.7}$$

- **Underlying event and parton shower (UEPS) model**: related to algorithmic or parametric differences in the modelling of the parton shower and hadronization.

  Partons produced from an interaction with a high-momentum transfer can subsequently radiate daughter partons that are either soft or collinear with the outgoing partons. These partons continue to radiate further daughter partons until their energy scale reaches the non-perturbative QCD regime (hadronization). This phenomenon is encapsulated in MC event generation by various *parton shower* algorithms which employ slightly different techniques [187].

  Soft hadronic activities caused by interactions between other partons that do not participate in the hard-scattering interaction are called *multiple-parton interactions*. Since these secondary partons are not colour-neutral, their interactions with the hard-scattering partons can be important for modelling the QCD colour flow and reconnection [187]. Multiple-parton interactions together with the fragmentation of beam remnants collectively constitute the *underlying event*.

  The MC generators used for these purposes include Pythia, Sherpa, and Herwig. The UEPS uncertainty for a particular process in a given analysis region is obtained by directly comparing the event yield (see Equation 5.1) of

the nominal MC sample with that of an alternate sample where the same hard-scatter matrix element model is used but interfaced with a different UEPS model. For instance, if PYTHIA is used in the UEPS modelling, HERWIG is used as an alternative model. However, for processes generated with SHERPA, both the ME and UEPS are modelled within SHERPA itself. In this case, a different parton shower recoil scheme (CSSKIN scheme: default [131], alternative [132]) is used for comparison.

- **Matching/merging of hard-scatter matrix element (ME) generator to UEPS model**: associated with the elimination of double counting from interfacing NLO or NNLO matrix element calculations to the UEPS model or from the combination of final states with different jet multiplicities respectively.

  Contrary to the UEPS uncertainty, here the UEPS model is fixed and the ME component is varied. If POWHEG is used as the ME generator, MADGRAPH5_aMC@NLO is used as an alternative generator for comparison. The associated uncertainty can be calculated from the definition given in Equation 5.1. However, in SHERPA, the overlap between jets from the ME and UEPS is handled by the CKKW algorithm [131, 134–136]. The nominal matching overlap scale is 20 GeV. The *down* and *up* variations for the CKKW scale are set to 15 and 30 GeV respectively. In addition, there is also another uncertainty associated with the resummation of soft gluon emissions [188] which is derived by varying the QSF parameter by a factor of 0.5 (*down*) and 2 (*up*) with respect to the nominal sample.

The QCD scale, PDF, and α_S uncertainties are always positive by definition, whereas the UEPS and ME uncertainties are directly calculated by subtracting the event yield of the nominal sample from that of the variation as given by Equation 5.1. As a result, the UEPS and ME uncertainties can be either positive or negative, and this becomes important later when dealing with *correlation* between systematic uncertainties in the fit. For example, a systematic uncertainty associated with the WW background in the SR is correlated with the same systematic uncertainty

in the WW CR. If both are positive, this leads to cancellation, and the impact of this uncertainty on the SR is reduced.

Additional process-specific theoretical uncertainties are also considered and are discussed individually in the following sections. A summary of the theoretical systematic uncertainties considered for the different processes as well as their methods of derivation is provided in Table 5.2.

5.3.1 Higgs signal processes

Variations in the QCD scales $\{\mu_R, \mu_F\}$ in each of the N_{jet} categories are employed to estimate the impact of missing higher-order corrections in fixed-order cross-section predictions. However, the QCD uncertainty may be underestimated due to cancellations between the perturbative corrections in the total cross-section and the exclusive N_{jet} categories. To mitigate this, the Stewart-Tackmann (ST) method [189] is utilized, resulting in an envelope of 20 weight variations for the ggF production and an envelope of 12 weight variations for the VBF production.

The uncertainty due to the ME matching and merging is not included in the $N_{\text{jet}} = 0$ and $N_{\text{jet}} = 1$ categories since the nominal POWHEG generates $N_{\text{jet}} = 0$ and 1 events without ME merging at the NLO level of precision.

A summary of the pre-fit theoretical systematic uncertainties on the ggF and VBF signal processes in the different analysis regions is given in Table 5.3. For other Higgs boson production processes which are treated as background processes (VH and $t\bar{t}H$), a flat, conservative $\pm 50\%$ normalization uncertainty is applied to all N_{jet} categories.

Another theoretical uncertainty pertaining to the Higgs boson production that needs to be considered is the uncertainty on the $H \to WW^*$ branching ratio, which is given by a flat normalization uncertainty of 2.16% [12].

5.3.2 WW background

The $q\bar{q} \to WW$ MC samples used in this analysis are generated with SHERPA, and the appropriate theoretical systematic uncertainties must be considered as described

Table 5.3: Pre-fit theoretical systematic normalization uncertainties (impacts) on the ggF and VBF signal processes in the SRs of the different N_{jet} categories arising from perturbative QCD scale, PDF, α_S, parton shower (UEPS), and matching/merging of matrix element (ME).

Analysis region	Pre-fit impact [%]									
	ggF					VBF				
	QCD	PDF	α_S	UEPS	ME	QCD	PDF	α_S	UEPS	ME
$N_{\text{jet}} = 0$ SR	3.9	2.7	1.0	5.0	-	1.3	1.7	0.9	11.4	19.6
$N_{\text{jet}} = 1$ SR	5.1	2.0	3.0	4.6	-	0.8	1.7	0.6	0.9	3.8
$N_{\text{jet}} \geq 2$ ggF-enriched SR	8.4	2.1	3.3	6.7	4.0	0.9	1.7	0.4	6.2	5.8
$N_{\text{jet}} \geq 2$ VBF-enriched SR	8.8	1.7	3.5	8.3	1.0	1.0	1.7	0.4	9.8	10.4

earlier in Section 5.3. However, alternative full reco-level samples are not available for the evaluation of the uncertainties on parton shower recoil scheme (CSSKIN), matching/merging of matrix element generator (CKKW), and resummation scale (QSF), whereby truth-level samples are used instead. For the CKKW and QSF uncertainties, only the *up* or *down* variation that produces the larger impact is selected and symmetrized. For the $N_{\text{jet}} = 0 + 1$ category as well as the $N_{\text{jet}} \geq 2$ VBF-enriched category, CKKW_{up} and QSF_{down} are used. In the case of $N_{\text{jet}} \geq 2$ ggF-enriched category, CKKW_{up} and QSF_{up} are used.

For the EW WW process, an alternative full reco-level sample is available to study the UEPS uncertainty. For ME generation, MadGraph5_aMC@NLO is used, and the EW VVV process is also included within the simulation. No ME matching/merging uncertainty is considered for this subleading process since there are no other available samples of combined EW WW and VVV production. Another uncertainty to consider is the EW scale correction uncertainty which originates from the NLO EW correction. Several studies have attempted to estimate this uncertainty in the same-sign-WW [190], WZ [191], and ZZ VBS processes [192]. A flat, conservative normalization uncertainty of $\pm 15\%$ is assigned to all N_{jet} categories.

A summary of the pre-fit theoretical systematic uncertainties on the non-resonant WW background process in the different analysis regions is given in Table 5.4.

Table 5.4: Pre-fit theoretical systematic normalization uncertainties (impacts) on the $q\bar{q} \to WW$ and EW WW background processes in the SRs and WW CRs of the different N_{jet} categories arising from perturbative QCD scale, PDF, α_{S}, parton shower recoil scheme (CSSKIN or UEPS), matching/merging of matrix element (CKKW), resummation scale (QSF), and EW scale correction (for EW WW only).

Analysis region		Pre-fit impact [%]										
		$q\bar{q} \to WW$						EW WW				
		QCD	PDF	α_{S}	CSSKIN	CKKW	QSF	QCD	PDF	α_{S}	UEPS	EW
$N_{\text{jet}} = 0$	SR	2.1	2.0	1.8	1.5	2.2	1.6	1.9	1.5	0.8	4.9	15.0
	WW CR	2.1	1.9	2.0	1.4	1.1	2.2	1.0	1.3	0.8	4.6	15.0
$N_{\text{jet}} = 1$	SR	9.2	1.5	3.0	0.3	3.0	3.2	1.3	1.5	0.5	2.3	15.0
	WW CR	9.0	1.3	3.1	0.9	2.4	1.3	4.4	1.5	0.3	5.0	15.0
$N_{\text{jet}} \geq 2$ ggF-enriched	SR	29.5	0.9	4.7	0.8	3.3	4.0	3.2	1.7	0.3	4.5	15.0
	WW CR	30.2	1.0	4.8	1.1	2.7	0.9	8.1	1.7	0.0	7.2	15.0
$N_{\text{jet}} \geq 2$ VBF-enriched	SR	24.9	1.1	3.7	6.6	3.2	8.9	7.5	1.7	0.1	7.1	15.0

5.3.3 Top quark background

For both the Wt and $t\bar{t}$ processes, the evaluation of the UEPS and ME generator matching/merging uncertainties is performed with AFII (fast simulation) samples as alternative full reco-level samples are not available.

The modelling of the initial-state radiation (ISR) and final-state radiation (FSR) needs to be considered, giving rise to two additional uncertainties for each of the top background processes. The uncertainty on the ISR covers the modelling of soft gluons that affect top quark production kinematics, while the FSR covers radiation emitted by the final-state b-jets and those from W-boson decays. The uncertainty on the ISR is evaluated by varying the internal weight Var3c in the Pythia8 A14 tune *up* and *down* [157]. The *up* and *down* variations correspond to an increase and decrease of α_{S} in the ISR. Therefore, a separate uncertainty on α_{S} is omitted for the top background. The uncertainty on the FSR is accounted for by varying the factorization scale μ_R in the FSR simulation by a factor of 0.5 (*down*) or 2 (*up*).

At NLO, single top quark production with an accompanying b-quark (Wtb) involves Feynman diagrams shown in Figure 5.1. The double resonance diagrams (see Figures 5.1b and 5.1c) are exactly the same as the $t\bar{t}$ pair production at LO. In the nominal sample, this overlap between Wtb and $t\bar{t}$ processes is removed via the

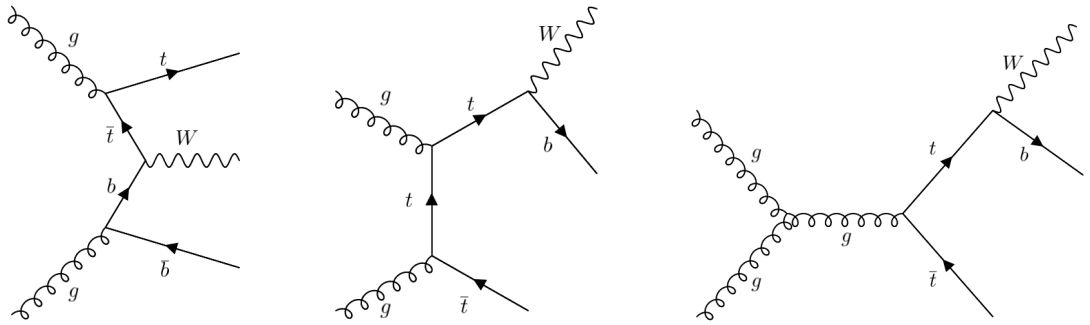

Figure 5.1: Examples of next-to-leading-order (NLO) Feynman diagrams for single top quark Wt production with an additional b-quark in the final state via: (a) a single off-shell top quark resonance; (b) a double top-top resonance; (c) a double gluon-top resonance.

Table 5.5: Pre-fit theoretical systematic normalization uncertainties (impacts) on the top ($Wt/t\bar{t}$) background process in the SRs and top CRs of the different N_{jet} categories arising from perturbative QCD scale, PDF, parton shower (UEPS), matching/merging of matrix element (ME), initial-state radiation (ISR), final-state radiation (FSR), and $Wt/t\bar{t}$ interference (for Wt only). The ISR or FSR uncertainty is derived from a pair of *up* and *down* variations, resulting in a two-sided (*high*/*low*) uncertainty where signs are given.

Analysis region		Pre-fit impact [%]												
		Wt							$t\bar{t}$					
		QCD	PDF	UEPS	ME	ISR	FSR	Int.	QCD	PDF	UEPS	ME	ISR	FSR
$N_{\text{jet}} = 0$	SR	4.3	1.9	2.5	8.4	$-1.1/+0.8$	$-3.7/+3.2$	2.3	11.8	1.5	0.9	17.7	$-0.4/+0.3$	$-5.3/+10.7$
	Top CR	4.1	1.9	4.4	3.6	$+0.1/+0.2$	$-1.3/+1.0$	5.5	11.1	1.5	1.7	16.9	$-0.2/+0.0$	$-3.1/+4.4$
$N_{\text{jet}} = 1$	SR	4.4	1.8	9.9	5.9	$-1.2/+1.1$	$-3.9/+6.9$	0.5	12.0	1.5	1.6	21.5	$-0.8/+0.6$	$-5.3/+7.4$
	Top CR	4.1	1.9	6.6	6.2	$-0.4/+0.4$	$+0.5/-1.2$	3.6	11.0	1.5	2.8	19.0	$-0.3/+0.2$	$-1.8/+2.9$
$N_{\text{jet}} \geq 2$ ggF-enriched	SR	7.0	1.8	24.1	8.8	$+0.3/-0.1$	$-1.5/+4.2$	0.1	16.0	1.6	3.0	13.7	$-0.4/+0.2$	$-3.7/+4.0$
	Top CR	6.4	1.8	18.5	1.7	$-0.4/+0.2$	$-4.7/+16.3$	4.9	15.5	1.6	5.2	20.8	$-0.1/-0.1$	$-4.8/+7.2$
$N_{\text{jet}} \geq 2$ VBF-enriched	SR	5.9	2.1	3.7	29.2	$-5.1/+4.6$	$+3.4/-16.0$	16.0	17.6	2.2	0.8	$-2.2/+2.2$	$+1.7/-1.8$	
	Top CR	5.0	1.9	1.0	0.0	$-0.6/+0.4$	$+1.3/-4.9$	3.5	12.0	1.5	0.4	27.9	$-0.6/+0.4$	$-0.8/+0.6$

diagram removal (DR) scheme [166] in which the amplitudes of the doubly-resonant NLO diagrams are set to zero, which additionally also removes the interference term between the singly- and doubly-resonant Wtb diagrams. Alternatively, there exists a different scheme called the diagram subtraction (DS) scheme [166] where a subtraction term is implemented to cancel the doubly-resonant contribution while retaining the interference term. The samples with the two different methods are compared to obtain the uncertainty on the $Wt/t\bar{t}$ interference.

A summary of the pre-fit theoretical systematic uncertainties on the $Wt/t\bar{t}$ background processes in the different analysis regions is given in Table 5.5.

5.3.4 Z/γ^* background

The MC samples for the Z/γ^* background are simulated with SHERPA like the WW process, and the systematic uncertainties should ideally be derived in the same manner per latest analysis group's recommendation. However, the Z/γ^* systematic samples that are currently available suffer from technical issues that make the event yields in the low m_{T} bins zero or negative, which in turn leads to inconsistencies in the calculation of uncertainties. Instead, the nominal SHERPA sample is compared to the alternative MADGRAPH5_AMC@NLO+PYTHIA8 which covers both the ME generator matching/merging and UEPS model.

The uncertainty on EW virtual corrections at NLO is also included for the Z/γ^* process, and examples of such Feynman diagrams are given in Figure 5.2. The EW virtual corrections can be combined with the QCD component using either the additive, multiplicative, or exponentiated approach [193]. In general, there is no clear preference for which approach to use. A 4-point envelope is formed, and the approach that produces the maximum difference from the nominal sample is taken as the uncertainty.

A summary of the pre-fit theoretical systematic uncertainties on the non-resonant Z/γ^* background process in the different analysis regions is given in Table 5.6. The Z/γ^* low-mass and high-mass processes are produced with two separate MC samples, and therefore each has its own set of systematic uncertainties.

5.3.5 Other background processes

Conservative estimates are given to account for the theory systematic uncertainties of the minor background processes with relatively low event yields.

For the $V\gamma$ process, a flat $^{+100\%}_{-50\%}$ normalization uncertainty is applied to all analysis regions to account for the potential mismodelling of the $\gamma \to e$ misidentification.

For other diboson VV and triboson VVV processes, a $\pm 12\%$ normalization uncertainty is assigned.

The loop-induced $gg \to WW$ process is not included as part of the WW CR which consists of the non-resonant $q\bar{q} \to WW$ and EW WW processes only. SHERPA

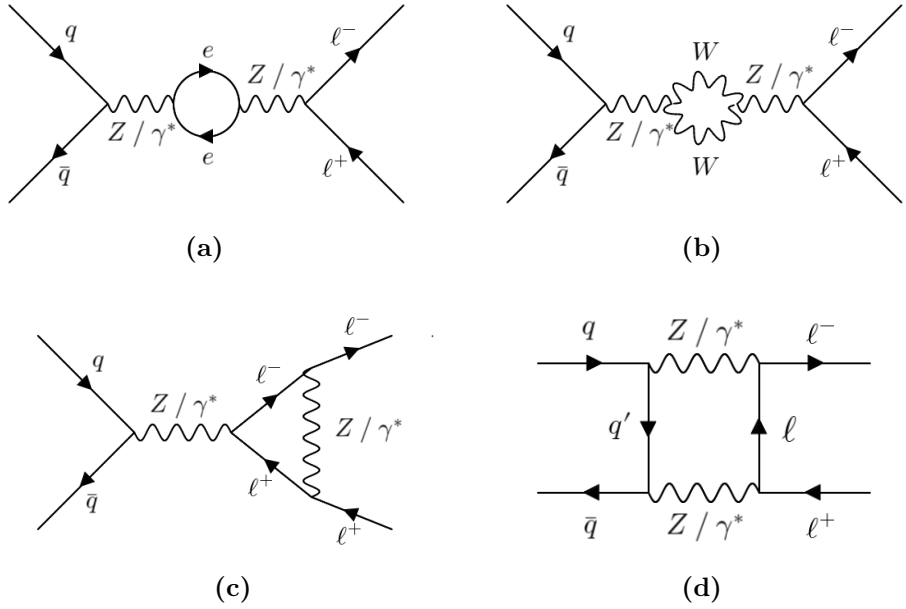

Figure 5.2: Examples of Feynman diagrams for the Z/γ^* process with electroweak (EW) virtual corrections at next-to-leading-order (NLO).

Table 5.6: Pre-fit theoretical systematic normalization uncertainties (impacts) on the Z/γ^* low-mass and high-mass background processes in the SRs and Z/γ^* CRs of the different N_{jet} categories arising from perturbative QCD scale, PDF, α_S, ME generator matching/merging and UEPS model, and EW virtual correction.

Analysis region		Pre-fit impact [%]									
		Z/γ^* low-mass					Z/γ^* high-mass				
		QCD	PDF	α_S	ME+UEPS	EW	QCD	PDF	α_S	ME+UEPS	EW
$N_{\text{jet}} = 0$	SR	21.5	0.4	4.2	29.2	2.2	16.4	0.2	5.2	0.1	0.9
	Z/γ^* low-mass CR	20.3	0.4	8.7	62.0	3.0					
	Z/γ^* high-mass CR						14.1	0.1	4.5	10.5	0.9
$N_{\text{jet}} = 1$	SR	29.3	0.6	5.9	6.8	2.1	25.1	0.2	4.5	2.0	1.2
	Z/γ^* low-mass CR	34.9	0.4	4.9	8.9	3.1					
	Z/γ^* high-mass CR						15.1	0.1	5.4	13.9	0.8
$N_{\text{jet}} \geq 2$ ggF-enriched	SR	42.1	0.4	5.6	11.8	2.6	33.0	0.2	5.3	7.9	1.8
	Z/γ^* low-mass CR	45.7	0.2	3.8	13.3	3.3					
	Z/γ^* high-mass CR						34.3	0.1	5.8	8.2	0.7
$N_{\text{jet}} \geq 2$ VBF-enriched	SR	70.7	0.7	11.5	20.1	1.9	42.0	0.7	7.0	18.4	1.9
	Z/γ^* CR	50.0	0.8	4.7	2.6	4.2	25.2	0.5	1.2	16.3	0.5

is used to calculate the ME at LO for up to one additional jet. Therefore, for the high jet multiplicity $N_{\text{jet}} \geq 2$ categories, a large, conservative $^{+100\%}_{-50\%}$ normalization uncertainty is applied. For the low jet multiplicity $N_{\text{jet}} = 0$ and $N_{\text{jet}} = 1$ categories, appropriate QCD scale uncertainties are individually assigned to the event yields via NLO calculations [194].

6

Statistical analysis and results

In order to extract the event yield of Higgs boson production observed in data, a statistical analysis of the data and MC predictions is performed using the *maximum likelihood formalism* fit to the discriminating variable m_{T} in the signal regions (SRs) and control regions (CRs) of all N_{jet} categories. How closely the Standard Model describes the observed data is measured by the signal strength parameter μ whose definition can be found in Equation 4.15.

The likelihood function is introduced in Section 6.1, and the corresponding test statistic as well as its interpretation can be found in Section 6.2. The methods for estimating the uncertainties on fit parameters are described in Section 6.3. The outline of the fit procedure is provided in Section 6.4. The expected and observed fit results are presented in Sections 6.5 and 6.6 respectively. And lastly, interpretations of the results as well as future improvements and prospects are provided in Section 6.7.

6.1 Maximum likelihood formalism

The likelihood function[1] $\mathcal{L}(\boldsymbol{\mu}, \boldsymbol{\theta}|N)$ quantifies the probability of obtaining specific sets of signal strength parameters $\boldsymbol{\mu} = \{\mu_a, \mu_b, ...\}$[2] and of *nuisance parameters* (NPs) $\boldsymbol{\theta} = \{\theta_\alpha, \theta_\beta, ...\}$ given a set of the numbers of observed events $N = \{N_A, N_B, ...\}$. In the statistical analysis, the signal strength parameters $\boldsymbol{\mu}$ are also referred to as *parameters of interest* (POIs) since it is our main objective to measure them. The NPs are required in the statistical model to reflect the impact of various systematic uncertainties. Expected (SM predicted) event yields of signal and background processes are described by vectors $\mathbf{S} = \{S_a, S_b, ...\}$[3] and $\mathbf{B} = \{B_p, B_q, ...\}$[4] respectively.

For this analysis where the analysis regions (SRs and CRs) of interest are defined in the particular manner described in Section 4.5.1, the likelihood function $\mathcal{L}$ is defined by a product of four groups of probability distribution functions:

$$\begin{aligned}\mathcal{L}(\boldsymbol{\mu}, \boldsymbol{\theta}|N) = &\underbrace{\prod_i^{n_{\text{SR}}} \prod_b^{n_{\text{bin}}} \mathcal{P}\Big(N_{ib}\Big|\boldsymbol{\mu}\cdot\mathbf{S}_{ib}(\boldsymbol{\theta}) + \boldsymbol{\beta}\cdot\mathbf{B}_{ib}(\boldsymbol{\theta})\Big)}_{\text{(i) Poisson for SRs}} \\ &\times \underbrace{\prod_l^{n_{\text{CR}}} \mathcal{P}\Big(N_l\Big|\boldsymbol{\mu}\cdot\mathbf{S}_l(\boldsymbol{\theta}) + \boldsymbol{\beta}\cdot\mathbf{B}_l(\boldsymbol{\theta})\Big)}_{\text{(ii) Poisson for CRs}} \\ &\times \underbrace{\prod_t^{n_{\text{NP}}} \mathcal{G}\Big(\vartheta_t\Big|\theta_t\Big)}_{\text{(iii) Gaussian for NPs}} \times \underbrace{\prod_b^{n_{\text{bin}}} \mathcal{P}\Big(\xi_b\Big|\zeta_b\cdot\theta_b\Big)}_{\text{(iv) Poisson for MC stats}} .\end{aligned} \tag{6.1}$$

(i) **The product of Poisson functions for the SRs**: A Poisson function $\mathcal{P}(N|\lambda)$ is the probability of observing N events given λ expected events. It is given by:

$$\mathcal{P}(N|\lambda) = \frac{e^{-\lambda}\lambda^N}{N!}. \tag{6.2}$$

For each bin b of the discriminating fit variable distribution in a given SR i, the expected value λ is the sum of event yields from the Higgs boson

[1] In the standard notation, $\mathcal{L}(\theta|x)$ is the likelihood function of parameter θ given known or observed value x.

[2] The index on signal strength parameter μ_c indicates Higgs boson production mode c which is either ggF or VBF in this analysis.

[3] The index on S_c indicates Higgs boson production mode c which is either ggF or VBF.

[4] The index on B_k runs over all of the background processes included in the analysis.

signal production modes $\mathbf{S}_{ib}(\boldsymbol{\theta})$ normalized by their corresponding signal strength parameters $\boldsymbol{\mu}$ and the background processes $\mathbf{B}_{ib}(\boldsymbol{\theta})$ normalized by their respective normalization factors $\boldsymbol{\beta}$ derived from dedicated CRs[5] (see Section 4.5.2).

(ii) **The product of Poisson functions for the CRs**: Dedicated CRs are designed to normalize their respective background processes in other analysis regions. Only total event yields are necessary for this purpose. Therefore, binned distributions of the discriminating fit variable for CRs are not required in the likelihood function. For each CR l, a Poisson function $\mathcal{P}$ is constructed in the same way as described in (i) except that there is no need to run over bins b. The normalization factors $\boldsymbol{\beta}$ are calculated and constrained simultaneously when the likelihood function is being maximized.

(iii) **The product of Gaussian functions for the NPs**: A given systematic uncertainty ϑ_t in the measurement is constrained in the likelihood function with an associated NP θ_t. This is modelled by a unit Gaussian function:

$$\mathcal{G}(\vartheta_t|\theta_t) = \frac{1}{\sqrt{2\pi}} e^{-(\theta_t-\vartheta_t)^2/2} \,. \tag{6.3}$$

(iv) **The product of Poisson functions for the MC statistical uncertainties**: This term accounts for the finite sample size of the MC samples used to model the background processes. The method proposed by Barlow-Beeston [195] is used here. It is assumed that there is only one statistical NP per bin for all background processes as a whole instead of assigning individual NPs for each of the processes. For each bin b of the discriminating fit variable distribution, the overall background yield is constrained with a Poisson function $\mathcal{P}(\xi_b|\lambda_b)$, where ξ_b is the nominal value of the background estimate and $\lambda_b = \zeta_b \cdot \theta_b$ is the Poisson expected value adjusted by MC statistical NP θ_b. For an uncertainty σ_b on an expected yield B_b in a given bin b, $\zeta_b = \left(\frac{B_b}{\sigma_b}\right)^2$.

[5] If background process k is not estimated with a dedicated CR, then $\beta_k = 1$.

The expected signal and background event yields are functions of various NPs $\boldsymbol{\theta}$. The impact of each NP θ_t on the nominal signal yield S_0 can be parameterized as:

$$S(\boldsymbol{\theta}) = S_0 \times \prod_t \nu(\theta_t) \tag{6.4}$$

where $\nu(\theta_t)$ is called the response function. A similar expression can be written for background process $B(\boldsymbol{\theta})$. The form of $\nu(\theta_t)$ depends on the nature of the systematic uncertainty with which θ_t is associated. There are three general cases:

(a) Flat (normalization) systematic uncertainties do not alter the shape of the discriminating fit variable distribution, affecting only the overall event yield. The response function is given by:

$$\nu_{\text{flat}}(\theta) = \kappa^{\theta} \tag{6.5}$$

where κ is determined by measuring event yields at $\theta = \pm 1$. The constraint on θ in the likelihood fit is applied through a unit Gaussian given by Equation 6.3. As a result, $\nu_{\text{flat}}(\theta)$ is log-normally distributed.

(b) Some systematic uncertainties can affect the shape of the discriminating fit variable distribution. The pure shape component is extracted from the flat component such that the overall expected yield is unaffected by varying the shape of the distribution. The pure shape component uses vertical linear interpolation which can be written as:

$$\nu_{\text{shape}}(\theta) = 1 + \epsilon\theta \tag{6.6}$$

where ϵ is determined by measuring event yields at $\theta = \pm 1$, and the constraint on θ is a unit Gaussian. Since the event yield cannot be negative, truncation is required such that $\nu_{\text{shape}}(\theta < \frac{-1}{\epsilon}) = 0$. If the systematic uncertainty has both the flat and shape components, $\nu_{\text{flat}}(\theta)$ and $\nu_{\text{shape}}(\theta)$ share the same θ.

(c) Purely statistical uncertainties from MC samples and data-driven estimation are modelled with the Poisson function as explained in (iv) above. In this case, the response function simply takes the form:

$$\nu_{\text{stat}}(\theta) = \theta. \tag{6.7}$$

The same NP (or equivalently systematic uncertainty) can have an impact on several different processes in both the same or other analysis regions in a *correlated* manner. However, not all NPs do so in the same way. For example, the theoretical QCD scale uncertainty of the Z/γ^* process will not affect the WW or top background of the same N_{jet} category. On the other hand, any of the experimental uncertainties will be correlated between all processes since they are applicable to all of the processes in the analysis.

To derive best estimates of the POIs and NPs, the likelihood function $\mathcal{L}(\boldsymbol{\mu}, \boldsymbol{\theta})$ is maximized with respect to all of these parameters simultaneously. However, direct optimization of the likelihood function requires a large amount of computational power. This can be mitigated by minimizing the negative log-likelihood function $-\ln \mathcal{L}(\boldsymbol{\mu}, \boldsymbol{\theta})$ instead. This process is often referred to as *fitting*.

The maximum likelihood formalism in this analysis is implemented through HistFitter [196], a Python-based, user-friendly statistical framework which executes external computational software compiled in C++ such as HistFactory [197], RooFit [198], RooStats [199], and Minuit2 [200].

6.2 Test statistic

In order to test a hypothesized value of signal strength μ, the profile likelihood ratio [201] is constructed as:

$$\lambda(\mu) = \begin{cases} \frac{\mathcal{L}(\mu, \hat{\hat{\boldsymbol{\theta}}}(\mu))}{\mathcal{L}(\hat{\mu}, \hat{\boldsymbol{\theta}})} & : \hat{\mu} \geq 0 \\ \frac{\mathcal{L}(\mu, \hat{\hat{\boldsymbol{\theta}}}(\mu))}{\mathcal{L}(0, \hat{\hat{\boldsymbol{\theta}}}(0))} & : \hat{\mu} < 0 \end{cases} \tag{6.8}$$

where the numerator in either case is the profile likelihood function given the hypothesized μ and the set of NPs $\hat{\hat{\boldsymbol{\theta}}}(\mu)$ that maximize $\mathcal{L}$ for this specific value of μ (*conditional* fit); the denominator in the first case is the globally maximized likelihood function corresponding to best estimates $\hat{\mu}$ and $\hat{\boldsymbol{\theta}}$ (*unconditional* fit); and the denominator in the second case is the likelihood function given $\mu = 0$ and the corresponding set of NPs $\hat{\hat{\boldsymbol{\theta}}}(0)$ that maximize it (*conditional* fit). The profile likelihood ratio $\lambda(\mu)$ ranges from 0 to 1 inclusive. $\lambda(\mu) \sim 1$ signifies

complete compatibility between the hypothesized μ and the best fit $\hat{\mu}$ obtained from the observed data.

The test statistic is defined using the profile likelihood ratio as:

$$q_\mu = \begin{cases} -2\ln\lambda(\mu) & : \hat{\mu} \leq \mu \\ 0 & : \hat{\mu} > \mu \end{cases} = \begin{cases} -2\ln\frac{\mathcal{L}(\mu,\hat{\hat{\boldsymbol{\theta}}}(\mu))}{\mathcal{L}(0,\hat{\hat{\boldsymbol{\theta}}}(0))} & : \hat{\mu} < 0 \\ -2\ln\frac{\mathcal{L}(\mu,\hat{\hat{\boldsymbol{\theta}}}(\mu))}{\mathcal{L}(\hat{\mu},\hat{\boldsymbol{\theta}})} & : 0 \leq \hat{\mu} \leq \mu \\ 0 & : \hat{\mu} > \mu \end{cases} \tag{6.9}$$

The value of the test statistic q_μ is zero when there is full agreement between the tested μ and the best fit $\hat{\mu}$.

The p-value p_0 is constructed from q_0 as a means to quantify how likely the *null* hypothesis, where only the known background exists ($\mu = 0$ and hence no signal) can have a statistical fluctuation at least as extreme as the observed data with q_0^{obs}. It is derived from a sampling distribution $f(q_\mu|\mu, \hat{\hat{\boldsymbol{\theta}}}(\mu))$ given $\mu = 0$:

$$p_0 = \int_{q_0^{\text{obs}}}^{\infty} f(q_0|0, \hat{\hat{\boldsymbol{\theta}}}(0))\mathrm{d}q_0 \ . \tag{6.10}$$

In the asymptotically large sample limit, the sampling distribution f can be described by a χ^2 probability distribution with one degree of freedom [202]. The statistical significance Z_0 from p_0 can be calculated from:

$$p_0 = 1 - \Phi(Z_0) \tag{6.11}$$

where $\Phi(Z)$ is the cumulative standard Gaussian distribution. In particle physics, it is a convention that the significance of 5σ must be achieved in order to claim a discovery of new physics, existence of a new particle, etc. For a one-tailed hypothesis test, the 5σ significance translates to $p_0 = 2.87 \times 10^{-7}$ [201]. The null hypothesis that $\mu = 0$ (only the known background exists) is rejected if the p-value of the test statistic falls below p_0.

Generally, for any given value μ that we wish to test as an *alternative* hypothesis, a modified frequentist method called CL_s [203] is used to compute 95% confidence intervals on the tested signal strength parameter μ. Since μ is positive by definition, the test statistic is one-sided with the constraint $0 \leq \hat{\mu} \leq \mu$ and takes the form of

the second case in Equation 6.9. The p-values p_μ and p_b are derived from sampling distributions $f(q_\mu|\mu, \hat{\hat{\boldsymbol{\theta}}}(\mu))$ and $f(q_\mu|0, \hat{\hat{\boldsymbol{\theta}}}(0))$ respectively:

$$p_\mu = \int_{q_\mu^{\text{obs}}}^{\infty} f(q_\mu|\mu, \hat{\hat{\boldsymbol{\theta}}}(\mu))\mathrm{d}q_\mu \ , \tag{6.12}$$

$$p_b = \int_{q_\mu^{\text{obs}}}^{\infty} f(q_\mu|0, \hat{\hat{\boldsymbol{\theta}}}(0))\mathrm{d}q_\mu \ . \tag{6.13}$$

The CL_s variable is then constructed as:

$$CL_s = \frac{p_\mu}{1 - p_b} \ , \tag{6.14}$$

and the 95% confidence level upper limit on μ is the solution to $CL_s = 0.05$.

6.3 Uncertainties of parameters

Within the MINUIT2 package, the uncertainties of parameters after a likelihood fit is performed can be evaluated via either the HESSE or MINOS algorithm [200].

6.3.1 HESSE

HESSE evaluates the uncertainty on each parameter θ_i by computing the covariance matrix[6] $\mathbf{V}$, which is the inverse of the Hessian matrix whose elements are second-order partial derivative of the negative log-likelihood function evaluated at its minimum:

$$(V^{-1})_{ij} = -\frac{\partial^2 \ln \mathcal{L}(\boldsymbol{\theta})}{\partial\theta_i \partial\theta_j}\bigg|_{\boldsymbol{\theta}=\hat{\boldsymbol{\theta}}} \tag{6.15}$$

where the indices i and j run over all free parameters in the model, and $\hat{\boldsymbol{\theta}}$ are the best-estimated values of the parameters that minimize the negative log-likelihood function. The minimization is performed by the MIGRAD algorithm [200].

The diagonal elements of the covariance matrix represent the squares of individual post-fit parameter uncertainties:

$$V_{ii} = (\Delta\hat{\theta}_i)^2 \tag{6.16}$$

[6]The covariance matrix is also commonly known as the error matrix.

and the off-diagonal elements contain covariances or correlations between all possible pairs of parameters.

The effects of correlations with the other parameters are spontaneously included in parameter uncertainties for the reason as follows. The Hessian matrix has diagonal elements as second-order partial derivatives with respect to one parameter at a time. However, when the Hessian matrix is inverted, the diagonal elements of the covariance matrix will also include contributions from all other elements, both diagonal and off-diagonal, of the original Hessian matrix.

Subsequently, the correlation matrix can be constructed by normalizing the covariance matrix. The elements of the correlation matrix are given by:

$$\rho_{ij} = \frac{V_{ij}}{\Delta\hat{\theta}_i \Delta\hat{\theta}_j} \tag{6.17}$$

which quantify the correlation between any given pair of parameters θ_i and θ_j in the range $[-1, +1]$. The two parameters are said to be (anti-)correlated if ρ_{ij} is positive (negative). The implication is that if one parameter becomes exactly known, i.e. its uncertainty suddenly reduces to zero, the uncertainty of the other parameter that is (anti-)correlated to it will decrease (increase).

HESSE can only produce one value of uncertainty for each parameter, and the 68% confidence interval is always symmetric as a result, i.e. $\hat{\theta}_i \pm \Delta\hat{\theta}_i$. This limitation is attributed to the fact that the log-likehood function in Equation 6.15 is assumed to be parabolic at least in the vicinity of its global minimum so that this Hessian matrix corresponds to the inverse of the covariance matrix in the definition of the generalized χ^2 distribution:

$$\chi^2 = (\boldsymbol{\theta} - \hat{\boldsymbol{\theta}})^{\mathrm{T}} \cdot \mathbf{V}^{-1} \cdot (\boldsymbol{\theta} - \hat{\boldsymbol{\theta}}) \ . \tag{6.18}$$

HESSE is a fast algorithm since it involves only numerical computation of second-order derivatives and matrix inversion. It is also the only tool that can produce coefficients to measure correlations between parameters in the fit.

6.3.2 MINOS

When the likelihood function contains a large number of free parameters and is described by products of several different probability distribution functions like Equation 6.1, the model is highly non-linear, and the uncertainties on parameters are generally asymmetric, which means that the parabolic log-likelihood approximation is no longer appropriate. Instead, MINOS uses the profile likelihood method to compute uncertainties on parameters.

The profile log-likelihood ratio [204] is given by:

$$-2\ln\lambda(\hat{\theta}_i) = -2\ln\frac{\mathcal{L}(\hat{\hat{\boldsymbol{\theta}}}(\hat{\theta}_i))}{\mathcal{L}(\hat{\boldsymbol{\theta}})} \tag{6.19}$$

where the denominator is the globally maximized likelihood function corresponding to best-estimated values $\hat{\boldsymbol{\theta}}$; and the numerator is the profile likelihood function, in which $\hat{\hat{\boldsymbol{\theta}}}(\hat{\theta}_i)$ are the values of parameters that maximize $\mathcal{L}$ given the assumed best-estimated value of $\hat{\theta}_i$.

In the asymptotic limit, the profile log-likelihood ratio is χ^2-distributed with k degrees of freedom, which is equal to the difference between the number of maximization parameters in the denominator and numerator, which is 1 in this case. In addition, the χ^2 variable with one degree of freedom[7] is also equivalent to the square of the z-score of the standard normal distribution[8]. Therefore, the 68% confidence interval[9] for a given $\hat{\theta}_i$ can be constructed by solving for $\Delta\hat{\theta}_i^+$ and $\Delta\hat{\theta}_i^-$ that make the profile log-likelihood ratio equal to 1:

$$-2\ln\lambda(\hat{\theta}_i \pm \Delta\hat{\theta}_i^{\pm}) = 1\ . \tag{6.20}$$

This equation can be solved iteratively by scanning over the values of $\hat{\theta}_i$ in small steps and running a full minimization of the profile log-likelihood function for all other parameters for each scan point. This process is slow and requires a huge amount of computational power, especially if there are a lot of free parameters and the model is highly non-linear as in this analysis. MINOS can only operate after

[7] For $k = 1$, $\chi^2 = (\frac{X-\mu}{\sigma})^2$.
[8] The z-score is given by $z = \frac{X-\mu}{\sigma}$.
[9] The 68% confidence interval of the standard normal distribution corresponds to $z = \pm 1$.

a good trial value has already been found. Because of this, HESSE is used in the backend to compute the covariance matrix for MINOS to use as a starting point.

Generally, $\Delta\hat{\theta}_i^+$ and $\Delta\hat{\theta}_i^-$ are not equal, resulting in an asymmetric confidence interval. The post-fit value of the parameter is reported as $\hat{\theta}_i{}^{+\Delta\hat{\theta}_i^+}_{-\Delta\hat{\theta}_i^-}$. Even though correlations between parameters are naturally taken into account during the minimization of the profile log-likelihood function, MINOS cannot produce explicit values of correlation coefficients like HESSE can.

6.4 Fitting framework

This section provides an overview of the framework used in the statistical treatment of the cut-based $H \to WW^* \to l\nu l\nu$ same-flavour analysis. Various inputs and parameters of the likelihood function are defined, including: signal regions (SRs), which are split further into sub-SRs for some N_{jet} categories to improve sensitivity; dedicated control regions (CRs) that are used to normalize background processes via normalization factors; and parameters of interest (POIs), which are signal strength parameters of the Higgs signal processes that we wish to measure. The *Asimov fit* is used as a tool to understand and validate the impacts of various nuisance parameters (NPs) on the POIs. In order to simulate the effect of background normalization more closely to the observed data fit, the more robust *hybrid fit* is used as an alternative to the Asimov fit in this analysis.

6.4.1 Inputs and parameters of the likelihood function

The cut-based $H \to WW^* \to l\nu l\nu$ same-flavour analysis has four event categories based on the number of jets that exist in an event. The $N_{\text{jet}} = 0$ and $N_{\text{jet}} = 1$ categories are dominated by the ggF Higgs production mode by default. For $N_{\text{jet}} \geq 2$, there are two separate categories, ggF-enriched and VBF-enriched, depending on their composition. The SRs for the different N_{jet} categories and CRs for the main background processes are constructed by defining appropriate event selection criteria (cuts) to maximize the event yields of the corresponding processes (see Section 4.5).

Table 6.1: The bins of the discriminating fit variable m_{T} distribution in the SRs of all N_{jet} categories. The lowest and highest bins are referred to as the *underflow* and *overflow* bins respectively.

	Bin of m_{T} fit distribution					
m_{T} [GeV]	$[0, 90)$	$[90, 100)$	$[100, 110)$	$[110, 120)$	$[120, 130)$	$[130, \infty)$

The distribution of transverse mass m_{T} (defined in Equation 4.4), is used as a discriminating fit variable in the likelihood function for all SRs. A fixed binning scheme is used for all N_{jet} categories with 6 bins to cover the full range of values as shown in Table 6.1. The bin boundaries are specified in this manner to ensure that the Higgs signal distribution is flat across the entire range of m_{T}, i.e. each bin should contain approximately the same number of signal events. It was found that a variable binning scheme used in the previous 36 fb^{-1} $H \to WW^* \to e\nu\mu\nu$ analysis [5] only improved the sensitivity of Higgs signal measurement slightly when compared to this uniform and slightly coarser binning in the full Run-2 analysis. The level of sensitivity was found to be within 1% of one another. Therefore, the identical fixed binning scheme is applied to all SRs of all N_{jet} categories in order to reduce complexity. Another benefit of fixed binning is that it also reduces statistical fluctuations in the estimation of systematic uncertainties, which involves the subtraction of backgrounds from the total yield, across the different categories.

The sensitivity of Higgs signal measurement can be enhanced by splitting the SR of each of the N_{jet} categories into sub-SRs based on leptonic kinematic observables m_{ll} and $p_{\mathrm{T}}^{\mathrm{sublead}}$ as summarized in Table 6.2.

For the $N_{\mathrm{jet}} = 0$ and $N_{\mathrm{jet}} = 1$ categories, the SRs are further split into 4 sub-SRs that are built from combinations of $\left\{ m_{ll} \;\middle|\; [12, 30)\ \text{GeV or } [30, 55)\ \text{GeV} \right\}$ and $\left\{ p_{\mathrm{T}}^{\mathrm{sublead}} \;\middle|\; [15, 20)\ \text{GeV or } [20, \infty)\ \text{GeV} \right\}$. The lower and upper bounds of m_{ll} are imposed by the cuts on $m_{ll} > 12$ GeV in the preselection and $m_{ll} < 55$ GeV in the SR respectively, while the lower bound of $p_{\mathrm{T}}^{\mathrm{sublead}}$ is imposed by the preselection cut on $p_{\mathrm{T}}^{\mathrm{sublead}} > 15$ GeV (see Table 4.3). This subdivision of the SR is motivated

by the kinematic signature of the Higgs signal process where a larger number of events are expected to populate the lower m_{ll} and $p_{\mathrm{T}}^{\mathrm{sublead}}$ bins.

For the $N_{\mathrm{jet}} \geq 2$ ggF-enriched category, only m_{ll} is split because it was found that splitting the SRs by $p_{\mathrm{T}}^{\mathrm{sublead}}$ did not improve the signal sensitivity. This is to be expected because the subleading lepton arising from the off-shell W^* boson is heavily boosted by the presence of the high-energy jets that recoil against the Higgs boson, leading to a high value of $p_{\mathrm{T}}^{\mathrm{sublead}}$.

For the $N_{\mathrm{jet}} \geq 2$ VBF-enriched category, there is no subdivision of the SR since the event yield of the VBF signal is already low. Splitting into sub-SRs would do more harm than good because the sub-SRs will contain even lower event yields, and statistical fluctuations will dominate these regions and exacerbate the sensitivity of the signal measurement.

The (sub-)SRs as well as the CRs used to normalize the background processes in each of the N_{jet} categories enter the likelihood function through the first two terms of Equation 6.1. The products run over all m_{T} bins of all (sub-)SRs and all event yields of all CRs in all N_{jet} categories included in the fit. The likelihood function also takes into account the statistical and systematic uncertainties associated with the different processes in the (sub-)SRs and CRs.

In each N_{jet} category, the non-resonant $q\bar{q} \to WW$ and EW WW processes share a common WW CR and normalization factor, whereas the loop-induced $gg \to WW$ is only normalized to theoretical predictions and is not included in the computation of the WW normalization factor due to its different topology. The Wt and $t\bar{t}$ processes also share a common top normalization factor. For the Z/γ^* background, two separate CRs are defined for all categories except the $N_{\mathrm{jet}} \geq 2$ VBF-enriched category to account for differences in data-MC agreement between the low and high m_{ll} regimes.

6.4.2 Asimov fit

For the most part of the analysis, observed data in the SRs are *blinded* with an exclusion window $80 < m_{\mathrm{T}} < 130$. A likelihood fit is first performed using an

Table 6.2: Summary of the (sub-)SRs, dedicated CRs for the background processes that are normalized to observed data, and signal strength POIs that enter the likelihood fit for each of the four N_{jet} catergories. The systematic uncertainties that are included in the fit as NPs are listed in Tables 5.1–5.2.

Category	(sub-)SRs	CRs	POI
$N_{\text{jet}} = 0$	$m_{ll} < 30$ GeV, $p_{\text{T}}^{\text{sublead}} < 20$ GeV $m_{ll} < 30$ GeV, $p_{\text{T}}^{\text{sublead}} \geq 20$ GeV $m_{ll} \geq 30$ GeV, $p_{\text{T}}^{\text{sublead}} < 20$ GeV $m_{ll} \geq 30$ GeV, $p_{\text{T}}^{\text{sublead}} \geq 20$ GeV	WW, Top quark Z/γ^* low-mass, high-mass	μ_{ggF}
$N_{\text{jet}} = 1$	$m_{ll} < 30$ GeV, $p_{\text{T}}^{\text{sublead}} < 20$ GeV $m_{ll} < 30$ GeV, $p_{\text{T}}^{\text{sublead}} \geq 20$ GeV $m_{ll} \geq 30$ GeV, $p_{\text{T}}^{\text{sublead}} < 20$ GeV $m_{ll} \geq 30$ GeV, $p_{\text{T}}^{\text{sublead}} \geq 20$ GeV	WW, Top quark Z/γ^* low-mass, high-mass	μ_{ggF}
$N_{\text{jet}} \geq 2$ ggF-enriched	$m_{ll} < 30$ GeV $m_{ll} \geq 30$ GeV	WW, Top quark Z/γ^* low-mass, high-mass	μ_{ggF}
$N_{\text{jet}} \geq 2$ VBF-enriched	No subdivision of SR	Top, Z/γ^*	μ_{VBF}

Asimov dataset [202], which is an idealized pseudo-dataset constructed from the sum of MC-simulated event yields of the signal and background processes. The Asimov fit is equivalent to fitting the model to itself. As a result, the post-fit values of parameters $\hat{\mu}$ and $\hat{\beta}$ are expected to be 1 by construction, and their uncertainties $\Delta\hat{\mu}$ and $\Delta\hat{\beta}$ can be estimated by MINOS.

To estimate the contribution of a given NP θ to the overall uncertainty of the POI, two fits are performed: firstly, a fully *unconditional* fit where the POI and all NPs are free to vary, which produces the globally best-estimated $\hat{\mu}$ and $\hat{\boldsymbol{\theta}}$[10] as a result; secondly, a *conditional* fit where the NP of interest is fixed to its best-estimated value $\hat{\theta}$ from the unconditional fit, and the conditionally best-estimated value of the signal strength parameter $\hat{\hat{\mu}}_{\hat{\theta}}$ is evaluated. The *breakdown* of a given NP θ is given by the quadratic difference between the uncertainties on the signal strength parameters from the unconditional fit $\Delta\hat{\mu}$ and conditional fit $\Delta\hat{\hat{\mu}}_{\hat{\theta}}$:

$$\text{breakdown}_{\theta} = \sqrt{(\Delta\hat{\mu})^2 - (\Delta\hat{\hat{\mu}}_{\hat{\theta}})^2} \ . \tag{6.21}$$

[10] In this notation, $\hat{\boldsymbol{\theta}} = \{\hat{\theta}_1, \hat{\theta}_2, ...\}$ is a set of all best-estimated NPs after a fully *unconditional* fit.

Another important validation tool to consider is the *pull* of a given NP θ, which is given by:

$$\text{pull}_\theta = \frac{\hat{\theta} - \theta_0}{\Delta\theta_0} \tag{6.22}$$

where $\hat{\theta}$ is the best-estimated value of the NP obtained after the fit; and θ_0 and $\Delta\theta_0$ are the pre-fit nominal value and uncertainty of the NP, which are 0 and 1 by construction respectively. The pull quantifies how much the post-fit value of an NP deviates from its initial value before the fit compared to the size of its own uncertainty.

When fitting to an Asimov dataset, the pulls of NPs should be found at 0 everywhere. Likewise, the post-fit uncertainties of NPs or *constraints* are expected to be 1 after the fit. An NP is said to be *over-constrained* if its post-fit uncertainty $\Delta\hat{\theta}$ is constrained to a smaller value than its pre-fit value of 1. On the other hand, if $\Delta\hat{\theta}$ is larger than 1, the NP is said to be *under-constrained*. Large over- or under-constraints indicate potential issues related to the NPs in question within the fit.

NPs are ranked by their breakdowns from highest to lowest in a so-called *ranking plot* to illustrate their importance and contribution to the precision of the measured sensitivity of the signal. Also depicted in the ranking plot are the pulls and constraints of the individual NPs. The problematic NPs that are noticeably *pulled* from 0 or heavily over- or under-constrained can be readily identified on the ranking plot.

Correlations between NPs are graphically represented in a *correlation table* produced by HESSE. Correlation coefficients are bound to the range $[-1, +1]$. The value very close ± 1 indicates an ill-posed problem with more free NPs than what can be determined by the model [200].

With the use of the Asimov fit, potential issues that could be present in the unblinded fit later can be resolved without introducing the experimenter bias into the analysis.

6.4.3 Hybrid fit

There is, however, an inherent flaw with the Asimov fit. Since the MC-simulated signal and background processes are fitted to the pseudo-dataset that is constructed from the MC samples themselves, the background normalization factors $\boldsymbol{\beta}$ are always unity by construction. Therefore, neither the event yields of the background processes in various analysis regions are scaled nor the post-fit uncertainties on $\boldsymbol{\beta}$ are meaningful. This poses a significant difference from an observed data fit, where $\boldsymbol{\beta}$ are treated as NPs and are derived from fitting the expected background yields in CRs to observed data. As a result, the Asimov fit is not representative of the full extent of the extrapolation of event yields from CRs to SRs that takes place in the observed data fit. These shortcomings of the Asimov fit can be fixed by performing a *hybrid fit* to observed data in CRs and MC samples in SRs. The procedure of the hybrid fit is as follows.

Firstly, a CR-only fit, where only CRs are included as inputs to the likelihood function, is performed. The sums of the MC-simulated signal and background event yields in the CRs are simultaneously fitted to observed data[11]. The normalization factors $\boldsymbol{\beta}$ associated with the different CRs enter the fit as floating NPs, and only the statistical uncertainties of the MC and data samples are considered. After the fit, the best-estimated values for the normalization factors $\hat{\boldsymbol{\beta}}_{\text{CR-only fit}}$ are obtained.

Secondly, a hybrid dataset is constructed by: for SRs, the background event yields are scaled by their corresponding normalization factors $\hat{\boldsymbol{\beta}}_{\text{CR-only fit}}$ before being added to the signal event yields; and for CRs, the event yields of observed data replace the total event yields of the MC samples.

And lastly, a likelihood fit is performed, for which observed data is used in the CRs and the normalized Asimov dataset is built for the SRs. Apart from the dataset templates used in the SRs and CRs, the fit inputs and parameters are identical to those for the Asimov fit. The post-fit POIs are still expected to be 1. The post-fit normalization factors should return to their initial values $\hat{\boldsymbol{\beta}}_{\text{CR-only fit}}$

[11] Unlike SRs, CRs are unblinded in m_{T} by default.

from the CR-only fit. The uncertainties on the post-fit normalization factors should reflect their true values that would be obtained from the unblinded fit.

6.4.4 Treatment of systematic uncertainties

As described in Section 5.2, there are two types experimental systematic uncertainties based on how they are derived: scale factor (SF) and 4-momentum (P4) systematics. In the case of SF systematics, only event weights are changed, and the event yields of the variations are fully correlated with the nominal yields. However, the derivation of P4 systematics involves changing the 4-momentum, which can cause events to migrate into or out of an SR or CR. The same effect is also applicable to the variation used for calculating the pile-up scale factor, which can effectively remove events from a region by changing their event weight to zero. If a particular process in a given SR or CR has very low event yields, this can create huge and unphysical variations. As such, P4 systematics are removed for processes with very small event yields relative to the total yield in a given analysis region. The complete list of P4 experimental systematics can be found in Table 5.1.

For each process, theoretical systematic uncertainties are allowed to be correlated within a given N_{jet} category in order to account for extrapolation uncertainties from the CR to the other analysis regions in the same category. However, decorrelations are made between the different N_{jet} categories because each theoretical systematic uncertainty separately contributes to the CR-SR extrapolation uncertainty in their respective category only. For instance, there are four separate WW QCD scale uncertainties in the combined fit, each per N_{jet} category; and in each category, there is only one WW QCD scale uncertainty across all SRs and CRs. However, an exception is made for the theoretical systematic uncertainties associated with the ggF and VBF signal processes, where correlations are allowed between all analysis regions across all N_{jet} categories.

In order to avoid double-counting MC statistical uncertainties as well as to simplify the convergence of the log-likelihood minimization procedure to reduce

execution time, the normalization or shape component of a given systematic uncertainty might be removed according to the following *pruning* procedure:

- Neglect the normalization uncertainty if it is smaller than 0.1%.
- Neglect the normalization uncertainty if it is larger than 80%.
- For P4 systematics, neglect the normalization uncertainty if it is smaller than 20% of the MC statistical uncertainty of the corresponding process in the analysis region.
- Symmetrize the normalization uncertainty if the *up*/*down* variations differ by more than a factor of 2, or if both vary the event yield in the same direction. The larger variation with respect to the nominal yield is fixed, and the smaller variation is symmetrized with respect to it.
- Symmetrize the shape uncertainty by fixing to the larger variation with respect to the nominal yield in each bin if there are more than one such bins with *up*/*down* variations in the same direction.
- Neglect the shape uncertainty if its p-value is less than 0.05. The p-value is a null hypothesis test statistic evaluated after removing differences in the normalization.

All systematic uncertainties except those given by flat, conservative estimates are subject to the pruning procedure. However, further manual removal of systematic uncertainties might be required to combat over- and under-constraints in the fit. More details can be found in the individual sub-sections of Section 6.5.

6.5 Expected fit results

Hybrid fits are performed separately for the $N_{\text{jet}} = 0$ and 1, $N_{\text{jet}} \geq 2$ ggF-enriched, and $N_{\text{jet}} \geq 2$ VBF-enriched categories in order to perform optimization and validation studies before a fit to observed data can be performed.

Table 6.3: Expected normalization factors for the WW, top quark, and Z/γ^* low-mass and high-mass backgrounds obtained from separate hybrid fits of the $N_{\text{jet}} = 0$ and 1, $N_{\text{jet}} \geq 2$ ggF-enriched, and $N_{\text{jet}} \geq 2$ VBF-enriched categories. The uncertainties include contributions from statistical, experimental, and theoretical systematic uncertainties. The $N_{\text{jet}} \geq 2$ VBF-enriched category has a single Z/γ^* CR and no WW CR.

Category	WW	$Wt/t\bar{t}$	Z/γ^* low-mass	Z/γ^* high-mass
$N_{\text{jet}} = 0$	$1.06^{+0.09}_{-0.08}$	$1.01^{+0.23}_{-0.17}$	$1.82^{+0.55}_{-0.42}$	$1.41^{+0.34}_{-0.25}$
$N_{\text{jet}} = 1$	$0.88^{+0.19}_{-0.18}$	$1.00^{+0.21}_{-0.16}$	$1.34^{+0.41}_{-0.29}$	$1.21^{+0.34}_{-0.24}$
$N_{\text{jet}} \geq 2$ ggF-enriched	$0.62^{+0.43}_{-0.35}$	$1.09^{+0.38}_{-0.26}$	$0.81^{+0.25}_{-0.18}$	$1.10^{+0.68}_{-0.35}$
$N_{\text{jet}} \geq 2$ VBF-enriched	–	$0.99^{+0.36}_{-0.23}$	$0.65^{+0.40}_{-0.26}$	$0.65^{+0.40}_{-0.26}$

6.5.1 $N_{\text{jet}} = 0$ and 1 category

The $N_{\text{jet}} = 0$ and $N_{\text{jet}} = 1$ categories are fitted simultaneously for validation purposes since both are ggF-enriched and share similar background compositions. A hybrid dataset is constructed using the method described in Section 6.4.3 and is used as a pseudo-observed dataset for fitting. The systematic uncertainties are treated with the pruning procedure described in Section 6.4.4. In order to prevent unphysical constraints caused by large statistical fluctuations in small MC samples, P4 experimental systematic uncertainties are removed from some processes with very low event yields in certain analysis regions (typically <1% of the total yield). A complete list of removed systematic uncertainties is provided in in Table 6.4. For the Other H, EW WW, $V\gamma$, and VVV processes, the shape components of SF systematics are also removed in all sub-SRs since they constitute tiny event yields per bin in the m_{T} distribution and meaningful shape uncertainties cannot be estimated as such. However, there are some sub-SRs where the available statistics is not sufficient to correctly estimate certain uncertainties but at the same time not low enough to justify complete removal. In these cases, the systematic uncertainties are evaluated in a more inclusive m_{ll} or/and $p_{\text{T}}^{\text{sublead}}$ SR first and are subsequently transferred to the sub-SRs. A summary of transfer of systematic uncertainties is given in Table 6.5.

Table 6.4: Summary of the removed experimental systematic uncertainties for the different processes and analysis regions in the $N_{\text{jet}} = 0$ and 1 category. Systematic uncertainties in the sub-SRs can have both shape and normalization (norm) components, while those in the CRs only have normalization components. The removal is done for the respective regions in both $N_{\text{jet}} = 0$ and $N_{\text{jet}} = 1$ sub-categories, unless stated otherwise.

Process	Region	Removed systematic
ggF VBF	all CRs	all P4 (norm)
$gg \to WW$ Other VV	Top quark CRs Z/γ^* low-mass, high-mass CRs	
Z/γ^* high-mass Z/γ^* low-mass	WW CRs Top quark CRs	
Wt	Z/γ^* low-mass CRs	
$t\bar{t}$	Z/γ^* low-mass CR (0-jet)	
Other H EW WW $V\gamma$ VVV	all CRs all sub-SRs	all P4 (norm and shape) all SF (shape)

Table 6.5: Summary of the transferred systematic uncertainties for the different processes in the $N_{\text{jet}} = 0$ and 1 category. Systematics are transferred from a more inclusive (sub-)SR to the sub-SRs with lower statistics in both $N_{\text{jet}} = 0$ and $N_{\text{jet}} = 1$ sub-categories. Both shape and normalization components are transferred.

Process	Systematic	Transfer from → to
VBF	all P4 shower matching	inclusive SR → all sub-SRs
$gg \to WW$	all P4	
$t\bar{t}$	matching	
Z/γ^* low-mass	generator MET	
Z/γ^* high-mass	generator	($m_{ll} \geq 30$ GeV, inclusive $p_{\text{T}}^{\text{sublead}}$) → (sub-SRs with $m_{ll} \geq 30$ GeV)
	all theo	inclusive SR → (sub-SRs with $m_{ll} < 30$ GeV)

The POI in the fit is the signal strength parameter for the ggF Higgs production mode with zero or one associated jet, whose value is found to be:

$$\begin{aligned}\mu_{\text{ggF01j}}^{\text{expected}} &= 1.00^{+1.14}_{-1.19} \\ &= 1.00^{+0.30}_{-0.30}(\text{stat.})\,^{+0.53}_{-0.56}(\text{exp.})\,^{+0.70}_{-0.77}(\text{theo.})\end{aligned} \tag{6.23}$$

where the stated uncertainties include all experimental and theoretical systematic uncertainties as well as statistical uncertainties. The signal strength parameter for the VBF process is fixed to a constant value of 1 and is neither considered as a POI nor an NP in the fit. The expected local signal significance Z_0 is found to be 0.85. The normalization factors associated with the WW, top quark, and Z/γ^* low-mass and high-mass CRs obtained from the hybrid fit are listed in Table 6.3. These post-fit normalization factors agree with the values obtained from the CR-only fit used to construct the hybrid dataset.

As expected for a hybrid fit, the pulls of all NPs are centred on zero, as shown in Figure 6.1. For the majority of the NPs, the constraints are close to zero. However, the NPs modelling the QCD scale and generator (ME+UEPS) uncertainties of the Z/γ^* low-mass process are heavily constrained up to 36% and 56% respectively. These over-constraints stem from the data-MC mismodelling issue of the nominal Sherpa 2.2.11 sample used for the Z/γ^* process in the low m_{ll} regime. From Figure 4.16, it can be seen that there are very large discrepancies between observed data and expected yields for $N_{\text{jet}} = 0$ and $N_{\text{jet}} = 1$ even at the preselection stage where such large data-MC discrepancies should not be observed. What the alternative scale or generator variation does is change the distribution of the discriminating fit variable as well as the overall event yield. Since the nominal sample is very different from the dataset it tries to model, it is likely that the variation might provide a better fit to the data than the nominal sample can. The consequence is that the data will prefer the variation to the nominal sample, or in other words the data is constrained by this NP. Another group of NPs with noticably large constraints is the jet energy resolution (JER), which is caused by their strong correlations with the Z/γ^* low-mass scale and generator systematics, as shown in the lower left corner of Figure 6.2. From the correlation matrix, it can be seen that the NPs

describing theoretical systematic uncertainties are generally strongly correlated with their respective normalization factor for a given process.

The top 50 NPs that contribute to the overall uncertainty on the POI the most are ranked in Figure 6.1. The NPs are grouped based on their common sources, and their collective contributions to the POI uncertainty are listed in Table 6.6. The theoretical systematic uncertainties are the most dominant group with 73% overall contribution; most of which can be attributed to the Z/γ^* process where the contribution is about 71% alone. The experimental systematic uncertainties account for 54% of the POI uncertainty, and the largest contributor of the group is the JER (44%) due to its strong correlation with the Z/γ^* low-mass scale and generator systematics.

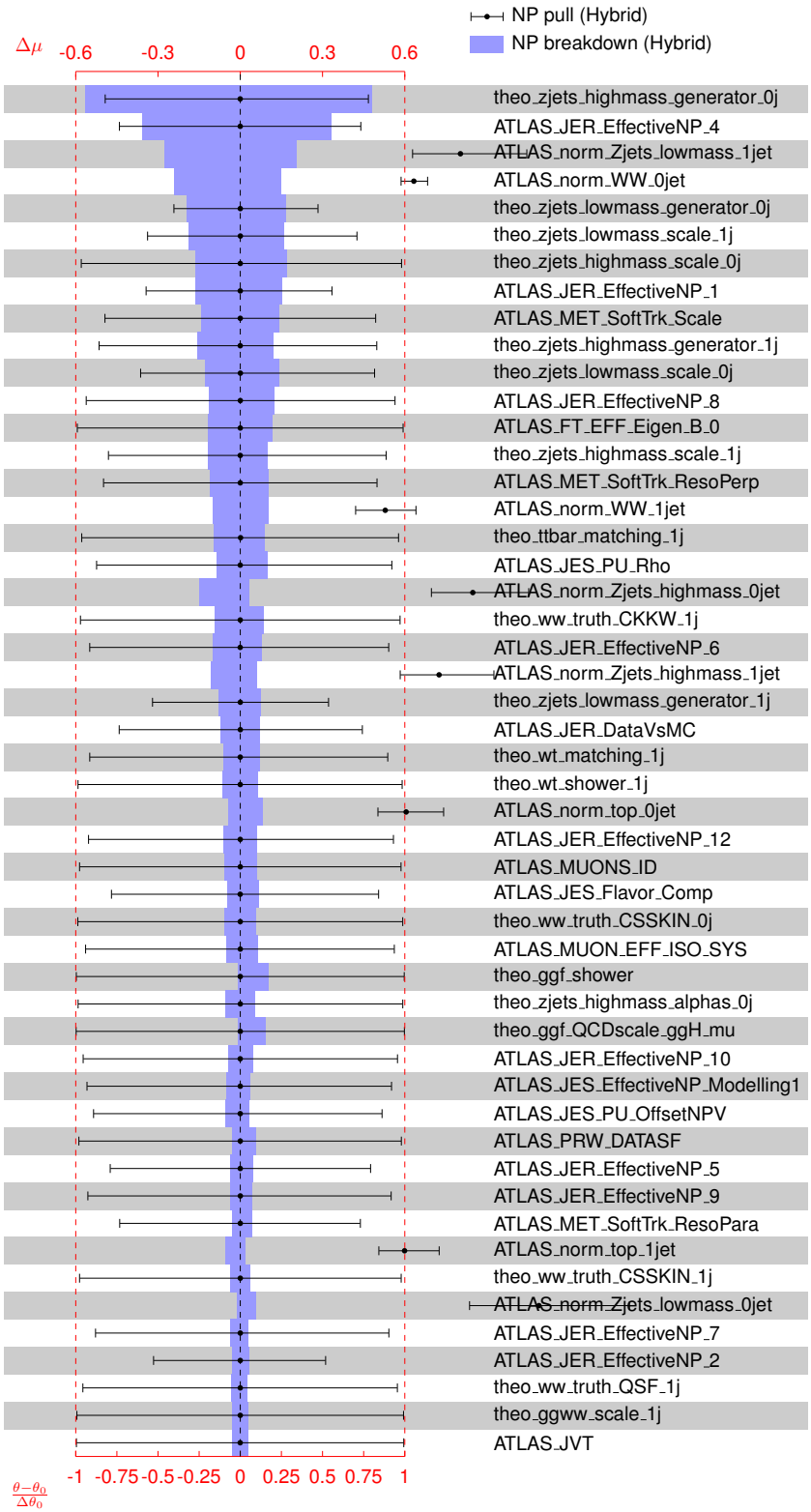

Figure 6.1: Ranking plot of the nuisance parameters (NPs) in the hybrid fit of the $N_{\text{jet}} = 0$ and 1 category. Their pulls and post-fit uncertainties are indicated by the black dots and lines respectively. The blue bands represent their contribution to the total uncertainty on μ (breakdowns). Only the top 50 NPs with largest breakdowns are shown.

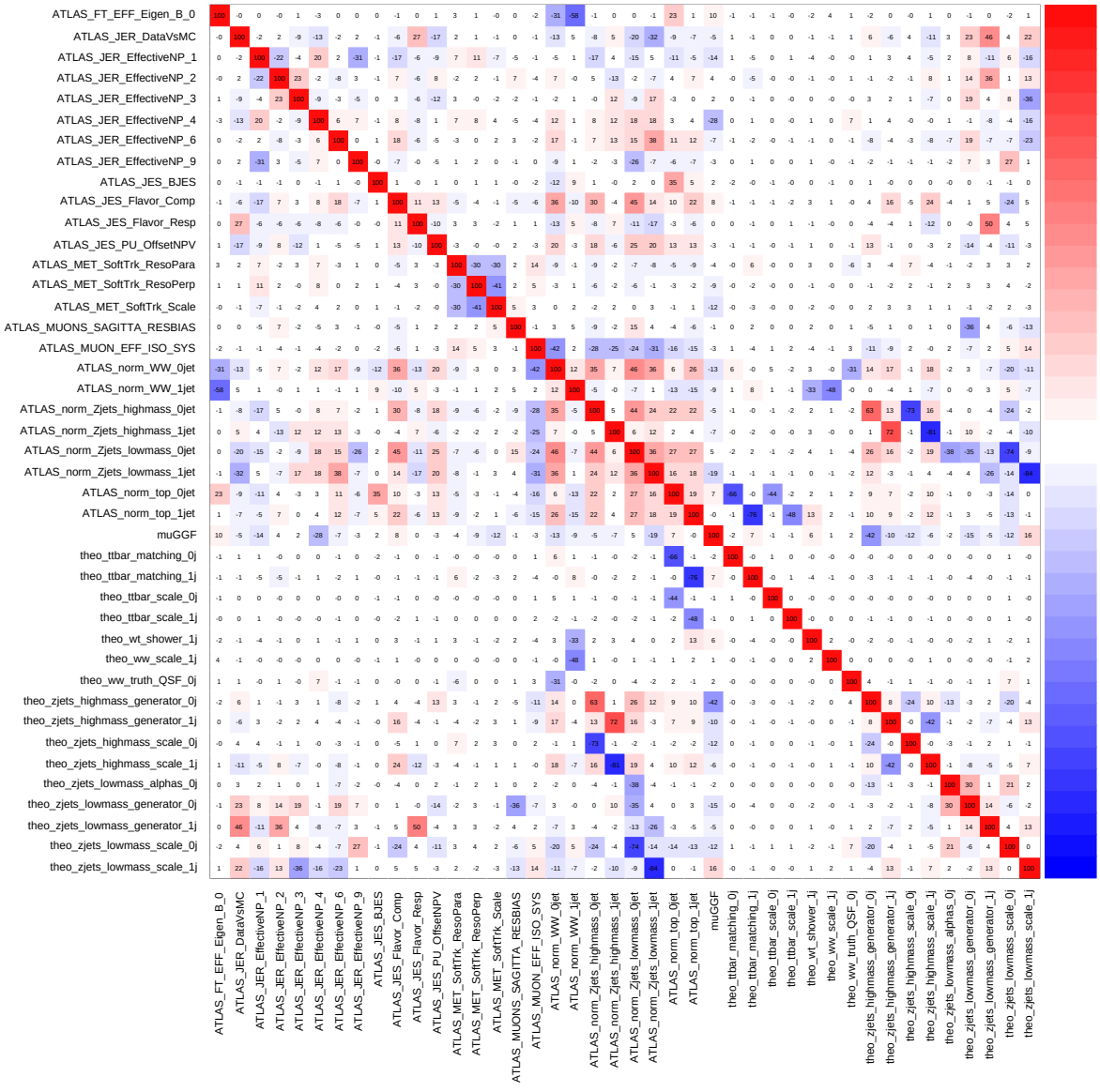

Figure 6.2: Correlation matrix of the nuisance parameters (NPs) in the hybrid fit of the $N_{\text{jet}} = 0$ and 1 category. Blue shades denote anti-correlations, while red shades denote correlations. Only NPs that have correlations or anti-correlations larger than 30% are shown.

Table 6.6: Summary of the contributions that the different sources of uncertainties have on expected μ_{ggF}, obtained from the hybrid fit of the $N_{\text{jet}} = 0$ and 1 category. The sum in quadrature of the individual components differs from the total uncertainty due to correlations between the components.

Source	$\Delta\mu_{\text{ggF}}[\%]$
Total	116.2
Data statistics	30.0
Total systematics	115.2
Theoretical systematics	73.4
ggF	8.8
VBF	0.8
Other H	0.9
Z/γ^*	70.8
Z/γ^* high-mass	60.2
Z/γ^* low-mass	31.2
Top	15.1
Wt	10.1
$t\bar{t}$	10.3
WW	12.5
$q\bar{q} \to WW$	12.0
$gg \to WW$	3.5
EW WW	0.7
$V\gamma$	2.4
Other VV	0.8
VVV	0.7
$H \to WW$ branching fractions	2.7
Experimental systematics	54.2
Flavour Tagging	12.0
Jet energy scale	15.0
Jet energy resolution	43.7
$E_{\text{T}}^{\text{miss}}$	30.2
Muons	8.7
Electrons	3.5
Fake factors	4.3
Pile-up	4.3
Luminosity	2.1
Background normalization	33.3
Z/γ^* normalization	28.1
Top normalization	8.2
WW normalization	20.9
MC statistics	97.9

6.5.2 $N_{\text{jet}} \geq 2$ ggF-enriched category

The overall strategy for the fitting of the $N_{\text{jet}} \geq 2$ ggF-enriched category follows that for the $N_{\text{jet}} = 0$ and 1 category, except that it is being treated separately for validation purposes from the other two ggF-enriched regions due to the difference in background composition as well as in how the SR and CRs are constructed. Systematic uncertainties associated with particular processes and analysis regions are removed or transferred according to Tables 6.7 and 6.8 respectively.

The signal strength parameter for the VBF process is fixed to a constant value of 1, and the value of the POI obtained from the hybrid fit is found to be:

$$\begin{aligned} \mu_{\text{ggF2j}}^{\text{expected}} &= 1.03^{+2.32}_{-2.71} \\ &= 1.03^{+1.11}_{-1.11}(\text{stat.})\,^{+1.21}_{-1.84}(\text{exp.})\,^{+1.23}_{-1.70}(\text{theo.})\ . \end{aligned} \tag{6.24}$$

The marginal deviation from 1 is likely a result of an inconsistency between the Asimov-like data in the SR and the sum of the templates present in the fit. For the background templates passed to the fit, bin entries are set to 10^{-12} if they are negative due to an excess of events with negative weights. The Asimov-like data used in the hybrid fit are the sum of the initial templates. The huge uncertainty manifests itself in an expected local significance Z_0 of the ggF signal of merely 0.41. The normalization factors associated with the WW, top quark, and Z/γ^* low-mass and high-mass CRs obtained from the hybrid fit are listed in Table 6.3, and they are all found to be consistent with the pre-fit values obtained from a CR-only fit.

In the ranking plot shown in Figure 6.3, it can be seen that only two NPs suffer from large over-constraints, namely the Z/γ^* low-mass scale (50%) and Z/γ^* high-mass generator (31%) uncertainties. The causes of these over-constraints should be similar to those described previously in Section 6.5.1. From Figure 4.16c, it can be seen that data-MC disagreement still exists for $N_{\text{jet}} \geq 2$ despite to a much smaller extent than for the lower jet bins. Even though such discrepancies between data and the nominal sample are small in the first place, data will always choose an alternative that can provide a better agreement if possible, leading to data over-constraining itself to one of the variations.

Table 6.7: Summary of the removed experimental systematic uncertainties for the different processes and analysis regions in the $N_{\text{jet}} \geq 2$ ggF-enriched category. Systematic uncertainties in the sub-SRs can have both shape and normalization (norm) components, while those in the CRs only have normalization components.

Process	Region	Removed systematic
ggF VBF	all CRs	all P4 (norm)
$gg \to WW$ Other VV	Top quark CR Z/γ^* low-mass, high-mass CRs	
Z/γ^* high-mass Z/γ^* low-mass	WW CR Top quark CR	
Other H EW WW $V\gamma$ VVV	all CRs all sub-SRs	all P4 (norm and shape) all SF (shape)
Z/γ^* high-mass	$m_{ll} < 30$ GeV sub-SR	

Table 6.8: Summary of the transferred systematic uncertainties for the different processes in the $N_{\text{jet}} \geq 2$ ggF-enriched category. Systematics are transferred from the inclusive SR to the sub-SRs with lower statistics. Both shape and normalization components are transferred.

Process	Systematic	Transfer from → to
$gg \to WW$	all P4	inclusive SR → all sub-SRs
Z/γ^* low-mass	scale	
Z/γ^* high-mass	generator	
	all theo	inclusive SR → ($m_{ll} < 30$ GeV sub-SR)

The contributions to the uncertainty on the POI by the different groups of uncertainties are summarized in Table 6.9. The largest contributor to the overall theoretical systematic uncertainty is the Z/γ^* low-mass process, which can be mainly attributed to the QCD scale uncertainty, where there is a mismodelling issue with the Sherpa 2.2.11 sample as mentioned earlier. In addition, positive correlations are observed between the Z/γ^* normalization factors and the problematic Z/γ^* low-mass scale uncertainty, as shown in Figure 6.4. Since the $N_{\text{jet}} \geq 2$ ggF-enriched category suffers from large contamination from the Z/γ^* background, the contribution of

this NP to the overall uncertainty is amplified further by these correlations. A similar effect is observed for the JER group, resulting in large contribution to the overall experimental systematic uncertainty. The $N_{\text{jet}} \geq 2$ ggF-enriched category also suffers from a very large statistical uncertainty, which is mainly due to the relatively small sample size of the WW CR.

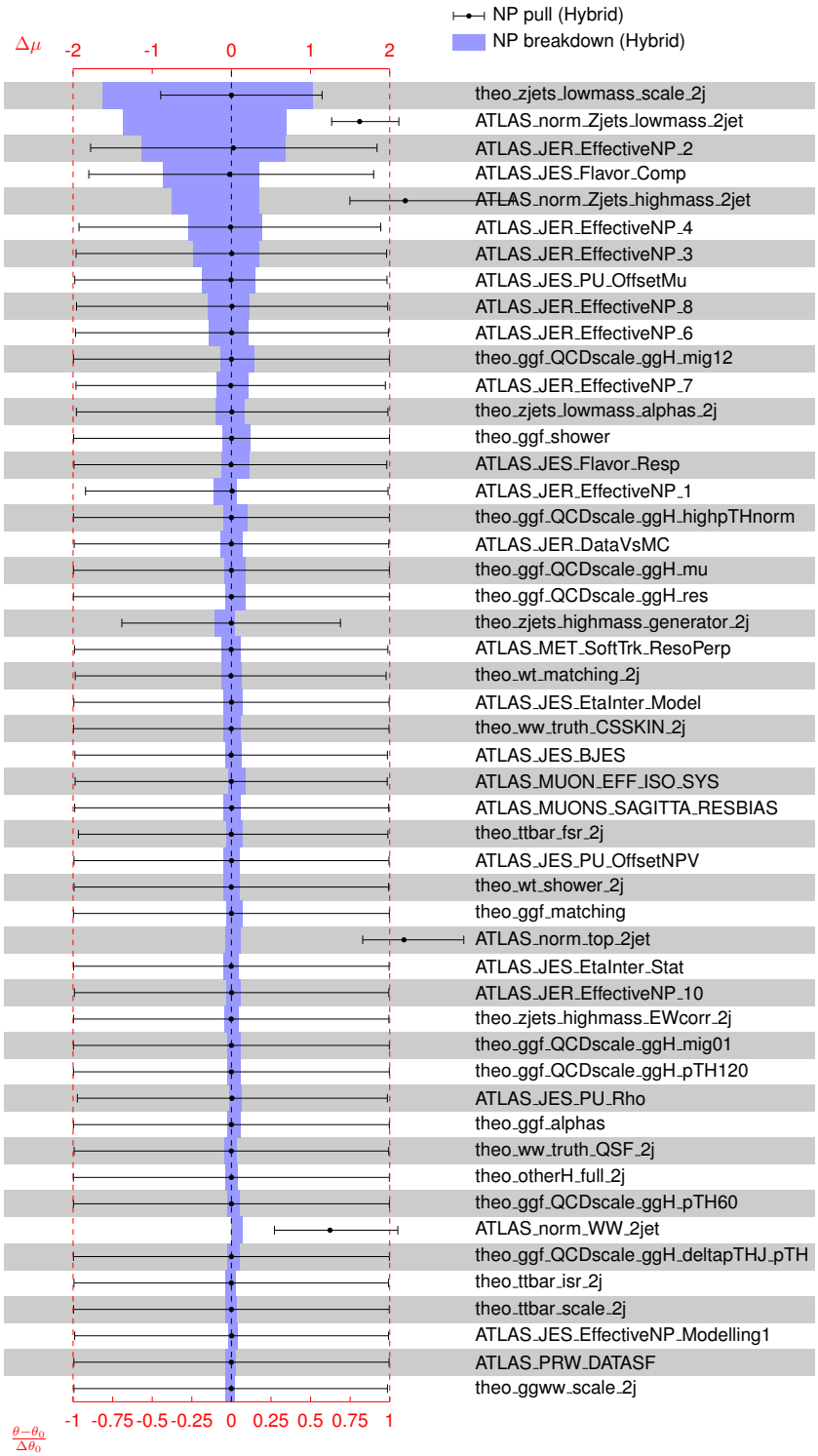

Figure 6.3: Ranking plot of the nuisance parameters (NPs) in the hybrid fit of the $N_{\text{jet}} \geq 2$ ggF-enriched category. Their pulls and post-fit uncertainties are indicated by the black dots and lines respectively. The blue bands represent their contribution to the total uncertainty on μ (breakdowns). Only the top 50 NPs with largest breakdowns are shown.

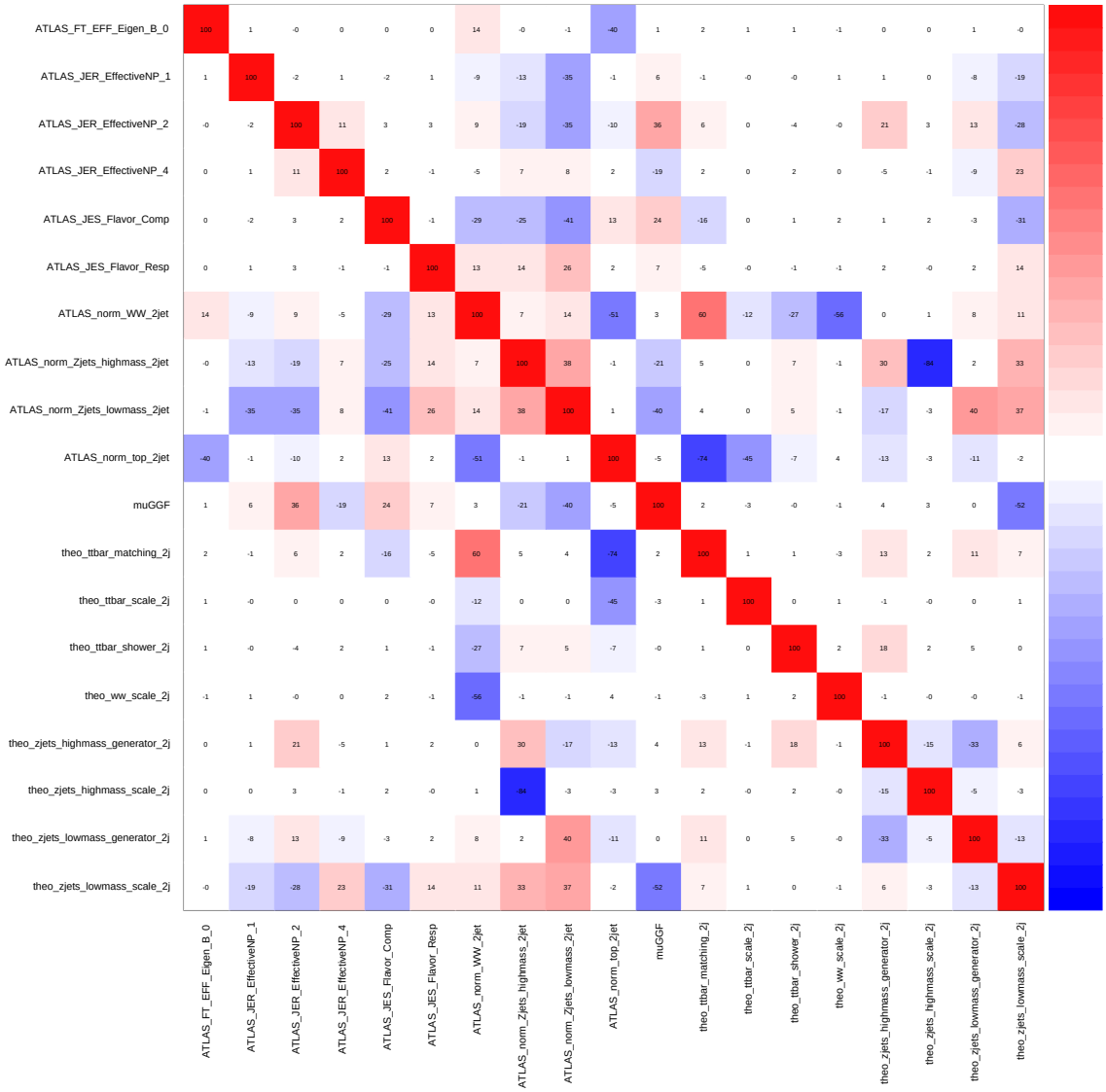

Figure 6.4: Correlation matrix of the nuisance parameters (NPs) in the hybrid fit of the $N_{\text{jet}} \geq 2$ ggF-enriched category. Blue shades denote anti-correlations, while red shades denote correlations. Only NPs that have correlations or anti-correlations larger than 20% are shown.

Table 6.9: Summary of the contributions that the different sources of uncertainties have on expected μ_{ggF}, obtained from the hybrid fit of the $N_{\text{jet}} \geq 2$ ggF-enriched category. The sum in quadrature of the individual components differs from the total uncertainty due to correlations between the components.

Source	$\Delta\mu_{\text{ggF}}[\%]$
Total	251.2
Data statistics	111.1
Total systematics	246.0
Theoretical systematics	146.4
ggF	42.3
VBF	1.7
Other H	8.0
Z/γ^*	135.0
Z/γ^* high-mass	17.6
Z/γ^* low-mass	133.8
Top	23.5
Wt	16.6
$t\bar{t}$	16.6
WW	15.5
$q\bar{q} \to WW$	14.1
$gg \to WW$	6.2
EW WW	0.5
$V\gamma$	0.6
Other VV	1.2
VVV	0.6
$H \to WW$ branching fractions	5.3
Experimental systematics	152.6
Flavour Tagging	5.4
Jet energy scale	79.0
Jet energy resolution	126.8
$E_{\text{T}}^{\text{miss}}$	12.9
Muons	16.0
Electrons	2.8
Fake factors	2.1
Pile-up	6.2
Luminosity	4.2
Background normalization	107.2
Z/γ^* normalization	104.5
Top normalization	9.8
WW normalization	7.4
MC statistics	141.1

6.5.3 $N_{\text{jet}} \geq 2$ VBF-enriched category

Due to small sample sizes, the shape components of all experimental and theoretical systematic uncertainties are removed for all processes in the $N_{\text{jet}} \geq 2$ VBF-enriched SR. In order to prevent unphysical over-constraints and potential migrations of event yields between analysis regions, the normalization components of P4 systematics associated with certain processes are removed for the regions where they constitute very low event yields, as summarized in Table 6.10. However, there is no transfer of systematics because only the inclusive SR is used as a fit region in this category.

The expected VBF signal strength obtained from a fit to the hybrid dataset is:

$$\begin{aligned} \mu_{\text{VBF}}^{\text{expected}} &= 1.00^{+1.68}_{-2.02} \\ &= 1.00^{+0.84}_{-0.83}(\text{stat.})\,^{+1.06}_{-1.42}(\text{exp.})\,^{+0.54}_{-0.52}(\text{theo.}) \ . \end{aligned} \tag{6.25}$$

The signal strength for the ggF process is fixed to unity in the fit. The expected signal significance Z_0 for the VBF signal in this category is 0.52. The normalization factors for the top quark and Z/γ^* backgrounds are listed in Table 6.3, which are found to be consistent with the pre-fit values used to construct the hybrid dataset.

From Figure 6.5, all NP pulls are centred on zero as expected, and no over-constraints are observed. The single NP with the largest breakdown is the Z/γ^* normalization factor, accounting for 81% of the overall POI uncertainty alone. Upon investigation, it is found to be caused by how the Z/γ^* CR is defined in this category (see Section 4.5.6). In order to preserve statistics, the cut on $m_{ll} < 55$ GeV is intentionally removed in the CR, and the entire m_{ll} range is used to model the Z/γ^* process as a result. On the other hand, the SR is confined to the low $m_{ll} < 55$ GeV range only. This conflict in the nature of the CR and SR is what leads to the large uncertainty of the normalization factor. From Table 6.11, it can be seen that the JER and $E_{\text{T}}^{\text{miss}}$ uncertainties are the largest contributors to the experimental systematic uncertainty, which is the consequence of their positive correlations with the Z/γ^* normalization factor, as observed in Figure 6.6. The $N_{\text{jet}} \geq 2$ VBF-enriched category suffers from a very large statistical uncertainty due to the small sizes of all analysis regions as expected.

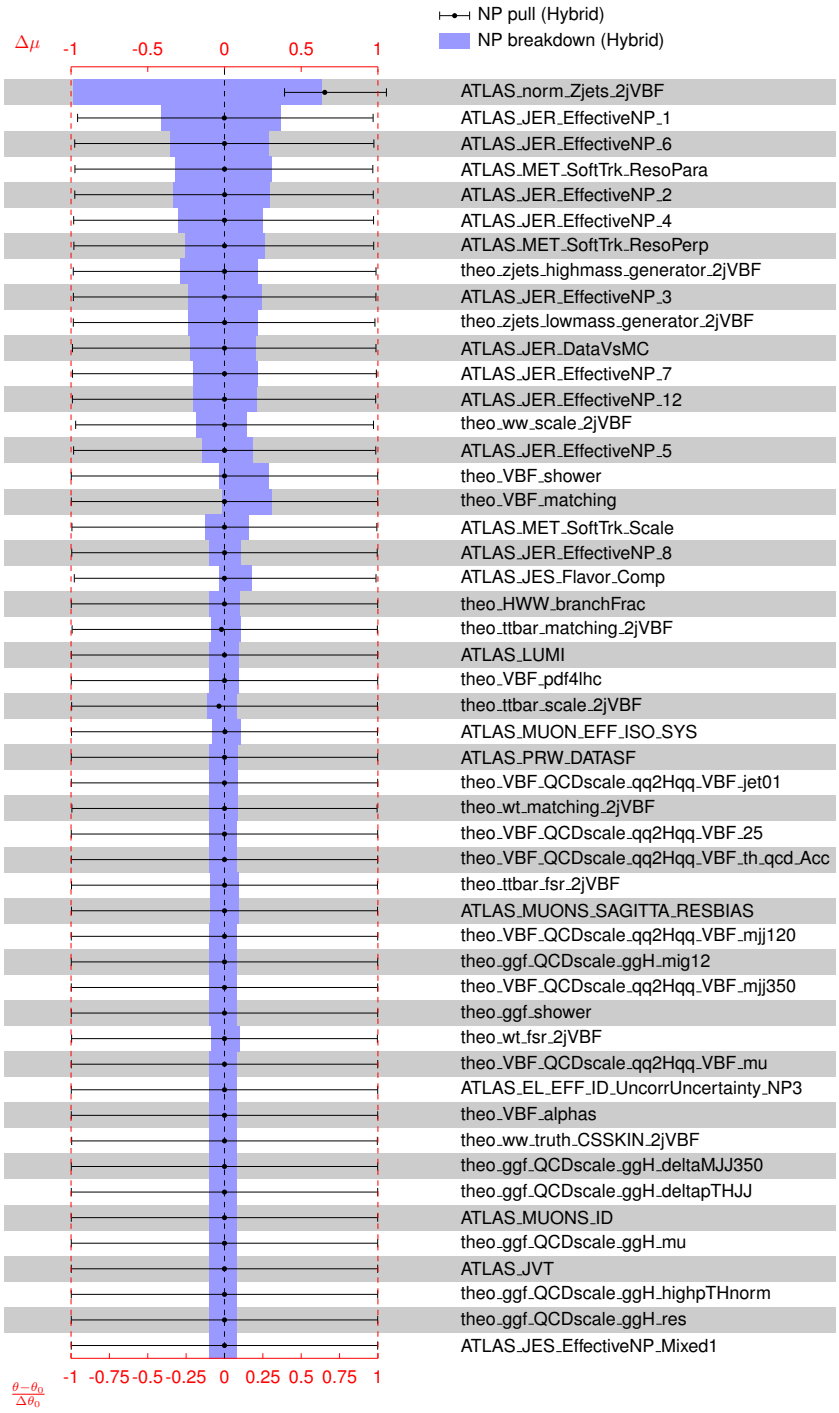

Figure 6.5: Ranking plot of the nuisance parameters (NPs) in the hybrid fit of the $N_{\text{jet}} \geq 2$ VBF-enriched category. Their pulls and post-fit uncertainties are indicated by the black dots and lines respectively. The blue bands represent their contribution to the total uncertainty on μ (breakdowns). Only the top 50 NPs with largest breakdowns are shown.

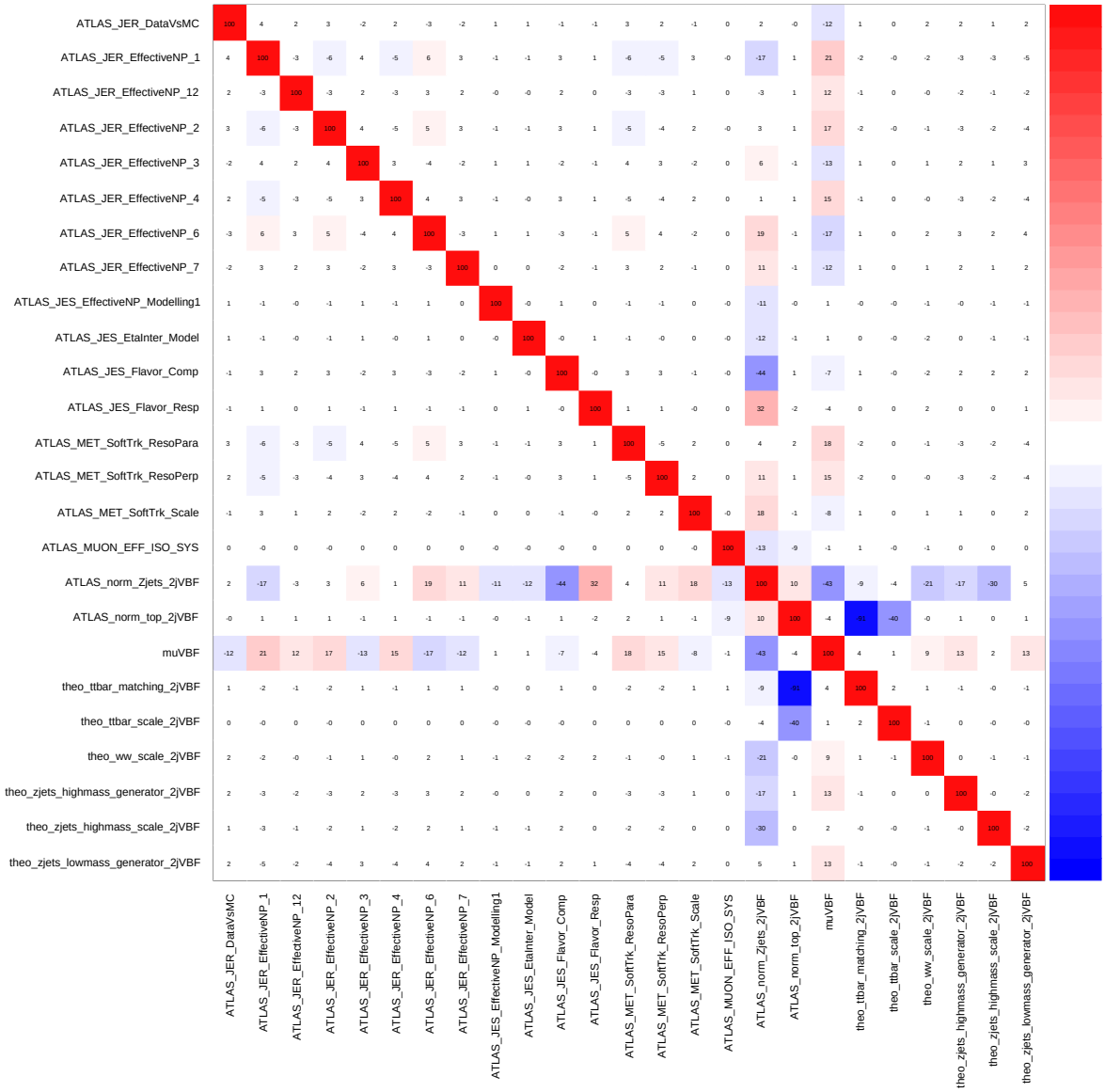

Figure 6.6: Correlation matrix of the nuisance parameters (NPs) in the hybrid fit of the $N_{\text{jet}} \geq 2$ VBF-enriched category. Blue shades denote anti-correlations, while red shades denote correlations. Only NPs that have correlations or anti-correlations larger than 10% are shown.

Table 6.10: Summary of the removed experimental systematic uncertainties for the different processes and analysis regions in the $N_{\text{jet}} \geq 2$ VBF-enriched category.

Process	Region	Removed systematic
all processes	SR	all systematics (shape)
ggF VBF	all CRs	all P4 (norm)
Z/γ^* high-mass Z/γ^* low-mass	Top quark CR	
Other H $gg \to WW$ EW WW Other VV $V\gamma$ VVV	all CRs SR	

Table 6.11: Summary of the contributions that the different sources of uncertainties have on expected μ_{VBF}, obtained from the hybrid fit of the $N_{\mathrm{jet}} \geq 2$ VBF-enriched category. The sum in quadrature of the individual components differs from the total uncertainty due to correlations between the components.

Source	$\Delta\mu_{\mathrm{VBF}}[\%]$
Total	185.0
Data statistics	83.8
Total systematics	177.3
Theoretical systematics	52.8
ggF	9.5
VBF	26.0
Other H	9.3
Z/γ^*	36.4
Z/γ^* high-mass	25.8
Z/γ^* low-mass	24.7
Top	10.3
Wt	9.0
$t\bar{t}$	6.9
WW	17.2
$q\bar{q} \to WW$	17.1
$gg \to WW$	9.2
EW WW	9.2
$V\gamma$	9.3
Other VV	9.2
VVV	9.3
$H \to WW$ branching fractions	10.3
Experimental systematics	123.9
Flavour Tagging	8.3
Jet energy scale	19.0
Jet energy resolution	96.0
$E_{\mathrm{T}}^{\mathrm{miss}}$	45.3
Muons	9.3
Electrons	9.3
Fake factors	9.3
Pile-up	9.5
Luminosity	9.9
Background normalization	81.3
Z/γ^* normalization	81.2
Top normalization	9.1
MC statistics	92.4

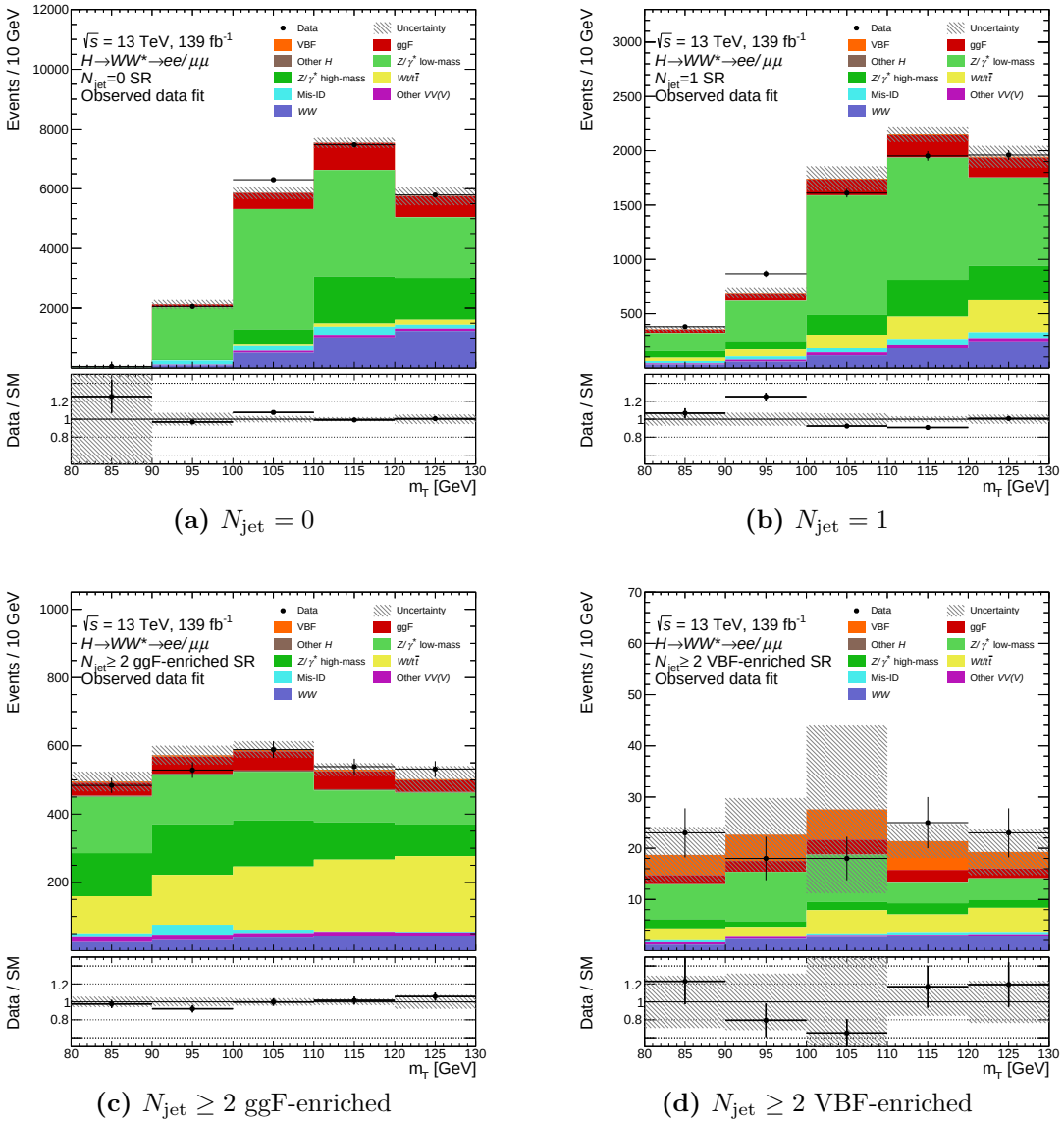

(a) $N_{\text{jet}} = 0$ **(b)** $N_{\text{jet}} = 1$

(c) $N_{\text{jet}} \geq 2$ ggF-enriched **(d)** $N_{\text{jet}} \geq 2$ VBF-enriched

Figure 6.7: Post-fit distributions of discriminating fit variable m_{T} with the binning scheme used for fitting in the SRs of the four N_{jet} categories after a fit to observed data.

Table 6.12: Post-fit normalization factors for the WW, top quark, and Z/γ^* low-mass and high-mass backgrounds obtained from the observed data fit. The uncertainties include contributions from statistical, experimental, and theoretical systematic uncertainties. The $N_{\text{jet}} \geq 2$ VBF-enriched category has a single Z/γ^* CR and no WW CR.

Category	WW	$Wt/t\bar{t}$	Z/γ^* low-mass	Z/γ^* high-mass
$N_{\text{jet}} = 0$	$1.02^{+0.08}_{-0.08}$	$0.95^{+0.21}_{-0.16}$	$1.56^{+0.44}_{-0.34}$	$1.42^{+0.34}_{-0.26}$
$N_{\text{jet}} = 1$	$0.88^{+0.18}_{-0.17}$	$0.91^{+0.18}_{-0.15}$	$1.12^{+0.34}_{-0.24}$	$1.17^{+0.33}_{-0.23}$
$N_{\text{jet}} \geq 2$ ggF-enriched	$0.57^{+0.41}_{-0.35}$	$1.07^{+0.37}_{-0.26}$	$0.80^{+0.17}_{-0.14}$	$1.12^{+0.64}_{-0.33}$
$N_{\text{jet}} \geq 2$ VBF-enriched	–	$0.98^{+0.37}_{-0.22}$	$0.67^{+0.33}_{-0.24}$	$0.67^{+0.33}_{-0.24}$

6.6 Observed data fit results

After obtaining expected results from fits to hybrid datasets, a fit to unblinded observed data is performed. The NPs in each of the N_{jet} categories are pruned, removed, or transferred using the procedures prescribed in the individual sub-sections of Section 6.5. A fit is performed by simultaneously considering all of the sub-SRs and CRs of all N_{jet} categories to produce the nominal values and uncertainties of the signal strength parameters for the ggF and VBF Higgs production modes, which are measured to be:

$$\begin{aligned} \mu_{\text{ggF}}^{\text{observed}} &= 2.88^{+1.05}_{-1.05} \\ &= 2.88^{+0.29}_{-0.29}(\text{stat.})\,^{+0.50}_{-0.52}(\text{exp.})\,^{+0.71}_{-0.71}(\text{theo.})\ , \end{aligned} \tag{6.26}$$

$$\begin{aligned} \mu_{\text{VBF}}^{\text{observed}} &= 1.44^{+1.45}_{-1.77} \\ &= 1.44^{+0.76}_{-0.74}(\text{stat.})\,^{+0.84}_{-1.22}(\text{exp.})\,^{+0.64}_{-0.77}(\text{theo.})\ . \end{aligned} \tag{6.27}$$

The observed signal significance Z_0 of the ggF and VBF processes are 2.71 and 0.82 respectively. The value of $\mu_{\text{ggF}}^{\text{observed}}$ deviates from the SM expectation of 1 by about 1.8σ, whereas $\mu_{\text{VBF}}^{\text{observed}}$ is consistent with the SM expectation. This is not, however, an indication of new physics, but rather a result of the various issues within the fit itself. By comparing the expected and post-fit normalization factors in Tables 6.3 and 6.12, a large change is observed for the Z/γ^* low-mass sample in the $N_{\text{jet}} = 0$ category, where it decreases from $1.82^{+0.55}_{-0.42}$ to $1.56^{+0.44}_{-0.34}$. From Figure 6.7a, it can be seen that the $[90, 100)$ GeV bin has an exceptionally high purity of the Z/γ^* low-mass sample, which is even purer than the dedicated Z/γ^* low-mass

CR designed to be enriched in this background process. The likelihood fit favours this particular bin over the CR when calculating the normalization factor since a smaller increase is needed to match the data. The consequence of the decrease in the Z/γ^* low-mass normalization factor is that it causes deficits in event yields in the other bins, and the ggF signal yields have to increase in order to compensate for these losses to match the data, resulting in a larger $\mu_{\text{ggF}}^{\text{observed}}$ than expected. A similar phenomenon occurs in the $N_{\text{jet}} = 1$ category, where the Z/γ^* low-mass normalization factor decreases from $1.34^{+0.41}_{-0.29}$ to $1.12^{+0.34}_{-0.24}$. In Figure 6.7b, it can be seen that the $[80, 90)$ GeV bin has a high Z/γ^* low-mass purity, and an excess of ggF signal events causes the predicted event yields to overshoot observed data in the other bins. Since all SRs are fitted simultaneously and $\mu_{\text{ggF}}^{\text{observed}}$ is shared between all categories, this causes a domino effect in the other SRs, resulting in the measured value of ggF signal strength to significantly deviate from 1. The post-fit event yields of the signal and background processes in each SR are provided in Table 6.13, and the post-fit m_{T} distributions are shown in Figure 6.8. The uncertainties stated in the table or displayed on the plots reflect the combined effect of all statistical and systematic uncertainties. The $N_{\text{jet}} \geq 2$ VBF-enriched SR features a very large uncertainty in each bin, which can be attributed to to the large MC statistical uncertainty due to limited sample sizes.

The measured uncertainties on $\mu_{\text{ggF}}^{\text{observed}}$ and $\mu_{\text{VBF}}^{\text{observed}}$ are smaller than the expected uncertainties obtained from the separate hybrid fits in Section 6.5 due to the combination effect where more data statistics available to the likelihood function results in an increase in sensitivity. The pulls and breakdowns of single NPs are shown in Figure 6.9, and the correlations between all NPs in the fit are illustrated in Figure 6.10. The NPs are grouped based on their common sources, and their collective contributions to the overall uncertainties on the measured ggF and VBF signal strengths are given in Table 6.14. The theoretical systematic uncertainties are dominated by the Z/γ^* processes due to their large contamination in the SRs as well as due to the mismodelling issues of the Sherpa 2.2.11 samples, as discussed in Sections 6.5.1 and 6.5.3. The largest contributor to the overall experimental

Table 6.13: Post-fit event yields of observed data and MC predictions for the signal and background processes in the signal regions of the four N_{jet} categories. The quoted uncertainties correspond to the statistical uncertainties combined with the experimental and theoretical systematic uncertainties.

Process	Signal region			
	$N_{\text{jet}} = 0$	$N_{\text{jet}} = 1$	$N_{\text{jet}} \geq 2$ ggF-enriched	$N_{\text{jet}} \geq 2$ VBF-enriched
H_{ggF}	2848 ± 1020	919 ± 326	346 ± 134	17 ± 7
H_{VBF}	19 ± 22	60 ± 65	34 ± 37	36 ± 38
Other Higgs	28 ± 14	26 ± 13	28 ± 14	0 ± 0
WW	6693 ± 298	2128 ± 353	423 ± 211	28 ± 6
Other $VV(V)$	487 ± 85	278 ± 41	141 ± 18	4 ± 1
$Wt/t\bar{t}$	1467 ± 155	3110 ± 280	1878 ± 241	38 ± 5
Z/γ^* high-mass	5428 ± 472	2323 ± 236	1192 ± 104	19 ± 11
Z/γ^* low-mass	14711 ± 768	5913 ± 329	1138 ± 130	55 ± 33
Mis-Id	991 ± 97	321 ± 36	95 ± 13	5 ± 1
Total	32673 ± 229	15078 ± 128	5275 ± 72	202 ± 14
Observed	32667 ± 181	15112 ± 123	5269 ± 73	205 ± 14

systematic uncertainties of both POIs is the JER due to their positive correlations with the Z/γ^* theoretical systematic uncertainties. The measured $\mu_{\text{VBF}}^{\text{observed}}$ also suffers from a very large statistical uncertainty due to the limited sample sizes of the $N_{\text{jet}} \geq 2$ VBF-enriched SR and its associated CRs.

Table 6.14: Summary of the contributions that the different sources of uncertainties have on the measured μ_{ggF} and μ_{VBF}, obtained from the observed data fit. The sum in quadrature of the individual components differs from the total uncertainty due to correlations between the components.

Source	$\Delta\mu_{\text{ggF}}[\%]$	$\Delta\mu_{\text{VBF}}[\%]$
Total	105.1	161.1
Data statistics	28.7	74.8
Total systematics	104.1	152.5
Theoretical systematics	71.0	70.8
ggF	22.8	11.4
VBF	1.1	27.2
Other H	1.6	0.9
Z/γ^*	65.6	56.5
Z/γ^* high-mass	55.5	40.0
Z/γ^* low-mass	31.7	36.2
Top	14.2	14.9
Wt	10.0	8.0
$t\bar{t}$	8.9	12.5
WW	9.2	21.2
$q\bar{q} \to WW$	8.7	21.0
$gg \to WW$	3.0	1.8
EW WW	0.6	1.8
$V\gamma$	2.5	1.2
Other VV	0.5	1.5
VVV	0.6	0.9
$H \to WW$ branching fractions	6.2	3.5
Experimental systematics	51.3	103.1
Flavour Tagging	10.2	6.0
Jet energy scale	18.1	23.7
Jet energy resolution	39.8	85.5
$E_{\text{T}}^{\text{miss}}$	27.3	48.8
Muons	11.2	9.1
Electrons	4.5	5.3
Fake factors	3.3	1.5
Pile-up	5.6	2.6
Luminosity	4.7	2.8
Background normalization	24.7	89.6
Z/γ^* normalization	21.9	88.6
Top normalization	7.3	13.2
WW normalization	13.7	7.9
MC statistics	85.5	99.7

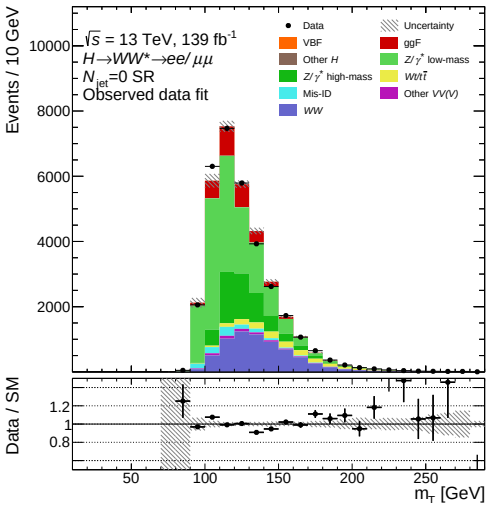

(a) $N_{\text{jet}} = 0$

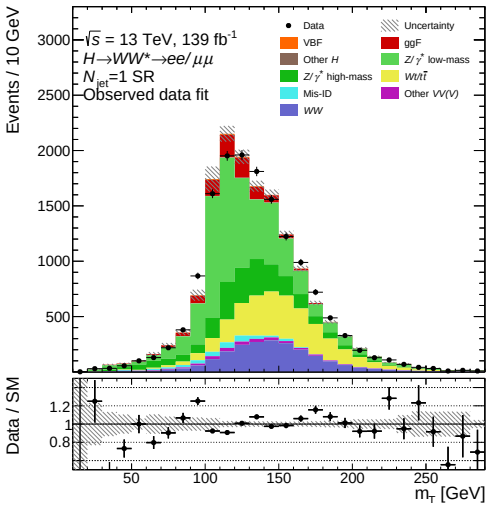

(b) $N_{\text{jet}} = 1$

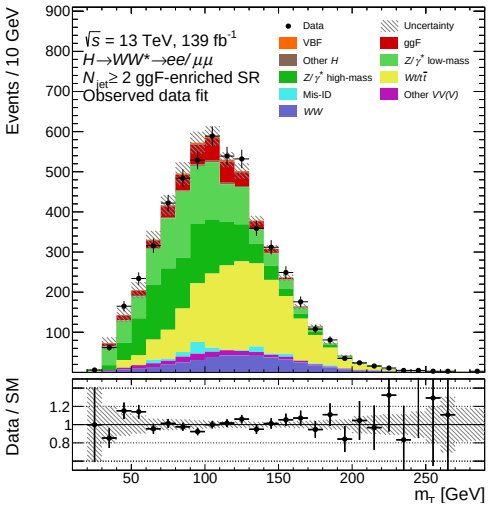

(c) $N_{\text{jet}} \geq 2$ ggF-enriched

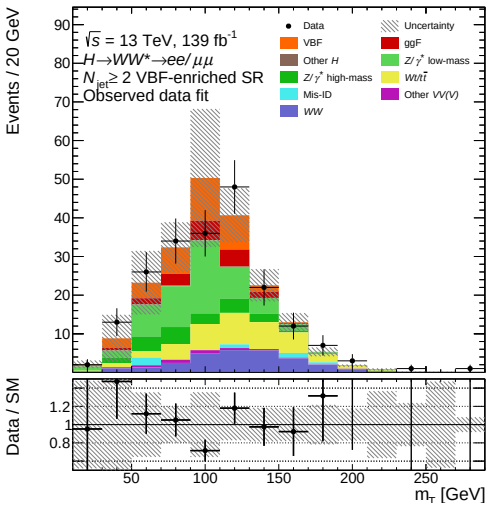

(d) $N_{\text{jet}} \geq 2$ VBF-enriched

Figure 6.8: Post-fit m_{T} distributions of the SRs of the four N_{jet} categories after a fit to observed data.

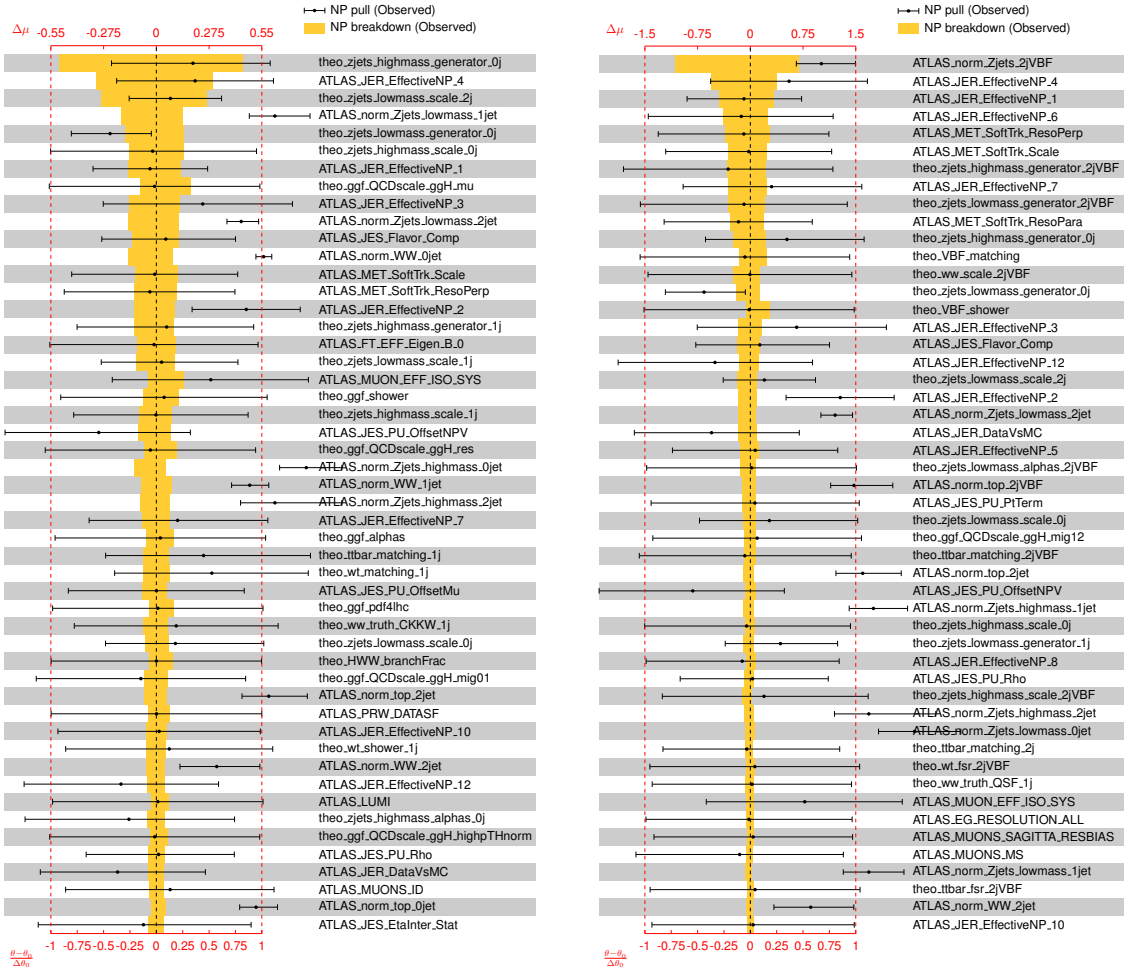

(a) μ_{ggF} **(b)** μ_{VBF}

Figure 6.9: Ranking plots of the nuisance parameters (NPs) in the (a) μ_{ggF} and (b) μ_{VBF} measurements of the observed data fit. Their pulls and post-fit uncertainties are indicated by the black dots and lines respectively. The yellow bands represent their contribution to the total uncertainty on μ (breakdowns). Only the top 50 NPs with largest breakdowns are shown.

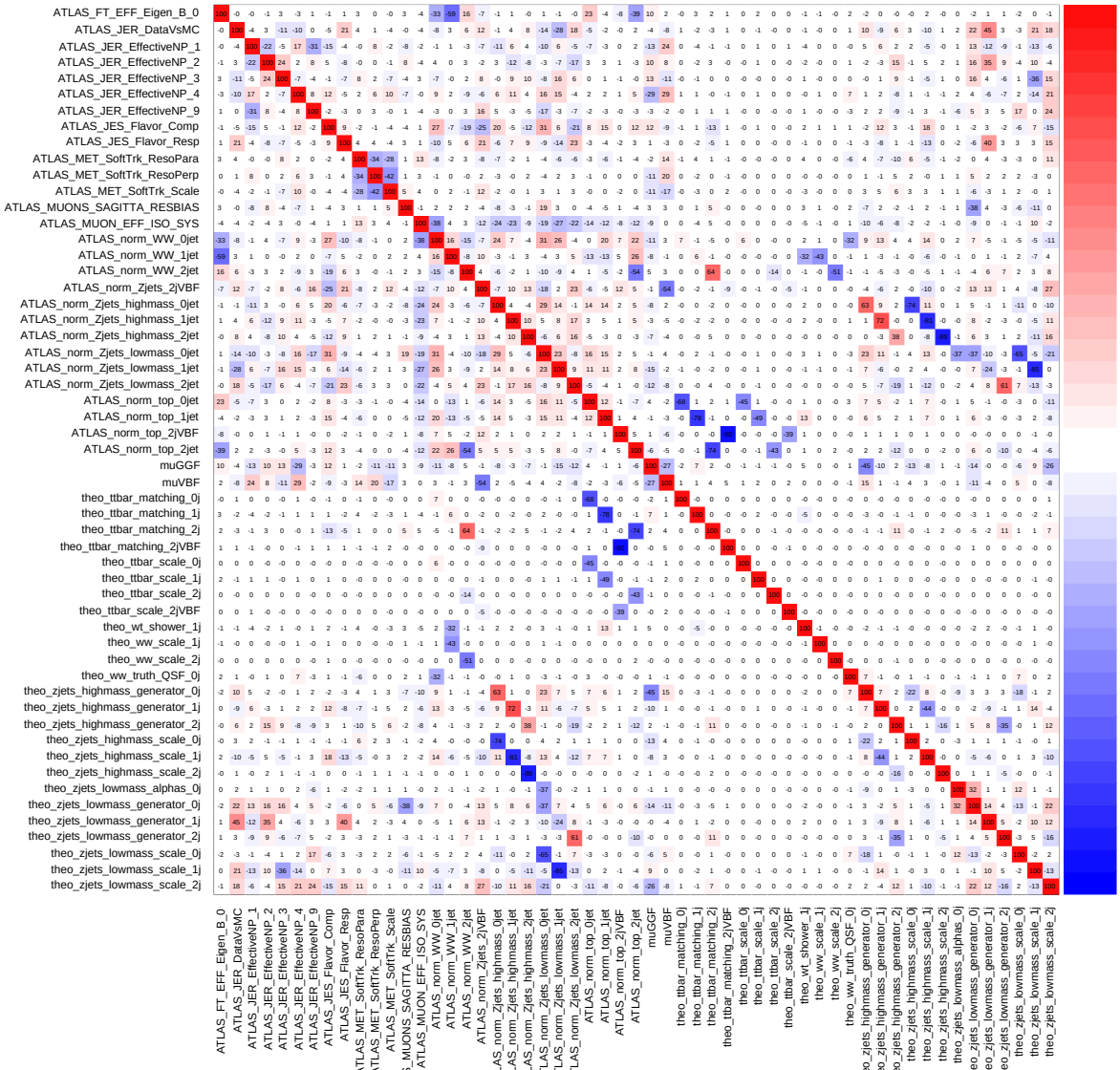

Figure 6.10: Correlation matrix of the nuisance parameters (NPs) in the observed data fit. Blue shades denote anti-correlations, while red shades denote correlations. Only NPs that have correlations or anti-correlations larger than 30% are shown.

6.7 Interpretations and future prospects

The values of the signal strength parameters obtained from the different-flavour (DF) channel using the full Run-2 dataset [6] are measured to be:

$$\begin{aligned}\mu_{\text{ggF}}^{\text{DF}} &= 1.15^{+0.14}_{-0.13} \\ &= 1.15^{+0.06}_{-0.06}(\text{stat.})\,^{+0.12}_{-0.12}(\text{syst.})\ ,\end{aligned} \tag{6.28}$$

$$\begin{aligned}\mu_{\text{VBF}}^{\text{DF}} &= 0.93^{+0.23}_{-0.20} \\ &= 0.93^{+0.14}_{-0.13}(\text{stat.})\,^{+0.18}_{-0.15}(\text{syst.})\ .\end{aligned} \tag{6.29}$$

The different-flavour channel yields significantly smaller uncertainties than the same-flavour channel since the WW and top quark backgrounds can be efficiently suppressed by using more simplified event selection criteria, which result in high signal acceptance in the SRs without having to trade off a large amount of sample statistics. On the other hand, the same-flavour channel is still overwhelmingly contaminated by the Z/γ^* background across all N_{jet} categories even with an application of stringent event selection criteria. Due to the requirements on the $E_{\text{T}}^{\text{miss}}$ significance observable, Z/γ^* events that remain in the SRs and CRs do not have genuine $E_{\text{T}}^{\text{miss}}$ but are rather a result of limited resolution and inefficiencies of object reconstruction, with jets in particular as reflected in the large JER uncertainty. With the advent of advanced machine learning techniques such as the DNN technique, the classification and discrimination of the signal and background processes in the same-flavour channel should be drastically improved compared to a cut-based approach employed in this analysis. This is an ongoing work in progress by the HWW working group.

The sample sizes of the SR and CRs in the $N_{\text{jet}} \geq 2$ VBF-enriched category can be enlarged by removing the cut on $\Delta\phi_{ll,E_{\text{T}}^{\text{miss}}} < 2$. Due to its dependency on the reconstructed $E_{\text{T}}^{\text{miss}}$, the removal of this observable should also reduce the uncertainties on $E_{\text{T}}^{\text{miss}}$ and the JER. The uncertainty on the Z/γ^* normalization factor can be reduced by applying a cut on $m_{ll} < 55$ GeV or 75 GeV in order to confine the phase space of the Z/γ^* CR to the low mass range so that it becomes more similar to the nature of the SR to which it extrapolates. The number of bins

of the discriminating fit variable m_{T} can also be reduced from six to three in order to increase event yields in each bin and reduce statistical fluctuations. With larger sample sizes, it would be possible to include the shape components of systematic uncertainties, and the measured uncertainties should be more reliable.

In the $N_{\mathrm{jet}} = 0$ and $N_{\mathrm{jet}} = 1$ categories, the definition of the Z/γ^* low-mass CR could be revised by applying a cut on m_{T} to select Z/γ^* events with small dilepton masses since these low-m_{T} regions are found to have higher purities than those in the dedicated CR, which is constructed by requiring $m_{ll} < 20$ GeV and $\Delta\phi_{ll} < 0.3$. The SR will also need to be redefined accordingly to make it mutually exclusive to the revised Z/γ^* low-mass CR.

The most significant contributors to the theoretical uncertainties of the measured signal strengths in this analysis are the Z/γ^* QCD scale and generator uncertainties. The recommendation by the Physics Modelling Group is to separately use the CKKW, QSF, and CSSKIN variations to estimate the uncertainties on matrix element (ME) matching/merging, resummation scale, and parton shower recoil scheme (UEPS) respectively for processes simulated with Sherpa. However, these variation samples were not available during the time of this analysis, and only a bulk generator comparison between the nominal Sherpa 2.2.11 and alternative MadGraph5_aMC@NLO+Pythia8 samples was possible, which inevitably led to large combined ME+UEPS uncertainties. And lastly, the mismodelling issue of the Sherpa 2.2.11 sample manifests in large QCD scale uncertainties for the Z/γ^* background in all analysis categories. It is important that this issue be addressed and fixed in the future version of Sherpa samples.

7 Conclusions

This thesis presents the measurements of the Standard Model (SM) Higgs boson production via the gluon-gluon fusion (ggF) and vector-boson fusion (VBF) processes using the $H \to WW^* \to l\nu l\nu$ decay mode where the leptons are of the same-flavour, i.e. either both electrons or both muons. The dataset used in the analysis consists of pp collisions at a centre-of-mass energy of 13 TeV collected by the ATLAS detector during LHC Run-2 between 2015 and 2018, which corresponds to an integrated luminosity of 139 fb^{-1}. Since the integrated luminosity significantly increased from Run-1, new techniques and methods of particle reconstruction were introduced in order to mitigate the impact that additional pp interactions in an event have on the measurement of the pp interaction of interest. The most notable additions include a new jet reconstruction method known as the particle flow algorithm and the utilization of the track-based soft term in the calculation of missing transverse momentum.

This $H \to WW^* \to l\nu l\nu$ same-flavour analysis opts for the traditional cut-based approach, where events are selected based on the threshold values of various kinematic and geometric observables. In order to cater to the different nature of the different topologies, the selected events are categorized based on jet multiplicity and Higgs production mode. The kinematic topology unique to each of the categories

is exploited in order to construct the so-called signal region, where the signal-to-background ratio is high. The processes that contribute to the overall background the most, namely WW, top quark, and Z/γ^*, are estimated using dedicated control regions, which are designed to be enriched in the respective processes. The transverse mass of the final-state leptons, m_{T}, is used as the discriminating fit variable in the statistical analysis, which employs the maximum likelihood formalism to fit SM predictions to observed data. The signal strength parameter, which is defined as the ratio of the measured cross-section multiplied by the $H \to WW^*$ decay branching fraction to that predicted by the SM, is measured separately for the ggF and VBF production modes:

$$\begin{aligned} \mu_{\mathrm{ggF}} &= 2.88^{+1.05}_{-1.05} \\ &= 2.88^{+0.29}_{-0.29}(\mathrm{stat.})\,^{+0.50}_{-0.52}(\mathrm{exp.})\,^{+0.71}_{-0.71}(\mathrm{theo.})\ , \end{aligned} \tag{7.1}$$

$$\begin{aligned} \mu_{\mathrm{VBF}} &= 1.44^{+1.45}_{-1.77} \\ &= 1.44^{+0.76}_{-0.74}(\mathrm{stat.})\,^{+0.84}_{-1.22}(\mathrm{exp.})\,^{+0.64}_{-0.77}(\mathrm{theo.})\ , \end{aligned} \tag{7.2}$$

where the three components of the overall uncertainty are statistical, experimental, and theoretical systematic uncertainties. The deviation from unity of μ_{ggF} is due to the constraining effect, where certain bins of the m_{T} distribution in the fit have higher purities than the dedicated Z/γ^* control regions. The uncertainty on μ_{ggF} is dominated by the large theoretical systematic uncertainties related to the Z/γ^* process, where a significant mismodelling issue has been found with the Monte Carlo samples used for this process. The uncertainty on μ_{VBF} is largely attributed to the large statistical uncertainty, which is caused by small sample sizes in both the signal region and Z/γ^* control region. The large experimental uncertainty is caused by an inappropriate definition of the Z/γ^* control, which makes it different from the signal region it tries to extrapolate to. Despite these shortcomings, this is the first time that a comprehensive $H \to WW^* \to l\nu l\nu$ same-flavour analysis is performed with the full Run-2 dataset. The results from this analysis should serve as a benchmark or cross-check for the ongoing analysis, where novel machine learning techniques are employed.

Appendices

A

Pre-fit experimental systematic uncertainties

The values of pre-fit experimental systematic normalization uncertainties defined in Section 5.2 are provided in the following tables for all four N_{jet} categories of the analysis.

Table A.1: Pre-fit experimental systematic normalization uncertainties of the different processes in the SR of the $N_{\text{jet}} = 0$ category. Only non-trivial systematic uncertainties whose values are not 0% are shown.

$N_{\text{jet}} = 0$ SR	Pre-fit impact high / low [%]													
Experimental systematic uncertainty	EW WW	Other VV	VVV	$V\gamma$	Z/γ^* high-mass	Z/γ^* low-mass	$gg WW$	Other H	$qq WW$	ggF	VBF	$t\bar{t}$	Wt	
ATLAS_EG_RESOLUTION_ALL	+0.4 / +0.1	+0.0 / +0.1	−0.1 / +0.2	+2.1 / −2.1	+0.1 / −0.1	+0.2 / −0.4	+0.0 / −0.1	+0.0 / +0.1	+0.0 / +0.1	+0.1 / +0.0	+0.0 / +0.1	−0.1 / −0.0	−0.1 / +0.1	
ATLAS_EG_SCALE_AF2														
ATLAS_EG_SCALE_ALL	+0.7 / −0.5	+0.2 / −0.2		+3.8 / −0.8	+0.2 / −0.1	+0.7 / −0.5	+0.1 / −0.1	−0.0 / −0.1	+0.1 / −0.1	+0.3 / −0.3	+0.2 / −0.2	+0.1 / −0.2	+0.1 / −0.2	
ATLAS_EL_EFF_ID_CorrUncertainty_NP0														
ATLAS_EL_EFF_ID_CorrUncertainty_NP1														
ATLAS_EL_EFF_ID_CorrUncertainty_NP10										−0.1 / +0.1	−0.1 / +0.1			
ATLAS_EL_EFF_ID_CorrUncertainty_NP11	+0.1 / −0.1	+0.1 / −0.1	+0.1 / −0.1	+0.3 / −0.3	+0.1 / −0.1	+0.1 / −0.1	+0.1 / −0.1	+0.1 / −0.1	+0.1 / −0.1	+0.1 / −0.1	+0.1 / −0.1	+0.1 / −0.1	+0.1 / −0.1	
ATLAS_EL_EFF_ID_CorrUncertainty_NP12	−0.1 / +0.1	−0.1 / +0.1	−0.1 / +0.1	−0.3 / +0.3	−0.1 / +0.1	−0.1 / +0.1	−0.1 / +0.1	−0.1 / +0.1	−0.1 / +0.1	−0.1 / +0.1	−0.1 / +0.1	−0.1 / +0.1	−0.1 / +0.1	
ATLAS_EL_EFF_ID_CorrUncertainty_NP13	−0.1 / +0.1	−0.1 / +0.1	−0.1 / +0.1		−0.1 / +0.1	−0.1 / +0.1	−0.1 / +0.1	−0.1 / +0.1	−0.1 / +0.1	−0.1 / +0.1	−0.1 / +0.1	−0.1 / +0.1	−0.1 / +0.1	
ATLAS_EL_EFF_ID_CorrUncertainty_NP14	−0.1 / +0.1	−0.0 / +0.1	+0.1 / −0.1	+0.4 / −0.3		−0.1 / +0.1				−0.1 / +0.1				
ATLAS_EL_EFF_ID_CorrUncertainty_NP15	−0.2 / +0.2	−0.2 / +0.2	−0.1 / +0.1	−0.6 / +0.6	−0.2 / +0.2	−0.2 / +0.2	−0.1 / +0.1	−0.1 / +0.1	−0.2 / +0.2	−0.2 / +0.2	−0.2 / +0.2	−0.1 / +0.1	−0.1 / +0.1	
ATLAS_EL_EFF_ID_CorrUncertainty_NP2														
ATLAS_EL_EFF_ID_CorrUncertainty_NP3														
ATLAS_EL_EFF_ID_CorrUncertainty_NP4														
ATLAS_EL_EFF_ID_CorrUncertainty_NP5														
ATLAS_EL_EFF_ID_CorrUncertainty_NP6														
ATLAS_EL_EFF_ID_CorrUncertainty_NP7														
ATLAS_EL_EFF_ID_CorrUncertainty_NP8														
ATLAS_EL_EFF_ID_CorrUncertainty_NP9														
ATLAS_EL_EFF_ID_UncorrUncertainty_NP0														
ATLAS_EL_EFF_ID_UncorrUncertainty_NP1														
ATLAS_EL_EFF_ID_UncorrUncertainty_NP10														
ATLAS_EL_EFF_ID_UncorrUncertainty_NP11														
ATLAS_EL_EFF_ID_UncorrUncertainty_NP12		+0.1 / −0.1		+0.7 / −0.7	+0.1 / −0.1	+0.1 / −0.1		+0.1 / −0.1		+0.1 / −0.1	+0.1 / −0.1	+0.1 / −0.1		
ATLAS_EL_EFF_ID_UncorrUncertainty_NP13				+0.2 / −0.2										
ATLAS_EL_EFF_ID_UncorrUncertainty_NP14				+0.1 / −0.1										
ATLAS_EL_EFF_ID_UncorrUncertainty_NP15				+0.1 / −0.1										
ATLAS_EL_EFF_ID_UncorrUncertainty_NP16														
ATLAS_EL_EFF_ID_UncorrUncertainty_NP17														
ATLAS_EL_EFF_ID_UncorrUncertainty_NP2														
ATLAS_EL_EFF_ID_UncorrUncertainty_NP3	+0.3 / −0.3	+0.3 / −0.3	+0.1 / −0.1	+0.3 / −0.3	+0.3 / −0.3	+0.4 / −0.4	+0.2 / −0.2	+0.2 / −0.2	+0.2 / −0.2	+0.4 / −0.4	+0.3 / −0.3	+0.3 / −0.3	+0.3 / −0.3	
ATLAS_EL_EFF_ID_UncorrUncertainty_NP4										+0.1 / −0.1				
ATLAS_EL_EFF_ID_UncorrUncertainty_NP5				+0.1 / −0.1										
ATLAS_EL_EFF_ID_UncorrUncertainty_NP6	+0.1 / −0.1		+0.1 / −0.1	+0.1 / −0.1	+0.1 / −0.1		+0.1 / −0.1	+0.1 / −0.1	+0.1 / −0.1	+0.1 / −0.1	+0.1 / −0.1	+0.1 / −0.1	+0.1 / −0.1	
ATLAS_EL_EFF_ID_UncorrUncertainty_NP7														
ATLAS_EL_EFF_ID_UncorrUncertainty_NP8														
ATLAS_EL_EFF_ID_UncorrUncertainty_NP9														
ATLAS_EL_EFF_Iso_TOTAL_1NPCOR_PLUS_UNCOR	+0.3 / −0.2	+0.2 / −0.2	+0.2 / −0.2	+0.9 / −0.9	+0.3 / −0.3	+0.3 / −0.3	+0.2 / −0.2	+0.2 / −0.2	+0.2 / −0.2	+0.3 / −0.3	+0.3 / −0.3	+0.3 / −0.3	+0.3 / −0.3	
ATLAS_EL_EFF_Reco_TOTAL_1NPCOR_PLUS_UNCOR	+0.2 / −0.2	+0.2 / −0.2	+0.2 / −0.2	+0.6 / −0.6	+0.2 / −0.2	+0.2 / −0.2	+0.2 / −0.2	+0.2 / −0.2	+0.2 / −0.2	+0.2 / −0.2	+0.2 / −0.2	+0.2 / −0.2	+0.2 / −0.2	
ATLAS_EL_EFF_TRIG_TOTAL_1NPCOR_PLUS_UNCOR														
ATLAS_FTAG_EXTRAP														
ATLAS_FT_EFF_Eigen_B_0					+0.1 / −0.1							+3.8 / −3.7	+2.2 / −2.2	
ATLAS_FT_EFF_Eigen_B_1												−0.3 / +0.3	−0.2 / +0.2	
ATLAS_FT_EFF_Eigen_B_2												+0.2 / −0.2	+0.1 / −0.1	
ATLAS_FT_EFF_Eigen_C_0	+0.6 / −0.6	+0.2 / −0.2	+0.4 / −0.4		+0.1 / −0.1	+0.2 / −0.2	+0.1 / −0.1	+0.3 / −0.3	+0.1 / −0.1		+0.2 / −0.2	+0.1 / −0.1	+0.1 / −0.1	
ATLAS_FT_EFF_Eigen_C_1														
ATLAS_FT_EFF_Eigen_C_2														
ATLAS_FT_EFF_Eigen_Light_0	+0.2 / −0.2	+0.1 / −0.1	+0.1 / −0.1	+0.1 / −0.1	+0.1 / −0.1	+0.1 / −0.1	+0.1 / −0.1	+0.1 / −0.1	+0.1 / −0.1	+0.1 / −0.1	+0.1 / −0.1	+0.2 / −0.2	+0.1 / −0.1	
ATLAS_FT_EFF_Eigen_Light_1														
ATLAS_FT_EFF_Eigen_Light_2														
ATLAS_FT_EFF_Eigen_Light_3														
ATLAS_FT_EFF_extrapolation_from_charm		−0.1 / +0.1	−0.4 / +0.4						−0.2 / +0.2					
ATLAS_JER_DataVsMC	−3.2 / +3.2	+0.1 / −0.2	+0.3 / −1.1	+0.7 / +2.0	+0.6 / +0.8	−0.7 / +0.9	+0.2 / −0.2	+0.1 / −0.2	+0.2 / −0.2	+0.1 / −0.1	−0.8 / +0.2	−0.4 / +0.3	−0.4 / −0.6	
ATLAS_JER_EffectiveNP_1	+3.1 / −4.1	−1.8 / +1.1	−1.0 / +2.4	−3.1 / +0.6	−0.1 / +1.9	+0.1 / −2.6	−1.4 / +1.2	−1.2 / +0.7	−1.2 / +0.9	−1.3 / +0.8	−0.6 / +0.1	−0.2 / +0.2	−1.9 / +0.8	
ATLAS_JER_EffectiveNP_10	−1.2 / −0.3	+0.3 / −0.3	−0.8 / −0.7	+0.0 / +0.2	+0.4 / +0.9	−0.2 / +1.2	+0.1 / −0.2	−0.1 / −0.2	−0.0 / −0.1	+0.0 / −0.2	−0.1 / −0.1	+0.0 / +0.5	−0.2 / −0.0	
ATLAS_JER_EffectiveNP_11	−0.5 / −0.8	−0.1 / +0.1	−0.8 / −0.6	+0.2 / +0.0	+0.0 / +1.0	+0.3 / +0.1	−0.2 / +0.0	−0.3 / −0.1	−0.1 / +0.0	−0.2 / +0.0	−0.2 / −0.1	+0.4 / +0.2	−0.1 / −0.0	
ATLAS_JER_EffectiveNP_12	−0.0 / −0.6	−0.0 / +0.2	−1.0 / −1.1	+0.2 / −0.0	+0.1 / +1.1	+0.4 / +0.9	−0.1 / +0.1	−0.2 / −0.1		−0.1 / −0.0	−0.1 / −0.1	+0.3 / −0.0	−0.2 / +0.1	
ATLAS_JER_EffectiveNP_2	+4.4 / −1.0	−1.0 / +0.1	−0.1 / −0.9	−0.2 / −0.2	+0.3 / +1.8	+0.9 / −2.2	−0.5 / +0.1	−0.2 / −0.2	−0.4 / +0.0	−0.3 / −0.1	+0.2 / −0.9	+1.6 / −0.7	+0.5 / −0.9	
ATLAS_JER_EffectiveNP_3	−3.3 / +2.9	+0.2 / −0.9	−0.7 / −0.9	−0.2 / −0.3	+1.8 / −0.4	−1.1 / +1.2	+0.3 / −0.7	+0.1 / −0.5	+0.2 / −0.5	+0.2 / −0.6	−0.3 / −0.5	−0.0 / +0.7	−0.1 / −0.5	
ATLAS_JER_EffectiveNP_4	+0.5 / +1.5	+0.7 / −0.9	+0.3 / −1.3	+0.3 / −2.2	+1.7 / +0.6	−1.3 / +2.7	+0.3 / −0.7	−0.1 / −0.5	+0.2 / −0.5	+0.3 / −0.5	+0.1 / −0.8	−0.0 / +0.8	−0.3 / −0.9	
ATLAS_JER_EffectiveNP_5	−2.3 / +0.5	−0.2 / −0.2	+1.5 / −1.6	+1.1 / −0.3	+0.5 / +0.4	+1.2 / −1.1	+0.0 / −0.1	+0.1 / −0.2	−0.1 / −0.1	−0.0 / −0.2	−0.3 / −0.4	+0.3 / +0.1	−0.8 / +0.1	
ATLAS_JER_EffectiveNP_6	+1.4 / −0.9	−0.2 / −0.3	+0.9 / −0.9	+0.6 / −2.3	+1.2 / −0.4	−0.7 / +0.5	−0.1 / −0.1	−0.3 / +0.0	−0.2 / +0.0	−0.1 / −0.1	−0.1 / −0.6	−0.4 / +0.6	−0.5 / +0.0	
ATLAS_JER_EffectiveNP_7	−1.8 / +1.0	−0.1 / +0.2	−0.8 / −0.7	+1.0 / +0.6	+0.4 / +0.9	+0.8 / +0.5	−0.2 / +0.1	−0.2 / −0.2	−0.1 / −0.1	−0.2 / +0.0	−0.3 / −0.1	+0.1 / +0.1	−0.6 / −0.2	
ATLAS_JER_EffectiveNP_8	+0.3 / +0.8	+0.4 / −0.1	+0.2 / −1.1	+2.6 / −0.0	+1.1 / +0.2	+1.0 / −0.2	−0.1 / −0.0	−0.0 / −0.2	+0.0 / −0.1	−0.2 / +0.1	+0.0 / −0.2	+0.5 / −0.0	−0.6 / −0.4	
ATLAS_JER_EffectiveNP_9	+1.4 / −1.5	−0.3 / +0.3	−0.8 / −0.1	−1.8 / −0.0	+0.4 / +1.0	+0.7 / +1.0	−0.1 / −0.0	−0.4 / −0.2	−0.0 / −0.1	−0.1 / −0.1	−0.1 / −0.2	+0.6 / −0.2	+0.1 / −0.4	
ATLAS_JES_BJES		−0.0 / +0.1			−0.0 / +0.1	−0.0 / +0.1		−0.0 / +0.1				−1.0 / +3.6	−0.6 / +1.8	
ATLAS_JES_EffectiveNP_Detector1	−0.3 / +0.0	−0.1 / +0.0			−0.1 / +0.1	−0.0 / +0.1		−0.1 / +0.1			−0.1 / +0.1	−0.2 / +0.1	−0.2 / +0.1	
ATLAS_JES_EffectiveNP_Detector2	−0.3 / 0.0													
ATLAS_JES_EffectiveNP_Mixed1	−0.3 / +0.0				−0.1 / +0.1	+0.0 / +0.1					−0.1 / +0.0	−0.1 / +0.1	−0.1 / +0.1	
ATLAS_JES_EffectiveNP_Mixed2	+0.3 / −0.5	+0.1 / −0.1	+0.1 / −0.0		+0.2 / −0.2	+0.1 / −0.2	+0.1 / −0.1	+0.1 / −0.1	+0.1 / −0.1	+0.1 / −0.1	+0.2 / −0.2	+0.2 / −0.3	+0.2 / −0.2	
ATLAS_JES_EffectiveNP_Mixed3	−0.3 / +0.0				−0.1 / +0.1	−0.0 / +0.1		−0.1 / +0.1			−0.1 / +0.0	−0.2 / +0.1	−0.1 / +0.1	
ATLAS_JES_EffectiveNP_Modelling1	−5.1 / +3.9	−1.2 / +0.9	−1.3 / +0.2	−0.0 / +1.3	−3.4 / +2.7	−3.1 / +3.2	−1.0 / +0.9	−1.6 / +1.4	−0.7 / +0.9	−1.0 / +1.1	−2.5 / +2.5	−3.8 / +3.8	−2.2 / +2.6	
ATLAS_JES_EffectiveNP_Modelling2	+0.0 / −0.3	+0.1 / −0.1		0.0 / −0.0	+0.2 / −0.2	+0.1 / −0.1	+0.1 / −0.1	+0.1 / −0.1		+0.0 / −0.1	+0.1 / −0.1	+0.2 / −0.2	+0.1 / −0.2	
ATLAS_JES_EffectiveNP_Modelling3	−0.3 / +0.0	−0.0 / +0.1			−0.2 / +0.1	−0.2 / +0.1		−0.1 / +0.1				−0.2 / +0.1	−0.1 / +0.1	
ATLAS_JES_EffectiveNP_Modelling4	−0.3 / +0.0				−0.0 / +0.1								−0.1 / +0.0	
ATLAS_JES_EffectiveNP_Statistical1	−0.3 / +0.0				−0.0 / +0.1									
ATLAS_JES_EffectiveNP_Statistical2	+0.3 / −1.1	+0.1 / −0.1	+0.0 / −0.1		+0.3 / −0.4	+0.2 / −0.4	+0.1 / −0.1	+0.1 / −0.2	+0.1 / −0.1	+0.1 / −0.1	+0.3 / −0.3	+0.4 / −0.5	+0.3 / −0.3	
ATLAS_JES_EffectiveNP_Statistical3	−0.3 / 0.0					0.0 / −0.0								
ATLAS_JES_EffectiveNP_Statistical4	+0.0 / −0.3			0.0 / −0.0										
ATLAS_JES_EffectiveNP_Statistical5	−0.3 / +0.0													
ATLAS_JES_EffectiveNP_Statistical6	−0.3 / +0.0				−0.0 / +0.1							−0.1 / +0.0	−0.1 / +0.1	
ATLAS_JES_EtaInter_Model	−5.6 / +8.6	−1.8 / +1.9	−1.9 / +0.3	−0.0 / +2.3	−5.5 / +4.9	−5.6 / +6.6	−1.7 / +1.6	−2.1 / +1.8	−1.3 / +1.2	−1.6 / +1.6	−5.2 / +5.6	−5.0 / +5.1	−3.0 / +3.3	
ATLAS_JES_EtaInter_NonClosure_highE														
ATLAS_JES_EtaInter_NonClosure_negEta			−0.7 / +0.0		−0.1 / +0.1	+0.0 / +0.3					−0.1 / +0.1	−0.1 / +0.1		
ATLAS_JES_EtaInter_NonClosure_posEta	−0.3 / +0.2	−0.0 / +0.1			−0.1 / +0.1	−0.2 / +0.3					−0.1 / +0.1	−0.1 / +0.1	−0.0 / +0.2	
ATLAS_JES_EtaInter_Stat	−2.2 / +1.7	−0.3 / +0.3	−0.1 / +0.1		−1.0 / +0.9	−0.8 / +1.3	−0.3 / +0.3	−0.4 / +0.3	−0.2 / +0.3	−0.3 / +0.3	−0.8 / +1.1	−0.9 / +1.0	−0.5 / +0.7	
ATLAS_JES_Flavor_Comp	−10.5 / +15.6	−4.6 / +4.2	−4.1 / +4.3	−5.9 / +4.9	−10.7 / +10.0	−11.1 / +14.2	−3.7 / +3.5	−5.0 / +4.9	−2.9 / +2.9	−3.5 / +3.6	−8.8 / +10.3	−10.5 / +7.6	−6.8 / +5.4	
ATLAS_JES_Flavor_Resp	+6.1 / −5.7	+1.7 / −1.9	+0.3 / −2.2	+2.9 / −1.7	+4.0 / −5.2	+5.4 / −4.9	+1.5 / −1.5	+2.1 / −2.4	+1.4 / −1.2	+1.6 / −1.5	+3.7 / −3.6	+3.2 / −4.9	+2.1 / −2.8	
ATLAS_JES_HighPt														
ATLAS_JES_PU_OffsetMu	−1.6 / +4.1	−1.2 / +1.0	−1.2 / +0.1	+0.0 / +4.3	−3.0 / +3.2	−3.2 / +3.3	−1.0 / +1.0	−1.2 / +1.1	−0.9 / +0.8	−1.0 / +1.0	−2.5 / +2.9	−2.2 / +2.4	−1.6 / +1.7	
ATLAS_JES_PU_OffsetNPV	−2.8 / +1.9	−0.9 / +0.7	−1.2 / +0.9	−0.0 / +1.6	−2.8 / +2.4	−2.0 / +2.7	−0.9 / +0.8	−1.2 / +0.9	−0.7 / +0.8	−0.9 / +0.9	−1.8 / +1.9	−2.8 / +3.1	−1.6 / +2.2	
ATLAS_JES_PU_PtTerm	−0.8 / +0.2	−0.1 / +0.0			−0.3 / +0.2	+0.1 / +0.2		−0.1 / +0.0			+0.0 / +0.1	+0.0 / −0.1	−0.1 / +0.1	
ATLAS_JES_PU_Rho	−7.2 / +8.3	−3.2 / +2.6	−3.3 / +3.1	−1.7 / +4.3	−6.8 / +6.3	−6.0 / +7.6	−2.3 / +2.2	−3.5 / +3.2	−1.8 / +1.9	−2.4 / +2.4	−5.3 / +5.6	−9.3 / +9.9	−5.6 / +6.0	
ATLAS_JES_PunchThrough														
ATLAS_JVT	−1.4 / +1.0	−0.5 / +0.3	−0.4 / +0.2	−0.5 / +0.2	−3.4 / +2.3	−4.2 / +3.0		−0.4 / +0.3		+0.0 / −0.1	−0.8 / +0.5	−0.9 / +0.6	−0.5 / +0.3	
ATLAS_LUMI		+1.7 / −1.7	+1.7 / −1.7	+1.7 / −1.7			+1.7 / −1.7	+1.7 / −1.7		+1.7 / −1.7	+1.7 / −1.7			
ATLAS_MET_SoftTrk_ResoPara														
ATLAS_MET_SoftTrk_ResoPerp														
ATLAS_MET_SoftTrk_Scale														
ATLAS_MUONS_ID	+1.1 / +0.4	−0.2 / +0.1	−0.2 / −0.0		−0.3 / +0.1	−0.9 / +0.8	−0.2 / +0.1	−0.2 / −0.0	−0.1 / +0.1	−0.1 / +0.1	−0.1 / +0.2	−0.1 / +0.1	−0.4 / +0.0	
ATLAS_MUONS_MS	−1.1 / +1.0	−0.3 / +0.3	−0.7 / +0.2		−0.4 / +0.2	−0.1 / +1.0	−0.2 / +0.2	−0.2 / +0.2	−0.2 / +0.2	−0.2 / +0.2	−0.1 / +0.2	−0.1 / +0.2	−0.1 / −0.0	
ATLAS_MUONS_SAGITTA_RESBIAS	+0.7 / +0.7	+0.8 / +0.7	−0.4 / −0.4		+0.8 / +0.7	+1.0 / +1.1	+0.6 / +0.5	+0.7 / +0.7	+0.7 / +0.7	+0.6 / +0.6	+0.7 / +0.6	+0.7 / +0.7	+0.3 / +0.2	
ATLAS_MUONS_SAGITTA_RHO														
ATLAS_MUONS_SCALE	+0.2 / +0.2	−0.4 / +0.3			−0.3 / −0.2	−0.7 / +0.8	−0.1 / +0.0	−0.1 / +0.1	−0.1 / +0.1	−0.5 / +0.3	−0.4 / +0.2	−0.0 / +0.1	−0.0 / −0.1	
ATLAS_MUON_EFF_ISO_STAT	+0.5 / −0.6	+0.5 / −0.6	+0.5 / −0.6		+0.5 / −0.5	+0.6 / −0.6	+0.4 / −0.4	+0.5 / −0.7	+0.4 / −0.5	+0.5 / −0.5	+0.5 / −0.5	+0.5 / −0.5	+0.5 / −0.5	
ATLAS_MUON_EFF_ISO_SYS	+4.1 / −3.9	+5.1 / −4.8	+3.7 / −3.5	+0.2 / −0.2	+4.7 / −4.4	+5.6 / −5.2	+4.0 / −3.8	+3.9 / −3.6	+4.6 / −4.3	+5.2 / −4.9	+4.7 / −4.4	+3.7 / −3.5	+3.8 / −3.6	
ATLAS_MUON_EFF_RECO_STAT	+0.1 / −0.1	+0.1 / −0.1	+0.1 / −0.1		+0.1 / −0.1	+0.1 / −0.1	+0.1 / −0.1	+0.1 / −0.1	+0.1 / −0.1	+0.1 / −0.1	+0.1 / −0.1	+0.1 / −0.1	+0.1 / −0.1	
ATLAS_MUON_EFF_RECO_STAT_LOWPT														
ATLAS_MUON_EFF_RECO_SYS	+0.3 / −0.3	+0.3 / −0.3	+0.3 / −0.3		+0.3 / −0.3	+0.3 / −0.3	+0.3 / −0.3	+0.3 / −0.3	+0.3 / −0.3	+0.3 / −0.3	+0.3 / −0.3	+0.3 / −0.3	+0.3 / −0.3	
ATLAS_MUON_EFF_RECO_SYS_LOWPT														
ATLAS_MUON_EFF_TTVA_STAT														
ATLAS_MUON_EFF_TTVA_SYS														
ATLAS_MUON_EFF_TrigStatUncertainty	+0.1 / −0.1	+0.1 / −0.1	+0.1 / −0.1		+0.1 / −0.1	+0.1 / −0.1	+0.1 / −0.1	+0.1 / −0.1	+0.1 / −0.1	+0.1 / −0.1	+0.1 / −0.1	+0.1 / −0.1	+0.1 / −0.1	
ATLAS_MUON_EFF_TrigSystUncertainty	−0.3 / +0.3	−0.3 / +0.3	−0.2 / +0.2		−0.3 / +0.3	−0.4 / +0.4	−0.3 / +0.3	−0.3 / +0.3	−0.3 / +0.3	−0.3 / +0.3	−0.3 / +0.3	−0.3 / +0.3	−0.3 / +0.3	
ATLAS_PRW_DATASF	−0.2 / +0.4	−1.3 / +1.2	−2.2 / +1.6	−5.5 / +4.6	−1.2 / +0.9	−1.5 / +1.6	−1.4 / +1.3	−1.4 / +1.2	−1.5 / +1.4	−1.6 / +1.5	−1.3 / +1.2	−1.6 / +1.5	−1.5 / +1.4	

Table A.2: Pre-fit experimental systematic normalization uncertainties of the different processes in the SR of the $N_{\text{jet}} = 1$ category. Only non-trivial systematic uncertainties whose values are not 0% are shown.

$N_{\text{jet}} = 1$ SR	Pre-fit impact high / low [%]												
Experimental systematic uncertainty	EW WW	Other VV	VVV	$V\gamma$	Z/γ^* high-mass	Z/γ^* low-mass	$gg WW$	Other H	$qq WW$	ggF	VBF	$t\bar{t}$	Wt
ATLAS_EG_RESOLUTION_ALL	−0.1 / −0.2		−0.0 / +0.1	+0.3 / +0.1	+0.2 / +0.1		−0.7 / −3.6		−0.0 / −0.5	−0.0 / −0.1	−0.0 / −0.1	+0.1 / +0.0	+0.2 / −0.1
ATLAS_EG_SCALE_AF2													
ATLAS_EG_SCALE_ALL	+0.1 / −0.1	+0.2 / −0.2	+0.2 / −0.2	−0.0 / −0.2	+0.2 / −0.0		+0.1 / −2.5	+0.3 / −0.4	+0.4 / −0.7	+0.1 / −0.1	+0.1 / −0.1	+0.1 / −0.1	+0.0 / −0.1
ATLAS_EL_EFF_ID_CorrUncertainty_NP0													
ATLAS_EL_EFF_ID_CorrUncertainty_NP1													
ATLAS_EL_EFF_ID_CorrUncertainty_NP10							−0.1 / +0.1		−0.1 / +0.1				
ATLAS_EL_EFF_ID_CorrUncertainty_NP11	+0.1 / −0.1	+0.1 / −0.1	+0.1 / −0.1	+0.1 / −0.1	+0.1 / −0.1	+0.1 / −0.1	+0.3 / −0.3	+0.1 / −0.1	+0.1 / −0.1	+0.1 / −0.1	+0.1 / −0.1	+0.1 / −0.1	+0.1 / −0.1
ATLAS_EL_EFF_ID_CorrUncertainty_NP12	−0.1 / +0.1	−0.1 / +0.1	−0.1 / +0.1	−0.1 / +0.1	−0.1 / +0.1	−0.1 / +0.1	−0.4 / +0.4	−0.1 / +0.1	−0.1 / +0.1	−0.1 / +0.1	−0.1 / +0.1	−0.1 / +0.1	−0.1 / +0.1
ATLAS_EL_EFF_ID_CorrUncertainty_NP13	−0.1 / +0.1	−0.1 / +0.1	−0.1 / +0.1	−0.1 / +0.1	−0.1 / +0.1	−0.1 / +0.1	−0.2 / +0.2	−0.1 / +0.1	−0.1 / +0.1	−0.1 / +0.1	−0.1 / +0.1	−0.1 / +0.1	−0.1 / +0.1
ATLAS_EL_EFF_ID_CorrUncertainty_NP14				−0.1 / +0.1		−0.1 / +0.1	−0.1 / +0.1		−0.2 / +0.2				
ATLAS_EL_EFF_ID_CorrUncertainty_NP15	−0.1 / +0.1	−0.1 / +0.1	−0.1 / +0.1	−0.1 / +0.1	−0.2 / +0.2	−0.2 / +0.2	−0.6 / +0.6	−0.1 / +0.1	−0.2 / +0.2	−0.1 / +0.1	−0.2 / +0.2	−0.1 / +0.1	−0.1 / +0.1
ATLAS_EL_EFF_ID_CorrUncertainty_NP2													
ATLAS_EL_EFF_ID_CorrUncertainty_NP3													
ATLAS_EL_EFF_ID_CorrUncertainty_NP4													
ATLAS_EL_EFF_ID_CorrUncertainty_NP5													
ATLAS_EL_EFF_ID_CorrUncertainty_NP6													
ATLAS_EL_EFF_ID_CorrUncertainty_NP7													
ATLAS_EL_EFF_ID_CorrUncertainty_NP8													
ATLAS_EL_EFF_ID_CorrUncertainty_NP9							−0.1 / +0.1						
ATLAS_EL_EFF_ID_UncorrUncertainty_NP0													
ATLAS_EL_EFF_ID_UncorrUncertainty_NP1													
ATLAS_EL_EFF_ID_UncorrUncertainty_NP10													
ATLAS_EL_EFF_ID_UncorrUncertainty_NP11													
ATLAS_EL_EFF_ID_UncorrUncertainty_NP12	+0.1 / −0.1	+0.1 / −0.1			+0.1 / −0.1		+0.4 / −0.4		+0.1 / −0.1		+0.1 / −0.1	+0.1 / −0.1	
ATLAS_EL_EFF_ID_UncorrUncertainty_NP13							+0.1 / −0.1						
ATLAS_EL_EFF_ID_UncorrUncertainty_NP14							+0.1 / −0.1						
ATLAS_EL_EFF_ID_UncorrUncertainty_NP15							+0.2 / −0.2						
ATLAS_EL_EFF_ID_UncorrUncertainty_NP16													
ATLAS_EL_EFF_ID_UncorrUncertainty_NP17							+0.1 / −0.1						
ATLAS_EL_EFF_ID_UncorrUncertainty_NP2													
ATLAS_EL_EFF_ID_UncorrUncertainty_NP3	+0.2 / −0.2	+0.3 / −0.3	+0.2 / −0.2	+0.3 / −0.3	+0.3 / −0.3	+0.2 / −0.2	+0.7 / −0.7	+0.2 / −0.2	+0.3 / −0.3	+0.3 / −0.3	+0.2 / −0.2	+0.3 / −0.3	+0.3 / −0.3
ATLAS_EL_EFF_ID_UncorrUncertainty_NP4						+0.1 / −0.1							
ATLAS_EL_EFF_ID_UncorrUncertainty_NP5													
ATLAS_EL_EFF_ID_UncorrUncertainty_NP6	+0.1 / −0.1	+0.1 / −0.1	+0.1 / −0.1	+0.1 / −0.1	+0.1 / −0.1	+0.1 / −0.1	+0.1 / −0.1	+0.1 / −0.1		+0.1 / −0.1	+0.1 / −0.1	+0.1 / −0.1	+0.1 / −0.1
ATLAS_EL_EFF_ID_UncorrUncertainty_NP7													
ATLAS_EL_EFF_ID_UncorrUncertainty_NP8													
ATLAS_EL_EFF_ID_UncorrUncertainty_NP9													
ATLAS_EL_EFF_Iso_TOTAL_1NPCOR_PLUS_UNCOR	+0.3 / −0.2	+0.3 / −0.3	+0.2 / −0.2	+0.3 / −0.3	+0.3 / −0.3	+0.2 / −0.2	+0.8 / −0.8	+0.2 / −0.2	+0.3 / −0.3	+0.2 / −0.2	+0.3 / −0.3	+0.3 / −0.3	+0.3 / −0.3
ATLAS_EL_EFF_Reco_TOTAL_1NPCOR_PLUS_UNCOR	+0.2 / −0.2	+0.2 / −0.2	+0.2 / −0.2	+0.2 / −0.2	+0.2 / −0.2	+0.2 / −0.2	+0.5 / −0.5	+0.2 / −0.2	+0.2 / −0.2	+0.2 / −0.2	+0.2 / −0.2	+0.2 / −0.2	+0.2 / −0.2
ATLAS_EL_EFF_TRIG_TOTAL_1NPCOR_PLUS_UNCOR													
ATLAS_FTAG_EXTRAP													
ATLAS_FT_EFF_Eigen_B_0	+0.1 / −0.1	+0.1 / −0.1			+0.1 / −0.1		−0.2 / +0.2	+0.1 / −0.1	+0.1 / −0.1	+0.1 / −0.1		+7.1 / −6.9	+5.6 / −5.6
ATLAS_FT_EFF_Eigen_B_1												+1.4 / −1.4	+1.3 / −1.3
ATLAS_FT_EFF_Eigen_B_2												−1.1 / +1.1	−1.0 / +1.0
ATLAS_FT_EFF_Eigen_C_0	+0.7 / −0.7	+0.2 / −0.2	+0.3 / −0.3	+0.5 / −0.5	+0.5 / −0.5	+0.6 / −0.6	+0.1 / −0.1	+0.4 / −0.4	+0.4 / −0.4	+0.2 / −0.2	+0.2 / −0.2	+0.1 / −0.1	+0.1 / −0.1
ATLAS_FT_EFF_Eigen_C_1													
ATLAS_FT_EFF_Eigen_C_2													
ATLAS_FT_EFF_Eigen_Light_0	+0.4 / −0.4	+0.4 / −0.4	+0.3 / −0.3	+0.4 / −0.4	+0.4 / −0.4	+0.5 / −0.5	+0.5 / −0.4	+0.4 / −0.4	+0.4 / −0.4	+0.4 / −0.4	+0.4 / −0.4	+0.3 / −0.3	+0.2 / −0.2
ATLAS_FT_EFF_Eigen_Light_1													
ATLAS_FT_EFF_Eigen_Light_2													
ATLAS_FT_EFF_Eigen_Light_3													
ATLAS_FT_EFF_extrapolation_from_charm	−0.7 / +0.7				−0.6 / +0.6	−0.5 / +0.5							
ATLAS_JER_DataVsMC	−0.0 / +0.4		−0.0 / +0.2	−0.0 / +0.4	−0.9 / +0.4	+0.5 / +1.5	−3.5 / −6.4	−1.7 / +0.9	+3.3 / −2.0	+0.0 / +0.3	+0.0 / +0.2	+0.2 / −0.1	+0.6 / −0.3
ATLAS_JER_EffectiveNP_1	+0.6 / −0.4	+0.8 / −0.2	−0.9 / +0.4	−0.3 / +0.4	+1.3 / −0.4	+0.7 / +1.2	+2.7 / −2.1	+2.6 / −1.8	−0.3 / +1.3	+1.4 / −0.9	+0.6 / −0.4	−0.6 / +0.8	−0.8 / +0.8
ATLAS_JER_EffectiveNP_10	+0.0 / +0.4	+0.2 / +0.3	−0.2 / +0.1	+0.0 / −0.1	−0.1 / −0.1	+0.4 / +1.2	−0.1 / +3.1	−0.5 / +0.4	−0.2 / +1.3	−0.2 / +0.4	+0.1 / −0.2	−0.1 / +0.2	−0.2 / +0.1
ATLAS_JER_EffectiveNP_11	+0.2 / +0.3	+0.1 / +0.4	−0.1 / +0.0	+0.2 / −0.2	+0.0 / +0.2	−0.1 / +1.0	−0.8 / −3.9	+1.0 / −0.8	+1.2 / +0.1	+0.1 / +0.1	−0.1 / +0.0	+0.0 / +0.1	+0.1 / −0.1
ATLAS_JER_EffectiveNP_12	+0.5 / −0.4	+0.1 / +0.3	−0.1 / −0.0	+0.1 / −0.3	+0.1 / −0.4	+0.3 / +2.1	−2.1 / +0.9	+0.9 / −0.8	+0.5 / +0.5	−0.0 / +0.1	−0.1 / +0.2	−0.1 / +0.1	−0.3 / +0.2
ATLAS_JER_EffectiveNP_2	+1.0 / +0.2	+0.8 / +0.1	+0.1 / −0.3	−0.0 / −0.2	+0.8 / −0.5	−1.3 / +4.2	+6.1 / −5.4	+3.5 / −2.0	−1.4 / +3.8	+0.6 / +0.4	+0.5 / −0.1	+0.7 / −0.3	−0.8 / +0.1
ATLAS_JER_EffectiveNP_3	−0.1 / +0.7	+0.2 / +0.6	+0.0 / −0.3	+0.1 / −0.1	−0.6 / +0.5	+3.7 / −0.6	−1.9 / +0.8	−0.4 / +2.6	+4.2 / −1.0	+0.2 / +0.7	+0.0 / +0.2	+0.1 / +0.0	+0.1 / −0.2
ATLAS_JER_EffectiveNP_4	+0.1 / +0.9	+0.3 / +0.5	+0.1 / −0.3	−0.8 / +0.1	−1.1 / +0.5	+2.4 / −1.7	−6.3 / +7.2	−0.3 / +1.5	+1.4 / −2.4	+0.3 / +0.8	+0.2 / +0.1	+0.2 / −0.0	+0.1 / −0.1
ATLAS_JER_EffectiveNP_5	−0.2 / +0.3	−0.2 / +0.5		+0.6 / −0.4	+0.4 / −0.1	−2.3 / +1.5	−6.0 / −3.9	−0.2 / +1.4	+0.1 / +1.8	−0.2 / +0.5	+0.1 / +0.3	−0.2 / +0.2	−0.3 / +0.0
ATLAS_JER_EffectiveNP_6	−0.1 / +0.3	+0.1 / +0.5	−0.1 / +0.0	−0.7 / +0.1	−0.6 / +0.5	+1.0 / −0.2	−10.6 / +6.7	−0.2 / +1.8	−0.7 / +3.4	+0.3 / +0.2	+0.5 / −0.1	−0.4 / +0.4	−0.3 / +0.1
ATLAS_JER_EffectiveNP_7		+0.4 / +0.0	−0.1 / −0.0	−0.4 / −0.0	+0.1 / −0.1	+2.3 / −0.2	+4.5 / +1.4	−0.1 / −0.1	+0.7 / −0.5	+0.3 / −0.0	−0.1 / +0.2	−0.2 / −0.1	+0.2 / −0.2
ATLAS_JER_EffectiveNP_8	−0.2 / −0.0	+0.4 / +0.2	+0.1 / −0.2	+0.5 / −0.4	−0.4 / −0.5	−0.3 / +0.6	−5.7 / −5.0	+0.3 / +0.5	+1.1 / −0.2	−0.0 / +0.4	−0.2 / +0.2	+0.2 / −0.3	−0.1 / −0.1
ATLAS_JER_EffectiveNP_9	+0.5 / −0.1	+0.1 / +0.4	+0.1 / −0.1	−0.2 / −0.3	+0.2 / −0.5	−0.6 / +1.6	+1.9 / +3.7	+1.7 / −1.0	+1.4 / +0.4	+0.3 / +0.2	+0.0 / +0.2	+0.0 / −0.2	−0.2 / −0.2
ATLAS_JES_BJES	−0.0 / +0.1							−0.0 / +0.1	+0.0 / +0.1			−0.3 / +1.8	+0.1 / +0.5
ATLAS_JES_EffectiveNP_Detector1		+0.1 / −0.0		−0.3 / +0.0	+0.1 / −0.0	−0.3 / +0.0		−0.2 / +0.1	−0.2 / +0.2	−0.1 / −0.1		−0.1 / +0.1	
ATLAS_JES_EffectiveNP_Detector2													
ATLAS_JES_EffectiveNP_Mixed1		+0.1 / −0.0	+0.1 / −0.1	−0.2 / +0.0	+0.1 / +0.0	−0.3 / +0.0		−0.0 / +0.1	−0.2 / −0.1				
ATLAS_JES_EffectiveNP_Mixed2	+0.1 / −0.0	−0.0 / +0.1		+0.1 / −0.2	+0.1 / +0.1	−0.0 / −0.3		+0.1 / −0.3	+0.2 / −0.3	−0.1 / +0.0	−0.0 / −0.1	+0.1 / −0.1	
ATLAS_JES_EffectiveNP_Mixed3			−0.0 / +0.1	−0.3 / +0.0	+0.1 / +0.0	−0.3 / +0.0		−0.1 / +0.1	−0.1 / +0.0			−0.1 / +0.1	
ATLAS_JES_EffectiveNP_Modelling1	−0.3 / +1.3	+0.3 / −0.6	−0.9 / +0.9	−1.5 / +2.2	−0.4 / +1.0	−1.4 / +1.2	−6.4 / +0.7	−1.2 / +2.3	−1.0 / −0.2	+0.4 / −0.7	−0.1 / −0.4	−2.1 / +2.0	−1.1 / +0.4
ATLAS_JES_EffectiveNP_Modelling2	+0.1 / −0.1		+0.1 / −0.1	+0.0 / −0.2		+0.0 / −0.3		+0.0 / −0.1	+0.2 / +0.0			+0.1 / −0.1	
ATLAS_JES_EffectiveNP_Modelling3	−0.1 / +0.0	−0.0 / +0.1	−0.1 / +0.1	−0.1 / +0.0		−0.3 / −0.0		−0.1 / −0.1	+0.1 / −0.0			−0.1 / +0.1	
ATLAS_JES_EffectiveNP_Modelling4								−0.1 / +0.0					
ATLAS_JES_EffectiveNP_Statistical1													
ATLAS_JES_EffectiveNP_Statistical2	+0.1 / −0.2		+0.1 / −0.1	+0.1 / −0.3	+0.1 / +0.1			+0.2 / −0.4	+0.5 / −0.1	−0.1 / +0.1	−0.0 / −0.1	+0.2 / −0.3	
ATLAS_JES_EffectiveNP_Statistical3													
ATLAS_JES_EffectiveNP_Statistical4						+0.0 / −0.4		−0.1 / −0.0	−0.1 / −0.0				
ATLAS_JES_EffectiveNP_Statistical5					+0.1 / +0.0	−0.4 / −0.0		+0.0 / −0.1	−0.1 / −0.0			−0.1 / +0.0	
ATLAS_JES_EffectiveNP_Statistical6				−0.1 / +0.0		−0.4 / +0.0		−0.1 / +0.0	−0.1 / −0.0				
ATLAS_JES_EtaInter_Model	−0.7 / +1.6	+0.3 / −0.5	−2.3 / +2.3	−3.5 / +3.4	−0.6 / +0.9	−1.4 / +1.7	−2.7 / −0.7	−3.3 / +3.5	−3.6 / +1.2	+1.0 / −1.4	+0.2 / −0.4	−2.8 / +2.6	−1.0 / +0.8
ATLAS_JES_EtaInter_NonClosure_highE													
ATLAS_JES_EtaInter_NonClosure_negEta				−0.1 / +0.2			+0.0 / +2.8	−0.0 / +0.1	−0.1 / −0.5			−0.1 / +0.1	
ATLAS_JES_EtaInter_NonClosure_posEta	−0.0 / +0.1				−0.1 / −0.1			−0.2 / +0.0	−0.2 / −0.4	+0.1 / −0.1		−0.1 / +0.1	
ATLAS_JES_EtaInter_Stat	−0.2 / +0.4	+0.0 / −0.1	−0.4 / +0.4	−0.6 / +1.1	−0.1 / +0.2		−3.0 / +0.8	−0.4 / +0.1	−0.7 / +0.2	+0.0 / −0.2	+0.0 / −0.1	−0.6 / +0.5	−0.1 / +0.1
ATLAS_JES_Flavor_Comp	−2.0 / +2.8	+0.9 / −1.3	−3.9 / +3.9	−7.0 / +7.4	−0.8 / +2.1	−5.6 / +5.2	−7.6 / +3.9	−5.1 / +6.5	−6.7 / +2.3	+2.3 / −2.7	+0.3 / −1.2	−6.5 / +4.1	−3.0 / +1.5
ATLAS_JES_Flavor_Resp	+1.8 / −0.5	−1.1 / +0.6	+1.1 / −1.0	+3.0 / −3.0	+1.1 / −0.5	+2.7 / −1.1	−0.0 / −8.3	+2.8 / −1.7	+0.5 / −2.7	−1.2 / +0.8	−0.7 / +0.1	+1.6 / −2.9	+0.5 / −1.5
ATLAS_JES_HighPt													
ATLAS_JES_PU_OffsetMu	−0.3 / +0.9	−0.1 / −0.2	−1.5 / +1.4	−2.3 / +1.8	−0.3 / +0.9	−0.1 / +0.2	−2.4 / +0.9	−1.5 / +2.5	−2.6 / +2.2	+0.2 / −0.6	+0.2 / −0.3	−1.5 / +1.3	−0.8 / +0.4
ATLAS_JES_PU_OffsetNPV	−0.4 / +1.4	−0.0 / −0.3	−0.8 / +0.8	−1.3 / +1.3	−0.5 / +1.4	−1.3 / +1.4	−0.6 / +3.7	−0.7 / +1.6	−3.0 / −0.7	+0.1 / −0.4	−0.3 / −0.1	−1.7 / +1.8	−0.9 / +0.2
ATLAS_JES_PU_PtTerm	+0.3 / +0.0	+0.1 / +0.0	+0.1 / −0.1	−0.0 / +0.1	+0.1 / −0.0	−0.8 / +0.3	−2.3 / +0.3	+0.1 / −0.2	−0.7 / +0.2	−0.1 / −0.0			+0.1 / −0.2
ATLAS_JES_PU_Rho	−1.3 / +2.7	+0.3 / −0.7	−2.2 / +2.2	−4.1 / +4.5	−0.2 / +1.9	−2.8 / +3.3	−11.3 / −0.2	−3.2 / +4.0	−4.3 / +1.9	+1.0 / −1.4	−0.2 / −0.7	−5.3 / +5.3	−2.4 / +1.7
ATLAS_JES_PunchThrough							0.0 / −0.0						
ATLAS_JVT	−0.3 / +0.1	+0.1 / −0.2	−0.2 / +0.1	−0.6 / +0.4	−0.4 / +0.2	−0.2 / +0.1	−0.7 / +0.5	−1.5 / +1.0	−1.8 / +1.2	+0.2 / −0.2	+0.1 / −0.1	−0.3 / +0.2	+0.0 / −0.1
ATLAS_LUMI	+1.7 / −1.7	+1.7 / −1.7	+1.7 / −1.7		+1.7 / −1.7	+1.7 / −1.7	+1.7 / −1.7			+1.7 / −1.7			
ATLAS_MET_SoftTrk_ResoPara	−0.1 / +0.1						−0.2 / +0.2	−0.1 / +0.1	+0.1 / −0.1				
ATLAS_MET_SoftTrk_ResoPerp							+0.2 / −0.2						
ATLAS_MET_SoftTrk_Scale	−0.0 / +0.1				+0.0 / +0.1			−0.2 / +0.2					
ATLAS_MUONS_ID	−0.0 / +0.1	−0.2 / +0.1	−0.2 / +0.1	−0.3 / −0.1	−0.0 / +0.1	−0.2 / −0.0		−0.0 / −0.1	−0.3 / +0.0	−0.0 / +0.1	−0.2 / +0.0	−0.1 / +0.2	−0.2 / +0.0
ATLAS_MUONS_MS	−0.2 / +0.2	−0.2 / +0.2	−0.2 / +0.2	−0.1 / −0.2	+0.0 / +0.2	+0.0 / −0.3		−0.3 / −0.2	+0.1 / −0.6	−0.2 / +0.2	−0.1 / +0.2	−0.2 / +0.2	−0.4 / +0.1
ATLAS_MUONS_SAGITTA_RESBIAS	+0.6 / +0.6	+0.6 / +0.6	+0.6 / +0.6	+0.6 / +0.6	+0.6 / +0.5	−0.6 / −0.6		+0.6 / +0.7	+1.9 / +1.8	+0.6 / +0.6	+0.6 / +0.6	+0.6 / +0.6	+0.6 / +0.6
ATLAS_MUONS_SAGITTA_RHO													
ATLAS_MUONS_SCALE	−0.2 / +0.2	−0.4 / +0.2	−0.2 / +0.1	−0.1 / −0.0	−0.2 / +0.2			−0.3 / +0.1	−1.1 / +0.7	−0.1 / +0.1	−0.1 / +0.1	−0.1 / +0.0	−0.1 / +0.0
ATLAS_MUON_EFF_ISO_STAT	+0.5 / −0.5	+0.5 / −0.5	+0.5 / −0.5	+0.5 / −0.5	+0.5 / −0.6	+0.5 / −0.6		+0.5 / −0.5	+0.5 / −0.5	+0.5 / −0.5	+0.5 / −0.5	+0.5 / −0.5	+0.5 / −0.5
ATLAS_MUON_EFF_ISO_SYS	+3.9 / −3.7	+4.4 / −4.1	+3.8 / −3.6	+3.7 / −3.4	+4.0 / −3.7	+3.6 / −3.4		+4.0 / −3.7	+4.2 / −3.9	+3.9 / −3.7	+3.9 / −3.7	+3.8 / −3.5	+3.6 / −3.4
ATLAS_MUON_EFF_RECO_STAT	+0.1 / −0.1	+0.1 / −0.1	+0.1 / −0.1	+0.1 / −0.1	+0.1 / −0.1	+0.1 / −0.1		+0.1 / −0.1	+0.1 / −0.1	+0.1 / −0.1	+0.1 / −0.1	+0.1 / −0.1	+0.1 / −0.1
ATLAS_MUON_EFF_RECO_STAT_LOWPT													
ATLAS_MUON_EFF_RECO_SYS	+0.3 / −0.3	+0.3 / −0.3	+0.3 / −0.3	+0.3 / −0.3	+0.3 / −0.3	+0.3 / −0.3		+0.3 / −0.3	+0.3 / −0.3	+0.3 / −0.3	+0.3 / −0.3	+0.3 / −0.3	+0.3 / −0.3
ATLAS_MUON_EFF_RECO_SYS_LOWPT													
ATLAS_MUON_EFF_TTVA_STAT													
ATLAS_MUON_EFF_TTVA_SYS													
ATLAS_MUON_EFF_TrigStatUncertainty	+0.1 / −0.1	+0.1 / −0.1	+0.1 / −0.1	+0.1 / −0.1	+0.1 / −0.1	+0.1 / −0.1		+0.1 / −0.1	+0.1 / −0.1	+0.1 / −0.1	+0.1 / −0.1	+0.1 / −0.1	+0.1 / −0.1
ATLAS_MUON_EFF_TrigSystUncertainty	−0.3 / +0.3	−0.3 / +0.3	−0.3 / +0.3	−0.2 / +0.3	−0.3 / +0.3	−0.2 / +0.2		−0.3 / +0.3	−0.3 / +0.3	−0.3 / +0.3	−0.3 / +0.3	−0.3 / +0.3	−0.2 / +0.3
ATLAS_PRW_DATASF	−0.9 / +1.0	−0.7 / +0.7	−1.1 / +1.0	−1.2 / +1.1	−1.1 / +1.0	−1.6 / +1.6	−3.8 / +1.7	+0.4 / −0.3	−0.3 / +0.5	−0.7 / +0.6	−0.9 / +0.9	−1.4 / +1.3	−1.2 / +1.2

Table A.3: Pre-fit experimental systematic normalization uncertainties of the different processes in the SR of the $N_{\text{jet}} \geq 2$ ggF-enriched category. Only non-trivial systematic uncertainties whose values are not 0% are shown.

$N_{\text{jet}} \geq 2$ ggF-enriched SR	Pre-fit impact high / low [%]													
Experimental systematic uncertainty	EW WW	Other VV	VVV	$V\gamma$	Z/γ^* high-mass	Z/γ^* low-mass	$gg WW$	Other H	$qq WW$	ggF	VBF	$t\bar{t}$	Wt
ATLAS_EG_RESOLUTION_ALL	+0.0 / +0.1	-0.1 / +0.1	-0.1 / +0.1	-0.0 / -0.2	+0.0 / -0.2	-0.1 / -0.5	-0.2 / +0.2	+0.1 / +0.1		-0.1 / +0.1	+0.1 / -0.1	+0.1 / +0.0	+0.2 / +0.1
ATLAS_EG_SCALE_AF2													
ATLAS_EG_SCALE_ALL	-0.1 / +0.2	-0.3 / +0.3		+0.0 / -0.6	-0.2 / +0.2	+0.3 / -0.0	-0.2 / +0.2	-0.0 / +0.1	-0.1 / +0.1	-0.1 / +0.0	+0.0 / +0.1	-0.0 / +0.2	+0.3 / +0.2
ATLAS_EL_EFF_ID_CorrUncertainty_NP0													
ATLAS_EL_EFF_ID_CorrUncertainty_NP1													
ATLAS_EL_EFF_ID_CorrUncertainty_NP10													
ATLAS_EL_EFF_ID_CorrUncertainty_NP11	+0.1 / -0.1	+0.1 / -0.1	+0.1 / -0.1	+0.3 / -0.3	+0.1 / -0.1	+0.1 / -0.1	+0.1 / -0.1	+0.1 / -0.1	+0.1 / -0.1	+0.1 / -0.1	+0.1 / -0.1	+0.1 / -0.1	+0.1 / -0.1
ATLAS_EL_EFF_ID_CorrUncertainty_NP12	−0.1 / +0.1	−0.1 / +0.1	−0.1 / +0.1	−0.2 / +0.2	−0.1 / +0.1	−0.1 / +0.1	−0.1 / +0.1	−0.1 / +0.1	−0.1 / +0.1	−0.1 / +0.1	−0.1 / +0.1	−0.1 / +0.1	−0.1 / +0.1
ATLAS_EL_EFF_ID_CorrUncertainty_NP13		−0.1 / +0.1	−0.1 / +0.1			−0.1 / +0.1						−0.1 / +0.1	
ATLAS_EL_EFF_ID_CorrUncertainty_NP14			−0.1 / +0.1	−0.3 / +0.3		−0.1 / +0.1	+0.1 / −0.1						
ATLAS_EL_EFF_ID_CorrUncertainty_NP15	−0.1 / +0.1	−0.2 / +0.2	−0.1 / +0.1	−1.1 / +1.1	−0.1 / +0.1	−0.1 / +0.1	−0.1 / +0.1	−0.1 / +0.1	−0.1 / +0.1	−0.1 / +0.1	−0.1 / +0.1	−0.1 / +0.1	−0.1 / +0.1
ATLAS_EL_EFF_ID_CorrUncertainty_NP2													
ATLAS_EL_EFF_ID_CorrUncertainty_NP3													
ATLAS_EL_EFF_ID_CorrUncertainty_NP4													
ATLAS_EL_EFF_ID_CorrUncertainty_NP5													
ATLAS_EL_EFF_ID_CorrUncertainty_NP6													
ATLAS_EL_EFF_ID_CorrUncertainty_NP7													
ATLAS_EL_EFF_ID_CorrUncertainty_NP8													
ATLAS_EL_EFF_ID_CorrUncertainty_NP9													
ATLAS_EL_EFF_ID_UncorrUncertainty_NP0													
ATLAS_EL_EFF_ID_UncorrUncertainty_NP1													
ATLAS_EL_EFF_ID_UncorrUncertainty_NP10													
ATLAS_EL_EFF_ID_UncorrUncertainty_NP11													
ATLAS_EL_EFF_ID_UncorrUncertainty_NP12			+0.1 / −0.1	+0.1 / −0.1	+0.1 / −0.1	+0.1 / −0.1							
ATLAS_EL_EFF_ID_UncorrUncertainty_NP13				+0.1 / −0.1									
ATLAS_EL_EFF_ID_UncorrUncertainty_NP14				+0.1 / −0.1									
ATLAS_EL_EFF_ID_UncorrUncertainty_NP15				+0.2 / −0.2									
ATLAS_EL_EFF_ID_UncorrUncertainty_NP16				+0.1 / −0.1									
ATLAS_EL_EFF_ID_UncorrUncertainty_NP17				+0.2 / −0.2									
ATLAS_EL_EFF_ID_UncorrUncertainty_NP2													
ATLAS_EL_EFF_ID_UncorrUncertainty_NP3	+0.2 / −0.2	+0.2 / −0.2	+0.3 / −0.3		+0.2 / −0.2	+0.2 / −0.2	+0.3 / −0.3	+0.2 / −0.2	+0.2 / −0.2	+0.2 / −0.2	+0.2 / −0.2	+0.2 / −0.2	+0.2 / −0.2
ATLAS_EL_EFF_ID_UncorrUncertainty_NP4													
ATLAS_EL_EFF_ID_UncorrUncertainty_NP5													
ATLAS_EL_EFF_ID_UncorrUncertainty_NP6	+0.1 / −0.1		+0.1 / −0.1	+0.1 / −0.1	+0.1 / −0.1		+0.1 / −0.1	+0.1 / −0.1	+0.1 / −0.1	+0.1 / −0.1	+0.1 / −0.1	+0.1 / −0.1	+0.1 / −0.1
ATLAS_EL_EFF_ID_UncorrUncertainty_NP7													
ATLAS_EL_EFF_ID_UncorrUncertainty_NP8	+0.1 / −0.1		+0.1 / −0.1	+0.1 / −0.1							+0.1 / −0.1		
ATLAS_EL_EFF_ID_UncorrUncertainty_NP9													
ATLAS_EL_EFF_Iso_TOTAL_1NPCOR_PLUS_UNCOR	+0.2 / −0.2	+0.3 / −0.3	+0.3 / −0.3	+0.6 / −0.6	+0.2 / −0.2	+0.3 / −0.3	+0.2 / −0.2	+0.2 / −0.2	+0.2 / −0.2	+0.2 / −0.2	+0.2 / −0.2	+0.2 / −0.2	+0.2 / −0.2
ATLAS_EL_EFF_Reco_TOTAL_1NPCOR_PLUS_UNCOR	+0.2 / −0.2	+0.2 / −0.2	+0.2 / −0.2	+0.4 / −0.4	+0.2 / −0.2	+0.2 / −0.2	+0.2 / −0.2	+0.2 / −0.2	+0.2 / −0.2	+0.2 / −0.2	+0.2 / −0.2	+0.2 / −0.2	+0.2 / −0.2
ATLAS_EL_EFF_TRIG_TOTAL_1NPCOR_PLUS_UNCOR													
ATLAS_FTAG_EXTRAP				−0.1 / +0.1									
ATLAS_FT_EFF_Eigen_B_0		+0.1 / −0.1			+0.1 / −0.1	+0.2 / −0.2	+0.1 / −0.1	+0.5 / −0.5	+0.1 / −0.1	+0.1 / −0.1	+0.1 / −0.1	+9.9 / −9.4	+6.8 / −6.7
ATLAS_FT_EFF_Eigen_B_1								+0.2 / −0.2				+2.8 / −2.8	+2.1 / −2.0
ATLAS_FT_EFF_Eigen_B_2								−0.1 / +0.1				−2.0 / +2.0	−1.3 / +1.3
ATLAS_FT_EFF_Eigen_C_0	+0.5 / −0.5	+0.8 / −0.8	+1.0 / −1.0	+0.3 / −0.3	+0.5 / −0.5	+0.6 / −0.6	+0.4 / −0.3	+0.9 / −0.9	+0.4 / −0.4	+0.3 / −0.3	+0.4 / −0.4	+0.3 / −0.3	+0.2 / −0.2
ATLAS_FT_EFF_Eigen_C_1	+0.1 / −0.1	+0.1 / −0.1	+0.1 / −0.1	+0.1 / −0.1				+0.1 / −0.1			+0.1 / −0.1		
ATLAS_FT_EFF_Eigen_C_2													
ATLAS_FT_EFF_Eigen_Light_0	+0.9 / −0.9	+1.0 / −1.0	+1.0 / −1.0	+1.0 / −1.0	+1.0 / −1.0	+0.9 / −0.9	+1.0 / −1.0	+0.9 / −0.9	+1.0 / −1.0	+0.9 / −0.9	+0.7 / −0.7	+0.7 / −0.7	+0.7 / −0.7
ATLAS_FT_EFF_Eigen_Light_1					+0.1 / −0.1	+0.1 / −0.1	+0.1 / −0.1						
ATLAS_FT_EFF_Eigen_Light_2													
ATLAS_FT_EFF_Eigen_Light_3													
ATLAS_FT_EFF_extrapolation_from_charm		−0.9 / +0.9	−0.3 / +0.3					−0.3 / +0.3					
ATLAS_JER_DataVsMC	+0.5 / −0.6	−1.6 / +0.8	−1.9 / +2.6	+12.0 / +14.5	−1.6 / +1.7	−3.8 / +6.2	−1.5 / +1.6	−0.2 / +0.0	+0.0 / −0.1	−0.6 / +0.4	+0.1 / +0.2	−0.3 / +0.1	−0.7 / +1.7
ATLAS_JER_EffectiveNP_1	+0.4 / −0.5	+2.4 / −1.6	+0.3 / −2.7	+23.7 / +2.7	+6.7 / −4.1	+14.1 / −6.1	+3.2 / −1.2	−0.2 / +0.2	+0.3 / −0.2	+1.9 / −0.5	+1.9 / −1.0	+0.8 / −0.5	+3.6 / −1.7
ATLAS_JER_EffectiveNP_10	−0.3 / −0.1	−0.0 / +0.7	+0.2 / −1.0	+6.6 / −0.0	−0.5 / +1.6	+1.0 / −0.0	+0.8 / +0.1	−0.1 / −0.0	+0.0 / +0.1	+0.1 / +0.3	+0.1 / +0.3	+0.1 / +0.3	−1.3 / +0.3
ATLAS_JER_EffectiveNP_11	+0.1 / −0.4	+0.1 / +0.5	−1.2 / −0.6	−2.7 / +9.8	+0.1 / +0.6	+1.4 / −0.2	+0.8 / +0.9	−0.2 / −0.0	+0.1 / +0.2	+0.4 / +0.1	+0.3 / +0.1	+0.2 / +0.0	−0.1 / −0.8
ATLAS_JER_EffectiveNP_12	−0.0 / −0.3	+0.8 / +0.1	+1.3 / −2.0	−2.7 / +0.0	+1.3 / −0.9	+3.9 / −4.1	+1.7 / −0.6	−0.1 / −0.0	−0.1 / +0.3	+0.4 / −0.1	+0.1 / +0.0	+0.3 / +0.0	+0.2 / −0.7
ATLAS_JER_EffectiveNP_2	−0.5 / −0.2	+1.6 / −1.7	−0.4 / −0.1	+23.0 / +1.8	+6.7 / −3.6	+15.8 / −3.2	+2.9 / −1.2	+0.5 / −0.2	+0.3 / −0.0	+1.6 / −0.9	+0.6 / +0.1	+1.1 / −0.4	+3.2 / −1.7
ATLAS_JER_EffectiveNP_3	−0.5 / −0.5	−0.5 / +1.4	−1.1 / +1.5	+1.3 / +23.9	−0.8 / +3.9	−1.4 / +12.3	−1.9 / +2.4	−0.1 / −0.2	+0.1 / +0.2	−0.5 / +1.0	−0.1 / +1.0	−0.3 / +0.8	−1.6 / +1.8
ATLAS_JER_EffectiveNP_4	+0.1 / −1.2	−0.5 / +0.5	+0.0 / −1.0	−1.1 / +24.2	−2.4 / +2.7	−2.4 / +7.9	−1.5 / +2.4	−0.3 / −0.1	−0.4 / +0.3	−0.7 / +1.1	−0.3 / +0.9	−0.2 / +0.5	−2.0 / +1.1
ATLAS_JER_EffectiveNP_5	−0.9 / +0.2	−0.4 / +0.9	−1.3 / −0.2	+3.6 / −0.9	−0.9 / +2.2	−0.8 / +3.5	+0.6 / −0.2	−0.4 / −0.3	+0.0 / +0.2	+0.5 / +0.4	+0.2 / +0.2	−0.1 / +0.4	−0.7 / +1.5
ATLAS_JER_EffectiveNP_6	−0.3 / −0.3	+0.4 / +0.3	−0.8 / −1.3	+10.9 / −0.6	−2.2 / +3.2	−0.3 / +7.3	+0.8 / +1.2	−0.2 / +0.0	+0.2 / +0.3	−0.2 / +0.9	+0.1 / +0.4	−0.2 / +0.3	−2.2 / +2.0
ATLAS_JER_EffectiveNP_7	−0.1 / −0.5	−0.1 / +0.7	−3.3 / +2.6	+0.0 / +0.8	−0.3 / −0.1	+0.2 / −0.1	+0.3 / +0.7	−0.3 / −0.2	+0.1 / −0.1	+0.0 / +0.1	+0.0 / +0.2	+0.1 / +0.1	+0.7 / +0.2
ATLAS_JER_EffectiveNP_8	+0.1 / −0.5	−0.1 / +0.8	+1.1 / +0.2	+19.5 / +7.1	−0.0 / +0.2	+1.0 / +0.6	+0.1 / +1.0	−0.2 / −0.1	+0.4 / −0.2	−0.2 / +0.2	+0.3 / +0.1	+0.1 / −0.1	+1.1 / −1.0
ATLAS_JER_EffectiveNP_9	−0.2 / −0.3	+1.1 / +0.1	+0.1 / −0.6	+9.8 / +0.5	+2.0 / −1.8	+2.1 / −0.5	+1.3 / −0.2	−0.3 / +0.0	−0.0 / +0.3	+0.6 / −0.1	+0.3 / −0.0	+0.4 / −0.1	+0.2 / −1.1
ATLAS_JES_BJES	−0.0 / −0.0					+0.0 / −0.6	+0.1 / +0.2	+0.0 / +0.1				+0.7 / +0.3	+0.2 / +0.8
ATLAS_JES_EffectiveNP_Detector1	−0.0 / −0.1	+0.1 / −0.2	−0.0 / −0.0		+0.1 / −0.1	+0.6 / +0.1	+0.1 / −0.1	+0.1 / −0.1	+0.0 / −0.1	+0.1 / −0.1	+0.1 / −0.1	+0.1 / −0.1	+0.2 / −0.2
ATLAS_JES_EffectiveNP_Detector2		−0.0 / −0.0		−0.0 / −0.0		+0.6 / −0.2	−0.0 / −0.0						
ATLAS_JES_EffectiveNP_Mixed1	+0.2 / −0.1	+0.2 / −0.3	−0.0 / −0.0		+0.2 / −0.3	+0.8 / −0.8	+0.1 / −0.2	+0.2 / −0.2	+0.1 / −0.2	+0.2 / −0.3	+0.2 / −0.3	+0.1 / −0.2	+0.4 / −0.2
ATLAS_JES_EffectiveNP_Mixed2	−0.2 / +0.1	−0.3 / +0.2			−0.4 / +0.1	−0.1 / +0.7	−0.3 / +0.2	−0.2 / +0.2	−0.2 / +0.2	−0.2 / +0.2	−0.3 / +0.2	−0.2 / +0.1	−0.1 / +0.2
ATLAS_JES_EffectiveNP_Mixed3	−0.0 / −0.0			−0.0 / −0.0	−0.0 / −0.0	+0.2 / +0.3	−0.0 / −0.1		+0.0 / −0.1	+0.1 / −0.1	+0.0 / −0.1	+0.1 / −0.1	+0.1 / −0.1
ATLAS_JES_EffectiveNP_Modelling1	+0.8 / −1.0	+1.4 / −1.3	+3.4 / −0.6	+3.8 / −0.0	+2.0 / −1.7	+7.3 / −5.2	+2.8 / −1.8	+1.0 / −1.3	+1.1 / −1.3	+2.0 / −1.6	+1.5 / −1.8	+0.6 / −0.7	+1.0 / −0.5
ATLAS_JES_EffectiveNP_Modelling2		−0.0 / −0.0		+0.0 / −2.7	+0.1 / −0.1	+0.8 / +0.2	−0.1 / +0.2	+0.0 / −0.1	−0.0 / −0.0	−0.0 / −0.0	−0.1 / −0.0		+0.1 / −0.1
ATLAS_JES_EffectiveNP_Modelling3	−0.1 / −0.1	−0.1 / −0.1		−2.7 / +0.0	−0.3 / +0.1	−0.3 / +1.2	−0.0 / −0.0	−0.1 / +0.1	−0.1 / +0.0	−0.1 / +0.0		−0.1 / +0.1	−0.0 / +0.1
ATLAS_JES_EffectiveNP_Modelling4		+0.0 / −0.1				+0.7 / −0.3			−0.0 / −0.0				+0.1 / −0.1
ATLAS_JES_EffectiveNP_Statistical1						+0.7 / −0.3		−0.0 / −0.0	−0.0 / −0.0				−0.0 / −0.1
ATLAS_JES_EffectiveNP_Statistical2	−0.2 / −0.0	−0.2 / +0.2	−0.0 / −0.0	+0.0 / −2.7	−0.1 / −0.1	−0.2 / +0.5	−0.5 / +0.5	−0.1 / +0.1	−0.1 / +0.1	−0.2 / +0.2	−0.2 / +0.1	−0.1 / +0.0	−0.3 / +0.3
ATLAS_JES_EffectiveNP_Statistical3	+0.0 / +0.1	−0.1 / +0.0				−0.0 / +0.3			−0.0 / −0.0				
ATLAS_JES_EffectiveNP_Statistical4	−0.0 / −0.0	+0.0 / −0.1	−0.0 / −0.0		+0.1 / −0.1	+0.6 / −0.2						+0.0 / −0.1	+0.1 / +0.1
ATLAS_JES_EffectiveNP_Statistical5	−0.0 / −0.0	−0.0 / −0.0			−0.1 / +0.1	−0.3 / +1.2	−0.1 / −0.0		−0.0 / −0.0				+0.0 / +0.1
ATLAS_JES_EffectiveNP_Statistical6	−0.0 / −0.0	+0.0 / −0.1			+0.0 / −0.1	+0.6 / −0.3			+0.0 / −0.1		+0.1 / −0.0		+0.1 / −0.0
ATLAS_JES_EtaInter_Model	+1.1 / −1.1	+1.1 / −1.3	+2.1 / +1.0	+2.9 / +0.0	+0.7 / −1.1	+4.2 / −3.1	+2.7 / −1.3	+0.5 / −0.8	+1.2 / −1.3	+2.3 / −1.7	+2.3 / −2.5	+0.6 / −0.7	+1.4 / −1.0
ATLAS_JES_EtaInter_NonClosure_highE									0.0 / −0.0				
ATLAS_JES_EtaInter_NonClosure_negEta	−0.0 / −0.1	−0.0 / −0.0				+0.0 / −0.2	+0.1 / −0.1			+0.0 / −0.1	+0.1 / −0.0		+0.1 / −0.0
ATLAS_JES_EtaInter_NonClosure_posEta	−0.0 / −0.1	−0.0 / −0.0			+0.1 / −0.0	+0.0 / +0.1	+0.0 / +0.1	+0.1 / −0.0		+0.1 / −0.0	+0.1 / −0.1	+0.1 / −0.0	+0.1 / −0.1
ATLAS_JES_EtaInter_Stat	+0.2 / −0.3	+0.2 / −0.5	+0.6 / −0.0	+4.3 / +0.0	+0.3 / −0.3	+1.5 / −1.0	+0.7 / −0.5	+0.1 / −0.1	+0.3 / −0.3	+0.4 / −0.3	+0.2 / −0.5	+0.1 / −0.1	+0.6 / −0.1
ATLAS_JES_Flavor_Comp	+1.6 / −2.3	+3.5 / −3.6	+5.5 / −2.1	+29.5 / −14.7	+6.3 / −5.9	+16.3 / −12.5	+7.7 / −5.7	+2.2 / −2.9	+3.5 / −3.9	+5.8 / −5.5	+5.4 / −5.2	+0.7 / −2.2	+3.9 / −3.8
ATLAS_JES_Flavor_Resp	−1.8 / +1.4	−3.1 / +2.7	−3.1 / +4.4	−8.8 / +13.6	−4.6 / +5.6	−11.8 / +13.6	−3.2 / +5.0	−2.6 / +2.0	−2.5 / +2.2	−3.3 / +3.8	−3.1 / +2.9	−1.4 / +0.7	−2.4 / +1.8
ATLAS_JES_HighPt													
ATLAS_JES_PU_OffsetMu	+0.2 / −0.3	+0.2 / −0.2	+0.8 / +1.9	+7.0 / −2.7	+0.1 / −0.5	+4.0 / −2.3	+1.3 / −0.8	+0.1 / −0.2	+0.5 / −0.5	+0.9 / −0.7	+1.3 / −1.5	+0.1 / −0.2	+0.1 / +0.2
ATLAS_JES_PU_OffsetNPV	+0.7 / −0.6	+0.9 / −0.6	+1.9 / −1.9	+7.0 / −11.5	+1.8 / −1.6	+6.7 / −4.6	+2.5 / −1.1	+0.5 / −0.6	+0.8 / −0.9	+1.5 / −1.2	+1.2 / −1.4	+0.3 / −0.4	+0.6 / +0.0
ATLAS_JES_PU_PtTerm	+0.2 / −0.3	+0.3 / −0.4	+1.6 / −0.0	+7.0 / −11.5	+0.9 / −0.8	+1.5 / −2.2	+0.4 / −0.2	+0.3 / −0.3	+0.2 / −0.3	+0.4 / −0.3	+0.3 / −0.4	+0.4 / −0.3	+0.7 / −0.5
ATLAS_JES_PU_Rho	+1.1 / −1.6	+2.0 / −1.9	+4.8 / −0.4	+13.6 / −8.8	+3.9 / −3.6	+11.8 / −7.9	+4.8 / −2.6	+1.2 / −1.6	+2.0 / −2.3	+3.5 / −3.0	+3.1 / −2.9	+0.5 / −0.4	+2.1 / −1.0
ATLAS_JES_PunchThrough						−0.0 / −0.1							
ATLAS_JVT	+0.1 / −0.2	−0.2 / +0.0	+0.1 / −0.2	+0.2 / −0.3	−0.2 / +0.0	−0.6 / +0.3	+0.4 / −0.4	+0.1 / −0.2	+0.2 / −0.3	+0.3 / −0.4	+0.1 / −0.2	+0.2 / −0.3	+0.3 / −0.3
ATLAS_LUMI		+1.7 / −1.7	+1.7 / −1.7	+1.7 / −1.7			+1.7 / −1.7	+1.7 / −1.7		+1.7 / −1.7	+1.7 / −1.7		
ATLAS_MET_SoftTrk_ResoPara		+0.1 / −0.1	−0.8 / +0.8		−0.6 / +0.6	+1.4 / −1.4	+0.5 / −0.5	−0.1 / +0.1	−0.1 / +0.1	+0.2 / −0.2	+0.6 / −0.6	+0.3 / −0.3	+0.1 / −0.1
ATLAS_MET_SoftTrk_ResoPerp			+0.8 / −0.8		−0.4 / +0.4	−0.7 / +0.7	+0.5 / −0.5		−0.1 / +0.1	+0.3 / −0.3	+0.6 / −0.6	+0.3 / −0.3	−0.2 / +0.2
ATLAS_MET_SoftTrk_Scale	+0.2 / −0.3	−0.1 / +0.0	+0.5 / +0.5		−0.7 / +0.8	+0.4 / +0.0	+0.4 / +0.2	−0.2 / +0.1	+0.1 / −0.1	+0.2 / −0.2	+0.3 / −0.1	+0.1 / −0.1	−0.2 / −0.1
ATLAS_MUONS_ID	−0.2 / +0.1	−0.0 / +0.1	+0.4 / −0.3		−0.2 / +0.2	−0.4 / +0.1	−0.2 / −0.3	−0.0 / +0.1	−0.1 / +0.0	−0.3 / +0.1	−0.2 / +0.1	−0.2 / +0.1	+0.4 / −0.1
ATLAS_MUONS_MS	+0.0 / +0.1				−0.1 / +0.1	+0.2 / +0.6	−0.2 / +0.2	−0.1 / +0.2	−0.2 / +0.1	−0.2 / +0.2	−0.1 / +0.2	−0.1 / +0.1	+0.1 / +0.2
ATLAS_MUONS_SAGITTA_RESBIAS	+1.1 / +1.0	+0.4 / +0.4	+0.4 / +0.4		+0.8 / +0.8	+0.8 / +0.8	+0.5 / +0.5	+0.6 / +0.6	+0.6 / +0.6	+0.5 / +0.5	+0.6 / +0.7	+0.6 / +0.6	+0.3 / +0.3
ATLAS_MUONS_SAGITTA_RHO													
ATLAS_MUONS_SCALE	+0.1 / +0.0	−0.2 / +0.1	−0.0 / −0.0		+0.2 / −0.2	+0.1 / −0.3	−0.0 / −0.2	−0.1 / +0.1	−0.0 / −0.0	−0.1 / +0.1	−0.1 / +0.1		+0.6 / +0.2
ATLAS_MUON_EFF_ISO_STAT	+0.5 / −0.6	+0.5 / −0.6	+0.5 / −0.5		+0.5 / −0.6	+0.5 / −0.6	+0.5 / −0.5	+0.5 / −0.6	+0.5 / −0.6	+0.5 / −0.5	+0.5 / −0.5	+0.5 / −0.5	+0.5 / −0.6
ATLAS_MUON_EFF_ISO_SYS	+3.0 / −2.8	+3.3 / −3.1	+2.7 / −2.6		+3.8 / −3.5	+4.1 / −3.8	+3.5 / −3.3	+3.1 / −2.9	+3.1 / −2.9	+3.1 / −2.9	+3.0 / −2.9	+3.5 / −3.3	+3.4 / −3.2
ATLAS_MUON_EFF_RECO_STAT	+0.1 / −0.1	+0.1 / −0.1	+0.1 / −0.1		+0.1 / −0.1	+0.1 / −0.1	+0.1 / −0.1	+0.1 / −0.1	+0.1 / −0.1	+0.1 / −0.1	+0.1 / −0.1	+0.1 / −0.1	+0.1 / −0.1
ATLAS_MUON_EFF_RECO_STAT_LOWPT													
ATLAS_MUON_EFF_RECO_SYS	+0.3 / −0.3	+0.3 / −0.3	+0.3 / −0.3		+0.3 / −0.3	+0.3 / −0.3	+0.3 / −0.3	+0.3 / −0.3	+0.3 / −0.3	+0.3 / −0.3	+0.3 / −0.3	+0.3 / −0.3	+0.3 / −0.3
ATLAS_MUON_EFF_RECO_SYS_LOWPT													
ATLAS_MUON_EFF_TTVA_STAT													
ATLAS_MUON_EFF_TTVA_SYS													
ATLAS_MUON_EFF_TrigStatUncertainty	+0.1 / −0.1	+0.1 / −0.1	+0.0 / −0.1		+0.1 / −0.1		+0.1 / −0.1	+0.1 / −0.1	+0.1 / −0.1	+0.1 / −0.1	+0.1 / −0.1	+0.1 / −0.1	+0.1 / −0.1
ATLAS_MUON_EFF_TrigSystUncertainty	−0.2 / +0.2	−0.2 / +0.2	−0.2 / +0.2		−0.2 / +0.3	−0.3 / +0.3	−0.2 / +0.2	−0.2 / +0.2	−0.2 / +0.2	−0.2 / +0.2	−0.2 / +0.2	−0.2 / +0.2	−0.2 / +0.2
ATLAS_PRW_DATASF	−0.2 / +0.2	−0.4 / +0.3	−1.9 / +1.6	−4.6 / +2.3	+1.4 / −1.6	+1.9 / −2.2	+0.1 / −0.0	−0.5 / +0.5	−0.2 / +0.2	−0.2 / +0.2	+0.2 / −0.3	−0.7 / +0.6	−0.3 / +0.1

Table A.4: Pre-fit experimental systematic normalization uncertainties of the different processes in the SR of the $N_{\text{jet}} \geq 2$ VBF-enriched category. Only non-trivial systematic uncertainties whose values are not 0% are shown.

$N_{\text{jet}} \geq 2$ VBF-enriched SR	Pre-fit impact high / low [%]												
Experimental systematic uncertainty	EW WW	Other VV	VVV	$V\gamma$	Z/γ^* high-mass	Z/γ^* low-mass	$gg WW$	Other H	$qq WW$	ggF	VBF	$t\bar{t}$	Wt
ATLAS_EG_RESOLUTION_ALL	+0.0 / +0.1	−0.1 / +0.1	−0.1 / +0.1	−0.0 / −0.2	+0.0 / −0.2	−0.1 / −0.5	−0.2 / +0.2	+0.1 / +0.1		−0.1 / +0.1	+0.1 / −0.1	+0.1 / +0.0	+0.2 / +0.1
ATLAS_EG_SCALE_AF2													
ATLAS_EG_SCALE_ALL	−0.1 / +0.2	−0.3 / +0.3		+0.0 / −0.6	−0.2 / +0.2	+0.3 / −0.0	−0.2 / +0.2	−0.0 / +0.1	−0.1 / +0.1	−0.1 / +0.0	+0.0 / +0.1	−0.0 / +0.2	+0.3 / +0.2
ATLAS_EL_EFF_ID_CorrUncertainty_NP0													
ATLAS_EL_EFF_ID_CorrUncertainty_NP1													
ATLAS_EL_EFF_ID_CorrUncertainty_NP10													
ATLAS_EL_EFF_ID_CorrUncertainty_NP11	+0.1 / −0.1	+0.1 / −0.1	+0.1 / −0.1	+0.3 / −0.3	+0.1 / −0.1	+0.1 / −0.1	+0.1 / −0.1	+0.1 / −0.1	+0.1 / −0.1	+0.1 / −0.1	+0.1 / −0.1	+0.1 / −0.1	+0.1 / −0.1
ATLAS_EL_EFF_ID_CorrUncertainty_NP12	−0.1 / +0.1	−0.1 / +0.1			−0.1 / +0.1		−0.1 / +0.1	−0.1 / +0.1	−0.1 / +0.1	−0.1 / +0.1	−0.1 / +0.1	−0.1 / +0.1	−0.1 / +0.1
ATLAS_EL_EFF_ID_CorrUncertainty_NP13		−0.1 / +0.1		+0.7 / −0.7		−0.1 / +0.1	−0.1 / +0.1	−0.1 / +0.1	−0.1 / +0.1	−0.1 / +0.1		−0.1 / +0.1	−0.1 / +0.1
ATLAS_EL_EFF_ID_CorrUncertainty_NP14	+0.1 / −0.1	−0.1 / +0.1		+1.4 / −1.4		+0.1 / −0.1	+0.2 / −0.2		−0.1 / +0.1	−0.1 / +0.1			−0.4 / +0.4
ATLAS_EL_EFF_ID_CorrUncertainty_NP15	−0.1 / +0.1	−0.2 / +0.2			−0.2 / +0.2			−0.1 / +0.1	−0.2 / +0.2	−0.1 / +0.1	−0.1 / +0.1	−0.1 / +0.1	−0.3 / +0.3
ATLAS_EL_EFF_ID_CorrUncertainty_NP2													
ATLAS_EL_EFF_ID_CorrUncertainty_NP3													
ATLAS_EL_EFF_ID_CorrUncertainty_NP4													
ATLAS_EL_EFF_ID_CorrUncertainty_NP5													
ATLAS_EL_EFF_ID_CorrUncertainty_NP6													
ATLAS_EL_EFF_ID_CorrUncertainty_NP7													
ATLAS_EL_EFF_ID_CorrUncertainty_NP8													
ATLAS_EL_EFF_ID_CorrUncertainty_NP9				−0.2 / +0.2			−0.1 / +0.1						
ATLAS_EL_EFF_ID_UncorrUncertainty_NP0													
ATLAS_EL_EFF_ID_UncorrUncertainty_NP1													
ATLAS_EL_EFF_ID_UncorrUncertainty_NP10													
ATLAS_EL_EFF_ID_UncorrUncertainty_NP11													
ATLAS_EL_EFF_ID_UncorrUncertainty_NP12		+0.1 / −0.1					+0.1 / −0.1						
ATLAS_EL_EFF_ID_UncorrUncertainty_NP13													
ATLAS_EL_EFF_ID_UncorrUncertainty_NP14													
ATLAS_EL_EFF_ID_UncorrUncertainty_NP15				+0.2 / −0.2									
ATLAS_EL_EFF_ID_UncorrUncertainty_NP16													
ATLAS_EL_EFF_ID_UncorrUncertainty_NP17				+1.4 / −1.4									
ATLAS_EL_EFF_ID_UncorrUncertainty_NP2													
ATLAS_EL_EFF_ID_UncorrUncertainty_NP3	+0.2 / −0.2	+0.5 / −0.5			+0.7 / −0.7		+0.6 / −0.6	+0.4 / −0.4	+0.2 / −0.2	+0.3 / −0.3	+0.2 / −0.2	+0.3 / −0.3	
ATLAS_EL_EFF_ID_UncorrUncertainty_NP4						+0.1 / −0.1							+0.1 / −0.1
ATLAS_EL_EFF_ID_UncorrUncertainty_NP5													
ATLAS_EL_EFF_ID_UncorrUncertainty_NP6	+0.1 / −0.1	+0.1 / −0.1			+0.1 / −0.1		+0.1 / −0.1	+0.1 / −0.1	+0.1 / −0.1	+0.1 / −0.1	+0.1 / −0.1	+0.1 / −0.1	+0.1 / −0.1
ATLAS_EL_EFF_ID_UncorrUncertainty_NP7													
ATLAS_EL_EFF_ID_UncorrUncertainty_NP8	+0.1 / −0.1							+0.1 / −0.1					
ATLAS_EL_EFF_ID_UncorrUncertainty_NP9													
ATLAS_EL_EFF_Iso_TOTAL_1NPCOR_PLUS_UNCOR	+0.2 / −0.2	+0.4 / −0.4		+1.0 / −0.9	+0.3 / −0.3	+0.2 / −0.2	+0.3 / −0.3	+0.3 / −0.3	+0.2 / −0.2	+0.2 / −0.2	+0.2 / −0.2	+0.3 / −0.2	+0.2 / −0.2
ATLAS_EL_EFF_Reco_TOTAL_1NPCOR_PLUS_UNCOR	+0.2 / −0.2	+0.3 / −0.3		+0.2 / −0.2	+0.3 / −0.3	+0.1 / −0.1	+0.2 / −0.2	+0.2 / −0.2	+0.2 / −0.2	+0.2 / −0.2	+0.2 / −0.2	+0.2 / −0.2	+0.2 / −0.2
ATLAS_EL_EFF_TRIG_TOTAL_1NPCOR_PLUS_UNCOR													
ATLAS_FTAG_EXTRAP													
ATLAS_FT_EFF_Eigen_B_0						+0.1 / −0.1		+0.1 / −0.1		+0.1 / −0.1		+5.1 / −5.0	+4.9 / −4.9
ATLAS_FT_EFF_Eigen_B_1						+0.1 / −0.1		+0.1 / −0.1				+1.3 / −1.3	+1.4 / −1.4
ATLAS_FT_EFF_Eigen_B_2												−0.9 / +0.9	−1.0 / +1.0
ATLAS_FT_EFF_Eigen_C_0	+0.2 / −0.2	+0.3 / −0.3	+0.2 / −0.2		+0.4 / −0.4		+0.2 / −0.2	+0.4 / −0.4	+0.2 / −0.2	+0.2 / −0.2	+0.2 / −0.2	+0.1 / −0.1	+0.1 / −0.1
ATLAS_FT_EFF_Eigen_C_1								+0.1 / −0.1	+0.1 / −0.1				
ATLAS_FT_EFF_Eigen_C_2													
ATLAS_FT_EFF_Eigen_Light_0	+0.5 / −0.5	+0.6 / −0.6	+0.6 / −0.6	+0.6 / −0.6	+0.5 / −0.5	+0.5 / −0.5	+0.6 / −0.6	+0.6 / −0.6	+0.6 / −0.6	+0.6 / −0.6	+0.4 / −0.4	+0.5 / −0.5	+0.4 / −0.4
ATLAS_FT_EFF_Eigen_Light_1													
ATLAS_FT_EFF_Eigen_Light_2				+0.1 / −0.1									
ATLAS_FT_EFF_Eigen_Light_3													
ATLAS_FT_EFF_extrapolation_from_charm		−0.4 / +0.4						−0.2 / +0.2					
ATLAS_JER_DataVsMC	+0.2 / +0.1	−3.9 / +5.8	+50.1 / −22.9	−594.9 / +595.0	+9.6 / −5.9	+14.0 / −10.6	+8.2 / +1.9	−0.9 / −2.5	−2.0 / +1.1	−1.2 / +2.6	+0.2 / −0.4	−2.4 / −0.2	−10.3 / −9.2
ATLAS_JER_EffectiveNP_1	−1.0 / +0.4	+0.6 / −8.4	−36.5 / +64.5	+594.9 / −594.9	+4.6 / −4.3	−16.8 / +22.2	+6.6 / −0.7	+6.3 / −0.8	+5.9 / −4.3	+1.9 / −1.6	−1.7 / +1.0	−0.3 / −1.8	−11.6 / +6.7
ATLAS_JER_EffectiveNP_10	+0.5 / −0.3	+2.3 / −3.5	−0.0 / +16.7		−7.8 / +4.9	−4.4 / +7.2	+6.0 / +2.3	+1.5 / −1.3	+0.2 / −0.8	+0.9 / −0.7	+0.0 / −0.5	−1.3 / −1.3	+7.9 / −9.6
ATLAS_JER_EffectiveNP_11	+0.4 / −0.2	+2.3 / −2.2	+16.7 / −0.0		−8.4 / −5.1	−1.6 / +2.0	+2.3 / +4.6	−1.4 / +2.9	−0.3 / −0.9	−0.6 / +0.7	+0.0 / −0.3	−0.5 / −2.8	−1.8 / +0.1
ATLAS_JER_EffectiveNP_12	+0.4 / −0.7	+0.8 / −3.1			−12.0 / +3.2	−11.8 / +6.6	−0.6 / +5.0	−0.5 / +0.9	+0.1 / −1.7	+1.6 / −1.4	−0.1 / −0.1	−1.8 / −1.3	+1.0 / −2.5
ATLAS_JER_EffectiveNP_2	+0.3 / +0.3	+9.4 / −2.2	+4.3 / +50.1	−594.9 / −7820622.2	−6.8 / −0.5	−4.1 / +23.2	+2.8 / −3.1	−2.4 / +4.9	−3.8 / −4.8	−0.9 / +2.3	−0.2 / −0.5	−0.1 / −2.0	−18.8 / −3.6
ATLAS_JER_EffectiveNP_3	+0.8 / −0.3	−4.2 / +6.1	+22.9 / −22.9	+0.0 / +594.9	+8.0 / −7.3	+10.5 / −12.3	+2.6 / +1.9	−0.6 / −0.4	−3.1 / +0.1	−0.8 / +0.8	+0.2 / −0.7	−3.5 / −0.6	+3.3 / −15.2
ATLAS_JER_EffectiveNP_4	−0.5 / +0.9	+2.2 / −0.2	+4.3 / +5.3	−7823217.9 / +595.0	−4.4 / +6.0	−21.8 / +16.9	+6.7 / −0.9	+2.5 / −2.2	−2.9 / −1.0	+3.4 / +0.9	+0.2 / −0.8	−2.0 / +2.0	−3.7 / −14.0
ATLAS_JER_EffectiveNP_5	+1.4 / −1.2	−0.2 / +3.0	+35.5 / +4.3	+594.9 / −594.9	+5.1 / −5.5	+13.9 / −3.5	+8.4 / +4.4	+6.6 / −2.2	−0.8 / −1.9	−0.7 / +0.3	−0.2 / −0.0	−1.0 / −1.1	+3.2 / −14.8
ATLAS_JER_EffectiveNP_6	−0.2 / +1.3	+0.4 / −0.9	+4.3 / +39.6		−4.7 / +5.0	+5.6 / −13.7	+3.4 / +10.1	+2.5 / −0.4	−2.3 / +0.3	−0.0 / +0.5	−0.0 / −0.1	−1.8 / −0.5	−6.9 / −5.2
ATLAS_JER_EffectiveNP_7	−1.0 / +1.2	−3.3 / +1.8	+50.1 / −22.9		−2.5 / −6.0	−1.4 / −6.2	+2.9 / +0.2	+0.3 / +1.3	−0.0 / −2.4	−0.4 / +0.8	−0.1 / −0.2	−1.7 / +0.5	−10.2 / −3.1
ATLAS_JER_EffectiveNP_8	+0.5 / −0.4	+0.6 / −5.4			−9.9 / −2.0	+2.5 / −3.7	+0.3 / +2.7	−0.3 / +5.0	+1.4 / −1.0	+1.5 / +0.2	−0.2 / −0.2	−0.3 / −3.2	−1.9 / −1.5
ATLAS_JER_EffectiveNP_9	+0.2 / +0.4	−1.4 / +2.6	−6.2 / +22.9		−7.2 / +4.6	−8.3 / +4.3	+0.6 / +4.4	−0.9 / +1.1	−0.6 / −1.7	+0.6 / −0.6	−0.3 / +0.1	−1.1 / −2.1	+0.2 / −5.7
ATLAS_JES_BJES					−0.0 / +0.3				−0.0 / −0.1	−0.0 / +0.1		+0.6 / +0.7	−1.5 / −1.4
ATLAS_JES_EffectiveNP_Detector1	+0.1 / −0.1	+2.7 / −0.2			+0.0 / −0.3	+0.0 / +0.2	−0.8 / −0.0	−0.3 / +0.0	+1.1 / −0.6	−0.1 / −0.2	+0.1 / −0.1	+0.5 / −0.1	−0.9 / −0.0
ATLAS_JES_EffectiveNP_Detector2		+2.6 / +0.0			+0.0 / +0.1				−0.0 / −0.1	−0.1 / +0.0			
ATLAS_JES_EffectiveNP_Mixed1	+0.2 / −0.4	+2.7 / −1.1			+0.5 / −0.5	+0.0 / −0.6	−0.8 / +0.0	+0.5 / −0.5	+0.8 / −0.2	+0.4 / −0.2	+0.2 / −0.3	+0.4 / −0.3	
ATLAS_JES_EffectiveNP_Mixed2	−0.3 / +0.2	−0.1 / +2.7			−0.4 / +0.2	−0.6 / +0.0	−0.0 / −0.8	−0.4 / +0.2	−0.5 / +1.3	−0.3 / +0.0	−0.1 / +0.2	−0.4 / +0.3	+0.0 / +1.5
ATLAS_JES_EffectiveNP_Mixed3	+0.1 / −0.1	+2.6 / −0.0			+0.0 / −0.3	+0.0 / +0.2	−0.8 / −0.0	−0.4 / +0.0	+0.6 / −0.4	−0.1 / +0.1		+0.1 / +0.1	
ATLAS_JES_EffectiveNP_Modelling1	+0.3 / +0.2	+3.6 / −2.6			+2.0 / −13.0	+1.3 / −4.2	−6.4 / +0.4	−0.9 / +0.9	+2.2 / −2.2	+1.6 / −1.2	+0.7 / −0.8	−0.5 / −0.7	+0.3 / −0.9
ATLAS_JES_EffectiveNP_Modelling2	−0.0 / −0.1	+3.7 / −0.2			−0.3 / +0.1	+0.2 / −0.1		+0.4 / −0.7	−0.4 / +1.1	+0.1 / −0.4	+0.1 / −0.1	−0.2 / +0.1	−0.0 / +1.5
ATLAS_JES_EffectiveNP_Modelling3	−0.1 / +0.1	−0.3 / +3.8			+0.3 / −0.3	−0.4 / +0.2	−0.0 / −0.8	−0.7 / +0.6	+1.1 / −0.2	−0.8 / +0.3	−0.1 / +0.2	−0.1 / +0.1	−0.9 / −0.0
ATLAS_JES_EffectiveNP_Modelling4		+2.6 / −0.1			−0.0 / +0.1	+0.0 / −0.1		+0.3 / −0.6	+0.5 / −0.1	−0.1 / +0.0	+0.0 / −0.1		
ATLAS_JES_EffectiveNP_Statistical1		+2.6 / +0.0				−0.0 / −0.1		−0.0 / −0.6	+0.5 / −0.1	−0.1 / +0.0			
ATLAS_JES_EffectiveNP_Statistical2	+0.1 / −0.0	+0.8 / +2.7			−0.1 / +0.0	+0.2 / −0.0	−0.1 / −2.4	+0.5 / −0.3	−0.5 / +1.1	−0.6 / −0.2	+0.0 / +0.1	+0.0 / +0.2	+0.0 / +1.5
ATLAS_JES_EffectiveNP_Statistical3	−0.1 / −0.0	+0.0 / +2.6				−0.1 / −0.0		−0.6 / +0.2		−0.1 / −0.0	−0.1 / +0.0		
ATLAS_JES_EffectiveNP_Statistical4		+2.6 / −0.1			−0.0 / +0.2			+0.3 / −0.6	−0.1 / +0.0	+0.2 / −0.1	+0.1 / −0.1		
ATLAS_JES_EffectiveNP_Statistical5	+0.0 / −0.1	−0.2 / +2.6			+0.2 / −0.0	−0.0 / −0.1	−0.0 / −0.8	−0.0 / −0.4		−0.4 / +0.3		+0.0 / +0.1	
ATLAS_JES_EffectiveNP_Statistical6	+0.1 / −0.0	+2.6 / −0.1			+0.0 / −0.1			+0.2 / +0.0	+0.5 / −0.1	−0.1 / +0.1		+0.1 / +0.1	
ATLAS_JES_EtaInter_Model	+0.5 / −0.3	+6.1 / −8.2	−0.0 / −22.9		+3.6 / −13.2	−4.2 / −4.9	−3.8 / +1.7	−0.9 / +0.6	+4.0 / −2.0	+4.7 / −2.9	+1.5 / −1.4	+1.8 / −3.0	+0.5 / +2.7
ATLAS_JES_EtaInter_NonClosure_highE													
ATLAS_JES_EtaInter_NonClosure_negEta	+0.1 / −0.0	−0.2 / +0.1			+0.1 / +3.3	−1.6 / −0.0	+1.2 / −0.0		+0.1 / −0.1	+0.3 / −0.1		+0.3 / −0.1	+2.3 / 0.0
ATLAS_JES_EtaInter_NonClosure_posEta	+0.0 / +0.1	−0.1 / +0.1			+0.2 / −0.2	−0.5 / −1.7		−0.0 / +0.3	−0.0 / −0.4	+0.0 / −0.1		+0.3 / +0.1	
ATLAS_JES_EtaInter_Stat		+3.3 / +1.9			+1.0 / −1.5	−0.9 / −0.2	−2.4 / −0.1	−0.4 / −0.1	+1.7 / −0.6	+0.2 / −0.3	+0.2 / −0.1	−0.0 / −0.1	+3.8 / +2.4
ATLAS_JES_Flavor_Comp	+0.2 / +0.7	+6.2 / −5.2	−27.2 / −22.9		+5.5 / −4.3	−3.8 / −32.7	−5.2 / +1.4	−0.0 / +0.9	+5.6 / −1.3	+7.6 / −6.2	+2.0 / −2.5	−0.8 / −3.1	+0.0 / −2.3
ATLAS_JES_Flavor_Resp	−0.3 / +1.1	−3.1 / +2.4			−9.3 / +4.8	−10.4 / −0.5	−3.5 / −5.7	+0.4 / −1.4	−2.0 / +4.4	−2.9 / +3.2	−1.8 / +1.7	−2.4 / +0.1	+0.4 / +2.2
ATLAS_JES_HighPt													
ATLAS_JES_PU_OffsetMu	+0.1 / −0.1	+8.1 / −5.8			+1.2 / −11.4	−8.0 / +5.5	+5.2 / −7.1	−1.3 / +1.3	+2.9 / −3.2	+1.6 / +0.9	−0.3 / +0.3	−0.8 / +0.3	−1.7 / −4.5
ATLAS_JES_PU_OffsetNPV	−0.1 / +0.7	+1.9 / −4.1			+1.0 / −11.1	−5.4 / −2.3	−1.8 / −2.2	−1.0 / +1.9	+2.9 / −3.6	+0.7 / +0.4	+0.0 / +0.2	−1.0 / +1.5	−3.7 / +3.4
ATLAS_JES_PU_PtTerm	+0.2 / −0.5	+3.4 / −0.9			+1.8 / −0.4	+7.4 / −1.1	−2.4 / −0.1	−1.2 / +0.0	+0.1 / −1.4	+2.1 / −1.3	+0.2 / −0.3	+0.1 / +0.3	−0.0 / +2.3
ATLAS_JES_PU_Rho	−0.2 / +1.2	+0.0 / −4.3	−0.0 / −22.9		+1.7 / −9.8	−4.8 / −5.7	−8.2 / +2.0	−4.7 / +1.4	+2.5 / −2.2	+2.1 / −0.8	+0.2 / −0.2	−1.9 / +0.8	−3.4 / −3.8
ATLAS_JES_PunchThrough	−0.0 / +0.1	+0.1 / +0.0					0.0 / −0.0	−0.0 / −0.2					
ATLAS_JVT	+0.1 / −0.1	−0.5 / +0.3			−0.3 / +0.2	−0.0 / −0.1	+0.3 / −0.4	−0.2 / +0.1	+0.1 / −0.1	+0.2 / −0.2	+0.1 / −0.1	−0.2 / +0.0	+0.3 / −0.3
ATLAS_LUMI		+1.7 / −1.7	+1.7 / −1.7	+1.7 / −1.7			+1.7 / −1.7	+1.7 / −1.7		+1.7 / −1.7	+1.7 / −1.7		
ATLAS_MET_SoftTrk_ResoPara		−1.6 / +1.6	−5.7 / +5.7	−100.0 / +100.0	−1.7 / +1.7	−24.7 / +24.7	−3.6 / +3.6	−2.1 / +2.1	−1.0 / +1.0	−2.0 / +2.0	−0.5 / +0.5	−1.1 / +1.1	+2.7 / −2.7
ATLAS_MET_SoftTrk_ResoPerp	−0.3 / +0.3	−0.2 / +0.2	+0.9 / −0.9		−2.0 / +2.0	−24.9 / +24.9	−2.2 / +2.2	−0.4 / +0.4	−1.0 / +1.0	−4.4 / +4.4	−0.7 / +0.7	−2.4 / +2.4	
ATLAS_MET_SoftTrk_Scale	−0.3 / +0.6	−0.7 / +0.8	0.0 / +0.4		−2.0 / +0.7	−3.9 / +0.8	−2.5 / −2.8	−1.3 / +1.9	−0.5 / −0.6	−2.1 / +0.2	−0.2 / +0.1	−1.1 / −0.7	+0.5 / −0.9
ATLAS_MUONS_ID	+0.0 / +0.3	+0.5 / −0.7			+2.3 / +1.0	−2.5 / −0.3	−2.0 / +0.0	−0.6 / −0.2	+0.5 / +0.4	+0.3 / −0.1	−0.3 / +0.1	−0.6 / +0.5	
ATLAS_MUONS_MS	+0.2 / +0.0	+0.1 / −0.3			+0.3 / +1.0	−3.0 / −0.8	−0.0 / −0.8	+0.1 / −0.1	+0.2 / +0.3	+0.1 / −0.5	−0.2 / +0.2	−0.3 / −0.1	
ATLAS_MUONS_SAGITTA_RESBIAS	+0.9 / +0.8	+0.4 / +0.4			+4.7 / +4.7	−0.2 / −0.2	−0.7 / −0.7	−1.2 / −1.2	+1.4 / +1.4	+0.5 / +0.5	+0.5 / +0.5	+1.0 / +1.0	0.0 / +2.1
ATLAS_MUONS_SAGITTA_RHO													
ATLAS_MUONS_SCALE	+0.1 / −0.1	+0.0 / +0.1			+0.5 / −0.5	−0.0 / −1.0	−0.8 / 0.0	−0.1 / 0.0	−0.0 / +0.8	−0.0 / −0.6		−0.0 / −0.4	
ATLAS_MUON_EFF_ISO_STAT	+0.5 / −0.6	+0.4 / −0.4	+1.3 / −1.3		+0.5 / −0.5	+0.7 / −0.7	+0.5 / −0.5	+0.5 / −0.5	+0.5 / −0.5	+0.5 / −0.5	+0.5 / −0.5	+0.5 / −0.5	+0.5 / −0.5
ATLAS_MUON_EFF_ISO_SYS	+3.2 / −3.0	+2.7 / −2.5	+4.0 / −3.8		+3.1 / −2.9	+5.2 / −4.8	+3.2 / −3.0	+3.3 / −3.1	+3.1 / −2.9	+3.2 / −3.0	+3.0 / −2.8	+3.8 / −3.6	+3.2 / −3.0
ATLAS_MUON_EFF_RECO_STAT	+0.1 / −0.1	+0.1 / −0.1	+0.1 / −0.1		+0.1 / −0.1	+0.1 / −0.1	+0.1 / −0.1	+0.1 / −0.1	+0.1 / −0.1	+0.1 / −0.1	+0.1 / −0.1	+0.1 / −0.1	+0.1 / −0.1
ATLAS_MUON_EFF_RECO_STAT_LOWPT													
ATLAS_MUON_EFF_RECO_SYS	+0.3 / −0.3	+0.2 / −0.2	+0.5 / −0.5		+0.2 / −0.2	+0.3 / −0.3	+0.2 / −0.2	+0.3 / −0.3	+0.3 / −0.3	+0.3 / −0.3	+0.3 / −0.3	+0.3 / −0.3	+0.3 / −0.3
ATLAS_MUON_EFF_RECO_SYS_LOWPT													
ATLAS_MUON_EFF_TTVA_STAT													
ATLAS_MUON_EFF_TTVA_SYS													
ATLAS_MUON_EFF_TrigStatUncertainty	+0.1 / −0.1	+0.1 / −0.1			+0.1 / −0.1	+0.1 / −0.1	+0.1 / −0.1	+0.1 / −0.1	+0.1 / −0.1	+0.1 / −0.1	+0.1 / −0.1	+0.1 / −0.1	+0.1 / −0.1
ATLAS_MUON_EFF_TrigSystUncertainty	−0.2 / +0.2	−0.2 / +0.2	−0.3 / +0.3		−0.2 / +0.2	−0.3 / +0.3	−0.2 / +0.2	−0.2 / +0.2	−0.2 / +0.2	−0.2 / +0.2	−0.2 / +0.2	−0.2 / +0.2	−0.2 / +0.2
ATLAS_PRW_DATASF	−1.4 / +1.1	−1.0 / +1.1	−2.3 / +3.8	+13.5 / −8.1	+1.6 / −1.8	−2.3 / +1.0	+0.4 / −0.7	+0.1 / +0.5	−0.6 / +0.7	+0.2 / −0.0	−1.6 / +1.4	−1.9 / +1.5	−2.0 / +2.3

Bibliography

[1] ATLAS Collaboration, *Observation of a new particle in the search for the Standard Model Higgs boson with the ATLAS detector at the LHC*, Phys. Lett. B **716** (2012) 1.

[2] CMS Collaboration, *Observation of a new boson with mass near 125 GeV in pp collisions at $\sqrt{s} = 7$ and 8 TeV*, J. High Energy Phys. **2013** (2013) 81.

[3] S. Heinemeyer et al., *Handbook of LHC Higgs cross sections: 3. Higgs properties*. CERN Yellow Rep.: Monogr. 2013. arXiv:1307.1347.

[4] ATLAS and CMS Collaborations, *Measurements of the Higgs boson production and decay rates and constraints on its couplings from a combined ATLAS and CMS analysis of the LHC pp collision data at $\sqrt{s} = 7$ and 8 TeV.*, J. High Energy Phys. **2016** (2016) 45.

[5] ATLAS Collaboration, *Measurements of gluon-gluon fusion and vector-boson fusion Higgs boson production cross-sections in the $H \to WW^* \to e\nu\mu\nu$ decay channel in pp collisions at $\sqrt{s} = 13\,TeV$ with the ATLAS detector*, Phys. Lett. B **789** (2019) 508.

[6] ATLAS Collaboration, *Measurements of Higgs boson production by gluon−gluon fusion and vector-boson fusion using $H \to WW^* \to e\nu\mu\nu$ decays in pp collisions at $\sqrt{s} = 13$ TeV with the ATLAS detector*, Phys. Rev. D **108** (2023) 032005.

[7] ATLAS Collaboration, *Observation and measurement of Higgs boson decays to WW^* with the ATLAS detector*, Phys. Rev. D **92** (2015) 012006.

[8] D. Galbraith and C. Burgard, *Standard Model standard infographic*, https://daveg.medium.com/standard-model-standard-infographic-fbf9ad981b30. licenced under CC-BY-4.0.

[9] M. Thomson, *Modern particle physics*. Cambridge University Press, 2013.

[10] J. Ellis, M. K. Gaillard, and D. V. Nanopoulos, *An updated historical profile of the Higgs boson*, tech. rep., 2015. arXiv:1504.07217.

[11] ATLAS and CMS Collaborations, *Combined measurement of the Higgs boson mass in pp collisions at $\sqrt{s} = 7$ and 8 TeV with the ATLAS and CMS experiments*, Phys. Rev. Lett. **114** (2015) 191803.

[12] D. de Florian et al., *Handbook of LHC Higgs cross sections: 4. Deciphering the nature of the Higgs sector*. CERN Yellow Rep.: Monogr. 2017. arXiv:1610.07922.

[13] Particle Data Group, *Review of particle physics*, Prog. Theor. Exp. Phys. **2022** (2022) 083C01.

[14] ALEPH, DELPHI, L3, OPAL, and LEPElectroweakWorkingGroup, *Electroweak measurements in electron-positron collisions at W-boson-pair energies at LEP*, Phys. Rep. **532** (2013) 119.

[15] L. Evans and P. Bryant, *LHC machine*, J. Instrum. **3** (2008) S08001.

[16] P. Mouche, *Overall view of the LHC*, 2014. https://cds.cern.ch/record/1708847. licenced under CC-BY-4.0.

[17] B. Schmidt, *The High-Luminosity upgrade of the LHC: Physics and technology challenges for the accelerator and the experiments*, J. Phys. Conf. Ser. **706** (2016) 022002.

[18] ATLAS Collaboration, *The ATLAS Experiment at the CERN Large Hadron Collider*, J. Instrum. **3** (2008) S08003, licenced under CC-BY-3.0.

[19] CMS Collaboration, *The CMS experiment at the CERN LHC*, J. Instrum. **3** (2008) S08004.

[20] LHCb Collaboration, *The LHCb detector at the LHC*, J. Instrum. **3** (2008) S08005.

[21] ALICE Collaboration, *The ALICE experiment at the CERN LHC*, J. Instrum. **3** (2008) S08002.

[22] J. Wenninger, *Machine protection and operation for LHC*, CERN Yellow Rep. **2** (2016) 377, licenced under CC-BY-4.0.

[23] E. Mobs, *The CERN accelerator complex - August 2018*, 2018. https://cds.cern.ch/record/2636343.

[24] ATLAS Collaboration, *ATLAS data quality operations and performance for 2015-2018 data-taking*, J. Instrum. **15** (2020) P04003, licenced under CC-BY-4.0.

[25] ATLAS Collaboration, *Measurement of the inelastic proton-proton cross section at* $\sqrt{s} = 13$ *TeV with the ATLAS detector at the LHC*, Phys. Rev. Lett. **117** (2016) 182002.

[26] E. Daw, *Lecture 7 - Rapidity and Pseudorapidity*, 2012. https://www.hep.shef.ac.uk/edaw/PHY206/Site/2012_course_files/phy206rlec7.pdf. Lecture note.

[27] ATLAS Collaboration, *ATLAS magnet system: technical design report, 1*, Tech. Rep. CERN-LHCC-97-018, 1997. https://cds.cern.ch/record/338080.

[28] ATLAS Collaboration, *ATLAS inner detector: technical design report, 1*, Tech. Rep. CERN-LHCC-97-016, 1997. https://cds.cern.ch/record/331063.

[29] J. Pequenao, *Computer generated image of the ATLAS inner detector*, 2008. https://cds.cern.ch/record/1095926.

[30] O. Pastor, *Novel methods in track-based alignment to correct for time-dependent distortions of the ATLAS Inner Detector*, J. Phys. Conf. Ser. **1136** (2018) 012003.

[31] M. S. Kayl, *Tracking performance of the ATLAS Inner Detector and observation of known hadrons*, Tech. Rep. ATL-PHYS-PROC-2010-085, 2010. https://cds.cern.ch/record/1295934.

[32] ATLAS Collaboration, *ATLAS pixel detector electronics and sensors*, J. Instrum. **3** (2008) P07007.

[33] ATLAS Collaboration, *ATLAS Insertable B-Layer technical design report*, Tech. Rep. CERN-LHCC-2010-013, 2010. https://cds.cern.ch/record/1291633.

[34] M. Keil, *Operational Experience with the ATLAS Pixel Detector at the LHC*, Phys. Procedia **37** (2012) 907–914, licenced under CC-BY-NC-ND-3.0.

[35] H. Pernegger, *The Pixel Detector of the ATLAS experiment for LHC Run-2*, J. Instrum. **10** (2015) C06012, licenced under CC-BY-4.0.

[36] A. Abdesselam et al., *The barrel modules of the ATLAS semiconductor tracker*, Nucl. Instrum. Meth. A **568** (2006) 642, licenced under CC-BY-4.0.

[37] A. Abdesselam et al., *The ATLAS semiconductor tracker end-cap module*, Nucl. Instrum. Meth. A **575** (2007) 353.

[38] E. Abat et al., *The ATLAS Transition Radiation Tracker (TRT) proportional drift tube: design and performance*, J. Instrum. **3** (2008) P02013.

[39] B. Mindur, *ATLAS Transition Radiation Tracker (TRT): Straw tubes for tracking and particle identification at the Large Hadron Collider*, Nucl. Instrum. Meth. A **845** (2017) 257.

[40] ATLAS Collaboration, *Performance of the ATLAS Transition Radiation Tracker in Run 1 of the LHC: tracker properties*, J. Instrum. **12** (2017) P05002.

[41] J. Pequenao, *Computer Generated image of the ATLAS calorimeter*, 2008. https://cds.cern.ch/record/1095927.

[42] ATLAS Collaboration, *ATLAS liquid-argon calorimeter: technical design report*, Tech. Rep. CERN-LHCC-96-041, 1996. https://cds.cern.ch/record/331061.

[43] ATLAS Collaboration, *Drift time measurement in the ATLAS liquid argon electromagnetic calorimeter using cosmic muons*, Eur. Phys. J. C **70** (2010) 755, licenced under CC-BY-3.0.

[44] ATLAS Collaboration, *ATLAS tile calorimeter: technical design report*, Tech. Rep. CERN-LHCC-96-042, 1996. https://cds.cern.ch/record/331062.

[45] ATLAS Collaboration, *ATLAS muon spectrometer: technical design report*, Tech. Rep. CERN-LHCC-97-022, 1997. https://cds.cern.ch/record/331068.

[46] J. Pequenao, *Computer generated image of the ATLAS Muons subsystem*, 2008. https://cds.cern.ch/record/1095929.

[47] M. Livan, *Monitored drift tubes in ATLAS*, Nucl. Instrum. Meth. A **384** (1996) 214.

[48] T. Argyropoulos et al., *Cathode strip chambers in ATLAS: Installation, commissioning and in situ performance*, IEEE Trans. Nucl. Sci. **56** (2009) 1568.

[49] G. Cattani, *The resistive plate chambers of the ATLAS experiment: Performance studies*, J. Phys. Conf. Ser. **280** (2011) 012001.

[50] ATLAS Collaboration, *Standalone vertex finding in the ATLAS muon spectrometer*, J. Instrum. **9** (2014) P02001, licenced under CC-BY-4.0.

[51] K. Nagai, *Thin gap chambers in ATLAS*, Nucl. Instrum. Meth. A **384** (1996) 219.

[52] G. Avoni et al., *The new LUCID-2 detector for luminosity measurement and monitoring in ATLAS*, J. Instrum. **13** (2018) P07017.

[53] S. A. Khalek et al., *The ALFA Roman Pot detectors of ATLAS*, J. Instrum. **11** (2016) P11013.

[54] ATLAS Collaboration, *Measurement of the total cross section and ρ-parameter from elastic scattering in pp collisions at $\sqrt{s}$=13 TeV with the ATLAS detector.*, Eur. Phys. J. C **83** (2023) 441.

[55] U. Amaldi et al., *Measurements of the proton-proton total cross section by means of coulomb scattering at the CERN intersecting storage rings*, Phys. Lett. B **43** (1973) 231.

[56] P. Jenni, M. Nessi, and M. Nordberg, *Zero Degree Calorimeters for ATLAS*, Tech. Rep. CERN-LHCC-2007-001, 2007. https://cds.cern.ch/record/1009649.

[57] ATLAS Collaboration, *ATLAS forward detectors*, 2018. https://cds.cern.ch/record/2627582.

[58] ATLAS Collaboration, *Operation of the ATLAS trigger system in Run 2*, J. Instrum. **15** (2020) P10004, licenced under CC-BY-4.0.

[59] J. Pequenao and P. Schaffner, *How ATLAS detects particles: diagram of particle paths in the detector*, 2013. https://cds.cern.ch/record/1505342.

[60] ATLAS Collaboration, *Performance of the ATLAS track reconstruction algorithms in dense environments in LHC run 2*, Eur. Phys. J. C **77** (2017) 673.

[61] R. Frühwirth, *Application of Kalman filtering to track and vertex fitting*, Nucl. Instrum. Meth. Phys. Res. A **262** (1987) 444.

[62] T. G. Cornelissen et al., *The global χ^2 track fitter in ATLAS*, J. Phys. Conf. Ser. **119** (2008) 032013.

[63] H. M. Gray, *The charged particle multiplicity at center of mass energies from 900 GeV to 7 TeV measured with the ATLAS experiment at the Large Hadron Collider*. PhD thesis, 2010. https://cds.cern.ch/record/1309943.

[64] T. G. Cornelissen et al., *Updates of the ATLAS tracking event data model (Release 13)*, Tech. Rep. ATL-SOFT-PUB-2007-003, 2007. https://cds.cern.ch/record/1038095.

[65] K. Grimm et al., *Primary vertex reconstruction at the ATLAS experiment*, J. Phys. Conf. Ser. **898** (2017) 042056.

[66] R. Fruhwirth, W. Waltenberger, and P. Vanlaer, *Adaptive vertex fitting*, J. Phys. G **34** (2007) N343.

[67] ATLAS Collaboration, *Topological cell clustering in the ATLAS calorimeters and its performance in LHC Run 1*, Eur. Phys. J. C **77** (2017) 490.

[68] ATLAS Collaboration, *Electron and photon performance measurements with the ATLAS detector using the 2015-2017 LHC proton-proton collision data*, J. Instrum. **14** (2019) P12006.

[69] ATLAS Collaboration, *Improved electron reconstruction in ATLAS using the Gaussian Sum Filter-based model for bremsstrahlung*, Tech. Rep. ATLAS-CONF-2012-047, 2012. https://cds.cern.ch/record/1449796.

[70] ATLAS Collaboration, *Electron and photon efficiencies in LHC Run 2 with the ATLAS experiment*, Tech. Rep. CERN-EP-2023-182, 2023. arXiv:2308.13362.

[71] ATLAS Collaboration, *Muon reconstruction and identification efficiency in ATLAS using the full Run 2 pp collision data set at* $\sqrt{s} = 13$ *TeV*, Eur. Phys. J. C **81** (2021) 578.

[72] S. Rettie, *Muon identification and performance in the ATLAS experiment*, PoS Proc. Sci. **DIS2018** (2018) 097.

[73] M. Cacciari, G. P. Salam, and G. Soyez, *The anti-k_t jet clustering algorithm*, J. High Energy Phys. **04** (2008) 063.

[74] Y. Dokshitzer, G. Leder, S. Moretti, and B. Webber, *Better jet clustering algorithms*, J. High Energy Phys. **08** (1997) 001.

[75] M. Wobisch and T. Wengler, *Hadronization corrections to jet cross-sections in deep inelastic scattering*, Tech. Rep. PITHA-99-16, 1998. arXiv:hep-ph/9907280.

[76] S. Catani, Y. L. Dokshitzer, M. H. Seymour, and B. R. Webber, *Longitudinally invariant K_t clustering algorithms for hadron hadron collisions*, Nucl. Phys. B **406** (1993) 187.

[77] S. D. Ellis and D. E. Soper, *Successive combination jet algorithm for hadron collisions*, Phys. Rev. D **48** (1993) 3160.

[78] ATLAS Collaboration, *Jet reconstruction and performance using particle flow with the ATLAS Detector*, Eur. Phys. J. C **77** (2017) 466.

[79] ATLAS Collaboration, *Jet energy scale and resolution measured in proton-proton collisions at* $\sqrt{s} = 13$ *TeV with the ATLAS detector*, Eur. Phys. J. C **81** (2021) 689.

[80] ATLAS Collaboration, *Jet energy scale measurements and their systematic uncertainties in proton-proton collisions at* $\sqrt{s} = 13$ *TeV with the ATLAS detector*, Phys. Rev. D **96** (2017) 072002.

[81] ATLAS Collaboration, *Performance of pile-up mitigation techniques for jets in pp collisions at* $\sqrt{s} = 8$ *TeV using the ATLAS detector*, Eur. Phys. J. C **76** (2016) 581.

[82] H. Voss, A. Höcker, J. Stelzer, and F. Tegenfeldt, *TMVA, the toolkit for multivariate data analysis with ROOT*, PoS Proc. Sci. **ACAT** (2009) 040.

[83] ATLAS Collaboration, *Tagging and suppression of pileup jets with the ATLAS detector*, Tech. Rep. ATLAS-CONF-2014-018, 2014. https://cds.cern.ch/record/1700870.

[84] ATLAS Collaboration, *Identification and rejection of pile-up jets at high pseudorapidity with the ATLAS detector*, Eur. Phys. J. C **77** (2017) 580.

[85] ATLAS Collaboration, *ATLAS flavour-tagging algorithms for the LHC Run 2 pp collision dataset*, Eur. Phys. J. C **83** (2023) 681.

[86] ATLAS Collarboration, *Optimisation and performance studies of the ATLAS b-tagging algorithms for the 2017-18 LHC run*, Tech. Rep. ATL-PHYS-PUB-2017-013, 2017. https://cds.cern.ch/record/2273281.

[87] ATLAS Collaboration, *Identification of jets containing b-hadrons with Recurrent Neural Networks at the ATLAS experiment*, Tech. Rep. ATL-PHYS-PUB-2017-003, 2017. https://cds.cern.ch/record/2255226.

[88] ATLAS Collaboration, *Secondary vertex finding for jet flavour identification with the ATLAS detector*, Tech. Rep. ATL-PHYS-PUB-2017-011, 2017. https://cds.cern.ch/record/2270366.

[89] ATLAS Collaboration, *Topological b-hadron decay reconstruction and identification of b-jets with the JetFitter package in the ATLAS experiment at the LHC*, Tech. Rep. ATL-PHYS-PUB-2018-025, 2018. https://cds.cern.ch/record/2645405.

[90] ATLAS Collaboration, *ATLAS b-jet identification performance and efficiency measurement with $t\bar{t}$ events in pp collisions at $\sqrt{s} = 13$ TeV*, Eur. Phys. J. C **79** (2019) 970.

[91] ATLAS Collaboration, *Performance of missing transverse momentum reconstruction with the ATLAS detector using proton-proton collisions at $\sqrt{s} = 13$ TeV*, Eur. Phys. J. C **78** (2018) 903.

[92] E. Bothmann et al., *Event generation with Sherpa 2.2*, SciPost Phys. **7** (2019) 034.

[93] S. Frixione, P. Nason, and C. Oleari, *Matching NLO QCD computations with parton shower simulations: the POWHEG method*, J. High Energy Phys. **11** (2007) 070.

[94] T. Sjöstrand, S. Mrenna, and P. Skands, *A brief introduction to PYTHIA 8.1*, Comput. Phys. Commun. **178** (2008) 852.

[95] ATLAS Collaboration, *Jet energy resolution in proton-proton collisions at $\sqrt{s} = 7$ TeV recorded in 2010 with the ATLAS detector.*, Eur. Phys. J. C **73** (2013) 2306.

[96] M. Abadi et al., *TensorFlow: Large-scale machine learning on heterogeneous distributed systems*, tech. rep., 2016. arXiv:1603.04467.

[97] J. Heaton, *Applications of deep neural networks with Keras*, tech. rep., 2020. arXiv:2009.05673.

[98] P. Baldi, P. Sadowski, and D. Whiteson, *Deep learning from four vectors*, tech. rep., 2022. arXiv:2203.03067.

[99] ATLAS Collaboration, *Performance of electron and photon triggers in ATLAS during LHC Run 2*, Eur. Phys. J. C **80** (2020) 47.

[100] ATLAS Collaboration, *Performance of the ATLAS muon triggers in Run 2*, J. Instrum. **15** (2020) P09015.

[101] S. Agostinelli et al., *Geant4—a simulation toolkit*, Nucl. Instrum. Meth. A **506** (2003) 250.

[102] ATLAS Collaboration, *The ATLAS simulation infrastructure*, Eur. Phys. J. C **70** (2010) 823.

[103] ATLAS Collaboration, *The Pythia 8 A3 tune description of ATLAS minimum bias and inelastic measurements incorporating the Donnachie-Landshoff diffractive model*, Tech. Rep. ATL-PHYS-PUB-2016-017, 2016. https://cds.cern.ch/record/2206965.

[104] R. D. Ball et al., *Parton distributions for the LHC run II*, J. High Energy Phys. **04** (2015).

[105] P. Nason, *A new method for combining NLO QCD with shower Monte Carlo algorithms*, J. High Energy Phys. **11** (2004) 040.

[106] S. Alioli, P. Nason, C. Oleari, and E. Re, *A general framework for implementing NLO calculations in shower Monte Carlo programs: the POWHEG BOX*, J. High Energy Phys. **06** (2010) 043.

[107] K. Hamilton, P. Nason, E. Re, and G. Zanderighi, *NNLOPS simulation of Higgs boson production*, J. High Energy Phys. **10** (2013) 222.

[108] K. Hamilton, P. Nason, E. Re, and G. Zanderighi, *Finite quark-mass effects in the NNLOPS POWHEG+MiNLO Higgs generator*, J. High Energy Phys. **05** (2015) 140.

[109] J. M. Campbell et al., *NLO Higgs boson production plus one and two jets using the POWHEG BOX, MadGraph4 and MCFM*, J. High Energy Phys. **07** (2012) 092.

[110] P. Nason and C. Oleari, *NLO Higgs boson production via vector-boson fusion matched with shower in POWHEG*, J. High Energy Phys. **02** (2010) 037.

[111] J. Butterworth et al., *PDF4LHC recommendations for LHC Run II*, J. Phys. G: Nucl. Part. Phys. **43** (2016) 023001.

[112] T. Sjöstrand et al., *An introduction to PYTHIA 8.2*, Comput. Phys. Commun. **191** (2015) 159.

[113] C. Anastasiou et al., *High precision determination of the gluon fusion Higgs boson cross-section at the LHC*, J. High Energy Phys. **05** (2016) 058.

[114] C. Anastasiou, C. Duhr, F. Dulat, F. Herzog, and B. Mistlberger, *Higgs boson gluon-fusion production in QCD at three loops*, Phys. Rev. Lett. **114** (2015) 212001.

[115] F. Dulat, A. Lazopoulos, and B. Mistlberger, *iHixs 2 — Inclusive Higgs cross sections*, Comput. Phys. Commun. **233** (2018) 243.

[116] R. V. Harlander and K. J. Ozeren, *Finite top mass effects for hadronic Higgs production at next-to-next-to-leading order*, J. High Energy Phys. **11** (2009) 088.

[117] R. V. Harlander and K. J. Ozeren, *Top mass effects in Higgs production at next-to-next-to-leading order QCD: Virtual corrections*, Phys. Lett. B **679** (2009) 467.

[118] R. V. Harlander, H. Mantler, S. Marzani, and K. J. Ozeren, *Higgs production in gluon fusion at next-to-next-to-leading order QCD for finite top mass*, Eur. Phys. J. C **66** (2010) 359.

[119] A. Pak, M. Rogal, and M. Steinhauser, *Finite top quark mass effects in NNLO Higgs boson production at LHC*, J. High Energy Phys. **02** (2010) 025.

[120] S. Actis, G. Passarino, C. Sturm, and S. Uccirati, *NLO electroweak corrections to Higgs boson production at hadron colliders*, Phys. Lett. B **670** (2008) 12.

[121] S. Actis, G. Passarino, C. Sturm, and S. Uccirati, *NNLO computational techniques: The cases $H \to \gamma\gamma$ and $H \to gg$*, Nucl. Phys. B **811** (2009) 182.

[122] M. Bonetti, K. Melnikov, and L. Tancredi, *Higher order corrections to mixed QCD-EW contributions to Higgs boson production in gluon fusion*, Phys. Rev. D **97** (2018) 056017.

[123] M. Ciccolini, A. Denner, and S. Dittmaier, *Strong and electroweak corrections to the production of a Higgs boson + 2 jets via weak interactions at the Large Hadron Collider*, Phys. Rev. Lett. **99** (2007) 161803.

[124] M. Ciccolini, D. A., and D. S., *Electroweak and QCD corrections to Higgs production via vector-boson fusion at the CERN LHC*, Phys. Rev. D **77** (2008) 013002.

[125] P. Bolzoni, F. Maltoni, S.-O. Moch, and M. Zaro, *Higgs boson production via vector-boson fusion at next-to-next-to-leading order in QCD*, Phys. Rev. Lett. **105** (2010) 011801.

[126] M. L. Ciccolini, S. Dittmaier, and M. Krämer, *Electroweak radiative corrections to associated WH and ZH production at hadron colliders*, Phys. Rev. D **68** (2003) 073003.

[127] O. Brein, A. Djouadi, and R. Harlander, *NNLO QCD corrections to the Higgs-strahlung processes at hadron colliders*, Phys. Lett. B **579** (2004) 149.

[128] O. Brein, R. V. Harlander, M. Wiesemann, and T. Zirke, *Top-quark mediated effects in hadronic Higgs-strahlung*, Eur. Phys. J. C **72** (2012) 1868.

[129] O. Brein, R. V. Harlander, and T. J. Zirke, *vh@nnlo—Higgs-strahlung at hadron colliders*, Comput. Phys. Commun. **184** (2013) 998.

[130] A. Denner, S. Dittmaier, S. Kallweit, and A. Mück, *HAWK 2.0: A Monte Carlo program for Higgs production in vector-boson fusion and Higgs strahlung at hadron colliders*, Comput. Phys. Commun. **195** (2015) 161.

[131] S. Höche, F. Krauss, S. Schumann, and F. Siegert, *QCD matrix elements and truncated showers*, J. High Energy Phys. **05** (2009) 053.

[132] S. Schumann and F. Krauss, *A parton shower algorithm based on Catani-Seymour dipole factorisation*, J. High Energy Phys. **03** (2008) 038.

[133] T. Gleisberg and S. Höche, *Comix, a new matrix element generator*, J. High Energy Phys. **12** (2008) 039.

[134] S. Höche, F. Krauss, M. Schönherr, and F. Siegert, *A critical appraisal of NLO+PS matching methods*, J. High Energy Phys. **09** (2012) 049.

[135] S. Höche, F. Krauss, M. Schönherr, and F. Siegert, *QCD matrix elements + parton showers. The NLO case*, J. High Energy Phys. **04** (2013) 027.

[136] S. Catani, F. Krauss, B. R. Webber, and R. Kuhn, *QCD Matrix Elements + Parton Showers*, J. High Energy Phys. **11** (2001) 063.

[137] F. Cascioli, P. Maierhöfer, and S. Pozzorini, *Scattering amplitudes with Open Loops*, Phys. Rev. Lett. **108** (2012) 111601.

[138] A. Denner, S. Dittmaier, and L. Hofer, *Collier: A fortran-based complex one-loop library in extended regularizations*, Comput. Phys. Commun. **212** (2017) 220.

[139] F. Buccioni et al., *OpenLoops 2*, Eur. Phys. J. C **79** (2019) 866.

[140] F. Caola, K. Melnikov, R. Röntsch, and L. Tancredi, *QCD corrections to W^+W^- production through gluon fusion*, Phys. Lett. B **754** (2016) 275.

[141] J. Alwall et al., *The automated computation of tree-level and next-to-leading order differential cross sections, and their matching to parton shower simulations*, J. High Energy Phys. **07** (2014) 079.

[142] F. Cascioli et al., *Precise Higgs-background predictions: merging NLO QCD and squared quark-loop corrections to four-lepton+0,1 jet production*, J. High Energy Phys. **01** (2014) 046.

[143] ATLAS Collaboration, *Modelling and computational improvements to the simulation of single vector-boson plus jet processes for the ATLAS experiment*, J. High Energy Phys. **08** (2022) 089.

[144] C. Anastasiou, L. Dixon, K. Melnikov, and F. Petriello, *High-precision QCD at hadron colliders: Electroweak gauge boson rapidity distributions at next-to-next-to leading order*, Phys. Rev. D **69** (2004) 094008.

[145] N. Kidonakis, *Two-loop soft anomalous dimensions for single top quark associated production with a W^- or H^-*, Phys. Rev. D **82** (2010) 054018.

[146] N. Kidonakis, *Top quark production*. Helmholtz International Summer School on Physics of Heavy Quarks and Hadrons. 2013. arXiv:1311.0283.

[147] M. Beneke, P. Falgari, S. Klein, and C. Schwinn, *Hadronic top-quark pair production with NNLL threshold resummation*, Nucl. Phys. B **855** (2012) 695.

[148] M. Cacciari, M. Czakon, M. Mangano, A. Mitov, and P. Nason, *Top-pair production at hadron colliders with next-to-next-to-leading logarithmic soft-gluon resummation*, Phys. Lett. B **710** (2012) 612.

[149] P. Bärnreuther, M. Czakon, and A. Mitov, *Percent-level-precision physics at the Tevatron: next-to-next-to-leading order QCD corrections to* $q\bar{q} \to t\bar{t} + X$, Phys. Rev. Lett. **109** (2012) 132001.

[150] M. Czakon and A. Mitov, *NNLO corrections to top-pair production at hadron colliders: the all-fermionic scattering channels*, J. High Energy Phys. **12** (2012) 054.

[151] M. Czakon and A. Mitov, *NNLO corrections to top pair production at hadron colliders: the quark-gluon reaction*, J. High Energy Phys. **01** (2013) 080.

[152] M. Czakon, P. Fiedler, and A. Mitov, *Total top-quark pair-production cross section at hadron colliders through* $O(\alpha_S^4)$, Phys. Rev. Lett. **110** (2013) 252004.

[153] K. Hamilton, P. Nason, and G. Zanderighi, *MINLO: multi-scale improved NLO*, J. High Energy Phys. **10** (2012) 155.

[154] K. Hamilton, P. Nason, C. Oleari, and G. Zanderighi, *Merging H/W/Z + 0 and 1 jet at NLO with no merging scale: a path to parton shower + NNLO matching*, J. High Energy Phys. **05** (2013) 155.

[155] S. Catani and M. Grazzini, *Next-to-next-to-leading-order subtraction formalism in hadron collisions and its application to Higgs-boson production at the Large Hadron Collider*, Phys. Rev. Lett. **98** (2007) 222002.

[156] ATLAS Collaboration, *Measurement of the* Z/γ^* *boson transverse momentum distribution in pp collisions at* $\sqrt{s} = 7$ *TeV with the ATLAS detector*, J. High Energy Phys. **09** (2014) 145.

[157] ATLAS Collaboration, *ATLAS Pythia 8 tunes to 7 TeV data*, Tech. Rep. ATL-PHYS-PUB-2014-021, 2014. https://cds.cern.ch/record/1966419.

[158] A. Djouadi, J. Kalinowski, and M. Spira, *HDECAY: a program for Higgs boson decays in the Standard Model and its supersymmetric extension*, Comput. Phys. Commun. **108** (1998) 56.

[159] A. Djouadi, M. M. Muhlleitner, and M. Spira, *Decays of supersymmetric particles: the program SUSY-HIT (SUspect-SdecaY-Hdecay-InTerface)*, Acta Phys. Polon. B **38** (2006) 635.

[160] M. Spira, *QCD effects in Higgs physics*, Fortsch. Phys. **46** (1998) 203.

[161] A. Bredenstein, A. Denner, S. Dittmaier, and M. M. Weber, *Radiative corrections to the semileptonic and hadronic Higgs-boson decays* $H \to WW/ZZ \to 4$ *fermions*, J. High Energy Phys. **02** (2007) 080.

[162] A. Bredenstein, A. Denner, S. Dittmaier, and M. M. Weber, *Precise predictions for the Higgs-boson decay* $H \to WW/ZZ \to 4$ *leptons*, Phys. Rev. D **74** (2006) 013004.

[163] A. Bredenstein, A. Denner, S. Dittmaier, and M. Weber, *Precision calculations for the Higgs decays* $H \to ZZ/WW \to 4$ *leptons*, Nucl. Phys. B Proc. Suppl. **160** (2006) 131.

[164] D. J. Lange, *The EvtGen particle decay simulation package*, Nucl. Instrum. Meth. A **462** (2001) 152.

[165] S. Frixione, E. Laenen, P. Motylinski, C. White, and B. R. Webber, *Single-top hadroproduction in association with a W boson*, J. High Energy Phys. **07** (2008) 029.

[166] F. Demartin, B. Maier, F. Maltoni, K. Mawatari, and M. Zaro, *tWH associated production at the LHC*, Eur. Phys. J. C **77** (2017) 34.

[167] ATLAS Collaboration, *Studies on top-quark Monte Carlo modelling for Top2016*, Tech. Rep. ATL-PHYS-PUB-2016-020, 2016. https://cds.cern.ch/record/2216168.

[168] M. Czakon, D. Heymes, A. Mitov, D. Pagani, I. Tsinikos, and M. Zaro, *Top-pair production at the LHC through NNLO QCD and NLO EW*, J. High Energy Phys. **10** (2017) 186.

[169] G. Borissov et al., *ATLAS strategy for primary vertex reconstruction during Run-2 of the LHC*, J. Phys. Conf. Ser. **664** (2015) 072041.

[170] M. Cacciari, G. P. Salam, and G. Soyez, *FastJet user manual*, Eur. Phys. J. C **72** (2012) 1896.

[171] ATLAS Collaboration, *Object-based missing transverse momentum significance in the ATLAS detector*, Tech. Rep. ATLAS-CONF-2018-038, 2018. https://cds.cern.ch/record/2630948.

[172] C. Lester and D. Summers, *Measuring masses of semi-invisibly decaying particle pairs produced at hadron colliders*, Phys. Lett. B **463** (1999) 99.

[173] A. Barr, C. Lester, and P. Stephens, *A variable for measuring masses at hadron colliders when missing energy is expected; m_{T2}: the truth behind the glamour*, J. Phys. G: Nucl. Part. Phys. **29** (2003) 2343.

[174] C. Lester, *The stransverse mass, m_{T2}, in special cases*, J. High Energy Phys. **5** (2011) 076.

[175] J. A. Nelder and R. Mead, *A simplex method for function minimization*, Comput. J. **7** (1965) 308.

[176] T. Plehn, D. Rainwater, and D. Zeppenfield, *A method for identifying $H \to \tau^+\tau^- \to e^\pm\mu^\mp p_T$ at the CERN LHC*, Phys. Rev. D **61** (2000) 093005.

[177] ATLAS Collarboration, *Formulae for estimating significance*, Tech. Rep. ATL-PHYS-PUB-2020-025, 2020. https://cds.cern.ch/record/2736148.

[178] ATLAS Collaboration, *Tools for estimating fake/non-prompt lepton backgrounds with the ATLAS detector at the LHC*, Tech. Rep. CERN-EP-2022-214, 2022. arXiv:2211.16178.

[179] ATLAS Collaboration, *Luminosity determination in pp collisions at $\sqrt{s} = 13$ TeV using the ATLAS detector at the LHC*, Tech. Rep. ATLAS-CONF-2019-021, 2019. https://cds.cern.ch/record/2677054.

[180] V. N. Gribov and L. N. Lipatov, *Deep inelastic ep scattering in perturbation theory*, Sov. J. Nucl. Phys. **15** (1972) 438.

[181] L. N. Lipatov, *The parton model and perturbation theory*, Sov. J. Nucl. Phys. **20** (1975) 94.

[182] G. Altarelli and G. Parisi, *Asymptotic freedom in parton language*, Nucl. Phys. B **126** (1977) 298.

[183] Y. L. Dokshitzer, *Calculation of the structure functions for deep inelastic scattering and e^+e^- annihilation by perturbation theory in quantum chromodynamics*, Sov. Phys. JETP **46** (1977) 641.

[184] F. Maltoni, T. McElmurry, R. Putman, and S. Willenbrock, *Choosing the factorization scale in perturbative QCD*, tech. rep., 2007. arXiv:hep-ph/0703156.

[185] C. Schmidt, J. Pumplin, and C.-P. Yuan, *Updating and optimizing error parton distribution function sets in the Hessian approach*, Phys. Rev. D **98** (2018) 094005.

[186] D. d'Enterria et al., *The strong coupling constant: State of the art and the decade ahead*, Tech. Rep. FERMILAB-CONF-22-148-T, 2022. arXiv:2203.08271.

[187] A. Buckley et al., *General-purpose event generators for LHC physics*, Phys. Rep. **504** (2011) 145.

[188] S. Catani, *Soft gluon resummation: A Short review*, Tech. Rep. LPTHE-ORSAY-97-46, 1997. arXiv:hep-ph/9709503.

[189] I. W. Stewart and F. J. Tackmann, *Theory uncertainties for Higgs mass and other searches using jet bins*, Phys. Rev. D **85** (2012) 034011.

[190] B. Biedermann, A. Denner, and M. Pellen, *Complete NLO corrections to W^+W^+ scattering and its irreducible background at the LHC*, J. High Energy Phys. **10** (2017) 124.

[191] A. Denner, S. Dittmaier, P. Maierhöfer, M. Pellen, and C. Schwan, *QCD and electroweak corrections to WZ scattering at the LHC*, J. High Energy Phys. **06** (2019) 067.

[192] A. Denner, R. Franken, M. Pellen, and T. Schmidt, *NLO QCD and EW corrections to vector-boson scattering into ZZ at the LHC*, J. High Energy Phys. **11** (2020) 110.

[193] S. Kallweit, J. M. Lindert, P. Maierhöfer, S. Pozzorini, and M. Schönherr, *NLO electroweak automation and precise predictions for W+multijet production at the LHC*, J. High Energ. Phys. **4** (2015) 012.

[194] M. Grazzini, S. Kallweit, M. Wiesemann, and J. Yook, *W^+W^- production at the LHC: NLO QCD corrections to the loop-induced gluon fusion channel*, Phys. Lett. B **804** (2020) 135399.

[195] R. Barlow and C. Beeston, *Fitting using finite Monte Carlo samples*, Comput. Phys. Commun. **77** (1993) 219.

[196] M. Baak et al., *HistFitter software framework for statistical data analysis*, Eur. Phys. J. C **75** (2015) 153.

[197] K. Cranmer et al., *HistFactory: A tool for creating statistical models for use with RooFit and RooStats*, Tech. Rep. CERN-OPEN-2012-016, 2012. http://cds.cern.ch/record/1456844.

[198] W. Verkerke and D. Kirkby, *The RooFit toolkit for data modeling*, tech. rep., 2003. arXiv:physics/0306116.

[199] L. Moneta et al., *The RooStats project*, tech. rep., 2011. arXiv:1009.1003.

[200] F. James, *MINUIT: Function minimization and error analysis reference manual*, Tech. Rep. CERNLIB-D506, 1998. https://cds.cern.ch/record/2296388.

[201] E. Gross, *Practical statistics for high energy physics*, CERN Yellow Rep.: Sch. Proc. **3** (2018) 199.

[202] G. Cowan, K. Cranmer, E. Gross, and O. Vitells, *Asymptotic formulae for likelihood-based tests of new physics*, Eur. Phys. J. C **71** (2011) 1554.

[203] A. L. Read, *Presentation of search results: the CL_s technique*, J. Phys. G: Nucl. Part. Phys. **28** (2002) 2693.

[204] G. Ranucci, *The profile likelihood ratio and the look elsewhere effect in high energy physics*, Nucl. Instrum. Methods Phys. Res. **661** (2012) 77.